

8-2018

## Impacts of Anisotropy, Wave Heating, and Neutral Winds on High-Latitude Ionospheric Dynamics

Meghan R. Burleigh

Follow this and additional works at: <https://commons.erau.edu/edt>



Part of the [Engineering Physics Commons](#)

---

### Scholarly Commons Citation

Burleigh, Meghan R., "Impacts of Anisotropy, Wave Heating, and Neutral Winds on High-Latitude Ionospheric Dynamics" (2018). *Dissertations and Theses*. 408.  
<https://commons.erau.edu/edt/408>

This Dissertation - Open Access is brought to you for free and open access by Scholarly Commons. It has been accepted for inclusion in Dissertations and Theses by an authorized administrator of Scholarly Commons. For more information, please contact [commons@erau.edu](mailto:commons@erau.edu).

IMPACTS OF ANISOTROPY, WAVE HEATING, AND NEUTRAL  
WINDS ON HIGH-LATITUDE IONOSPHERIC DYNAMICS

BY  
MEGHAN R. BURLEIGH

A Dissertation  
Submitted to the Department of Physical Sciences  
In partial fulfillment of the requirements  
for the degree of  
Doctor of Philosophy in Engineering Physics

08/2018  
Embry-Riddle Aeronautical University  
Daytona Beach, Florida

© Copyright by Meghan R. Burleigh 2018  
All Rights Reserved


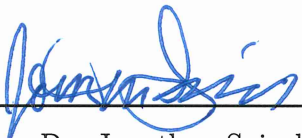
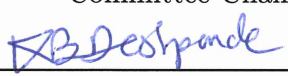
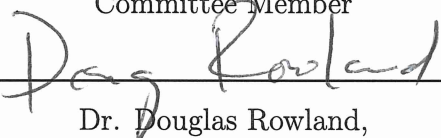
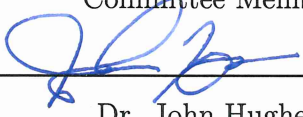
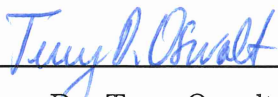
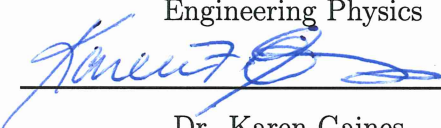
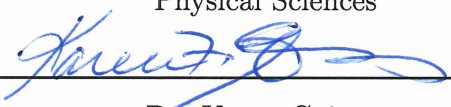
IMPACTS OF ANISOTROPY, WAVE HEATING, AND NEUTRAL  
WINDS ON HIGH-LATITUDE IONOSPHERIC DYNAMICS

by

Meghan R. Burleigh

This dissertation was prepared under the direction of the candidate's Dissertation Committee Chair, Dr. Matthew Zettergren, Associate Professor, Daytona Beach Campus, and Dissertation Committee Members Dr. Jonathan Snively, Associate Professor, Daytona Beach Campus, and Dr. Kshitija Deshpande, Assistant Professor, Daytona Beach Campus, Dr. Douglas Rowland, GSFC, NASA and has been approved by the Dissertation Committee. It was submitted to the Department of Physical Sciences in partial fulfillment of the requirements for the degree of Doctor of Philosophy in Engineering Physics

DISSERTATION COMMITTEE:

 <hr/>	 <hr/>
Dr. Matthew Zettergren, Committee Chair	Dr. Jonathan Snively, Committee Member
 <hr/>	 <hr/>
Dr. Kshitija Deshpande, Committee Member	Dr. Douglas Rowland, Committee Member
 <hr/>	 <hr/>
Dr. John Hughes, Acting Graduate Program Chair, Engineering Physics	Dr. Terry Oswalt, Department Chair, Physical Sciences
 <hr/>	 <hr/>
Dr. Karen Gaines, Dean, College of Arts and Sciences	Dr. Karen Gaines, Dean of Research and Graduate Studies

# Abstract

Significant amounts of ionospheric plasma can be transported to high altitudes (ion upflow) in response to a variety of plasma heating and uplifting processes such as DC electric fields and precipitation. Once ions have been lifted to high altitudes, transverse ion acceleration by broadband ELF waves can give the upflowing ions sufficient energy for the mirror force to propel these ions to escape into the magnetosphere (ion outflow). In order to accurately examine the connection between upflow and outflow processes, a new two dimensional, anisotropic fluid model is developed.

The new model, named GEMINI-TIA, is based on a Bi-Maxwellian distribution function and solves the time-dependent, nonlinear equations of conservation of mass, momentum, parallel energy, and perpendicular energy for six ion species important to the E-, F-, and topside ionospheric regions:  $O^+$ ,  $NO^+$ ,  $N_2^+$ ,  $O_2^+$ ,  $N^+$ , and  $H^+$ . Electrons have also been included using an isotropic description. The effects of photoionization, electron impact ionization, wave particle interactions and chemical and collisional interactions with the neutral atmosphere are included. In order to facilitate comparisons with data, the model accepts as inputs the main drivers of ion upflow and outflow: particle precipitation, electric fields, ELF wave power, and neutral winds and densities. GEMINI-TIA is used here in parametric and realistic case studies of ion upflow and outflow.

In this research, GEMINI-TIA is first used in direct comparison with its parent isotropic model GEMINI to examine differences between isotropic and anisotropic descriptions of ionospheric upflow driven by DC electric fields. Further differences between isotropic and anisotropic descriptions of ionospheric upflow are examined

through an additional comparison study that utilizes ionospheric drivers with realistic spatial and temporal variations. GEMINI-TIA, and its parent isotropic model GEMINI, are constrained by the MICA sounding rocket campaign data and respective outputs compared to analyze the impacts of anisotropy on low altitude ionospheric dynamics, specifically density cavity formation and related upflow.

Next, GEMINI-TIA is used in a parametric study to examine ionospheric upflow driven by DC electric fields, possible effects of low-altitude wave heating, and impacts of neutral winds on ion upflow. Simulations show significant responses at low altitudes to wave heating for very large power spectral densities, but ion temperature anisotropies below the F region peak are dominated by frictional heating from DC electric fields. The time history of the neutral winds is also shown to affect the amount of ions transported to higher altitudes by DC electric fields and BBELF waves.

Then, the role of neutral wind disturbances regulating ion outflow is further explored through model coupling between GEMINI-TIA and a neutral dynamics model guided by Sondrestrom ISR data. Specifically, a sequence of simulations with varying wave amplitude are conducted to determine responses to a range of transient forcing reminiscent of the ISR data. Thermospheric motions due to acoustic gravity waves (GWs) drive ion upflow in the F region, modulating the topside ionosphere in a way that can contribute to ion outflow.

Lastly, GEMINI-TIA is used to study the spatiotemporal limitations of data driven modeling using the ISINGLASS sounding rocket campaign. Realistic variability of energy inputs into the ionosphere, from both the thermosphere and magnetosphere, are important when accurately determining the ion upflow/outflow response. Ground data driven simulations capture the shape and duration of ion upflows/downflows more accurately by containing both time and space variability but at the loss of the fine scale details that are present in in situ measurements. During the ISINGLASS campaign, the auroral arc had a pronounced southward drift, not captured in the rocket measurements, which slowly moves energization regions across the ionosphere generating a finite amount of heating in any given location. The overall ionospheric response, including the locations and strengths of upflows and downflow, is highly dependent on the time history of the ionosphere.

# Acknowledgments

First I would express my gratitude to my advisor, Dr. Zettergren, for his guidance and expertise. His endless encouragement and optimism have fueled my determination to succeed. Second I would like to thank my Dissertation Committee, Drs. Snively, Deshpande, and Rowland. I greatly appreciate the time they have taken to help me improve this body of work and those fun moments when we have just talked Science. Many thanks the ISINGLASS sounding rocket team for providing data and guidance. Lastly, I would like to give a big thanks to Matt K.; you know what you did. For this work I have been supported by NSF grant AGS-1255181 and NASA grant NNX14AH07G. Science funding is something we need more of in this world.

# Contents

<b>Abstract</b>	<b>iv</b>
<b>Acknowledgments</b>	<b>vi</b>
<b>1 The Earth’s high-latitude ionosphere</b>	<b>1</b>
1.1 Motivation . . . . .	5
1.2 Dissertation organization . . . . .	10
<b>2 Modeling the high latitude ionosphere</b>	<b>11</b>
2.1 Derivation of the 16-moment transport equations . . . . .	11
2.2 GEMINI-TIA: anisotropic fluid model . . . . .	21
2.2.1 Electrostatic approximation . . . . .	27
2.2.2 Wave-particle interactions . . . . .	29
2.2.3 Collision frequency . . . . .	30
2.2.4 Coulomb collisions . . . . .	32
2.2.5 Maxwell interactions . . . . .	34
2.3 Numerical methods . . . . .	36
2.3.1 Advection . . . . .	36
2.3.2 Non-stiff Sources . . . . .	38
2.3.3 Diffusion . . . . .	39
2.3.4 Stiff Sources . . . . .	41
<b>3 Comparisons with parent model</b>	<b>43</b>
3.1 Impacts of anisotropies . . . . .	43



3.2	MICA case study . . . . .	46
3.3	Chapter conclusions . . . . .	54
<b>4</b>	<b>Ionospheric upflow</b>	<b>56</b>
4.1	Low-altitude wave heating effects on ion upflow . . . . .	59
4.2	Thermospheric wind effects on ion upflow . . . . .	64
4.3	Chapter conclusions . . . . .	71
<b>5</b>	<b>Gravity waves modulate ionospheric upflow</b>	<b>73</b>
5.1	Data Motivating and Guiding Modeling Efforts . . . . .	75
5.2	Modeling Approach . . . . .	78
5.3	Ionospheric Response to Gravity Wave Forcing . . . . .	80
5.4	Chapter conclusions . . . . .	97
<b>6</b>	<b>Ionospheric outflow</b>	<b>99</b>
6.1	Overview of ISINGLASS B . . . . .	100
6.2	Ionospheric response to transient forcing . . . . .	103
6.2.1	In situ driven simulations . . . . .	106
6.2.2	Comparing in situ to ground data . . . . .	114
6.2.3	Ground data driven simulations . . . . .	116
6.3	Chapter conclusions . . . . .	122
<b>7</b>	<b>Conclusions and future work</b>	<b>124</b>
7.1	Science sub-queries . . . . .	124
7.2	Future work . . . . .	128
7.2.1	RENU2 . . . . .	129
7.2.2	VISIONS . . . . .	130
7.3	GEMINI-TIA 3D . . . . .	131
7.3.1	Convection effects on transient upflows . . . . .	131
7.3.2	Nonlinear gravity waves . . . . .	132
7.4	Open-sourcing the code . . . . .	132

# List of Tables

2.1	Isotropic and anisotropic term differences in the collisional frequency equation. . . . .	32
2.2	Values for O <sup>+</sup> -O resonant interactions from <i>Gaimard et al.</i> (1998) for various electric fields. . . . .	35
3.1	Density depletions identified in the Poker Flat ISR measurements during the MICA sounding rocket campaign. . . . .	47
4.1	The wave power spectral density, $ E_0 ^2$ , and DC electric field, $E_{0\perp}$ , used in simulations I - XII plotted in Figure 4.2 and 4.3. . . . .	64
4.2	The power spectral densities, DC electric fields, and geographic neutral winds, used in simulations I - VIII plotted in Figure 4.4 . . . . .	66
4.3	The power spectral densities, DC electric fields, and geographic neutral winds used in simulations I - III plotted in Figure 4.5 . . . . .	69
4.4	The DC electric fields, $E_{0\perp}$ and geographic neutral winds, $v_{n,0}$ , used in simulations I - V plotted in Figure 4.7. . . . .	71
6.1	ISINGLASS sounding rocket campaign data used to drive the model .	106

# List of Figures

1.1	Ion, electron, and neutral specie density profiles. . . . .	1
1.2	Electron heating-driven upflows can be found above auroral arcs. . . . .	2
1.3	Upflow and outflow processes. . . . .	4
3.1	Isotropic vs. anisotropic model response. . . . .	45
3.2	Model and MICA experiment setup . . . . .	47
3.3	Cavity events . . . . .	49
3.4	Cavity event 1 . . . . .	50
3.5	Density cavity comparison . . . . .	51
3.6	Connecting DCE and temperature anisotropy . . . . .	53
3.7	Electron density along the flight trajectory. . . . .	54
4.1	O <sup>+</sup> response to a DC electric field, wave heating, and both energy sources applied simultaneously . . . . .	60
4.2	The O <sup>+</sup> temperature anisotropy factor and field aligned velocity from different combinations of DC electric fields and wave heating . . . . .	63
4.3	O <sup>+</sup> flux vs. time for combinations of DC electric field and wave heating	65
4.4	Impact thermospheric winds have on ion upflow at $t_0+10$ minutes . . . . .	67
4.5	Perpendicular temperature vs. altitude and meridional distance after ten minutes of heating with different configurations of winds . . . . .	68
4.6	The O <sup>+</sup> flux from three simulations at 1000 km and 2500 km . . . . .	69
4.7	The O <sup>+</sup> flux, field aligned velocity, and density at 1000 km for five simulations illustrating the effects of neutral wind onset time on upflow	70

5.1	Sondrestrom incoherent scatter radar (ISR) data on May 31st 2003 . . . . .	76
5.2	The ionospheric and atmospheric model grid alignment. . . . .	80
5.3	The field-aligned velocity component of the GWs generated by the neutral dynamics model. . . . .	82
5.4	The ion dynamics along the center field line of the model grid from 1:00-8:00 UT . . . . .	84
5.5	Morelet wavelet analysis of the field-aligned O <sup>+</sup> velocity . . . . .	87
5.6	Chain of processes responsible for ion upflow. . . . .	89
5.7	A comparison of the production, loss, and inflow transport terms, for O <sup>+</sup> . . . . .	90
5.8	Electron collisional cooling and photoionization heating rates. . . . .	92
5.9	GW driven topside transport alters ion populations available for secondary acceleration processes. . . . .	94
5.10	Transverse wave heating effects are modulated by the GWs. . . . .	96
6.1	Space weather conditions that prompted the launch of ISINGLASS B	102
6.2	Rocket trajectory overlaying aurora imagery from VEE . . . . .	104
6.3	The model (outlined in $\triangle$ ), PFISR (location $\circ$ and beams - - - -), and sounding rocket trajectory (—) locations. . . . .	105
6.4	ISINGLASS B in situ measurements . . . . .	107
6.5	Ionospheric response to the in situ energy sources using only the time variability . . . . .	109
6.6	Ionospheric response to the in situ energy sources using only the space variability . . . . .	111
6.7	Temporal evolution of the ionospheric response of the spatially variable inputs . . . . .	112
6.8	Impact of in situ transverse wave heating . . . . .	113
6.9	PFISR interpolated DCE . . . . .	114
6.10	Trajectory trace of the ground measurements compared to the in situ data . . . . .	115
6.11	The ground data used to drive the model . . . . .	117

6.12 E region effects of pre-heating. . . . .	118
6.13 F region effects of preheating . . . . .	119
6.14 The O <sup>+</sup> flux evolution over time at 1000 km during the rocket flight .	120
6.15 Integration the O <sup>+</sup> flux from Figure 6.14 over time calculates the total O <sup>+</sup> transport at 1000 km for Simulations 2a, 2b, 3, and 4. . . . .	121
7.1 PMAFs observed the night of the RENU2 launch . . . . .	129

# Chapter 1

## The Earth's high-latitude ionosphere

The ionosphere is the ionized portion of the upper atmosphere covering altitudes from ~60 km to >1000 km. Within the ionosphere, density profiles contain distinct peaks (see Figure 1.1) differentiating different layers: D, E, F<sub>1</sub>, and F<sub>2</sub> regions. The D and E regions (~60-100 km and ~100-150 km respectively) are dominated by molecular ions (NO<sup>+</sup>, O<sub>2</sub><sup>+</sup>, and N<sub>2</sub><sup>+</sup>) embedded in a dense concentration of neutrals (N<sub>2</sub>, O<sub>2</sub>, and O). Chemical processes, including ion production and loss, typically dominate in these regions. The ion density is of the order of 10<sup>11</sup> m<sup>-3</sup> which is much less than the local neutral density, typically on the order of 10<sup>17</sup> m<sup>-3</sup>, so the plasma is only weakly ionized. This places more emphasis on the local chemistry and neutral transport than plasma transport processes in most situations. In the F<sub>1</sub> region (~150-250 km) the main

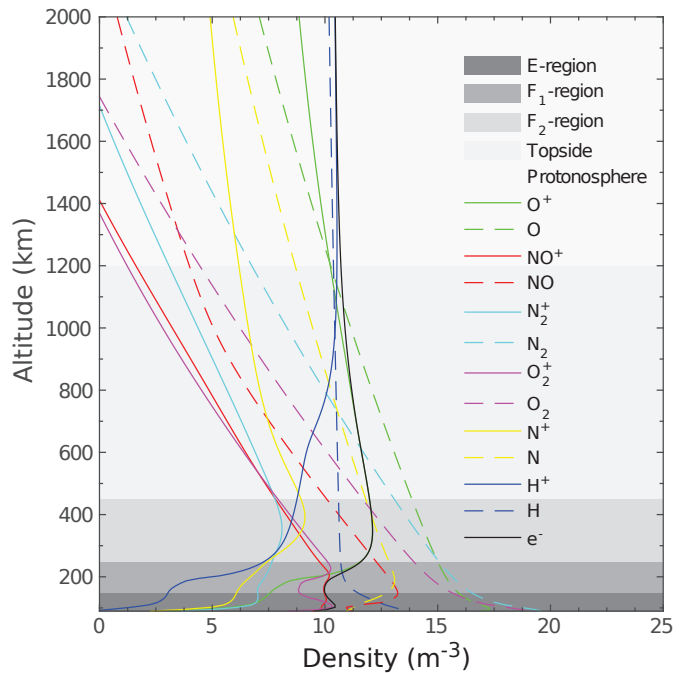


Figure 1.1: Example ion, electron, and neutral specie density profiles with ionospheric regions in gray.

ion population transitions to atomic species, primarily  $O^+$ . The  $F_2$  region ( $\sim 250$ - $450$  km) is where the maximum ionization occurs creating a daytime peak density on the order of  $\sim 10^{12} \text{ m}^{-3}$ . Within the F region, plasma transport gains importance and the plasma is considered partially ionized with both ion-ion and ion-neutral collisions being important. The topside ionosphere, the region directly above the F region peak, is where the plasma can finally be considered fully ionized and the collisions are primarily ion-ion. The protonosphere is a similar region, above the topside ionosphere, where the main ion species transition to  $H^+$  and  $He^+$ . At these altitudes plasma transport processes dominate and the ionosphere is considered collisionless.

Ion production, loss, and transport in the high-latitude F region ionosphere are regulated by electric fields and auroral precipitation, both of which can lead to strong ( $>100 \text{ m/s}$ ) thermal plasma upflow. Efforts have been made to explain the cause of observed field-aligned ion outflows as being due to plasma heating and the resulting plasma expansion (*Jones et al.*, 1988, 1990), expansion of plasma into low density magnetospheric auroral cavities (*Singh et al.*, 1989), field-aligned currents in auroral

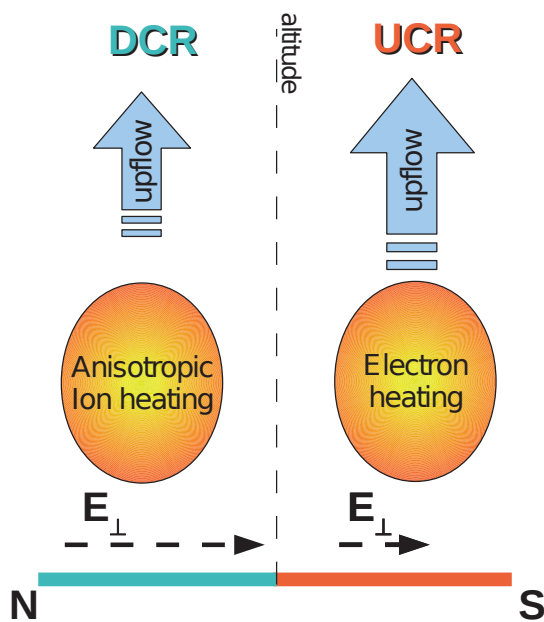


Figure 1.2: Electron heating-driven upflows are found above auroral arcs and are usually stronger than anisotropic ion heating upflows (Courtesy of M. Zettergren).

arcs (*Block and Falthammar*, 1968), expansion of the neutral atmosphere because of plasma heating (*Bates*, 1973), and as a response to auroral precipitations (*Wahlund et al.*, 1992; *Whitaker*, 1977). Despite the many physical processes (and coupling of these processes) that can induce ion upflow, *Wahlund et al.* (1992) introduced two categories, type 1 and type 2, which are still widely used to classify ion upflows.

Frictional heating-driven upflow (type-1 of *Wahlund et al.* (1992)) events are associated with elevated ion temperatures, strong convection electric fields, and minimal auroral precipitation. Strong convection through the neutral atmosphere leads

to frictional heating of the ions in the E and F regions of the ionosphere, resulting in anisotropic ion distributions (*St-Maurice and Schunk, 1979*) and large pressure gradients that accelerate ions upward along the field lines (*Keating et al., 1990; Foster and Lester, 1996; Zettergren and Semeter, 2012*). Observations of frictional heating-driven ion upflows often show a lifted F region peak location, low electron densities below 300 km, and little increase in electron temperature (*Wahlund et al., 1992*).

In contrast, electron heating-driven upflow (type-2 of *Wahlund et al. (1992)*) events are associated with auroral precipitation that increases electron densities and temperatures, hence electron pressure, throughout the F-region and topside ionosphere. This increases the ambipolar electric field which creates an upward, field-aligned flow of plasma (*Liu et al., 1995; Foster and Lester, 1996; Ogawa et al., 2000; Burchill et al., 2010*). Electron heating-driven upflows are found above auroral arcs, seem to occur more often, and are usually stronger than frictional heating-driven upflows (*Wahlund et al., 1992; Foster and Lester, 1996; Ogawa et al., 2003*). Velocity shears drive ion heating and upflow through lowering the threshold for field-aligned current-driven instabilities to excite ion cyclotron waves at lower altitudes (*Nishikawa et al., 1990; Ganguli et al., 1994; Liu and Lu, 2004; Semeter et al., 2003*).

The ionosphere can also be modulated by thermospheric winds. As discussed in (*Schunk and Nagy, 2000, p. 28*) solar forcing, caused by the influence of the EUV and Xrays from the solar wind, is a driver of thermospheric winds (*King and Kohl, 1965; Lindzen, 1966; Rishbeth, 1972*). This effect, driven by a global pressure gradient from dayside to nightside, will be strongest around solar max. Another potential source of intense thermospheric winds is provided by magnetosphere-ionosphere coupling in the polar latitudes (*Rishbeth and Garriott, 1969*). When the ions are moving rapidly in the dual cell convection pattern found in the polar region, motion is imparted to the neutrals from collisions with the ions (*de la Beaujardiere et al., 1991; Titheridge, 1995*). Because there are many more neutral particles than ions, the motion of the ions must be extreme in order for an appreciable amount of momentum to be imparted. Thermospheric motions in the form of acoustic-gravity waves may also drive ion motions (*Hunsucker, 1982; Hocke and Schlegel, 1996; Fritts and Alexander, 2003; Vlasov et al., 2011; Oberheide et al., 2015; Yiğit et al., 2016*). Acoustic-gravity



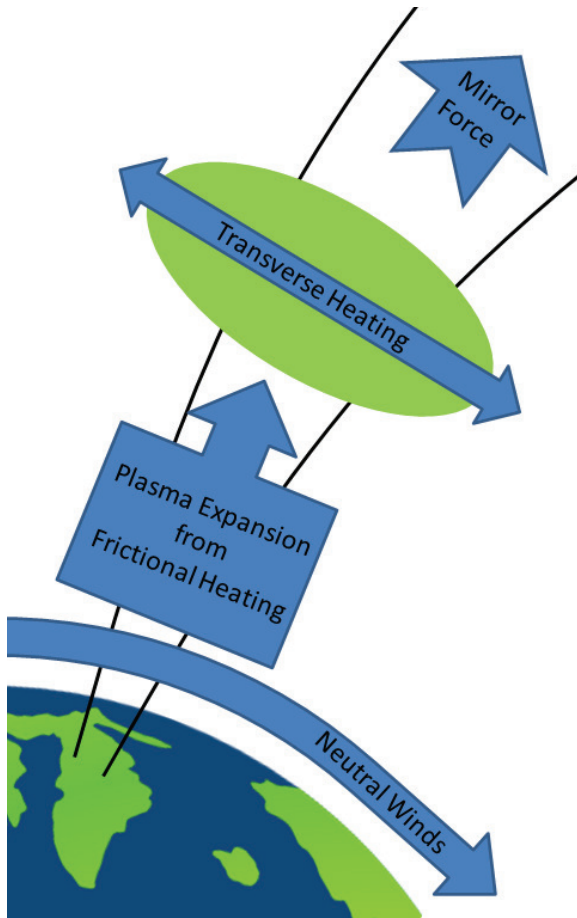


Figure 1.3: Neutral winds interact with ionospheric plasma, through collisions, driving upflow. Other ion upflow drivers, such as electric potentials and auroral precipitation, may also be present. Ions undergo further acceleration from transverse heating and at high altitudes mirror force propels ions to escape velocities, resulting in outflow to the magnetosphere.

to provide source populations for higher altitude energization processes. Once ions have been lifted to high altitudes, transverse ion acceleration by ion cyclotron resonance heating (*Chang et al.*, 1986; *Whalen et al.*, 1991) may give the upflowing ions sufficient energy, when acted on by the mirror force, to outflow into the magnetosphere (*Moore*, 1991; *Kintner et al.*, 1996; *Andre et al.*, 1998; *Moore et al.*, 1999).

The existence of a multi-step ion outflow process, such as that described here,

waves (*Hines*, 1960) are often driven at high latitudes by heating produced by auroral electric fields, energetic particle precipitation, and shear forces in the ionosphere (*Hocke and Schlegel*, 1996). Studies have also shown that the solar terminator or the Moon's umbra projected onto the Earth during a solar eclipse may produce gravity waves (*Fritts and Luo*, 1993; *Altadill and Sole*, 2001; *Sauli et al.*, 2006; *MacDougall and Jayachandran*, 2011). Orographic and weather effects are additional common GW sources (*Fritts and Alexander*, 2003, and references therein). Thermospheric winds affect ionospheric motions through collisions (viz. ion-neutral drag) (*Kohl and King*, 1967; *Yiğit et al.*, 2008), and alter upflow or perpendicular motions, potentially modifying source populations available for secondary acceleration mechanisms.

Thermal ion upflow mechanisms may not be strong enough to accelerate ions to escape velocities but instead are likely

has been suggested by various studies focusing on the coexistence of difference energy sources driving outflow (Yoshida *et al.*, 1999; Strangeway *et al.*, 2005; Lynch *et al.*, 2007; Ogawa *et al.*, 2008). Observations by (Skjaeveland *et al.*, 2011) found some upflows were greater than expected from ambipolar diffusion alone, suggesting that ion-neutral frictional heating contributed to upflow events. Correlations between the occurrence rates of ion upflows and magnetic local time (MLT) (Keating *et al.*, 1990; Endo *et al.*, 1999; Ma *et al.*, 2018; Zhao *et al.*, 2018), season (Kelley, 2009), solar cycle (Foster *et al.*, 1998; Ogawa *et al.*, 2010), Kp (Foster *et al.*, 1998; Endo *et al.*, 1999; Ogawa *et al.*, 2009; David *et al.*, 2018) and solar wind (Ogawa *et al.*, 2009) have been investigated.

Ionospheric outflow transfers mass, momentum, and energy to the magnetosphere. Energetic ions from the ionosphere are routinely observed in the magnetospheric plasmashet and ring current during periods of strong solar wind driving (Shelley *et al.*, 1972; Klumpp, 1979; Lennartsson *et al.*, 1981; Sharp *et al.*, 1985). For example, cluster satellites have indicated that  $H^+$ ,  $He^+$ , and  $O^+$  are injected into the tail of the magnetosphere from the nightside ionosphere and account for 80% of the  $O^+$  population in the mid-tail plasmashet (Sauvaud *et al.*, 2004; Lotko, 2007). Studies have indicated that this ionospheric outflow directly affects the dynamic response of the magnetosphere to solar wind variations (Garcia *et al.*, 2010; Brambles *et al.*, 2011; Yu and Ridley, 2013) through a wide range of mechanisms such as mass-loading that can affect Alfvén- and ULF-wave propagation (Kozyra *et al.*, 1984), alteration of reconnection rates (Shay *et al.*, 2004), and impacts on the acceleration and loss rates of energetic particles (Jordanova *et al.*, 1996; Daglis *et al.*, 1999).

## 1.1 Motivation

The existence of a multi-step process, such as that depicted in Figure 1.3, which results in ionospheric outflow is supported by observations of concurrent ion upflow and outflow drivers (fields, precipitation, ELF waves, etc.) (Yoshida *et al.*, 1999; Strangeway *et al.*, 2005; Lynch *et al.*, 2007; Ogawa *et al.*, 2008). Despite the myriad measurements of concurrent ion upflow and outflow energy drivers there is a distinct

lack of studies focused on the possible effects of transverse heating from wave-particle interactions in the collisional regime, the implications of temperature anisotropy that develops during times of strong heating, and the effects of thermospheric winds on upflow and outflow mechanisms.

The primary science question addressed in this dissertation is: **What is the connection between energy inputs and upflow/outflow response in the high-latitude ionosphere and how do thermospheric winds impact that connection?** This broad science question will be broken into several specific sub-queries:

- **What are the impacts of temperature anisotropy on low altitude ionospheric dynamics?**
- **To what degree can low altitude transverse plasma waves generate anisotropy and ion upflow?**
- **What is the role of neutral winds in regulating ion outflow?**

To address these queries a new model, called GEMINI-TIA (Geospace Environment Model for Ion-Neutral Interactions with Transverse Ion Acceleration), has been developed and used in a series of parametric, data inspired, and data-driven studies.

A variety of prior modeling studies have established many of the general characteristics of electron heating-driven upflows and outflows driven by auroral processes. The Dynamic Fluid-Kinetic model (DyFK) (*Wu et al.*, 1999) is a one-dimensional ionospheric model consisting of the FLIP model of the ionosphere (*Richards and Torr*, 1996) coupled with a generalized semi-kinetic model (*Wilson et al.*, 1990) for higher altitudes where ion distributions become non-Maxwellian. Studies using DyFK have shown that soft electron precipitation and perpendicular ion heating can act together to produce intense plasma upflows and outflows (*Wu et al.*, 1999, 2002; *Zeng and Horwitz*, 2007). *Sadler et al.* (2012) have used a three-fluid model (with ion, electron, and neutral fluids) to describe electromagnetic interactions between the ionosphere and the magnetosphere and resulting ion outflow. They found altitude-dependent neutral density enhancements accompany ion upwelling driven by soft electron precipitation. *Sydorenko and Rankin* (2013) also developed a multi-fluid model which was used to

demonstrate that ion upwelling is strongly affected by enhanced ambipolar electric fields produced by soft electron precipitation. Soft electron precipitation is ultimately more efficient at driving ion upflow than high-energy precipitation. High-energy particles penetrate to lower altitudes where heated electrons cool rapidly due to heat exchange through ion-neutral collisions, hence minimizing the upflow response *Su et al.* (1999).

Frictional heating-driven upflows are frequently observed in PFISR and RISR experiments, and show strong evidence of anisotropy (*Zettergren et al.*, 2014; *Perry et al.*, 2015). Significant anisotropies are predicted to occur anytime the DC electric fields exceeds  $\sim 50\text{-}75$  mV/m (*St-Maurice and Schunk*, 1979; *Raman et al.*, 1981). *Zettergren and Semeter* (2012) have used a 5-moment isotropic fluid ionospheric model to look at contributions of frictional heating, current closure, and ion upflow to auroral density depletions. Their simulations have shown that F-region density depletions can form in a matter of minutes due to frictional heating, generation of molecular ions, and enhanced recombination. This depletion process does not significantly inhibit upward fluxes of ions generated by this heating since the upflows seem to be initiated, in the topside ionosphere, on similar time scales. However any subsequent heating processes occurring in the same region would have access to a more tenuous plasma, which would ultimately impact any upflows that would be generated. *Zettergren et al.* (2014) and *Fernandes et al.* (2016) used data from the MICA sounding rocket to drive the ionospheric model developed in *Zettergren and Semeter* (2012) to examine fine-scale ion upflow and downflow patterns near a series of expansion phase auroral arcs. These studies have shown a correlation between ion temperature and the ELF wave power near one of the auroral arcs the sounding rocket flew through. This suggests that wave-particle interactions play a role in generating temperature anisotropies larger than that which is explained by steady frictional heating alone and that the effects of wave-particle interactions can occur to some extent in the highly collisional region below 500 km. This observation is corroborated by the results from a recent study in which the SWARM satellites observed apparent ion temperature anisotropies up to 5 at altitudes as low as 500 km, exceeding values predicted by theory given the measured electric fields (*Archer et al.*, 2015).

Ion temperature anisotropies in the F region ionosphere, observed in investigations employing incoherent scatter radar, satellite, and sounding rocket data, highlight the need for a model that can quantitatively determine the anisotropy that develops as a consequence of energy inputs associated with ion upflow. A few models that resolve anisotropy exist, none have yet been developed specifically for application to the ion upflow problem, even though ion heating-driven upflows, for example, are driven by strong DC fields which will also generate significant anisotropy.

While most ionospheric models use an isotropic, collisional fluid description, several theoretical and numerical fluid treatments have included temperature anisotropies. Most of these are 13-moment descriptions (e.g. *Zettergren et al.*, 2010) (based on an expansion about a Maxwellian distribution) or 16-moment descriptions (e.g. *Marchaudon and Blelly*, 2015) (based on an expansion about a Bi-Maxwellian distribution). Both of these formulations include separate parallel and perpendicular pressures and appropriate collision terms, however, only systems based off of a Bi-Maxwellian distribution are appropriate for large temperature anisotropies (*Barakat and Schunk*, 1982a).

Transport equations based on a Bi-Maxwellian distribution function were first derived by *Chew et al.* (1956) for a fully ionized, collisionless, anisotropic plasma. Heat flow contributions to the transport equations were neglected and the resulting parallel and perpendicular energy equations were termed “double-adiabatic” energy equations. That work was expanded by *Chodura and Pohl* (1971) to include both collisionless and collisional transport effects for a fully ionized plasma thus allowing for heat flow, viscosity, and Coulomb (ion-ion) collisions. *Demars and Schunk* (1979) extended those Bi-Maxwellian transport equations even further to an anisotropic plasma of an arbitrary degree of ionization. Like *Chodura and Pohl* (1971), *Demars and Schunk* (1979) also include heat flow and viscosity but their collision terms were calculated for an arbitrary inverse-power interaction potential which encompassed Coulomb, Maxwell, hard sphere, and resonant charge exchange interactions as special situations. *Barakat and Schunk* (1982a) extended the transport equations of *Demars and Schunk* (1979) to include additional physical parameters, such as mirror effects, by removing the assumption of straight magnetic field lines. Finally, *Blelly and Schunk* (1993)

analyzed the differences between 5, 8, 13, and 16-moment transport descriptions by numerically modeling the response of each system to transients.

In order to address the primary science question and specific sub queries, a new 2D anisotropic, multi-fluid ionospheric model is required. The model developed in this work, based on a modified 16-moment transport description, is an extension of the isotropic, 5-moment model presented in *Zettergren and Semeter (2012)* and *Zettergren and Snively (2015)*. The new model, hereafter referred to as GEMINI-TIA, solves the time-dependent, nonlinear equations of conservation of mass, momentum, parallel energy, and perpendicular energy for six ion species important to the E, F, and topside ionospheric regions:  $O^+$ ,  $NO^+$ ,  $N_2^+$ ,  $O_2^+$ ,  $N^+$ , and  $H^+$ , and functions at altitudes from the lower E-region all the way up to several Earth radii. Electrons are included using an isotropic description. This model includes chemical and collisional interactions with the neutral atmosphere, as well as the effects of photoionization (*Solomon and Qian, 2005*) and electron impact ionization (*Fang et al., 2008*). Neutral densities and temperatures needed for these calculations are usually taken from the NRL-MSISE-00 empirical model (*Picone et al., 2002*) but can also be constrained by models of neutral dynamics (e.g. as in *Zettergren and Snively, 2013*). Development of this model has been the primary goal of research comprising the first part of this dissertation work.

For the second part of this work, the model has been used to connect responses deep in the ionosphere to observed energized ions as well as identify the types and sources of neutral disturbances that can significantly affect upflow. In order to facilitate comparisons with data, the model is designed to accept as inputs the main drivers of ion upflow and outflow: particle precipitation, electric fields, ELF wave power, and neutral winds and densities. GEMINI-TIA has very flexible functionality and in this dissertation is coupled to a neutral dynamics model, as well as being used alongside rocket and ISR experiments, to simulate ionospheric responses to specified energy sources and neutral wind patterns.

## 1.2 Dissertation organization

This chapter has provided a background description of the Earth's high-latitude ionosphere. Chapter 2 gives an in depth description of the new Bi-Maxwellian ionospheric model, GEMINI-TIA, developed as part of this dissertation. Comparisons between this new model and its parent version are presented in Chapter 3. The Magnetosphere-Ionosphere Coupling in the Alfvén Resonator (MICA) sounding rocket campaign is used as a case study for this comparison. Chapter 4 describes the parametric study conducted to examine synergistic effects of frictional heating and transverse wave heating at low altitudes, with neutral winds, on ionospheric upflow. In Chapter 5 the new ionospheric model, GEMINI-TIA, discussed to Chapter 2, is coupled with an atmospheric model, informally called MAGIC (Model for Acoustic and Gravity wave Interactions and Coupling), to explore how linear and nonlinear gravity waves can modulate ionospheric upflow. In Chapter 6, realistic temporally and spatially varying energy sources, from the Ionospheric Structuring: In Situ and Groundbased Low Altitude Studies (ISINGLASS) sounding rocket campaign, are used to drive the model and examine how transient forcing impacts ionospheric outflow. Chapter 7 provides summary and concluding remarks and outlines potential promising avenues for future work.

# Chapter 2

## Modeling the high latitude ionosphere

### 2.1 Derivation of the 16-moment transport equations

The Boltzman equation is the starting point for the derivation of the 16-moment transport description. With Boltzman's approach it is not the motion of individual particles that is of interest but instead with the distribution of the particles. Each species is represented by a separate distribution function,  $f_s(\mathbf{r}, \mathbf{v}_s, t)$  where position,  $\mathbf{r}$ , velocity,  $\mathbf{v}_s$ , and time,  $t$  are independent variables, that can be viewed as a probability density in the  $(\mathbf{r}, \mathbf{v}_s)$  phase space. The temporal evolution of  $f_s$  is determined by the flow, in phase space, of particles under the influence of external forces and the net effect of collisions. The main external forces acting on charged particles of the Earth's high-latitude ionosphere are the Lorentz and gravitational forces. The mathematical description of the evolution of the distribution function over time is given by the Boltzmann equation

$$\frac{\partial f_s}{\partial t} + \mathbf{v}_s \cdot \nabla f_s + \left[ \mathbf{G} + \frac{q_s}{m_s} (\mathbf{E} + \mathbf{v}_s \times \mathbf{B}) \right] \cdot \nabla_v f_s = \frac{\delta f_s}{\delta t} \quad (2.1)$$

where  $q_s$  is the charge and  $m_s$  is the mass of species  $s$ ,  $\mathbf{G}$  is the acceleration due to gravity,  $\mathbf{E}$  is the electric field, and  $\mathbf{B}$  is the magnetic field. Note that  $\nabla$  is the gradient operator in configuration space while  $\nabla_v$  is the gradient operator in velocity space. At lower latitudes of the ionosphere, or considering the neutral species of the



atmosphere, Coriolis and centripetal forces can also play an important role. The right hand side of this equation,  $\delta f_s/\delta t$ , represents the effects collisions have of the distribution function. If collisions were to be neglected then the Boltzmann equation simplifies to the Vlasov equation.

For binary elastic collisions between particles (with symmetric force fields) the appropriate collision operator is the Boltzmann collision integral

$$\frac{\delta f_s}{\delta t} = \sum_j \iint g_{sj} \sigma_{sj}(g, \theta) (f'_s f'_j - f_s f_j) d\mathbf{v}_j d\Omega \quad (2.2)$$

where  $g_{sj}$  is the relative speed of the colliding particles  $s$  and  $j$ ,  $\sigma_{sj}(g, \theta)$  is the differential scattering cross section defined as the number of molecules scattered per solid angle  $d\Omega$  per unit time divided by the incident intensity,  $d\mathbf{v}_j$  is the velocity-space volume element of species  $j$ ,  $d\Omega$  is an element of solid angle in the  $s$  particle reference frame, and the primes denote quantities calculated after collisions. The effect of a collision is an instantaneous change to the velocity of a particle resulting in the sudden appearance and disappearance of particles in velocity space. This Boltzmann collision integral is a good description for collisions between species as well as self-collisions. It is applicable for Coulomb collisions, elastic ion-neutral collisions, and resonant charge exchange interactions when the net energy loss is small. There is an inherent assumption of molecular chaos within this collision integral so there is no correlation between the positions and velocities of different particles before collisions.

Solving the Boltzmann equation directly for the individual velocity distribution functions of each species in the ionosphere can only be done in a few simple situations. It is possible though to calculate the physically significant velocity moments of each given species to describe the bulk plasma. These velocity moments can be defined with respect to the average drift velocity of that species (*Burgers, 1969; Chodura and Pohl, 1971; Demars and Schunk, 1979; Barakat and Schunk, 1981*). In terms of the average drift velocity,  $\mathbf{u}_s$ , the thermal velocity,  $\mathbf{c}_s$ , is defined as

$$\mathbf{c}_s = \mathbf{v}_s - \mathbf{u}_s \quad (2.3)$$

The physically significant velocity moments of the species distribution function are the average drift velocity, parallel temperature, perpendicular temperature, heat flow vector for parallel energy, heat flow vector for perpendicular energy, pressure tensor, stress tensor, higher-order pressure tensor related to parallel energy, higher-order pressure tensor related to perpendicular energy, and heat flow tensor which are respectively given by

$$\mathbf{u}_s = \langle \mathbf{v}_s \rangle \quad (2.4)$$

$$T_{s,\parallel} = m_s \langle c_{s,\parallel}^2 \rangle / k \quad (2.5)$$

$$T_{s,\perp} = m_s \langle c_{s,\perp}^2 \rangle / 2k \quad (2.6)$$

$$\mathbf{q}_{s,\parallel} = n_s m_s \langle c_{s,\parallel}^2 \mathbf{c}_s \rangle \quad (2.7)$$

$$\mathbf{q}_{s,\perp} = n_s m_s \langle c_{s,\perp}^2 \mathbf{c}_s / 2 \rangle \quad (2.8)$$

$$\mathbf{P}_s = n_s m_s \langle \mathbf{c}_s \mathbf{c}_s \rangle \quad (2.9)$$

$$\boldsymbol{\tau}_s = \mathbf{P}_s - p_{s,\perp} \mathbf{I} - (p_{s,\parallel} - p_{s,\perp}) \hat{\mathbf{e}}_{\parallel} \hat{\mathbf{e}}_{\parallel} \quad (2.10)$$

$$\mu_{s,\parallel} = n_s m_s \langle c_{s,\parallel}^2 \mathbf{c}_s \mathbf{c}_s \rangle \quad (2.11)$$

$$\mu_{s,\perp} = n_s m_s \langle c_{s,\perp}^2 \mathbf{c}_s \mathbf{c}_s \rangle \quad (2.12)$$

$$\mathbf{Q}_s = n_s m_s \langle \mathbf{c}_s \mathbf{c}_s \mathbf{c}_s \rangle \quad (2.13)$$

where  $n_s$  is the number density of species  $s$  calculated by integrating the distribution function over all velocities for a volume element,  $d\mathbf{r}_s$ , at time  $t$ ,  $k$  is Boltzmann's constant,  $\parallel$  denotes quantities parallel to the magnetic field,  $\perp$  denotes quantities perpendicular to the magnetic field, and the angle brackets signify average

$$\langle \mathbf{A} \rangle = \frac{1}{n_s} \int \mathbf{A} f_s d\mathbf{v}_s \quad (2.14)$$

The partial pressure is defined as  $p_{s,\parallel} = n_s k T_{s,\parallel}$  and  $p_{s,\perp} = n_s k T_{s,\perp}$  for parallel and perpendicular directions respectively.  $\mathbf{I} = \hat{\mathbf{e}}_{\perp}^1 \hat{\mathbf{e}}_{\perp}^1 + \hat{\mathbf{e}}_{\perp}^2 \hat{\mathbf{e}}_{\perp}^2 + \hat{\mathbf{e}}_{\parallel} \hat{\mathbf{e}}_{\parallel}$  is the unit dyadic where  $\hat{\mathbf{e}}_{\perp}^1$ ,  $\hat{\mathbf{e}}_{\perp}^2$ ,  $\hat{\mathbf{e}}_{\parallel}$  are orthogonal unit vectors with  $\hat{\mathbf{e}}_{\parallel}$  aligned along the magnetic field

lines. The parallel and perpendicular temperatures are defined such that

$$T_s = \frac{1}{3}T_{s,\parallel} + \frac{2}{3}T_{s,\perp} \quad (2.15)$$

where  $T_s = m_s \langle c_s^2 \mathbf{c}_s \rangle / 3k$  is the absolute temperature of species  $s$ . The heat flow vectors have a similar relationship

$$\mathbf{h}_s = \frac{1}{2}\mathbf{h}_{s,\parallel} + \mathbf{h}_{s,\perp} \quad (2.16)$$

where  $\mathbf{h}_s = n_s m_s \langle c_s^2 \mathbf{c}_s \rangle / 2$ . Additional, higher order, moments can be calculated depending on the level of detail desired and physical processes deemed important for region of interest.

General transport equations can be obtained, describing the spatial and temporal evolution of these velocity moments, by multiplying the Boltzmann equation with a velocity moment and integrating over velocity space. First, it is convenient to rewrite the Boltzmann equation taking advantage of the following equalities:

$$\mathbf{v}_s \cdot \nabla f_s = \mathbf{v}_s \cdot \nabla f_s + f_s (\nabla \cdot \mathbf{v}_s) = \nabla \cdot (f_s \mathbf{v}_s) \quad (2.17)$$

and

$$\mathbf{a}_s \cdot \nabla_v f_s = \mathbf{a}_s \cdot \nabla_v f_s + f_s (\nabla_v \cdot \mathbf{a}_s) = \nabla_s \cdot (f_s \mathbf{a}_s) \quad (2.18)$$

since  $\nabla_v \cdot \mathbf{a}_s = 0$  for the acceleration processes ( $\mathbf{a}_s = [\mathbf{G} + q_s (\mathbf{E} + \mathbf{v}_s \times \mathbf{B}) / m_s]$ ) considered relevant to the ionosphere. Thus the new form of the Boltzmann equation becomes

$$\frac{\partial f_s}{\partial t} + \nabla \cdot (f_s \mathbf{v}_s) + \nabla_v \cdot \left( f_s \left[ \mathbf{G} + \frac{q_s}{m_s} (\mathbf{E} + \mathbf{v}_s \times \mathbf{B}) \right] \right) = \frac{\delta f_s}{\delta t}. \quad (2.19)$$

Now an equation describing the evolution of the species mass density is obtained by multiplying equation 2.19 by  $m_s$  and integrating over all velocities

$$\int m_s \left[ \frac{\partial f_s}{\partial t} + \nabla \cdot (f_s \mathbf{v}_s) + \nabla_v \cdot \left( f_s \left[ \mathbf{G} + \frac{q_s}{m_s} (\mathbf{E} + \mathbf{v}_s \times \mathbf{B}) \right] \right) \right] d\mathbf{v}_s$$

$$= \int m_s \left[ \frac{\delta f_s}{\delta t} \right] d\mathbf{v}_s \quad (2.20)$$

where

$$\int m_s \left[ \frac{\partial f_s}{\partial t} \right] d\mathbf{v}_s = m_s \frac{\partial}{\partial t} \int f_s d\mathbf{v}_s = \frac{\partial \rho_s}{\partial t}, \quad (2.21)$$

$$\int m_s [\nabla \cdot (f_s \mathbf{v}_s)] d\mathbf{v}_s = m_s \nabla \cdot \int f_s \mathbf{v}_s d\mathbf{v}_s = \nabla \cdot (\rho \mathbf{u}_s), \quad (2.22)$$

$$\int m_s [\nabla_v \cdot (f_s \mathbf{a}_s)] d\mathbf{v}_s = \int_S dA_v (f_s \mathbf{a}_s) \cdot \hat{\mathbf{n}}_v = 0, \quad (2.23)$$

$$\int m_s \frac{\delta f_s}{\delta t} d\mathbf{v}_s \equiv \frac{\delta \rho_s}{\delta t} \quad (2.24)$$

Substituting equations 2.21 - 2.24 into equation 2.20 yields the continuity equation.

$$\frac{\partial \rho_s}{\partial t} + \nabla \cdot (\rho \mathbf{u}_s) = \frac{\delta \rho_s}{\delta t} \quad (2.25)$$

Additional general transport equations can also be calculated using the same method. Instead of  $m_s$ , substitute in a different velocity function, such as those used in equations 2.4 to 2.13, to multiply equation 2.19 by and integrate over all velocities. There is a fair amount of algebra involved, see *Schunk and Nagy* (2000, Chapter 3) for more information.

In total, multiplying equation 2.19 by  $m_s$ ,  $m_s \mathbf{c}_s$ ,  $m_s c_{s,\parallel}^2$ ,  $m_s c_{s,\perp}^2/2$ ,  $m_s \mathbf{c}_s \mathbf{c}_s$ ,  $m_s c_{s,\parallel}^2 \mathbf{c}_s$ , or  $m_s c_{s,\perp}^2 \mathbf{c}_s/2$  and then integrating over velocity space the continuity, momentum, parallel energy, perpendicular energy, pressure tensor, parallel heat flow or perpendicular heat flow equation, respectively, for species  $s$  is obtained. The stress tensor equation is obtained by subtracting  $\hat{\mathbf{e}}_{\parallel} \hat{\mathbf{e}}_{\parallel}$  times the parallel energy equation and  $(I - \hat{\mathbf{e}}_{\parallel} \hat{\mathbf{e}}_{\parallel})$  times the perpendicular energy equation from the pressure tensor equation (equation 2.10). These resulting transport equations describe the spatial and temporal behavior of the physically significant moments of the distribution function.

From this method, general transport equations can be written as

Continuity:

$$\frac{\partial \rho_s}{\partial t} + \nabla \cdot (\rho \mathbf{u}_s) = \frac{\delta \rho_s}{\delta t} \quad (2.26)$$

Momentum:

$$\rho_s \frac{D_s \mathbf{u}_s}{Dt} + \nabla_{\perp} p_{s,\perp} + \nabla_{\parallel} p_{s,\parallel} + \nabla \cdot \boldsymbol{\tau}_s - \rho_s \mathbf{G} - n_s q_s (\mathbf{E} + \mathbf{u}_s \times \mathbf{B}) = \frac{\delta \mathbf{M}_s}{\delta t} \quad (2.27)$$

Parallel Energy:

$$\begin{aligned} & \frac{D_s p_{s,\parallel}}{Dt} + p_{s,\parallel} (\nabla \cdot \mathbf{u}_s + 2\nabla_{\parallel} \cdot \mathbf{u}_s) + 2\hat{\mathbf{e}}_{\parallel} \hat{\mathbf{e}}_{\parallel} : [\boldsymbol{\tau}_s \cdot \nabla \mathbf{u}_s] \\ & + \nabla \cdot \mathbf{h}_s^{\parallel} - \boldsymbol{\tau}_s : \frac{D_s}{Dt} (\hat{\mathbf{e}}_{\parallel} \hat{\mathbf{e}}_{\parallel}) - \mathbf{Q}_s : \nabla (\hat{\mathbf{e}}_{\parallel} \hat{\mathbf{e}}_{\parallel}) = \frac{\delta E_{s,\parallel}}{\delta t} \end{aligned} \quad (2.28)$$

Perpendicular Energy:

$$\begin{aligned} & \frac{D_s p_{s,\perp}}{Dt} + p_{s,\perp} (\nabla \cdot \mathbf{u}_s + \nabla_{\perp} \cdot \mathbf{u}_s) + (\mathbf{I} - \hat{\mathbf{e}}_{\parallel} \hat{\mathbf{e}}_{\parallel}) : [\boldsymbol{\tau}_s \cdot \nabla \mathbf{u}_s] \\ & + \nabla \cdot \mathbf{h}_s^{\perp} + \frac{1}{2} \boldsymbol{\tau}_s : \frac{D_s}{Dt} (\hat{\mathbf{e}}_{\parallel} \hat{\mathbf{e}}_{\parallel}) + \frac{1}{2} \mathbf{Q}_s : \nabla (\hat{\mathbf{e}}_{\parallel} \hat{\mathbf{e}}_{\parallel}) = \frac{\delta E_{s,\perp}}{\delta t} \end{aligned} \quad (2.29)$$

Stress Tensor:

$$\begin{aligned} & \frac{D_s \boldsymbol{\tau}_s}{Dt} + p_{s,\parallel} [\nabla_{\parallel} \mathbf{u}_s + (\nabla_{\parallel} \mathbf{u}_s)^T - 2\hat{\mathbf{e}}_{\parallel} \hat{\mathbf{e}}_{\parallel} \nabla_{\parallel} \cdot \mathbf{u}_s] + p_{s,\perp} [\nabla_{\perp} \mathbf{u}_s + (\nabla_{\perp} \mathbf{u}_s)^T \\ & - (\mathbf{I} - \hat{\mathbf{e}}_{\parallel} \hat{\mathbf{e}}_{\parallel}) \nabla_{\perp} \cdot \mathbf{u}_s] + \boldsymbol{\tau}_s (\nabla \cdot \mathbf{u}_s) + \boldsymbol{\tau}_s \cdot \nabla \mathbf{u}_s + (\boldsymbol{\tau}_s \cdot \nabla \mathbf{u}_s)^T \\ & - 2\hat{\mathbf{e}}_{\parallel} \hat{\mathbf{e}}_{\parallel} \hat{\mathbf{e}}_{\parallel} \hat{\mathbf{e}}_{\parallel} : [\boldsymbol{\tau}_s \cdot \nabla \mathbf{u}_s] - (\mathbf{I} - \hat{\mathbf{e}}_{\parallel} \hat{\mathbf{e}}_{\parallel}) (\mathbf{I} - \hat{\mathbf{e}}_{\parallel} \hat{\mathbf{e}}_{\parallel}) : [\boldsymbol{\tau}_s \cdot \nabla \mathbf{u}_s] + \nabla \cdot \mathbf{Q}_s \\ & - \hat{\mathbf{e}}_{\parallel} \hat{\mathbf{e}}_{\parallel} \nabla \cdot \mathbf{h}_s^{\parallel} - (\mathbf{I} - \hat{\mathbf{e}}_{\parallel} \hat{\mathbf{e}}_{\parallel}) \nabla \cdot \mathbf{h}_s^{\perp} + \boldsymbol{\Omega}_s \times \boldsymbol{\tau}_s - \boldsymbol{\tau}_s \times \boldsymbol{\Omega}_s + (p_{s,\parallel} - p_{s,\perp}) \frac{D_s}{Dt} (\hat{\mathbf{e}}_{\parallel} \hat{\mathbf{e}}_{\parallel}) \\ & - \frac{1}{2} (\mathbf{I} - 3\hat{\mathbf{e}}_{\parallel} \hat{\mathbf{e}}_{\parallel}) \times \left[ \boldsymbol{\tau}_s : \frac{D_s}{Dt} (\hat{\mathbf{e}}_{\parallel} \hat{\mathbf{e}}_{\parallel}) + \mathbf{Q}_s : \nabla (\hat{\mathbf{e}}_{\parallel} \hat{\mathbf{e}}_{\parallel}) \right] = \frac{\delta \boldsymbol{\tau}_s}{\delta t} \end{aligned} \quad (2.30)$$

Parallel Heat Flow:

$$\begin{aligned} & \frac{D_s \mathbf{h}_s^{\parallel}}{Dt} + 2[\mathbf{Q}_s \cdot \nabla \mathbf{u}_s] : \hat{\mathbf{e}}_{\parallel} \hat{\mathbf{e}}_{\parallel} + \mathbf{h}_s^{\parallel} \nabla \cdot \mathbf{u}_s + \mathbf{h}_s^{\parallel} \cdot \nabla \mathbf{u}_s + \nabla \cdot \mu_s^{\parallel} \\ & + \left[ \frac{D_s \mathbf{u}_s}{Dt} - \frac{e_s}{m_s} (\mathbf{E} + \mathbf{u}_s \times \mathbf{B}) \right] \cdot [p_{s,\parallel} \mathbf{I} + 2\hat{\mathbf{e}}_{\parallel} \hat{\mathbf{e}}_{\parallel} \cdot (p_{s,\parallel} \mathbf{I} + \boldsymbol{\tau}_s)] \\ & + \boldsymbol{\Omega}_s \times \mathbf{h}_s^{\parallel} - \mathbf{Q}_s : \frac{D_s}{Dt} (\hat{\mathbf{e}}_{\parallel} \hat{\mathbf{e}}_{\parallel}) - \mathbf{R}_s : \nabla (\hat{\mathbf{e}}_{\parallel} \hat{\mathbf{e}}_{\parallel}) = \frac{\delta \mathbf{h}_s^{\parallel}}{\delta t} \end{aligned} \quad (2.31)$$

Perpendicular Heat Flow:

$$\begin{aligned}
& \frac{D_s \mathbf{h}_s^\perp}{Dt} + [\mathbf{Q}_s \cdot \nabla \mathbf{u}_s] : (\mathbf{I} - \hat{\mathbf{e}}_\parallel \hat{\mathbf{e}}_\parallel) + \mathbf{h}_s^\perp \nabla \cdot \mathbf{u}_s + \mathbf{h}_s^\perp \cdot \nabla \mathbf{u}_s + \frac{1}{2} \nabla \cdot \mu_s^\perp \\
& + \left[ \frac{D_s \mathbf{u}_s}{Dt} - \frac{e_s}{m_s} (\mathbf{E} + \mathbf{u}_s \times \mathbf{B}) \right] \cdot [p_{s,\perp} \mathbf{I} + (\mathbf{I} - \hat{\mathbf{e}}_\parallel \hat{\mathbf{e}}_\parallel) \cdot (p_{s,\perp} \mathbf{I} + \boldsymbol{\tau}_s)] \\
& + \boldsymbol{\Omega}_s \times \mathbf{h}_s^\perp + \frac{1}{2} \mathbf{Q}_s : \frac{D_s}{Dt} (\hat{\mathbf{e}}_\parallel \hat{\mathbf{e}}_\parallel) + \frac{1}{2} \mathbf{R}_s : \nabla (\hat{\mathbf{e}}_\parallel \hat{\mathbf{e}}_\parallel) = \frac{\delta \mathbf{h}_s^\perp}{\delta t}
\end{aligned} \tag{2.32}$$

where  $D_s/Dt$  is the convective derivative

$$\frac{D_s}{Dt} = \frac{\partial}{\partial t} + \mathbf{u}_s \cdot \nabla \tag{2.33}$$

a superscript  $T$  on a tensor indicates the transpose,  $\boldsymbol{\Omega}_s = (q_s/m_s c) \mathbf{B}$  is the cyclotron frequency, and the right hand side of these equations represent the effects of collisions. The parallel and perpendicular components of a vector  $\mathbf{A}$  are defined as  $\mathbf{A}_\parallel = \hat{\mathbf{e}}_\parallel \hat{\mathbf{e}}_\parallel$  and  $\mathbf{A}_\perp = (\mathbf{I} - \hat{\mathbf{e}}_\parallel \hat{\mathbf{e}}_\parallel) \cdot \mathbf{A}$  respectively.

The general transport equations, as calculated above, produce a system of equations that is not a closed set. The equation from the moment of order  $y$  contains a term with the moment of order  $y + 1$ . In order to close the system it is necessary to use an approximation for the species distribution function (*Schunk and Nagy, 2000*). Assuming an expression for the velocity distribution function will also allow the collision integrals to be evaluated. While there are many choices for this approximation, an expression based on a bi-Maxwellian species distribution function, as was done in *Demars and Schunk (1979)*, is used here such that

$$f_s = f_{so} (1 + \Xi_s) \tag{2.34}$$

where the zeroth-order Bi-Maxwellian distribution is given by

$$f_{so} = n_s \left( \frac{m_s}{2\pi k T_{s,\perp}} \right) \left( \frac{m_s}{2\pi k T_{s,\parallel}} \right)^{1/2} \exp^{-\frac{1}{2} \left( \frac{c_{s,\perp}^2}{k T_{s,\perp}} + \frac{c_{s,\parallel}^2}{k T_{s,\parallel}} \right)} \tag{2.35}$$

and where

$$\begin{aligned}
\Xi_s = & \frac{m_s}{2\rho_s k T_{s,\perp}} \left[ \frac{m_s}{k T_{s,\perp}} (c_{s,1}^2 - c_{s,2}^2) (\boldsymbol{\tau}_s : \hat{\mathbf{e}}_\perp^1 \hat{\mathbf{e}}_\perp^1) + 2 \frac{m_s}{k T_{s,\perp}} (\boldsymbol{\tau}_s : \hat{\mathbf{e}}_\perp^1 \hat{\mathbf{e}}_\perp^2) c_{s,1} c_{s,2} \right. \\
& \left. + 2 \frac{m_s}{k T_{s,\parallel}} \boldsymbol{\tau}_s : \mathbf{c}_{s,\perp} \mathbf{c}_{s,\parallel} \right] - \frac{m_s^2}{\rho_s k_b^2 T_{s,\perp}^2} \left( 1 - \frac{m_s c_{s,\perp}^2}{4 k_b T_{s,\perp}} \right) \mathbf{h}_s^\perp \cdot \mathbf{c}_{s,\perp} \\
& - \frac{m_s^2}{\rho_s k_b^2 T_{s,\perp} T_{s,\parallel}} \left( 1 - \frac{m_s c_{s,\perp}^2}{2 k_b T_{s,\perp}} \right) \mathbf{h}_s^\perp \cdot \mathbf{c}_{s,\parallel} - \frac{m_s^2}{2 \rho_s k_b^2 T_{s,\parallel}^2} \left( 1 - \frac{m_s c_{s,\parallel}^2}{3 k_b T_{s,\parallel}} \right) \mathbf{h}_s^\parallel \cdot \mathbf{c}_{s,\parallel} \\
& - \frac{m_s^2}{2 \rho_s k_b^2 T_{s,\perp} T_{s,\parallel}} \left( 1 - \frac{m_s c_{s,\parallel}^2}{k_b T_{s,\parallel}} \right) \mathbf{h}_s^\parallel \cdot \mathbf{c}_{s,\perp}
\end{aligned} \tag{2.36}$$

By multiplying the approximate distribution function (Equation 2.34), instead of the Boltzmann equation, by  $m_s$ ,  $m_s \mathbf{c}_s$ ,  $m_s c_{s,\parallel}^2$ ,  $m_s c_{s,\perp}^2/2$ , or  $m_s \mathbf{c}_s \mathbf{c}_s$  and integrating over velocity space the continuity, momentum, parallel energy, perpendicular energy, pressure tensor, respectively, transport equations for species  $s$  are derived. This set of transport equations accurately reproduce the general transport equations for the lower moments and modify the higher order moments by allowing them to be expressed in terms of the lower order moments thus closing the system.

Continuity:

$$\frac{\partial \rho_s}{\partial t} + \nabla \cdot (\rho_s \mathbf{u}_s) = \frac{\delta \rho_s}{\delta t} \tag{2.37}$$

Momentum:

$$\rho_s \frac{D_s \mathbf{u}_s}{Dt} + \nabla_\perp p_{s,\perp} + \nabla_\parallel p_{s,\parallel} + \nabla \cdot \boldsymbol{\tau}_s - \rho_s \mathbf{G} - n_s q_s (\mathbf{E} + \mathbf{u}_s \times \mathbf{B}) = \frac{\delta \mathbf{M}_s}{\delta t} \tag{2.38}$$

Parallel Energy:

$$\begin{aligned}
& \frac{D_s p_{s,\parallel}}{Dt} + p_{s,\parallel} (\nabla \cdot \mathbf{u}_s + 2 \nabla_\parallel \cdot \mathbf{u}_s) + 2 \hat{\mathbf{e}}_\parallel \hat{\mathbf{e}}_\parallel : [\boldsymbol{\tau}_s \cdot \nabla \mathbf{u}_s] + \nabla \cdot \mathbf{h}_s^\parallel \\
& - \boldsymbol{\tau}_s : \frac{D_s}{Dt} (\hat{\mathbf{e}}_\parallel \hat{\mathbf{e}}_\parallel) - 2 \left[ \mathbf{h}_s^\parallel \hat{\mathbf{e}}_\parallel : \nabla \hat{\mathbf{e}}_\parallel + (\mathbf{h}_s^\perp \cdot \hat{\mathbf{e}}_\parallel) (\nabla \cdot \hat{\mathbf{e}}_\parallel) \right] = \frac{\delta E_{s,\parallel}}{\delta t}
\end{aligned} \tag{2.39}$$

Perpendicular Energy:

$$\frac{D_s p_{s,\perp}}{Dt} + p_{s,\perp} (\nabla \cdot \mathbf{u}_s + \nabla_\perp \cdot \mathbf{u}_s) + (\mathbf{I} - \hat{\mathbf{e}}_\parallel \hat{\mathbf{e}}_\parallel) : [\boldsymbol{\tau}_s \cdot \nabla \mathbf{u}_s] + \nabla \cdot \mathbf{h}_s^\perp$$

$$+\frac{1}{2}\boldsymbol{\tau}_s : \frac{D_s}{Dt}(\hat{\mathbf{e}}_{\parallel}\hat{\mathbf{e}}_{\parallel}) + \left[ \mathbf{h}_s^{\parallel}\hat{\mathbf{e}}_{\parallel} : \nabla\hat{\mathbf{e}}_{\parallel} + (\mathbf{h}_s^{\perp} \cdot \hat{\mathbf{e}}_{\parallel})(\nabla \cdot \hat{\mathbf{e}}_{\parallel}) \right] = \frac{\delta E_{s,\perp}}{\delta t} \quad (2.40)$$

Stress Tensor:

$$\begin{aligned} & \frac{D_s \boldsymbol{\tau}_s}{Dt} + p_{s,\parallel} \left[ \nabla_{\parallel} \mathbf{u}_s + (\nabla_{\parallel} \mathbf{u}_s)^T - 2\hat{\mathbf{e}}_{\parallel}\hat{\mathbf{e}}_{\parallel} \nabla_{\parallel} \cdot \mathbf{u}_s \right] + p_{s,\perp} \left[ \nabla_{\perp} \mathbf{u}_s + (\nabla_{\perp} \mathbf{u}_s)^T \right. \\ & \quad - (\mathbf{I} - \hat{\mathbf{e}}_{\parallel}\hat{\mathbf{e}}_{\parallel}) \nabla_{\perp} \cdot \mathbf{u}_s \left. \right] + \boldsymbol{\tau}_s (\nabla \cdot \mathbf{u}_s) + \boldsymbol{\tau}_s \cdot \nabla \mathbf{u}_s + (\boldsymbol{\tau}_s \cdot \nabla \mathbf{u}_s)^T \\ & \quad - 2\hat{\mathbf{e}}_{\parallel}\hat{\mathbf{e}}_{\parallel}\hat{\mathbf{e}}_{\parallel}\hat{\mathbf{e}}_{\parallel} : [\boldsymbol{\tau}_s \cdot \nabla \mathbf{u}_s] - (\mathbf{I} - \hat{\mathbf{e}}_{\parallel}\hat{\mathbf{e}}_{\parallel})(\mathbf{I} - \hat{\mathbf{e}}_{\parallel}\hat{\mathbf{e}}_{\parallel}) : [\boldsymbol{\tau}_s \cdot \nabla \mathbf{u}_s] \\ & \quad + \nabla_{\parallel} \mathbf{h}_s^{\parallel} + (\nabla_{\parallel} \mathbf{h}_s^{\parallel})^T + \hat{\mathbf{e}}_{\parallel}\hat{\mathbf{e}}_{\parallel} \nabla \cdot (\mathbf{h}_s^{\parallel} - 2\mathbf{h}_{s,\parallel}^{\parallel}) + \frac{1}{2} \left[ \nabla_{\perp} (\mathbf{h}_s^{\perp} + \mathbf{h}_{s,\parallel}^{\perp}) \right. \\ & \quad \left. + (\nabla_{\perp} (\mathbf{h}_s^{\perp} + \mathbf{h}_{s,\parallel}^{\perp}))^T + (\mathbf{I} - \hat{\mathbf{e}}_{\parallel}\hat{\mathbf{e}}_{\parallel}) \nabla \cdot (\mathbf{h}_s^{\perp} + \mathbf{h}_{s,\parallel}^{\perp}) \right] + \left( \mathbf{h}_s^{\parallel} - \frac{1}{2} \mathbf{h}_s^{\perp} - \frac{1}{2} \mathbf{h}_{s,\parallel}^{\perp} \right) \nabla \cdot (\hat{\mathbf{e}}_{\parallel}\hat{\mathbf{e}}_{\parallel}) \\ & \quad + \nabla \cdot (\hat{\mathbf{e}}_{\parallel}\hat{\mathbf{e}}_{\parallel}) \left( \mathbf{h}_s^{\parallel} - \frac{1}{2} \mathbf{h}_s^{\perp} - \frac{1}{2} \mathbf{h}_{s,\parallel}^{\perp} \right) + \left( \mathbf{h}_s^{\parallel} - 2\mathbf{h}_{s,\parallel}^{\parallel} - \frac{1}{2} \mathbf{h}_s^{\perp} - \frac{1}{2} \mathbf{h}_{s,\parallel}^{\perp} \right) \cdot \nabla \hat{\mathbf{e}}_{\parallel}\hat{\mathbf{e}}_{\parallel} \\ & \quad - \hat{\mathbf{e}}_{\parallel}\hat{\mathbf{e}}_{\parallel} \nabla \cdot \mathbf{h}_s^{\parallel} - (\mathbf{I} - \hat{\mathbf{e}}_{\parallel}\hat{\mathbf{e}}_{\parallel}) \nabla \cdot \mathbf{h}_s^{\perp} + \boldsymbol{\Omega}_s \times \boldsymbol{\tau}_s - \boldsymbol{\tau}_s \times \boldsymbol{\Omega}_s \\ & \quad + (p_{s,\parallel} - p_{s,\perp}) \frac{D_s}{Dt}(\hat{\mathbf{e}}_{\parallel}\hat{\mathbf{e}}_{\parallel}) - \frac{1}{2}(\mathbf{I} - 3\hat{\mathbf{e}}_{\parallel}\hat{\mathbf{e}}_{\parallel}) \times \left[ \boldsymbol{\tau}_s : \frac{D_s}{Dt}(\hat{\mathbf{e}}_{\parallel}\hat{\mathbf{e}}_{\parallel}) \right. \\ & \quad \left. + \left[ \mathbf{h}_s^{\parallel}\hat{\mathbf{e}}_{\parallel} : \nabla\hat{\mathbf{e}}_{\parallel} + (\mathbf{h}_s^{\perp} \cdot \hat{\mathbf{e}}_{\parallel})(\nabla \cdot \hat{\mathbf{e}}_{\parallel}) \right] \right] = \frac{\delta \boldsymbol{\tau}_s}{\delta t} \quad (2.41) \end{aligned}$$

Parallel Heat Flow:

$$\begin{aligned} & \frac{D_s \mathbf{h}_s^{\parallel}}{Dt} + 2 \left[ \left( \mathbf{h}_s^{\parallel}\hat{\mathbf{e}}_{\parallel}\hat{\mathbf{e}}_{\parallel} + \hat{\mathbf{e}}_{\parallel}\mathbf{h}_s^{\parallel}\hat{\mathbf{e}}_{\parallel} + \hat{\mathbf{e}}_{\parallel}\hat{\mathbf{e}}_{\parallel}\mathbf{h}_s^{\parallel} - 2\mathbf{h}_{s,\parallel}^{\parallel}\hat{\mathbf{e}}_{\parallel}\hat{\mathbf{e}}_{\parallel} + \frac{1}{2}[\mathbf{h}_s^{\perp}(\mathbf{I} - \hat{\mathbf{e}}_{\parallel}\hat{\mathbf{e}}_{\parallel}) + \hat{\mathbf{e}}_{\perp}^1 \mathbf{h}_s^{\perp} \hat{\mathbf{e}}_{\perp}^1 \right. \right. \\ & \quad \left. \left. + \hat{\mathbf{e}}_{\perp}^2 \mathbf{h}_s^{\perp} \hat{\mathbf{e}}_{\perp}^2 + (\mathbf{I} - \hat{\mathbf{e}}_{\parallel}\hat{\mathbf{e}}_{\parallel}) \mathbf{h}_s^{\perp} \right] + \frac{1}{2}[\mathbf{h}_{s,\parallel}^{\perp}(\mathbf{I} - \hat{\mathbf{e}}_{\parallel}\hat{\mathbf{e}}_{\parallel}) + \hat{\mathbf{e}}_{\perp}^1 \mathbf{h}_{s,\parallel}^{\perp} \hat{\mathbf{e}}_{\perp}^1 + \hat{\mathbf{e}}_{\perp}^2 \mathbf{h}_{s,\parallel}^{\perp} \hat{\mathbf{e}}_{\perp}^2 \right. \\ & \quad \left. + (\mathbf{I} - \hat{\mathbf{e}}_{\parallel}\hat{\mathbf{e}}_{\parallel}) \mathbf{h}_{s,\parallel}^{\perp} \right] \cdot \nabla \mathbf{u}_s \left. \right] : \hat{\mathbf{e}}_{\parallel}\hat{\mathbf{e}}_{\parallel} + \mathbf{h}_s^{\parallel} \nabla \cdot \mathbf{u}_s + \mathbf{h}_s^{\parallel} \cdot \nabla \mathbf{u}_s \\ & \quad + \nabla \cdot \left( \frac{p_{s,\parallel}}{\rho_s} [3p_{s,\parallel}\hat{\mathbf{e}}_{\parallel}\hat{\mathbf{e}}_{\parallel} + p_{s,\perp}(\mathbf{I} - \hat{\mathbf{e}}_{\parallel}\hat{\mathbf{e}}_{\parallel}) + \boldsymbol{\tau}_s + 2\boldsymbol{\tau}_s \cdot \hat{\mathbf{e}}_{\parallel}\hat{\mathbf{e}}_{\parallel} + 2\hat{\mathbf{e}}_{\parallel}\hat{\mathbf{e}}_{\parallel} \cdot \boldsymbol{\tau}_s] \right) \\ & \quad + \left[ \frac{D_s \mathbf{u}_s}{Dt} - \frac{e_s}{m_s} (\mathbf{E} + \mathbf{u}_s \times \mathbf{B}) \right] \cdot [p_{s,\parallel} \mathbf{I} + 2\hat{\mathbf{e}}_{\parallel}\hat{\mathbf{e}}_{\parallel} \cdot (p_{s,\parallel} \mathbf{I} + \boldsymbol{\tau}_s)] \\ & \quad + \boldsymbol{\Omega}_s \times \mathbf{h}_s^{\parallel} - 2 \left[ \hat{\mathbf{e}}_{\parallel}\mathbf{h}_s^{\parallel} \cdot \frac{D_s \hat{\mathbf{e}}_{\parallel}}{Dt} + \hat{\mathbf{e}}_{\parallel} \cdot \mathbf{h}_s^{\perp} \frac{D_s \hat{\mathbf{e}}_{\parallel}}{Dt} \right] \\ & \quad - \frac{2}{\rho_s} \left[ \mathbf{P}_s : (\nabla \hat{\mathbf{e}}_{\parallel}) \hat{\mathbf{e}}_{\parallel} \cdot \mathbf{P}_s + \mathbf{P}_s \cdot (\nabla \hat{\mathbf{e}}_{\parallel}) \hat{\mathbf{e}}_{\parallel} : \mathbf{P}_s + \mathbf{P}_s : \hat{\mathbf{e}}_{\parallel} (\nabla \hat{\mathbf{e}}_{\parallel}) \cdot \mathbf{P}_s \right] \quad (2.42) \end{aligned}$$



$$-\boldsymbol{\tau}_s : (\nabla \hat{\mathbf{e}}_{\parallel}) \hat{\mathbf{e}}_{\parallel} \cdot \boldsymbol{\tau}_s - \boldsymbol{\tau}_s \cdot (\nabla \hat{\mathbf{e}}_{\parallel}) \hat{\mathbf{e}}_{\parallel} : \boldsymbol{\tau}_s - \boldsymbol{\tau}_s : \hat{\mathbf{e}}_{\parallel} (\nabla \hat{\mathbf{e}}_{\parallel}) \cdot \boldsymbol{\tau}_s \Big] = \frac{\delta \mathbf{h}_s^{\parallel}}{\delta t} \quad (2.43)$$

Perpendicular Heat Flow:

$$\begin{aligned} & \frac{D_s \mathbf{h}_s^{\perp}}{Dt} + \left[ \left( \mathbf{h}_s^{\parallel} \hat{\mathbf{e}}_{\parallel} \hat{\mathbf{e}}_{\parallel} + \hat{\mathbf{e}}_{\parallel} \mathbf{h}_s^{\parallel} \hat{\mathbf{e}}_{\parallel} + \hat{\mathbf{e}}_{\parallel} \hat{\mathbf{e}}_{\parallel} \mathbf{h}_s^{\parallel} - 2 \mathbf{h}_{s,\parallel}^{\parallel} \hat{\mathbf{e}}_{\parallel} \hat{\mathbf{e}}_{\parallel} + \frac{1}{2} [\mathbf{h}_s^{\perp} (\mathbf{I} - \hat{\mathbf{e}}_{\parallel} \hat{\mathbf{e}}_{\parallel}) + \hat{\mathbf{e}}_{\perp}^1 \mathbf{h}_s^{\perp} \hat{\mathbf{e}}_{\perp}^1 \right. \right. \\ & \quad \left. \left. + \hat{\mathbf{e}}_{\perp}^2 \mathbf{h}_s^{\perp} \hat{\mathbf{e}}_{\perp}^2 + (\mathbf{I} - \hat{\mathbf{e}}_{\parallel} \hat{\mathbf{e}}_{\parallel}) \mathbf{h}_s^{\perp} \right] + \frac{1}{2} [\mathbf{h}_{s,\parallel}^{\perp} (\mathbf{I} - \hat{\mathbf{e}}_{\parallel} \hat{\mathbf{e}}_{\parallel}) + \hat{\mathbf{e}}_{\perp}^1 \mathbf{h}_{s,\parallel}^{\perp} \hat{\mathbf{e}}_{\perp}^1 + \hat{\mathbf{e}}_{\perp}^2 \mathbf{h}_{s,\parallel}^{\perp} \hat{\mathbf{e}}_{\perp}^2 \right. \\ & \quad \left. + (\mathbf{I} - \hat{\mathbf{e}}_{\parallel} \hat{\mathbf{e}}_{\parallel}) \mathbf{h}_{s,\parallel}^{\perp} \right] \cdot \nabla \mathbf{u}_s \Big] : (\mathbf{I} - \hat{\mathbf{e}}_{\parallel} \hat{\mathbf{e}}_{\parallel}) + \mathbf{h}_s^{\perp} \nabla \cdot \mathbf{u}_s + \mathbf{h}_s^{\perp} \cdot \nabla \mathbf{u}_s \\ & \quad + \frac{1}{2} \nabla \cdot \left( \frac{p_{s,\perp}}{\rho_s} [2p_{s,\parallel} \hat{\mathbf{e}}_{\parallel} \hat{\mathbf{e}}_{\parallel} + 4p_{s,\perp} (\mathbf{I} - \hat{\mathbf{e}}_{\parallel} \hat{\mathbf{e}}_{\parallel}) + 6\boldsymbol{\tau}_s - 2\boldsymbol{\tau}_s \cdot \hat{\mathbf{e}}_{\parallel} \hat{\mathbf{e}}_{\parallel} - 2\hat{\mathbf{e}}_{\parallel} \hat{\mathbf{e}}_{\parallel} \cdot \boldsymbol{\tau}_s] \right) \\ & \quad + \left[ \frac{D_s \mathbf{u}_s}{Dt} - \frac{e_s}{m_s} (\mathbf{E} + \mathbf{u}_s \times \mathbf{B}) \right] \cdot [p_{s,\perp} \mathbf{I} + (\mathbf{I} - \hat{\mathbf{e}}_{\parallel} \hat{\mathbf{e}}_{\parallel}) \cdot (p_{s,\perp} \mathbf{I} + \boldsymbol{\tau}_s)] \\ & \quad + \boldsymbol{\Omega}_s \times \mathbf{h}_s^{\perp} + \left[ \hat{\mathbf{e}}_{\parallel} \mathbf{h}_s^{\parallel} \cdot \frac{D_s \hat{\mathbf{e}}_{\parallel}}{Dt} + \hat{\mathbf{e}}_{\parallel} \cdot \mathbf{h}_s^{\perp} \frac{D_s \hat{\mathbf{e}}_{\parallel}}{Dt} \right] \\ & \quad + \frac{1}{\rho_s} \left[ \mathbf{P}_s : (\nabla \hat{\mathbf{e}}_{\parallel}) \hat{\mathbf{e}}_{\parallel} \cdot \mathbf{P}_s + \mathbf{P}_s \cdot (\nabla \hat{\mathbf{e}}_{\parallel}) \hat{\mathbf{e}}_{\parallel} : \mathbf{P}_s + \mathbf{P}_s : \hat{\mathbf{e}}_{\parallel} (\nabla \hat{\mathbf{e}}_{\parallel}) \cdot \mathbf{P}_s \right. \\ & \quad \left. - \boldsymbol{\tau}_s : (\nabla \hat{\mathbf{e}}_{\parallel}) \hat{\mathbf{e}}_{\parallel} \cdot \boldsymbol{\tau}_s - \boldsymbol{\tau}_s \cdot (\nabla \hat{\mathbf{e}}_{\parallel}) \hat{\mathbf{e}}_{\parallel} : \boldsymbol{\tau}_s - \boldsymbol{\tau}_s : \hat{\mathbf{e}}_{\parallel} (\nabla \hat{\mathbf{e}}_{\parallel}) \cdot \boldsymbol{\tau}_s \right] = \frac{\delta \mathbf{h}_s^{\perp}}{\delta t} \quad (2.44) \end{aligned}$$

where  $\mathbf{P}_s$ , the pressure tensor, is related to the stress tensor by  $\mathbf{P}_s = \boldsymbol{\tau}_s + p_{s,\perp} \mathbf{I} + (p_{s,\parallel} - p_{s,\perp}) \hat{\mathbf{e}}_{\parallel} \hat{\mathbf{e}}_{\parallel}$ . This 16-moment transport description corresponds to a generalization of Grad's expansion of the distribution function in a series of Hermite polynomials and truncation after the third order polynomial (see *Grad (1949)* and *Oraevskii et al. (1968)* for the full mathematical discussion; *Chodura and Pohl (1971)*; *Demars and Schunk (1979)*; *Barakat and Schunk (1981, 1982a)* and *Blilly and Schunk (1993)* for extensive equation development and full collision description).

The extensive system of equations present in Equations 2.37 to 2.44, coupled with Maxwell's equations, represent a closed set of transport equations suitable for describing the high-latitude ionosphere. Solving this system in it's current form is computationally prohibitive. Further assumptions must be applied to reduce this set to a workable level while retaining the fundamental Bi-Maxwellian plasma description.

## 2.2 GEMINI-TIA: anisotropic fluid model

In order to simplify the system, equations of state are adopted for parallel and perpendicular heat flow equations. It is assumed that only the parallel component of the heat fluxes exists.

$$\begin{aligned}\mathbf{h}_s^{\parallel} &= h_{s,\parallel} \hat{\mathbf{e}}_{\parallel} \\ \mathbf{h}_s^{\perp} &= h_{s,\perp} \hat{\mathbf{e}}_{\parallel}\end{aligned}\tag{2.45}$$

This modifies the heat flux terms in equations 2.39 and 2.40

$$\begin{aligned}& [(\mathbf{h}_s^{\parallel} \hat{\mathbf{e}}_{\parallel}) : (\nabla \hat{\mathbf{e}}_{\parallel}) + (\mathbf{h}_s^{\perp} \cdot \hat{\mathbf{e}}_{\parallel})(\nabla \cdot \hat{\mathbf{e}}_{\parallel})] \\ &= [(h_{s,\parallel} \hat{\mathbf{e}}_{\parallel} \hat{\mathbf{e}}_{\parallel}) : (\nabla \hat{\mathbf{e}}_{\parallel}) + (h_{s,\perp} \hat{\mathbf{e}}_{\parallel} \cdot \hat{\mathbf{e}}_{\parallel})(\nabla \cdot \hat{\mathbf{e}}_{\parallel})] \\ &= h_{s,\perp} (\nabla \cdot \hat{\mathbf{e}}_{\parallel})\end{aligned}\tag{2.46}$$

where  $\hat{\mathbf{e}}_{\parallel} \hat{\mathbf{e}}_{\parallel} : \nabla \hat{\mathbf{e}}_{\parallel} = 0$ .

Due to the high altitudes that this model can span, there may be both collisional and collisionless regions. For the region of the model where collisions are significant (both Maxwell and Coulomb), traditional Fourier's Law descriptions are used where the time rate of heat transfer is proportional to the negative temperature gradient.

$$h_{s,\parallel} = -\frac{2}{3} \lambda_s \nabla_{\parallel} T_{s,\parallel} \cdot \hat{\mathbf{e}}_{\parallel}\tag{2.47}$$

$$h_{s,\perp} = -\frac{2}{3} \lambda_s \nabla_{\parallel} T_{s,\perp} \cdot \hat{\mathbf{e}}_{\parallel}\tag{2.48}$$

where  $\lambda_s$  is the thermal conductivity for ion species  $s$ , which is calculated using the parallel temperature (e.g. *Singh*, 1992). It is assumed that only the parallel component of the heat flux exists (viz. only the parallel *transport* of parallel and perpendicular thermal energy is considered). For the collisionless region the maximum heat flux is given by the transport of the thermal energy density by the parallel thermal velocity

$$h_{s,\parallel,\text{collisionless}} = (\epsilon \eta n_s k_b T_{s,\parallel} \mathbf{u}_{th}) \cdot \hat{\mathbf{e}}_{\parallel}\tag{2.49}$$

$$h_{s,\perp,\text{collisionless}} = (\epsilon\eta n_s k_b T_{s,\perp} \mathbf{u}_{th}) \cdot \hat{\mathbf{e}}_{\parallel} \quad (2.50)$$

where  $\epsilon$  is either 1 or -1 depending on the local temperature gradient,  $\eta$  is a weight introduced to compensate for damping from the presence of strong plasma turbulence, and  $\mathbf{u}_{th}$  is the thermal velocity

$$\mathbf{u}_{th} = \left( \frac{k_b T_{s,\parallel}}{m_s} \right)^{1/2} \quad (2.51)$$

which always uses the parallel temperature (*Singh*, 1992, Equation 5). Transitioning between collisional and collisionless regions, and the heat flux descriptions most appropriate to each, the heat flux equation of state is

$$h_{s,\parallel} = (A)h_{s,\parallel,\text{collisional}} + (1 - A)h_{s,\parallel,\text{collisionless}} \quad (2.52)$$

$$h_{s,\perp} = (A)h_{s,\perp,\text{collisional}} + (1 - A)h_{s,\perp,\text{collisionless}} \quad (2.53)$$

and employs a transition relationship

$$A = \frac{1}{2} - \frac{1}{2} \tanh \left( \frac{z - z_o}{z_w} \right), \quad (2.54)$$

where  $z$  is the altitude,  $z_o$  is the transition altitude (as determined by the Knudsen number), and  $z_w$  is the width of the transition region. Equation 2.54 serves to scale the transition between the collisional and collisionless regions allowing the most appropriate assumption to be describing the heat flux. In order to determine where the plasma transitions from collisional to collisionless the Knudsen number ( $Kn$ ) is calculated.

$$Kn = \frac{\lambda_{mfp}}{dx_1 h_1} = \frac{\mathbf{u}_{\parallel}}{\nu_s dx_1 h_1} \quad (2.55)$$

where  $\lambda_{mfp}$  is the mean free path,  $dx_1$  is the change in altitude,  $h_1$  is a metric coefficient, and  $\nu_s$  is the collision frequency. The middle of the transition between collisional and collisionless is set to the first grid cell where  $Kn > 1$ .

Currently, the heat flux can be set to one of three configuration options. Either 1) the heat flux equations of state utilize a Fourier description for the entire altitudinal

range of the model (collisional limit), 2) the heat flux transitions from a collisional to a collisionless description, as discussed above, or 3) the heat flux transitions to zero for the upper altitudes the model grid where the Knudsen number is greater than one (collisionless limit). This transition occurs at roughly 2500 km for commonly used conditions. This functionality allows for a broader range of physical plasma conditions to be accurately described. At even higher altitudes, the grid mostly serves as a buffer zone to prevent boundary conditions from affecting the numerical solutions.

The stress tensor has been set to zero (the term “stress” is used in the sense defined in *Barakat and Schunk (1982a)*), a common assumption in ionospheric models (c.f. *Schunk, 1975*). Most ionospheric models do not include ion stress since it significantly complicates application of the transport equations and the full generalized stress transport equation validity is uncertain, especially in the near collisionless regime (c.f. *Palmadesso et al., 1988*). Additionally, simpler descriptions of ion stress like the Navier-Stokes approximations are not likely to be valid at altitudes where ion stress matters (c.f. *Schunk, 1975*, section 5, part c). Hence, stress is neglected here rather than included as a potentially problematic physical formulation.

Plugging the heat flux and stress assumptions into the parallel and perpendicular energy equations gives

$$\frac{D_s p_{s,\parallel}}{Dt} + p_{s,\parallel} (\nabla \cdot \mathbf{u}_s + 2\nabla_{\parallel} \cdot \mathbf{u}_s) + \nabla \cdot h_{s,\parallel} \hat{\mathbf{e}}_{\parallel} - 2h_{s,\perp} (\nabla \cdot \hat{\mathbf{e}}_{\parallel}) = \frac{\delta E_{s,\parallel}}{\delta t} \quad (2.56)$$

$$\frac{D_s p_{s,\perp}}{Dt} + p_{s,\perp} (\nabla \cdot \mathbf{u}_s + \nabla_{\perp} \cdot \mathbf{u}_s) + \nabla \cdot h_{s,\perp} \hat{\mathbf{e}}_{\parallel} + h_{s,\perp} (\nabla \cdot \hat{\mathbf{e}}_{\parallel}) = \frac{\delta E_{s,\perp}}{\delta t} \quad (2.57)$$

Note, in particular, that the perpendicular heat flux appears in the parallel energy equation. This complicates numerical solution of the parallel energy equation and is discussed further in Section 2.3. The last step needed to bring the energy equations into the form used in the model is to expand the convective derivative,  $D_s/Dt = \partial/\partial t + \mathbf{u}_s \cdot \nabla$ . Taking advantage of the relationship  $\mathbf{u}_s \cdot \nabla a + a \nabla \cdot \mathbf{u}_s = \nabla \cdot (a \mathbf{u}_s)$  where  $a$  is either  $p_{s,\parallel}$  or  $p_{s,\perp}$  these equations reach their final implemented form.

Modifying the momentum equation, first a steady state momentum approximation

is used for perpendicular ion drifts. This is an appropriate assumption here because the principle charge carriers, ions in the perpendicular direction and electrons in the parallel direction, obtain a steady-state in a time scale that are much shorter than any other time scale of interest to this study. The ions drift perpendicular to the magnetic field in a steady-state on time scales much greater than the cyclotron period and the electron parallel motion is in a steady-state on time scales much longer than the electron collision time, which is smaller than  $10^{-2}$  seconds throughout most of the ionosphere. The time steps used in the model are usually two orders of magnitude larger than these values. Using a stationary perpendicular momentum assumption has the benefit of simplifying the transport equations and relaxing stability constraints on the simulation time step by excluding MHD wave modes involving perpendicular plasma oscillations (shear Alfvén waves and magnetosonic waves).

As a result of this assumption, only the parallel component of the full momentum equation 2.38 is required. Dotting equation 2.38 with  $\hat{e}_{\parallel}$ , and setting  $\boldsymbol{\tau}_s = 0$ , yields:

$$\rho_s \frac{D_s \mathbf{u}_s}{Dt} \cdot \hat{e}_{\parallel} + \nabla_{\parallel} p_{s,\parallel} \cdot \hat{e}_{\parallel} - \rho_s g_{\parallel} + n_s q_s E_{\parallel} - (p_{s,\parallel} + p_{s,\perp}) [\nabla \cdot (\hat{e}_{\parallel} \hat{e}_{\parallel})] \cdot \hat{e}_{\parallel} = \frac{\delta M_{s,\parallel}}{\delta t} \quad (2.58)$$

Note that solving only along the  $\hat{e}_{\parallel}$  direction removes the need for the  $\mathbf{u}_s \times \mathbf{B}$  term. The mirror term in the momentum equation can now be simplified:

$$[\nabla \cdot (\hat{e}_{\parallel} \hat{e}_{\parallel})] \cdot \hat{e}_{\parallel} = (\nabla \cdot \hat{e}_{\parallel})(\hat{e}_{\parallel} \cdot \hat{e}_{\parallel}) + \hat{e}_{\parallel} \hat{e}_{\parallel} : \nabla \hat{e}_{\parallel} = \nabla \cdot \hat{e}_{\parallel}, \quad (2.59)$$

where  $\hat{e}_{\parallel} \hat{e}_{\parallel} : \nabla \hat{e}_{\parallel} = 0$  has been invoked.

Further development of the momentum equation involves three steps to expand the convective derivative and bring this transport equation into the form used in the model. First, working only with the convective derivative term from the momentum equation:

$$\rho_s \frac{D_s \mathbf{u}_s}{Dt} = \rho_s \frac{\partial \mathbf{u}_s}{\partial t} + \rho_s \mathbf{u}_s \cdot \nabla \mathbf{u}_s \quad (2.60)$$

Next, using the relationship

$$\frac{\partial(\rho_s \mathbf{u}_s)}{\partial t} = \rho_s \frac{\partial \mathbf{u}_s}{\partial t} + \mathbf{u}_s \frac{\partial \rho_s}{\partial t} \quad (2.61)$$

updates Equation 2.60 to

$$\rho_s \frac{D_s \mathbf{u}_s}{Dt} = \frac{\partial(\rho_s \mathbf{u}_s)}{\partial t} - \mathbf{u}_s \frac{\partial \rho_s}{\partial t} + \rho_s \mathbf{u}_s \cdot \nabla \mathbf{u}_s \quad (2.62)$$

Then applying the continuity equation (without collisions)  $\partial \rho_s / \partial t = -\nabla \cdot (\rho_s \mathbf{u}_s)$  further develops this term to

$$\rho_s \frac{D_s \mathbf{u}_s}{Dt} = \frac{\partial(\rho_s \mathbf{u}_s)}{\partial t} + \mathbf{u}_s \nabla \cdot (\rho_s \mathbf{u}_s) + \rho_s \mathbf{u}_s \cdot \nabla \mathbf{u}_s \quad (2.63)$$

and allows for the relationship  $\mathbf{u}_s \cdot \nabla \rho_s \mathbf{u}_s + \rho_s \mathbf{u}_s \nabla \cdot \mathbf{u}_s = \nabla \cdot (\rho_s \mathbf{u}_s \mathbf{u}_s)$  to be used to bring this term to the final form

$$\rho_s \frac{D_s \mathbf{u}_s}{Dt} = \frac{\partial(\rho_s \mathbf{u}_s)}{\partial t} + \nabla \cdot (\rho_s \mathbf{u}_s \mathbf{u}_s) \quad (2.64)$$

Including this convective derivative relationship results in the final implemented form of the momentum equation.

Finally, the continuity equation is modified with the inclusion of the  $P_s$  term to include chemical production, photoionization, and impact ionization. The  $L_s$  term has been added to include chemical loss processes. This is the last step used to bring this set of transport equations into the form used within the model. Expanding the collision terms, where the summations over index “ $j$ ” describe ion-ion interactions and the summations over index “ $n$ ” describe ion-neutral interactions, the final form of the equations used in the model are:

Continuity:

$$\frac{\partial \rho_s}{\partial t} + \nabla \cdot (\rho_s \mathbf{u}_s) = m_s P_s - L_s \rho_s \quad (2.65)$$

Momentum:

$$\frac{\partial(\rho_s \mathbf{u}_s)}{\partial t} \cdot \hat{\mathbf{e}}_{\parallel} + [\nabla \cdot (\rho_s \mathbf{u}_s \mathbf{u}_s)] \cdot \hat{\mathbf{e}}_{\parallel} = \rho_s g_{\parallel} - \nabla p_{s,\parallel} \cdot \hat{\mathbf{e}}_{\parallel} + n_s q_s E_{\parallel} - (p_{s,\parallel} - p_{s,\perp}) \nabla \cdot \hat{\mathbf{e}}_{\parallel}$$

$$\begin{aligned}
& - \sum_j \frac{3\nu_{sj}}{4\pi k_b} \left[ 2k_b n_s m_s \frac{\sigma_{sj,\perp}}{\sigma_{sj,\parallel}} I_{002} \left( \mathbf{u}_s - \mathbf{u}_j \right)_{\parallel} \right] \\
& - \sum_n n_s m_s \nu_{sn} \left( \mathbf{u}_s - \mathbf{u}_n \right)_{\parallel}
\end{aligned} \tag{2.66}$$

Parallel Energy:

$$\begin{aligned}
\frac{\partial p_{s,\parallel}}{\partial t} + \nabla \cdot (p_{s,\parallel} \mathbf{u}_s) &= -2p_{s,\parallel} (\nabla_{\parallel} \cdot \mathbf{u}_s) - \nabla \cdot (h_{s,\parallel} \hat{\mathbf{e}}_{\parallel}) + 2h_{s,\perp} (\nabla \cdot \hat{\mathbf{e}}_{\parallel}) \\
& + \sum_j \frac{3}{2\pi} \frac{m_s n_s k_b \nu_{sj}}{m_s + m_j} \left[ 2 \frac{\sigma_{sj,\perp}}{\sigma_{sj,\parallel}} I_{002} (T_{j,\parallel} - T_{s,\parallel}) \right. \\
& \left. + m_j \left( \frac{2\pi}{3} (\mathbf{u}_s - \mathbf{u}_j)^2 + 2\sigma_{sj,\perp} (I_{200} - I_{002}) \right) \right] \\
& - \sum_n \frac{n_s m_s \nu_{sn}}{(m_s + m_n)} \left[ 2k_b (T_{s,\parallel} - T_{n,\parallel}) - 2m_n (\mathbf{u}_s - \mathbf{u}_n)_{\parallel}^2 \right. \\
& \left. + \frac{m_n Q_{sn}^{(2)}}{2Q_{sn}^{(1)}} \left( 2k_b (\sigma_{sn,\parallel} - \sigma_{sn,\perp}) - (\mathbf{u}_s - \mathbf{u}_n)^2 + 3(\mathbf{u}_s - \mathbf{u}_n)_{\parallel}^2 \right) \right]
\end{aligned} \tag{2.67}$$

Perpendicular Energy:

$$\begin{aligned}
\frac{\partial p_{s,\perp}}{\partial t} + \nabla \cdot (p_{s,\perp} \mathbf{u}_s) &= -p_{s,\perp} (\nabla_{\perp} \cdot \mathbf{u}_s) - \nabla \cdot (h_{s,\perp} \hat{\mathbf{e}}_{\parallel}) + \dot{W}_{s,\perp} - h_{s,\perp} (\nabla \cdot \hat{\mathbf{e}}_{\parallel}) \\
& + \sum_j \frac{3}{4\pi} \frac{m_s n_s k_b \nu_{sj}}{m_s + m_j} \left[ 4I_{200} (T_{j,\perp} - T_{s,\perp}) \right. \\
& \left. + m_j \left( \frac{4\pi}{3} (\mathbf{u}_s - \mathbf{u}_j)^2 + 2\sigma_{sj,\perp} (I_{002} - I_{200}) \right) \right] \\
& - \sum_n \frac{n_s m_s \nu_{sn}}{(m_s + m_n)} \left[ 2k_b (T_{s,\perp} - T_{n,\perp}) - m_n (\mathbf{u}_s - \mathbf{u}_n)_{\perp}^2 \right. \\
& \left. + \frac{m_n Q_{sn}^{(2)}}{4Q_{sn}^{(1)}} \left( 2k_b (\sigma_{sn,\perp} - \sigma_{sn,\parallel}) - 2(\mathbf{u}_s - \mathbf{u}_n)^2 + 3(\mathbf{u}_s - \mathbf{u}_n)_{\perp}^2 \right) \right].
\end{aligned} \tag{2.68}$$

In these equations  $\rho_s$  is the mass density,  $m_s$  is the ion mass, and  $\mathbf{u}_s$  is the drift velocity of species  $s$ . Parallel and perpendicular pressures are  $p_{s,\parallel} = \rho_s k_B T_{s,\parallel} / m_s$

and  $p_{s,\perp} = \rho_s k_B T_{s,\perp} / m_s$  respectively,  $q_s$  is the charge of each species,  $E_{\parallel}$  is the parallel electric field, and  $\hat{\mathbf{e}}_{\parallel}$  is the unit vector along the geomagnetic field. Additional variables (i.e. collision term quantities) within these transport equations are defined in greater detail in paragraphs that follow.

### 2.2.1 Electrostatic approximation

The multi-fluid system of Equations 2.65-2.68 is closed through an electrostatic treatment of the auroral currents using Equation 2.69.

$$\nabla_{\perp} \cdot (\boldsymbol{\sigma}_{\perp} \cdot \nabla_{\perp} \Phi) + \nabla_{\parallel} \cdot (\sigma_0 \nabla_{\parallel} \Phi) = \nabla_{\perp} \cdot \left( \sum_s n_s m_s \nu_s \mu_{s\perp} \cdot \mathbf{u}_{n\perp} \right) \quad (2.69)$$

where  $\Phi$  is the electric potential,  $\boldsymbol{\sigma}_{\perp}$  is the perpendicular conductivity tensor, and  $\sigma_0$  is the parallel conductivity (conductivities are defined in *Zettergren and Semeter (2012)*).

The electric field is composed of both an ambipolar field,  $\mathbf{E}_a$ , which is always present and a response field,  $\mathbf{E}_r$ , which results from magnetospherically imposed currents and/or neutral winds. When solving for the electric potential in Equation 2.69 the ambipolar electric field is not included, so the potential represents the part of the electric field that is due to the ionospheric resistivity (viz. collisions). When solving the momentum equation, the ambipolar electric field (computed from electron pressure) is added to the electric field which is a result of driving a field-aligned current through the resistive ionosphere. Hence, both the electron pressure and resistive parts of the electric field are resolved in GEMINI-TIA. Tests indicate that this approach does not impact the solution for the electric field.

The electric field in the perpendicular direction is found from  $\mathbf{E}_{\perp} = -\nabla_{\perp} \Phi$ , while the parallel electric field is obtained by superposing the resistive part of the field (as computed from Equation 2.69) and the ambipolar electric field

$$\mathbf{E}_{\parallel} = -\nabla_{\parallel} \Phi + \frac{1}{n_e q_e} \nabla_{\parallel} p_e \quad (2.70)$$



A static geomagnetic field, presently a dipole model, is used to calculate the conductivities in equations 2.69, the ion mobilities in Equation 2.71, and the metric coefficients needed to solve the system of equations defined by Equations 2.65 - 2.69 (*Huba et al.*, 2000).

Consistent with the use of an electrostatic treatment, a steady state momentum approximation is used for the perpendicular ion drifts.

$$\mathbf{u}_{s,\perp} = \boldsymbol{\mu}_{s,\perp} \cdot \left( \mathbf{E}_\perp + \frac{m_s \nu_s}{q_s} \mathbf{u}_{n,\perp} \right) \quad (2.71)$$

where  $\boldsymbol{\mu}_{s,\perp}$  is the ion mobility tensor and  $\nu_s$  is the total ion-neutral collision frequency.

Under a steady state momentum assumption ion and electron drifts are determined by the mobility and forces on each population. Since the electron mobility is much higher than the ion mobility in the parallel direction, the parallel ion drift contributions to current are neglected and the electrons are assumed to carry all of the parallel current. Even though the ions are not in a steady state, they contribute negligibly to the parallel current. This allows for the parallel ion momentum to be described in a time-dependent manner while still using a current continuity equation that encodes a steady-state momentum balance.

The electrons are treated differently from the ions (e.g. *Zettergren and Snively*, 2015). The density is found via quasi-neutrality

$$n_e = \sum_{s \neq e} n_s, \quad (2.72)$$

and the velocity is calculated from the current density provided by solving the electrostatic equation (Equation 2.69):

$$\mathbf{u}_e = -\frac{1}{n_e q_e} \left( \sum_{s \neq e} n_s q_s \mathbf{u}_s - \mathbf{J} \right). \quad (2.73)$$

Unlike the ions, the electrons are considered to be isotropic so only a single transport

equation is solved for the electron energy

$$\begin{aligned} \frac{\partial(\rho_e \epsilon_e)}{\partial t} + \nabla \cdot (\rho_e \epsilon_e \mathbf{u}_e) = p_e (\nabla \cdot \mathbf{u}_e) - \nabla \cdot \mathbf{h}_e + \frac{Q_e}{(\gamma_e - 1)} \\ - \frac{1}{\gamma_e - 1} \sum_s \frac{\rho_e k_b \nu_{es}}{m_e + m_s} \left[ 2(T_e - T_s) - \frac{2m_s}{3k_b} (\mathbf{u}_e - \mathbf{u}_t)^2 \right] \end{aligned} \quad (2.74)$$

where  $\epsilon_e = p_e / [(\gamma_e - 1)\rho_e]$  is the specific internal energy. This electron energy equation differs from the ion energy equations in that it also includes inelastic cooling terms (*Schunk and Nagy, 1978*) and heating by photoelectrons in the  $Q_e$  term (*Swartz and Nisbet, 1972*). It also includes a thermoelectric component in the heat flux (e.g. *Schunk and Nagy, 1978; Zettergren and Snively, 2015*).

### 2.2.2 Wave-particle interactions

The resonant heating term,  $\dot{W}_{s,\perp}$ , in Equation 2.67 parameterizes the acceleration of ions by transverse plasma waves. This gyroresonant (cyclotron) energy transfer requires low ion-neutral collision rates and is therefore rarely observed below 500 km except in extreme cases (e.g. *Whalen et al., 1978*). Because this type of heating occurs primarily in collisionless regions, the resulting ion distributions remain highly anisotropic and are accelerated by the mirror force, attaining large field aligned velocities high above the heating region. The present form of the model uses an empirical specification of this heating term:

$$\dot{W}_{s,\perp}(\omega) = 2\rho_s \left( \frac{\eta q_s^2}{4m_s^2} \right) |E_0|^2 \left( \frac{\omega}{\omega_o} \right)^{-\alpha} \quad (2.75)$$

where  $\omega$  is the local gyrofrequency for each ion,  $\eta$  is the fraction of the wave field which is left-hand polarized, assumed to be 0.125 (*Chang et al., 1986*),  $\alpha$  is the spectral power index, assumed to be 1.7 (*Crew et al., 1990*), and  $|E_0|^2$  is the wave power spectral density at some reference frequency  $\omega_o$ , where  $\omega_o$  is taken to be 6.5 Hz unless specified otherwise (*Zeng and Horwitz, 2008; Zeng et al., 2006; Retterer et al., 1983*). The wave heating term is evaluated at the local gyro-frequency of each ion species for every point in the simulation and truncated at the top of the simulation,

similar to what was done in *Wu et al.* (1999), to prevent boundary artifacts. Note that even though the wave power spectral density is specified as constant with altitude (*Bouhram et al.*, 2003) the heating rate will still be altitude dependent since the ion gyrofrequency and density changes with altitude.

### 2.2.3 Collision frequency

All of the collision terms within Equations 2.65-2.68 utilize the momentum-transfer collision frequency, following *Demars and Schunk* (1979, equations), suitable for a 16-moment description. This is described by

$$\nu_{st} = \frac{8\sqrt{\pi}}{3} (2k_b)^{-n/2} A_1(a) \Gamma\left(\frac{5-n}{2}\right) \frac{n_t m_t}{m_s + m_t} \left(\frac{K_{st}}{\xi_{st}}\right)^{(n+1)/2} \sigma_{st,\parallel}^{-1/2} \sigma_{st,\perp}^{-(n-1)/2} \quad (2.76)$$

where the reduced mass is

$$\xi_{st} = \frac{m_s m_t}{m_s + m_t}, \quad (2.77)$$

and

$$\begin{aligned} \sigma_{\parallel} &= \frac{T_{s,\parallel}}{m_s} + \frac{T_{t,\parallel}}{m_t} \\ \sigma_{\perp} &= \frac{T_{s,\perp}}{m_s} + \frac{T_{t,\perp}}{m_t} \end{aligned} \quad (2.78)$$

The subscript “*t*” indicates either an ion or neutral specie.  $A_1(a)$  is a pure number dependent only on the constant  $a$  (tabulated in *Schunk and Nagy* (2000, table 4.2)),  $\Gamma$  is the gamma function,  $K_{st}$  is a constant, and  $n = (5-a)/(a-1)$  (see *Demars and Schunk* (1979) for details).

In an attempt to simplify the numerical process of including this collision frequency, the collision frequency presented in *Schunk and Nagy* (2000) is examined. There, an isotropic temperature system is being described with the corresponding

collision frequency

$$\nu_{st} = \frac{8\sqrt{\pi}}{3}(2k_b)^{-n/2}A_1(a)\Gamma\left(\frac{5-n}{2}\right)\frac{n_t m_t}{m_s + m_t}\left(\frac{K_{st}}{\xi_{st}}\right)^{(n+1)/2}\sigma_{sj}^{(a-5)/(2(a-1))} \quad (2.79)$$

where

$$\sigma_{st} = \frac{T_s}{m_s} + \frac{T_t}{m_t} = \frac{T_{st}}{\xi_{st}} \quad (2.80)$$

and the reduced temperature is

$$T_{st} = \frac{T_s T_t}{T_s + T_t} \quad (2.81)$$

Their collision frequency equation is simplified for different situations. Ion-ion interactions described by Coulomb collisions, in which  $a = 2$ , reduces equation 2.79 to

$$\nu_{sj} = B_{sj}\frac{n_j}{T_{sj}^{3/2}} \quad (2.82)$$

where  $n_j$  is the density of ion specie  $j$ , and  $B_{sj}$  is the calculated coefficient from everything else in equation 2.79 and is tabulated in *Schunk and Nagy* (2000, Table 4.3) for relevant ionospheric species. The collision frequency used in Maxwell molecule interactions, in which  $a = 5$ , simplifies equation 2.79 to

$$\nu_{sn} = C_{sn}n_n \quad (2.83)$$

where  $n$  indicates the neutral specie, and  $C_{sn}$  is the calculated coefficient from everything but the neutral density specie in equation 2.79. It is tabulated in *Schunk and Nagy* (2000, Table 4.4 for non-resonant interactions and Table 4.5 resonant interactions).

It should be noted that when  $T_{s,\parallel} = T_{s,\perp}$ , the anisotropic collision frequency (Equation 2.76) is equivalent to the isotropic collision frequency (Equation 2.79). This equivalence supports a modification of the simplified isotropic collision frequencies for

Coulomb collisions and Maxwell interactions (Equations 2.82 and 2.83) to include the temperature anisotropies while keeping the tabulated constants valid. In Table 2.1 the reduced temperature term differences are shown for clarity.

Table 2.1: Isotropic and anisotropic term differences in the collisional frequency equation.

Difference in $\nu_{st}$	<i>Schunk and Nagy</i> (2000) $T_{st}^{(a-5)/(2(a-1))}$	<i>Demars and Schunk</i> (1979) $T_{st,\parallel}^{-1/2} T_{st,\perp}^{((a-5)/(2(a-1))+1/2)}$
Coulomb [ $a = 2$ ]	$T_{st}^{-3/2}$	$T_{st,\parallel}^{-1/2} T_{st,\perp}^{-1}$
Maxwell [ $a = 5$ ]	1	$T_{st,\parallel}^{-1/2} T_{st,\perp}^{1/2}$

Updating equations 2.82 and 2.83 using the information in Table 2.1 gives for Coulomb and Maxwell interactions respectively

$$\nu_{sj} = B_{sj} n_j T_{sj,\parallel}^{-1/2} T_{sj,\perp}^{-1} \quad (2.84)$$

$$\nu_{sn} = C_{sn} n_n T_{sn,\parallel}^{-1/2} T_{sn,\perp}^{1/2} \quad (2.85)$$

This is the form of the collision frequency used in the model.

## 2.2.4 Coulomb collisions

The Coulomb collision terms used to describe ion-ion interactions (the summations over index “ $j$ ” in Equations 2.66-2.68), are taken from *Blelly and Schunk* (1993, equations 61, 63, 66). These terms were derived for small stress and heat flows, low speed plasma flows where the species drift velocity differences are small in comparison to the thermal speeds, arbitrary difference between species temperatures, and an arbitrary difference between parallel and perpendicular temperatures for the same species. This summation represents the response to a collisional interaction between ion species  $s$  and  $j$ . The  $I_{LMN}$  quantities are defined in *Demars and Schunk* (1979) as

$$I_{LMN} = \int_{-\infty}^{\infty} \int_{-\infty}^{\infty} \int_{-\infty}^{\infty} \frac{x_1^L x_2^M x_3^N}{(x_1^2 + x_2^2 + x_3^2)^{3/2}} e^{-(x_1^2 + x_2^2 + \frac{\sigma_{sj,\perp}}{\sigma_{sj,\parallel}} x_3^2)} dx_1 dx_2 dx_3 \quad (2.86)$$

which are the same as the  $K_{LMN}$  quantities in *Chodura and Pohl* (1971) multiplied by  $\pi$ . Numerically solving the triple integral is difficult. Referring to *Demars and Schunk* (1979), the triple integral can be converted to a hypergeometric function (*Chodura and Pohl*, 1971; *Barakat and Schunk*, 1981). For  $LMN = 200$  this is

$$I_{200} = \pi \Gamma \left( \frac{5-n}{2} \right) (Y_{0,5}^{(n)} - Y_{2,5}^{(n)}) \quad (2.87)$$

and for  $LMN = 002$  it is

$$I_{002} = 2\pi \Gamma \left( \frac{5-n}{2} \right) Y_{2,5}^{(n)} \quad (2.88)$$

where  $\Gamma$  is the gamma function,  $Y_{l,m}^{(n)}$  is

$$\frac{1}{l+1} {}_2F_1 \left( \frac{m-n}{2}, \frac{l+1}{2}; \frac{l+3}{2}; -\lambda \right) \quad (2.89)$$

and  $\lambda$  is  $\sigma_{\perp}/\sigma_{\parallel} - 1$ . Expanding the hypergeometric function into its Fourier series, and with  $n = 3$ , results in, for  $LMN = 200$

$$I_{200} = \frac{\pi}{\lambda} \left( \frac{(1+\lambda) \operatorname{atan}(\sqrt{\lambda})}{\sqrt{\lambda}} - 1 \right) \quad (2.90)$$

and for  $LMN = 002$

$$I_{002} = \frac{2\pi}{\lambda} \left( 1 - \frac{\operatorname{atan}(\sqrt{\lambda})}{\sqrt{\lambda}} \right) \quad (2.91)$$

As indicated by the Coulomb collision summation in Equation 2.66, the rate of change of momentum is proportional to ion-ion drag. Within the Coulomb collision summations in Equations 2.67 and 2.68, the rate of change of parallel and perpendicular energy is proportional the terms which, left to right, represent heat exchange, frictional heating, and the parallel-perpendicular heat transfer within a species having a temperature anisotropy.

### 2.2.5 Maxwell interactions

The Maxwell interaction terms describing the ion-neutral interactions (summations over index “ $n$ ” in equations 2.66-2.68) are taken from *Barakat and Schunk* (1982a, equations 33-35) and *Demars and Schunk* (1979, equations 23a-23c). These terms were derived for arbitrary relative drifts between different species, arbitrary temperature anisotropies for each species, and arbitrary temperature differences between species. Each summation represents the response from a collisional interaction between an ion of species  $s$  and a neutral of species  $n$ . The neutral species currently included are O, N, NO, O<sub>2</sub>, N<sub>2</sub>, and H.

The  $Q_{sn}^{(2)}/Q_{sn}^{(1)}$  ratios used in Equations 2.67 and 2.68 have been updated from the original values used by *Barakat and Schunk* (1982b) to take into consideration the relative energy between colliding particles. As the relative energy of colliding particles changes, the nature of their interaction varies as well. At low energies, collisions are dominated by the polarization attraction between ions and neutrals. At higher energies, a repulsive  $1/r^{12}$  potential takes over and changes the generalized collision cross section. This variation in the collision cross section was explored in *Gaimard et al.* (1998) through their comparison between analytical results and Monte Carlo simulations. In analytical calculations the speed dependence of the collision cross section has to be neglected. This restriction is not present in the Monte Carlo simulations where the cross section is allowed to change with the relative energy of the colliding particles producing more accurate temperatures. *Gaimard et al.* (1998) developed a set of cross sections that vary with respect to the DC electric field strength in such a way as to take account of the modifications in the nature of the ion-neutral interactions as the relative energy of the colliding particles changes. The generalized collision cross section can be described by

$$Q(l) = 2\pi \int_0^\pi \sigma g(1 - \cos^l \theta) \sin(\theta) d\theta \quad (2.92)$$

where  $\sigma$  is the collision cross section (*Maurice and Schunk*, 1977) which varies with respect to the collision angle,  $\theta$ , and  $g$  is the relative speed between colliding particles. *Schunk* (1977, appendix A) relates the  $Q$  terms to the  $A$  terms originally present in

Table 2.2: Values for O<sup>+</sup>-O resonant interactions from *Gaimard et al.* (1998) for various electric fields.

E field (mV/m)	0	25	50	75	100	125	150	175	200	225	250
Q(2)/Q(1)	0.52	0.49	0.42	0.33	0.30	0.27	0.25	0.24	0.23	0.22	0.21

*Barakat and Schunk* (1982a, Equations 34 and 35) used to describe Maxwell molecule interactions. From *Schunk* (1977)

$$Q_{sn}^{(l)} = 2\pi A_l(a) \left( \frac{K_{st}}{\mu_{st} g_{st}^2} \right)^{2/(a-1)} \quad (2.93)$$

where  $a$  and  $K_{st}$  are constants. Conveniently, ratios are used in the Maxwell interaction terms. Specifically,

$$\frac{Q_{sn}^{(2)}}{Q_{sn}^{(1)}} = \frac{2\pi A_2(5) \left( \frac{K_{st}}{\mu_{st} g_{st}^2} \right)^{1/2}}{2\pi A_1(5) \left( \frac{K_{st}}{\mu_{st} g_{st}^2} \right)^{1/2}} \quad (2.94)$$

which simplifies to

$$\frac{Q_{sn}^{(2)}}{Q_{sn}^{(1)}} = \frac{A_2(5)}{A_1(5)} \quad (2.95)$$

and completely removes the need to calculate  $g_{st}$ .

Using the  $Q$  ratios in *Gaimard et al.* (1998) instead of the  $A$  ratios from *Schunk and Nagy* (2000) should correct for the previously unaccounted dependence on the relative energy of the colliding particles. A  $Q_{sn}^{(2)}/Q_{sn}^{(1)}$  ratio of 0.85 is a good average for almost all of the ion-neutral interactions (*Gaimard et al.*, 1998) but it should be noted that the charge exchange cross section is much larger, compared to the polarization cross section for ion-neutral collisions. The  $Q_{sn}^{(2)}/Q_{sn}^{(1)}$  ratio value for O<sup>+</sup>-O resonant interactions will therefore have a strong dependence on the electric field. A simple polynomial fit to the values from Table 2.2, reproduced from *Gaimard et al.* (1998, Table 1), for various electric fields is used in the model for the O<sup>+</sup>-O resonant interaction. This polynomial fit given by:

$$\frac{Q_{sn}^{(2)}}{Q_{sn}^{(1)}} = 6.284 \times 10^{-6} E^2 - 2.833 \times 10^{-3} E + 0.5348. \quad (2.96)$$



where  $E$  is the magnitude of the electric field.

As indicated by the Maxwell interaction summation in Equations 2.66, the rate of change of momentum from this process is proportional to ion-neutral drag. Within the Maxwell interaction summations in Equations 2.67 and 2.68, the rate of change of parallel and perpendicular energy is proportional the terms which, left to right, represent heat transfer between different species, frictional heating, heat transfer between parallel and perpendicular directions and two more terms of frictional heating.

## 2.3 Numerical methods

GEMINI-TIA uses a wide variety of numerical methods, each of which are discussed in detail in the following sections. The primary ion transport equations (Equations 2.65 - 2.68) can be organized into advection, diffusion, stiff, and non-stiff source terms. These terms are computed sequentially in the model using a split time-step procedure that separates the original equation into a sequence of subequations. To implement the time-step splitting, an order in which to resolve the the different substeps must be selected. In principle any ordering will produce an approximate solution to the full equation, but solving the terms in order of increasing numerical stiffness results in the most stable, and accurate, outputs. Specifically, first advection is solved, then non-stiff sources, followed by diffusion terms, and finally stiff source terms. Note that only the energy equations contain all of these substeps; the continuity and momentum equations are solved in two steps: an advection substep and then a stiff sources substep.

### 2.3.1 Advection

Starting with advection, this substep solves

$$\frac{\partial f}{\partial t} + \nabla \cdot (f\mathbf{u}) = 0 \quad (2.97)$$

where  $f$  represents  $\rho_s$ ,  $\rho_s u_s$ ,  $p_{s,\parallel}$ , or  $p_{s,\perp}$  for the continuity, momentum, parallel energy, and perpendicular energy equations respectively, using a flux-limited, finite volume

method (MC flux limiter).

With GEMINI-TIA being a 2D model, advection in multiple dimensions is achieved by dimensional splitting Equation 2.97 into a sequence of 1D advection problems. This expands the advection substep into a sequence of subsubsteps, one for each spatial dimension:

$$\frac{\partial f}{\partial t} + \frac{1}{h_1 h_2 h_3} \frac{\partial}{\partial x_1} (h_2 h_3 f u_1) = 0 \quad (2.98)$$

$$\frac{\partial f}{\partial t} + \frac{1}{h_1 h_2 h_3} \frac{\partial}{\partial x_2} (h_1 h_3 f u_2) = 0 \quad (2.99)$$

Now 1D, each advection subsubstep is advanced in time using a MC flux-limited, finite volume method in the form of

$$f_i^{n+1} = f_i^n + \frac{\Delta t}{h_{1,i} h_{2,i} h_{3,i} \Delta x_{i,1/2}} (h_{i+1/2}^\alpha \varphi_{i+1/2}^n - h_{i-1/2}^\alpha \varphi_{i-1/2}^n) \quad (2.100)$$

where  $i$  is a position indicator,  $n$  is the time step indicator,  $\Delta t$  is the amount of time being advanced,  $\Delta x_{i,1/2}$  is the half difference between  $i$  locations,  $h_1$  is the metric factor for  $x_1$ , the along the magnetic field line dimension (“downwards” is positive in direction), and  $h_2$  is the metric factor for  $x_2$ , the dimension perpendicular to  $x_1$ . These are the primary two dimensions of the model. There are numerical cases where  $h_3$ , the metric factor corresponding to the other perpendicular dimension  $x_3$  is needed to properly compute values on the tilted dipole grid the model uses.  $h^\alpha$  is the multiple of the metric factors that are not of the dimension currently being solved over and  $\varphi_{i-1/2}$  is

$$\varphi_{i-1/2} = \begin{cases} u_{i-1/2} f_i^n - \frac{1}{2} u_{i-1/2} \left( \Delta x_{k,i,b} + \frac{u_{k,i-1/2}}{h_{k,i-1/2}} \Delta t \right) \sigma_i^n & (u_{i-1/2} < 0) \\ u_{i-1/2} f_{i-1}^n + \frac{1}{2} u_{i-1/2} \left( \Delta x_{k,i,b} - \frac{u_{k,i-1/2}}{h_{k,i-1/2}} \Delta t \right) \sigma_{i-1}^n & (u_{i-1/2} \geq 0) \end{cases} \quad (2.101)$$

where  $\sigma$  is an approximation of the slope of function  $f$ ,  $b$  indicated a backwards difference, and  $k$  is the dimension index.

Spatial differences between locations indicated by  $i$  can be considered in three ways: forwards, backwards, and half. Forwards is the distance between  $i$  and  $i + 1$ .

Backwards is the distance between  $i$  and  $i - 1$ . Half is the average distance halfway between forwards and backwards equal to  $((i + 1) - i) + (i - (i - 1)))/2$  or also considered as the distance between the locations  $i + 1/2$  and  $i - 1/2$ . For further information about basic finite difference methods see *LeVeque* (2002).

### 2.3.2 Non-stiff Sources

Next, the partially updated value of  $f$  (which has been advected) is then processed through the non-stiff source step. The compression term is solved in this substep.

$$\frac{\partial f_{\parallel,\perp}}{\partial t} = -af_{\parallel,\perp} (\nabla_{\parallel,\perp} \cdot \mathbf{u}_s) \quad (2.102)$$

where  $a$  is either equal to 2 for the parallel energy equation or 1 for the perpendicular energy equation. Expanding the general equation into the form solved for the parallel energy equation

$$\frac{\partial f}{\partial t} = -2f \frac{1}{h_1 h_2 h_3} \left( \frac{\partial}{\partial x_1} (h_2 h_3 u_1) \right) \quad (2.103)$$

and for the perpendicular energy equation

$$\frac{\partial f}{\partial t} = -f \frac{1}{h_1 h_2 h_3} \left( \frac{\partial}{\partial x_2} (h_1 h_3 u_2) \right) \quad (2.104)$$

Note that the parallel energy equation has a factor of 2. These equations are solved using a two-step Runge-Kutta method for the time integration, while computing the spatial derivatives with centered differences:

$$f_i^{n+1/2} = f_i^n - \frac{\Delta t}{2} f_i^n \frac{1}{h_1 h_2 h_3} \left( \frac{\partial}{\partial x_k} (h^a u_k) \right) \quad (2.105)$$

$$f_i^{n+1} = f_i^{n+1/2} - \Delta t f_i^{n+1/2} \frac{1}{h_1 h_2 h_3} \left( \frac{\partial}{\partial x_k} (h^a u_k) \right) \quad (2.106)$$

where  $k$  indicates either the  $x_1$  or  $x_2$  dimension, and the factor of two needs to be included when solving the parallel energy equation terms.

### 2.3.3 Diffusion

Now  $f$ , which has been advected and updated with the non-stiff sources, is used in the diffusion substep. First the parallel and perpendicular energies, which were expressed in a pressure form, are converted to a temperature description via the ideal gas law.

$$f = p_{s,\parallel,\perp} = n_s k_b T_{s,\parallel,\perp} \quad (2.107)$$

This conversion facilitates calculating the diffusion substep update because the heat flux equation of state, Equations 2.47 and 2.48, are described in a temperature format.

$$\frac{\partial(n_s k_b T_{s,\parallel})}{\partial t} = -\nabla \cdot (h_{s,\parallel} \hat{e}_{\parallel}) + 2h_{s,\perp} (\nabla \cdot \hat{e}_{\parallel}) + \frac{\delta E_{\parallel}}{\delta t} \quad (2.108)$$

$$\frac{\partial(n_s k_b T_{s,\perp})}{\partial t} = -\nabla \cdot (h_{s,\perp} \hat{e}_{\parallel}) + \dot{W}_{s,\perp}(\omega) - h_{s,\perp} (\nabla \cdot \hat{e}_{\parallel}) + \frac{\delta E_{\perp}}{\delta t} \quad (2.109)$$

Expanding these equations into numerical form

$$\begin{aligned} \frac{\partial T_{s,\parallel}}{\partial t} = & \frac{1}{n_s k_b} \left[ \frac{1}{h_1 h_2 h_3} \frac{\partial}{\partial x_1} \left( \frac{h_2 h_3}{h_1} \frac{2}{3} \lambda_s \frac{\partial T_{s,\parallel}}{\partial x_1} \right) - \frac{4}{3 h_1} \lambda_s \frac{\partial T_{s,\perp}}{\partial x_1} \right. \\ & \left. + \frac{\delta E_{\parallel,\parallel}}{\delta t} T_{s,\parallel} + \frac{\delta E_{\parallel,\perp}}{\delta t} T_{s,\perp} + \frac{\delta E_{\parallel,P}}{\delta t} \right] \end{aligned} \quad (2.110)$$

$$\begin{aligned} \frac{\partial T_{s,\perp}}{\partial t} = & \frac{1}{n_s k_b} \left[ \frac{1}{h_1 h_2 h_3} \frac{\partial}{\partial x_1} \left( \frac{h_2 h_3}{h_1} \frac{2}{3} \lambda_s \frac{\partial T_{s,\perp}}{\partial x_1} \right) + \dot{W}_{s,\perp}(\omega) \right. \\ & \left. + \frac{2}{3 h_1} \lambda_s \frac{\partial T_{s,\perp}}{\partial x_1} + \frac{\delta E_{\perp,\perp}}{\delta t} T_{s,\perp} + \frac{\delta E_{\perp,\parallel}}{\delta t} T_{s,\parallel} + \frac{\delta E_{\perp,P}}{\delta t} \right] \end{aligned} \quad (2.111)$$

where the collision terms,  $\frac{\delta E_{\parallel}}{\delta t}$  and  $\frac{\delta E_{\perp}}{\delta t}$ , have been divided into different subcategories to facilitate using this numerical method. There are the terms in the parallel equation that depend on the parallel temperature  $\frac{\delta E_{\parallel,\parallel}}{\delta t}$ . There are the terms in the parallel equation that depend on the perpendicular temperature  $\frac{\delta E_{\parallel,\perp}}{\delta t}$ . There are terms in the perpendicular equation that depend on the perpendicular temperature  $\frac{\delta E_{\perp,\perp}}{\delta t}$ . There are terms in the perpendicular equation that depend on the parallel temperature  $\frac{\delta E_{\perp,\parallel}}{\delta t}$ . There are also collision terms that do not contain temperature. These are dubbed production terms and there is one for the parallel temperature equation  $\frac{\delta E_{\parallel,P}}{\delta t}$

and one for the perpendicular temperature equation  $\frac{\delta E_{\perp,P}}{\delta t}$ .

Equations 2.110 and 2.111 fit the general form for a finite difference approximation

$$\begin{aligned} \frac{\partial T_{s,\parallel}}{\partial t} &= A_{\parallel,\parallel} T_{s,\parallel} + B_{\parallel,\parallel} \frac{\partial T_{s,\parallel}}{\partial x_1} + C_{\parallel,\parallel} \frac{\partial}{\partial x_1} \left( D_{\parallel,\parallel} \frac{\partial T_{s,\parallel}}{\partial x_1} \right) + E_{\parallel,\parallel} \\ A_{\parallel,\perp} T_{s,\perp} &+ B_{\parallel,\perp} \frac{\partial T_{s,\perp}}{\partial x_1} + C_{\parallel,\perp} \frac{\partial}{\partial x_1} \left( D_{\parallel,\perp} \frac{\partial T_{s,\perp}}{\partial x_1} \right) + E_{\parallel,\perp} \end{aligned} \quad (2.112)$$

$$\begin{aligned} \frac{\partial T_{s,\perp}}{\partial t} &= A_{\perp,\perp} T_{s,\perp} + B_{\perp,\perp} \frac{\partial T_{s,\perp}}{\partial x_1} + C_{\perp,\perp} \frac{\partial}{\partial x_1} \left( D_{\perp,\perp} \frac{\partial T_{s,\perp}}{\partial x_1} \right) + E_{\perp,\perp} \\ A_{\perp,\parallel} T_{s,\parallel} &+ B_{\perp,\parallel} \frac{\partial T_{s,\parallel}}{\partial x_1} + C_{\perp,\parallel} \frac{\partial}{\partial x_1} \left( D_{\perp,\parallel} \frac{\partial T_{s,\parallel}}{\partial x_1} \right) + E_{\perp,\parallel} \end{aligned} \quad (2.113)$$

where

$$\begin{aligned} A_{\parallel,\parallel} &= \frac{1}{n_s k_b} \frac{\delta E_{\parallel,\parallel}}{\delta t} & A_{\parallel,\perp} &= \frac{1}{n_s k_b} \frac{\delta E_{\parallel,\perp}}{\delta t} \\ B_{\parallel,\parallel} &= 0 & B_{\parallel,\perp} &= \frac{1}{n_s k_b} \frac{-4}{3h_1} \lambda_s \\ C_{\parallel,\parallel} &= \frac{1}{n_s k_b} \frac{1}{h_1 h_2 h_3} & C_{\parallel,\perp} &= 0 \\ D_{\parallel,\parallel} &= \frac{h_2 h_3}{h_1} \frac{2}{3} \lambda_s & D_{\parallel,\perp} &= 0 \\ E_{\parallel,\parallel} &= \frac{1}{n_s k_b} \frac{\delta E_{\parallel,P}}{\delta t} & E_{\parallel,\perp} &= 0 \\ \\ A_{\perp,\perp} &= \frac{1}{n_s k_b} \frac{\delta E_{\perp,\perp}}{\delta t} & A_{\perp,\parallel} &= \frac{1}{n_s k_b} \frac{\delta E_{\perp,\parallel}}{\delta t} \\ B_{\perp,\perp} &= \frac{1}{n_s k_b} \frac{2}{3h_1} \lambda_s & B_{\perp,\parallel} &= 0 \\ C_{\perp,\perp} &= \frac{1}{n_s k_b} \frac{1}{h_1 h_2 h_3} & C_{\perp,\parallel} &= 0 \\ D_{\perp,\perp} &= \frac{h_2 h_3}{h_1} \frac{2}{3} \lambda_s & D_{\perp,\parallel} &= 0 \\ E_{\perp,\perp} &= \frac{1}{n_s k_b} \frac{\delta E_{\perp,P}}{\delta t} + \dot{W}_{s,\perp}(\omega) & E_{\perp,\parallel} &= 0 \end{aligned}$$

These equations are solved simultaneously; each using a backward Euler implicit

method for each set ( $\parallel, \parallel, \parallel, \perp, \perp, \perp$ , and  $\perp, \parallel$ ) of coefficients  $A$ - $E$

$$\begin{aligned} \frac{f_i^{n+1} - f_i^n}{\Delta t} = & f_i^{n+1} \left[ \frac{C_i D_{i-1/2}}{h_{1,i} h_{2,i} h_{3,i} \Delta x_{1,i,1/2} \Delta x_{1,i,b}} \frac{h_{2,i} h_{3,i}}{h_{1,i}} - \frac{B_i}{\Delta x_{1,i,b} + \Delta x_{1,i,f}} \frac{1}{h_{1,i}} \right] \\ & + f_i^{n+1} \left[ A_i - \left( \frac{C_i}{h_{1,i} h_{2,i} h_{3,i}} \right) \left( \frac{h_{2,i+1} h_{3,i+1}}{h_{1,i+1}} \frac{D_{i+1/2}}{\Delta x_{1,i,1/2} \Delta x_{1,i,f}} - \frac{h_{2,i} h_{3,i}}{h_{1,i}} \frac{D_{i-1/2}}{\Delta x_{1,i,1/2} \Delta x_{1,i,b}} \right) \right] \\ & + f_{i+1}^{n+1} \left[ \left( \frac{C_i}{h_{1,i} h_{2,i} h_{3,i}} \right) \frac{h_{2,i+1} h_{3,i+1} D_{i+1/2}}{h_{1,i+1} \Delta x_{1,i,1/2} \Delta x_{1,i,f}} + \frac{B_i}{h_{1,i} (\Delta x_{1,i,b} + \Delta x_{1,i,f})} \right] + E_i \end{aligned} \quad (2.114)$$

allowing the final coupled form of the diffusion substep to be solved

$$f^{n+1} = \mathbf{M} \setminus f^n. \quad (2.115)$$

where  $\mathbf{M}$  is a sparse diagonal matrix containing the elements of Equation 2.114 for each set of coefficients from both the parallel temperature and perpendicular temperature simultaneously. As a non-detailed reference

$$f^{n+1} = \begin{bmatrix} T_{s,\parallel} \\ T_{s,\perp} \end{bmatrix}^{n+1} = \begin{bmatrix} \parallel, \parallel & \perp, \perp \\ \perp, \perp & \perp, \parallel \end{bmatrix} \setminus \begin{bmatrix} T_{s,\parallel} \\ T_{s,\perp} \end{bmatrix}^n \quad (2.116)$$

illustrates the matrix organization used for the coupled system.

### 2.3.4 Stiff Sources

The last split step is a solution for the stiff source terms. The remainder of the continuity and momentum equations, after the advection is solved, can be expressed as a simple local production/loss ODE for each grid point. These equations are all of the form:

$$\frac{\partial f}{\partial t} = A - Bf, \quad (2.117)$$

which for constant values of  $A$  and  $B$  has the analytical solution using an exponential time differencing method:

$$f^{n+1} = f^n e^{-B^n \Delta t} + \frac{A^n}{B^n} (1 - e^{-B^n \Delta t}) \quad (2.118)$$

### Continuity stiff source terms

For the continuity equation, neglecting the previously solved advection terms, there remains

$$\frac{\partial \rho_s}{\partial t} = m_s P_s - L_s \rho_s. \quad (2.119)$$

which has the analytical solution

$$\rho_s^{n+1} = \rho_s^n e^{-L_s^n \Delta t} + \frac{m_s P_s^n}{L_s^n} (1 - e^{-L_s^n \Delta t}) \quad (2.120)$$

### Momentum stiff source terms

The remaining momentum equation terms provide the following equation for this last substep

$$\frac{\partial (\rho_s u_{s,\parallel})}{\partial t} = \rho_s g_1 - \frac{1}{h_1} \frac{\partial p_{s,\parallel}}{\partial x_1} + \frac{\rho_s q_s}{m_s} E_{\parallel} + \frac{\delta \mathbf{M}}{\delta t} \quad (2.121)$$

The solution is exactly the same form of Equation 2.120 with the production and loss terms of

$$\begin{aligned} P_s &= \rho_s g_1 - \frac{1}{h_1} \frac{\partial p_{s,\parallel}}{\partial x_1} + \frac{\rho_s q_s}{m_s} E_{\parallel} - (p_{s,\parallel} - p_{s,\perp}) \nabla \cdot \hat{\mathbf{e}}_{\parallel} + \frac{\delta \mathbf{M}_{\mathbf{P}}}{\delta t} \\ L_s &= \frac{\delta \mathbf{M}_{\mathbf{L}}}{\delta t} \end{aligned} \quad (2.122)$$

where  $\frac{\delta \mathbf{M}_{\mathbf{P}}}{\delta t}$  is the portion of the momentum equation collision terms that are production and  $+\frac{\delta \mathbf{M}_{\mathbf{L}}}{\delta t}$  are the remain portion of the momentum collision terms that are loss.

# Chapter 3

## Comparisons with parent model

The new anisotropic model GEMINI-TIA, and its isotropic parent version (*Zettergren and Snively, 2015*) are run with identical drivers and initial conditions to clearly identify and assess ionospheric response differences frictional heating under different transport formulations. Significant anisotropies are predicted to occur anytime the DC electric fields exceeds  $\sim 50\text{-}75$  mV/m (*St-Maurice and Schunk, 1979; Raman et al., 1981*). GEMINI-TIA is formulated to resolve these anisotropies and may provide a more accurate description of high-latitude ionospheric dynamics.

### 3.1 Impacts of anisotropies

GEMINI-TIA and its isotropic parent model are initially compared through an identical analysis of the ionospheric response to a DC electric field,  $E_{0\perp}$ , of 80 mV/m applied in both models using a Gaussian envelope centered in the domain to prevent side boundary condition artifacts. This electric field is imposed using Dirichlet boundary conditions with a topside potential specified as:

$$\Phi(x_2) = E_{0\perp} \frac{h_2 c \sqrt{\pi}}{2} \operatorname{erf} \left( \frac{x_2 - b}{c} \right) \quad (3.1)$$

where  $E_{0\perp}$  is the strength of the DC electric field (V/m),  $c$  is the standard deviation set here to 1/7th of the domain,  $b$  is the location of the center field line of the



simulation, and  $h_2$  is the metric factor corresponding to the L-shell dimension of the model. Frictional heating resulting from this strong electric field leads to anisotropies not resolved in the Maxwellian model (*St-Maurice and Schunk, 1979*) and differences in the upflow simulated by each model.

The  $O^+$  flux and velocity parallel to the geomagnetic field from both simulations are shown in Figure 3.1. The top four panels (a-d) show snapshots of the model output after the DC electric field has been applied for 250 s with the isotropic model responses in the left column and the anisotropic model responses in the right column. The top row illustrates the differences in  $O^+$  flux rates and the second row illustrates the differences in field aligned velocity. In general, a significant difference in the Maxwellian vs. Bi-Maxwellian response can be noted. The isotropic model's  $O^+$  flux is 48% larger at 1000 km (with a value of  $3.1 \times 10^{13} \text{ m}^{-2} \text{ s}^{-1}$ ) than the anisotropic model's  $O^+$  response of  $2.1 \times 10^{13} \text{ m}^{-2} \text{ s}^{-1}$ . The isotropic model  $O^+$  field aligned velocity is 33% larger at 1000km (with a value of  $\sim 600 \text{ m/s}$ ) at this point in time than the anisotropic velocity response of  $\sim 450 \text{ m/s}$ . Figure 3.1, panel e, shows how ion fluxes at 1000 km evolve over the duration the simulation on the center field line of the grid. It takes approximately four minutes for the main ion perturbation to reach this altitude (the flux peak and following plateau seen in Figure 3.1 at about 240 s onwards). From then, the heating from the DC electric field at lower altitudes supports that rate of upflow for several more minutes, in the anisotropic case, before the ionospheric plasma pressure begins to re-establish a force balance and the fluxes begin to decrease. In the isotropic model, the larger flux rate begins to decrease right after peaking at  $\sim 240 \text{ s}$ , but still remains larger than the anisotropic model flux rates for the remainder of the simulation.

The difference in the ion flux response in the two models is due to the fact that the frictional heating, in reality (and in the Bi-Maxwellian-based model), leads to a larger perpendicular temperature than parallel temperature. The average temperature in the Bi-Maxwellian simulation,  $T_s = \frac{1}{3}T_{s,\parallel} + \frac{2}{3}T_{s,\perp}$ , is very similar to what is simulated by the Maxwellian model, there is just a different partitioning of the energy between the parallel and perpendicular directions. Specifically, the Maxwellian model assumes equal partitioning in both directions, while the anisotropic model correctly accounts

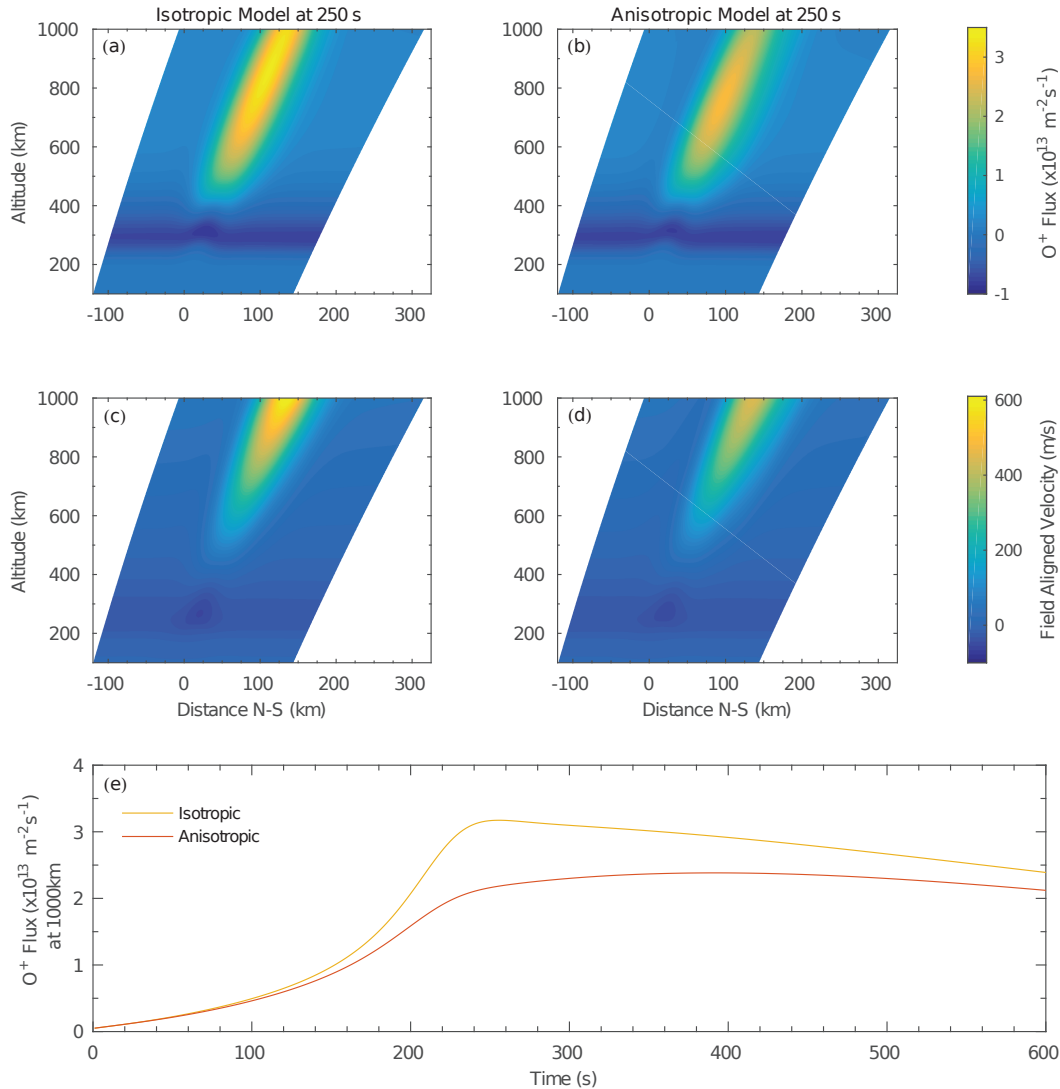


Figure 3.1: A comparison of the O<sup>+</sup> flux (panels a, b, and e) and field aligned velocity (panels c and d) between the new 16-moment (anisotropic) model and the parent 5-moment (isotropic) model after 250 s of an applied DC electric field of 80 mV/m. There is a significantly larger response in the isotropic model compared to the anisotropic model, 48% larger at 250 s at 1000 km. The field aligned velocity is also larger with a 33% increase in the isotropic velocity response when compared to the anisotropic response. The bottom panel tracks the O<sup>+</sup> flux at 1000km, on the center field line of the simulation, for the entire duration of the simulation and serves to highlight the consistency of the isotropic flux response to be larger than the anisotropic flux response.

for a larger fraction of the energy being distributed into the field-perpendicular direction. Ion upflow in the anisotropic model depends on the parallel pressure gradient term in Equation 2.66, while it depends on the average pressure gradient term in the isotropic model (*Zettergren and Snively, 2015*, equation A8). Hence, the difference in flux responses in these models is primarily due to the overestimation of the pressure gradient force by the isotropic model. It is worth noting that there are also a few differences present in the way the collisions are described, however, the difference in the pressure gradient terms in the bulk momentum transport equations is the primary cause of the smaller upward field aligned velocities and weaker  $O^+$  flux response in the anisotropic model versus the isotropic model. This exercise shows that isotropic fluid models may overestimate ionospheric velocities and the amount of plasma supplied to higher altitudes by as much as 48% at 1000 km (the case shown here), and illustrates that anisotropies significantly affect the intensity of type-1 upflow. As a final note, a modest enhancement in ion upflow begins almost as soon as the simulation starts. This is an indirect effect that results from heat transfer from the frictionally heated ions to the electrons.

## 3.2 MICA case study

GEMINI-TIA and its isotropic parent model are further compared through an identical analysis of the Magnetosphere-Ionosphere Coupling in the Alfvén Resonator (MICA) sounding rocket campaign. On February 19th, 2012 MICA was launched at 5:41:06 UT into a substorm expansion. This flight lasted 552 seconds with an apogee of  $\sim 325.4$  km. There were complementary ground ISR and all-sky camera measurements running several hours before and after the flight from  $\sim 2-8$  UT.

Figure 3.2 shows the spatial coverage overlap of the instruments involved in the MICA campaign. PFISR ( $\bigcirc$ ) used a set of 15 beams (---) with both long pulse and alternating code options. Electric fields measured with the long pulse beam code are used in this study. Fabry-Perot interferometer (FPI) data ( $\blacktriangleright$  and  $\blacktriangleleft$ ) is shown at the individual observation locations within the field of view.

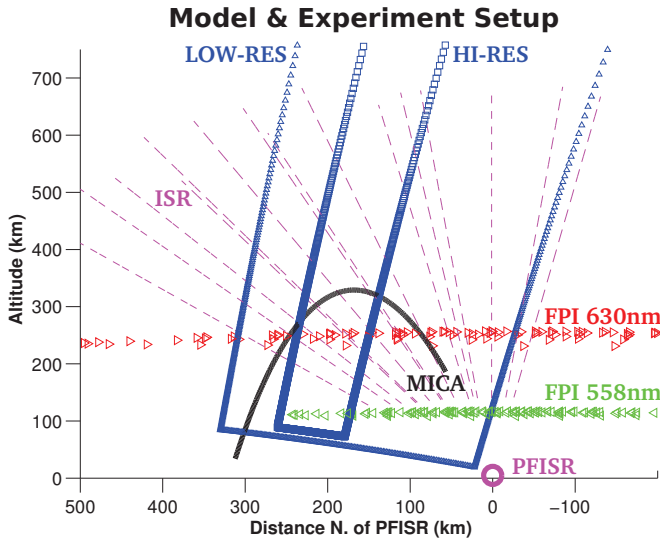


Figure 3.2: The model grid and experiment setup. (Updated from *Zettergren et al. (2014)*).

The all-sky camera field of view is not shown. The model grid (outlined in  $\triangle$  or  $\square$ ) can be set to different resolutions. For the simulations here, the grid spans L shells from 5.85-7.6 and covers altitudes from  $\sim 80$  to 4250 km on a grid of  $243 \times 175$  points. The grid cells have a resolution in the E region of roughly  $2 \text{ km} \times 2 \text{ km}$  and in the topside is roughly  $75 \text{ km} \times 4 \text{ km}$ . MICA’s trajectory (—) travels through the spatial locations of all of these. This ground data

provides the DC electric fields (from ISR measurements) and particle precipitation (from all-sky camera measurements) ingested by the models to drive realistic plasma dynamics. For a full discussion of the MICA mission see *Zettergren et al. (2014)*; *Lynch et al. (2015)* and *Fernandes et al. (2016)*.

As described by *Zettergren et al. (2014)*, cavity events have been identified in the Poker Flat ISR (PFISR) data from the MICA campaign by visually identifying structures that (1) are extended in longitude ( $>100 \text{ km}$ ) and altitude ( $>50 \text{ km}$ ), (2) have at least one well-defined edge with a sharp density gradient, (3) are temporally

Table 3.1: Density depletions identified in the Poker Flat ISR measurements during the MICA sounding rocket campaign. Note that none of these events encompass the MICA flight time,  $\sim 5:41-5:50$ . Table reproduced from *Zettergren et al. (2014)*.

Event	Cavity Visibility	Heating Duration	Comments
1	2:48-3:10 UT	2:20-3:10 UT	Arc in field of view after 3:10
2	3:56-4:21 UT	3:50-4:10 UT	Two separate consecutive cavities
3	4:59-5:33 UT	4:50-5:10 UT	Not clearly visible after 5:33 UT
4	6:26-6:32 UT	6:15-6:30 UT	Possibly obscured by arc after 6:32
5	7:38-7:50 UT	7:35-7:45 UT	Exists until end of ISR experiment

coherent (present in at least two consecutive integration periods), and (4) have depletions of  $\sim 20\%$  or more relative to the maximum density adjacent to the cavity. These density depletions are listed in Table 3.1. For reference, the MICA time of flight is  $\sim 5:41-5:50$  UT. None of the density depletion events encompass MICA's flight time.

The five density cavities identified in Table 3.1 are modeled using identical initial conditions and grids for both the anisotropic and isotropic models. The initial conditions are determined via separate model runs set in a "steady-state" configuration (i.e. no auroral forcing or additional energization inputs). This allows for the background conditions to reach equilibrium and avoids nonphysical transients that occur when plasma parameters are not self-consistently evolved.

The northward DC electric field (Figure 3.3, panel a), a standard data product of PFISR (*Heinselman and Nicolls, 2008*), and particle precipitation information (panels b and c) from the all-sky camera are ingested by both models to drive ion motions with realistic spatial and temporal variability. The five identified cavity events in Table 3.1 are marked by the vertical red lines in Figure 3.3 and the flight time of the sounding rocket is boxed in red. Each density cavity event is accompanied by a corresponding increase in the DC electric field (panel a). The substorm onset that prompted the call for launch of the sounding rocket is responsible for the sudden increase in characteristic energy (panel b).

The DC electric field (DCE) measurements are included within the models by first interpolating the electric field onto the model grid. Then the DCE is scaled from the measurement altitude to the top boundary and integrated to provide a potential versus L shell profile. Side boundaries are taken to be equipotentials with the top corner grid points. Particle precipitation information, the characteristic energy and total energy flux derived from all-sky camera data, is ingested directly into the model and uses the *Fang et al. (2008)* parametrization scheme.

Within both models, cavity event 1 is generated solely by DCE because the all-sky camera data does not start until 3:40 UT. The simulation runs from 2:10 to 3:25 UT. GEMINI-TIA results are shown in Figure 3.4 with the y-axis representing time. There is an increase in DCE around  $\sim 2:50-3:05$  UT, that reaches a maximum of  $\sim 140$  mV/m around  $\sim 3:00$ UT, and drives upflow above the F region peak (panel a).

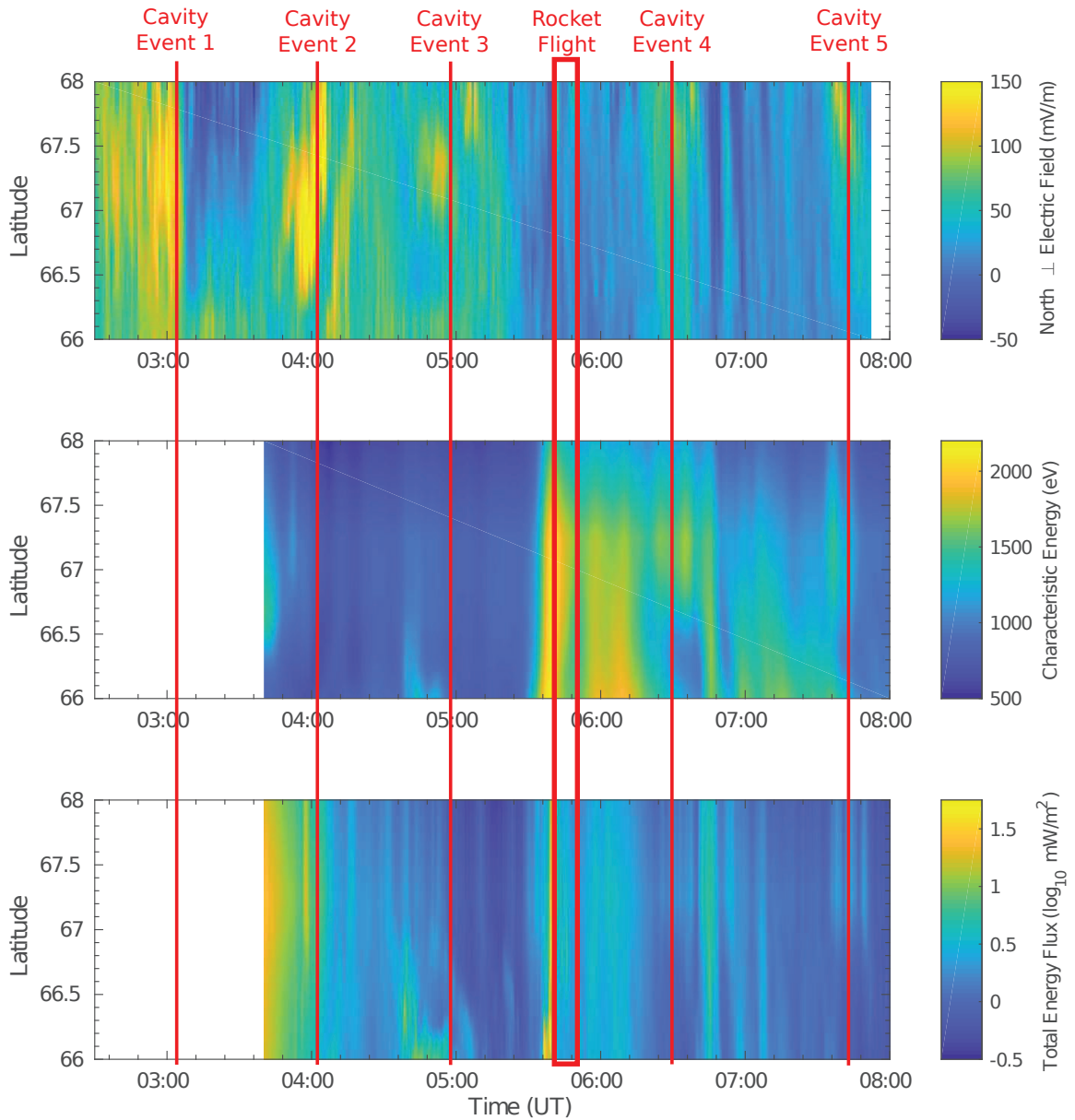


Figure 3.3: DC electric fields (panel a), and particle precipitation, in the form of measured characteristic energy (panel b) and total energy flux (panel c), observed during the MICA sounding rocket campaign.

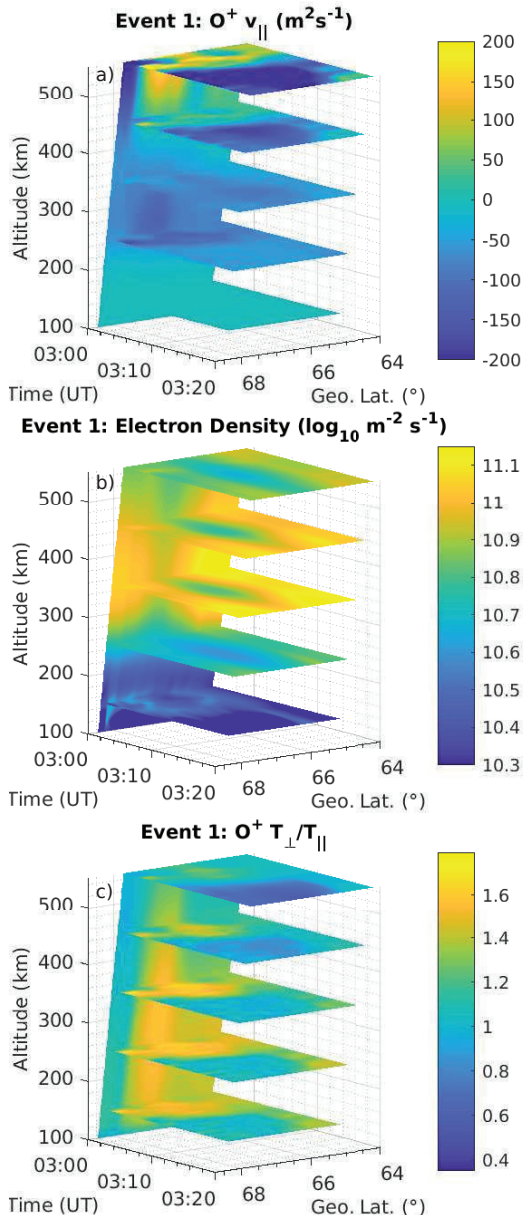


Figure 3.4: Altitudinal slices showing the time evolution of the O<sup>+</sup> field aligned velocity (panel a), electron density (panel b), and O<sup>+</sup> temperature anisotropy (panel c) during cavity event 1.

For the cavity events that have all-sky data, the cavities form adjacent to fairly bright, stationary auroral arcs where the electric fields are strong. For each cavity

The resulting localized, frictional heating produces anisotropies greater than 1.4 at altitudes below 400 km (panel c) and through enhanced recombination generates a density cavity most clearly seen at 350 km (panel b). Cessation of the frictional heating causes the density depletion to begin to refill, further upflow is not supported, and downflow begins. The downflow generates a moderate amount of compressional heating which elevates the parallel temperature and results in an anisotropy factor of less than 1 at altitudes greater than ~400 km. The density depletion outlasts the ion frictional heating as there is not a significant ionization source in the cavity to rapidly regenerate ion densities.

A similar sequence of processes generates and fills all of the identified cavity events. Precipitation influences cavity dynamics through impact ionization but molecular ion generation, from DCE leading to enhanced recombination, is the most important process contributing to the observed depletions during the MICA campaign (Zettergren *et al.*, 2014). Figure 3.5 shows a comparison of the density cavities generated by DCE and precipitation measurements.

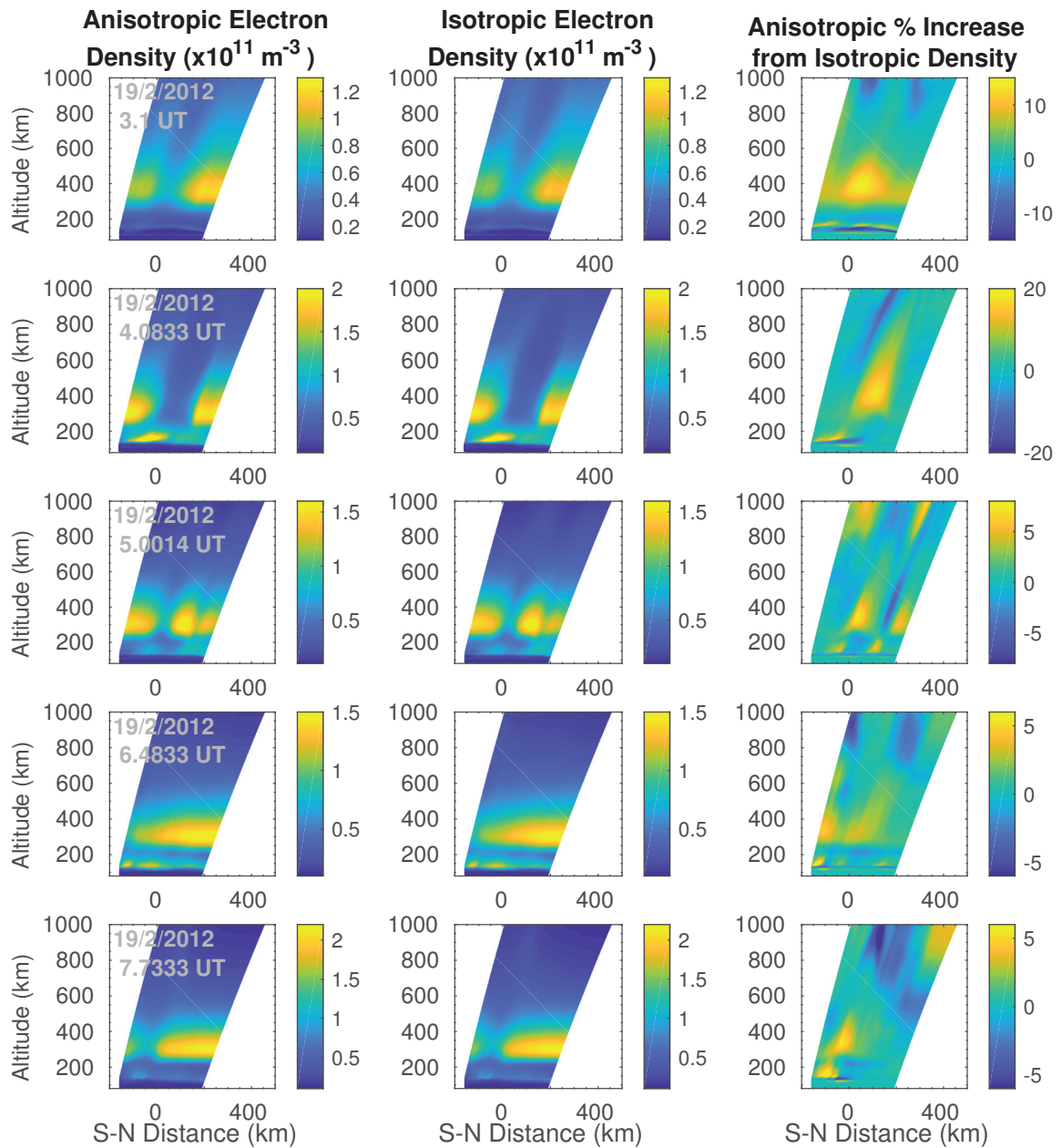


Figure 3.5: A comparison of the density cavities generated by the conversion of  $\text{O}^+$  into  $\text{NO}^+$  in response to observed DC electric fields and particle precipitation during the MICA sounding rocket campaign.



event respectively, there is an increase in the DC electric around ~2:50-3:05 UT (maximum of ~140 mV/m), ~3:40-4:10 UT (~200 mV/m), ~4:40-5:10 UT (~110 mV/m), ~6:20-6:40 UT (~90 mV/m), and ~7:30-7:45 UT (~100 mV/m). This increase drives the conversion of F region  $O^+$  into  $NO^+$  (a very temperature sensitive process) which then recombines quickly (*McFarland et al.*, 1973; *Schunk*, 1977; *Torr et al.*, 1977; *St.-Maurice and Torr*, 1978; *Doe et al.*, 1993; *Diloy et al.*, 1996; *St.-Maurice and Laneville*, 1998; *Zettergren and Semeter*, 2012; *Zettergren et al.*, 2014). The modeled density cavities develop to a lesser degree in the Bi-Maxwellian model due to the energy partitioning used which changes the molecular ion generation and enhanced recombination reaction rates. The reaction rate of  $O^+$  with atmospheric neutral species is dependent on the effective temperature with is given by

$$T_{eff} = \frac{m_n}{m_s + m_n} \left( \frac{m_s U^2}{3k_b} + T_s - T_n \right) + T_n \quad (3.2)$$

where  $U$  is the magnitude of the relative drift difference between ion species  $s$  and neutral species  $n$  (*St.-Maurice and Laneville*, 1998). The average temperature,  $T_s$ , is a combination of the parallel and perpendicular ion temperatures ( $T_s = 2/3 T_{s,\perp} + 1/3 T_{s,\parallel}$ ) in the Bi-Maxwellian model and simply the ion temperature in the Maxwellian model.

As discussed in the previous parametric comparison with the parent model, the pressure term within the momentum transport equation is responsible for differences in ion velocity between the GEMINI-TIA and GEMINI and as a result directly impacts the reaction rate through  $U$ , the relative drift difference between ions and neutrals, as the ions in GEMINI have a larger velocity than the ion in GEMINI-TIA. The isotropic model also generates larger ion temperatures than the average temperature equivalent in the anisotropic model due to the respective energy partitioning approaches. Both of these model differences impact the effective temperature used to calculate the reaction rate for the conversion of  $O^+$  into  $NO^+$ . As a result of both transport and chemistry, the density depletions in the anisotropic model, GMEINI-TIA, are not as deep as the density cavities in the isotropic model, GEMINI by as much as ~20%, such as that which develops in cavity event 2.

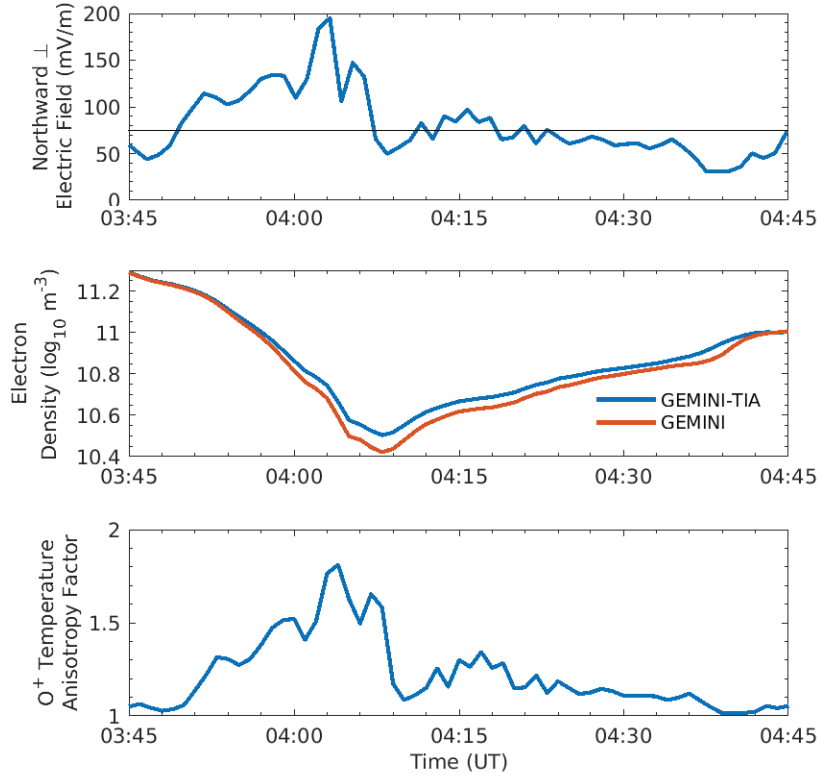


Figure 3.6: A comparison of the second density cavity event identified during the MICA sounding rocket campaign and the resulting temperature anisotropy within GEMINI-TIA at 400 km along the center field line of the grid which corresponds closely to the center of the cavity.

Examining cavity event 2 further, the anisotropies generated within GEMINI-TIA at altitude of 400 km along the center field line of the simulation domain are shown in Figure 3.6; this is within the density depletion region. As the DCE increases from  $\sim 50$  to 195 mV/m over the time span of 3:45 to 4:03 (panel a). There is a corresponding increase in the  $O^+$  temperature anisotropy factor (calculated by  $T_{\perp}/T_{\parallel}$ ) from nearly isotropic to an anisotropy factor of 1.8. As the anisotropy increases over time there is also a corresponding increase in density depletion difference between the models. As the DCE decreases from 4:03 UT to the end of the plot, the temperature anisotropy factor also approaches isotropy and the densities within the two models converge.

The time of the rocket flight has also been simulated in both models (Figure 3.7). During this time, there is an increase in precipitation but not a corresponding increase

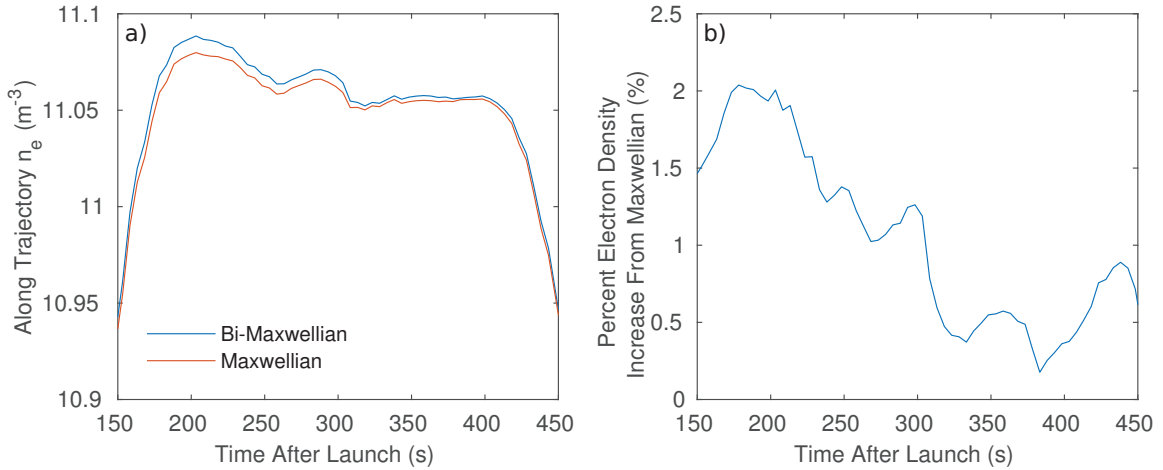


Figure 3.7: The modeled electron density along the MICA rocket trajectory (panel a) and the percent increase in density of the Bi-Maxwellian model from the Maxwellian model (panel b).

in DCE. The DC electric fields during this time are consistently  $<50$  mV/m which is less than the suggested minimum threshold for significant temperature anisotropies (*Schunk, 1975*). As a result, large anisotropies are not expected along the flight path and a general agreement between the models is evident. The modeled densities along the flight path (panel a) are within 2% (panel b).

### 3.3 Chapter conclusions

Ion temperature anisotropies in the F-region ionosphere, observed in investigations employing incoherent scatter radar, satellite, and sounding rocket data, highlight the need for a model that can quantitatively determine the anisotropy that develops as a consequence of energy inputs associated with ion upflow. While a few models that resolve anisotropy exist, none had been developed specifically for the ion upflow problem, even though ion heating-driven upflows, for example, are driven by strong DC fields which will also generate significant anisotropy. Only systems based off of a Bi-Maxwellian distribution are appropriate for large temperature anisotropies (*Barakat and Schunk, 1982a*), such as those which occurred during the MICA campaign. GEMINI-TIA properly accounts for these important anisotropies and is used

throughout this dissertation to address the science queries discussed in Chapter 1.

When comparing GEMINI-TIA with its parent model, the difference in ion response between the two models is due to the fact that the frictional heating, in reality (and in the Bi-Maxwellian-based model), leads to a larger perpendicular temperature than parallel temperature. The average temperature in the Bi-Maxwellian simulation,  $T_s = \frac{1}{3}T_{s,\parallel} + \frac{2}{3}T_{s,\perp}$ , is very similar to what is simulated by the Maxwellian model, there is just a different partitioning of the energy between the parallel and perpendicular directions. Specifically, the Maxwellian model assumes equal partitioning in both directions, while the anisotropic model correctly accounts for a larger fraction of the energy being distributed into the field-perpendicular direction.

Ion upflow in the anisotropic model depends on the parallel pressure gradient term in Equation 2.67, while it depends on the average pressure gradient term in the isotropic model (*Zettergren and Snively, 2015*, equation A8). Hence, the difference in responses in these models is primarily due to the overestimation of the pressure gradient force by the isotropic model. While there are a few differences in the way collisions are described, the difference in the pressure gradient terms in the bulk momentum transport equations is the primary cause of the smaller upward field aligned velocities, weaker  $O^+$  flux response, and smaller density depletions in the anisotropic model versus the isotropic model. The comparisons within this chapter show that isotropic fluid models may overestimate many ionospheric responses to situations of strong forcing or wave heating and supports the need for an anisotropic fluid model.

## Chapter 4

# Ionospheric upflow: effects of low-altitude anisotropy and thermospheric winds

From statistical studies of topside auroral upflows (*Foster et al.*, 1998; *Ogawa et al.*, 2010; *Burleigh*, 2013), approximately 80% of observed upflow events had an associated increase in electron temperature or F-region density; signatures of type 2 upflows. Between 50 to 60% of observed upflows had an increase in ion temperature; indicative of a type 1 upflow. There have also been observations of ion upflows with both ion and electron heating present and cases where neither heating signatures are seen (*Foster et al.*, 1998; *Ogawa et al.*, 2009). The observations containing neither heating signature but field aligned velocities were greater than 100 m/s, suggests the existence of other upflow mechanisms.

Neutral winds are a likely candidate for driving the ions upward. Strong thermospheric (neutral) winds have been observed often at high-latitudes and are known to play a role in regulating F-region ion dynamics. (*Skjaeveland et al.*, 2011) found that some upflows were greater than expected from ambipolar diffusion alone, suggesting that ion-neutral frictional heating contributed to upflow events. Neutral winds, while rarely be large enough to, alone, generate a large upflow, coupled with other upflow mechanisms (e.g. DC electric fields and wave heating) may regulate upward ion fluxes

and velocities.

Few studies have examined the thermospheric impacts on outflow in a systematic way. As a good example, *Redmon et al.* (2012) used the FLIP model, a one-dimensional model that calculates the plasma densities and temperatures along a magnetic flux tube from 80 km in the Northern Hemisphere through the plasmasphere to 80 km in the Southern Hemisphere, to examine neutral wind and electron precipitation impacts on ion upflow as the flux tube traverses the day/night boundary. Taking a different modeling approach, GEMINI-TIA has been developed to study the thermospheric modulation of the ionosphere, and resulting impacts on ion upflow and outflow. Specifically, this model is being used here in a parametric study of neutral wind effects on upflow and outflow highlighting how low-altitude processes affect ion outflow through the regulation of source plasma available to higher altitudes.

A similar model configuration is used for each simulation with each simulation run for ten minutes at a two second output cadence. The adaptive time stepping of the model is such that stability is retained at every time step and a typical time step is  $\sim 0.5$  s. The model is run to a steady state for the initial conditions and all of the simulations in this section start at 15 UT creating a consistent set of background conditions for each run. The simulation results presented here use a dipole mesh (*Huba et al.*, 2000; *Zettergren and Snively*, 2015) spanning L-shells 12-16, centered roughly on the location of the Sondrestrom research facility on the west coast of Greenland ( $67^\circ$ ,  $309^\circ$ ), a location of interest for ion upflow (*Semeter et al.*, 2003; *Zettergren et al.*, 2008; *Sanchez and Strømme*, 2014). For this study, GEMINI-TIA was run for multiple combinations of DC electric fields, transverse wave heating, and neutral winds implemented using the configurations described in the paragraphs below.

In the simulations that use a DC electric field, it is applied using a Gaussian envelope centered in the domain to prevent side boundary condition artifacts. This electric field is imposed using Dirichlet boundary conditions with a topside potential specified as:

$$\Phi(x_2) = E_{0\perp} \frac{h_2 c \sqrt{\pi}}{2} \operatorname{erf} \left( \frac{x_2 - b}{c} \right) \quad (4.1)$$

where  $E_{0\perp}$  is the strength of the DC electric field (V/m),  $c$  is the standard deviation

set here to 1/7th of the domain,  $b$  is the location of the center field line of the simulation, and  $h_2$  is the metric factor corresponding to the L-shell dimension of the model.

The wave heating term,  $\dot{W}_{s,\perp}$ , when used, depends on an adjustable wave power spectral density parameter  $|E_0|^2$  ( $\text{V}^2/\text{m}^2/\text{Hz}$ ) and a reference  $\text{O}^+$  gyrofrequency  $\omega_0$  used here as 6.5 Hz (Zeng *et al.*, 2006). Similar to how a Gaussian spatial envelope is used for the DC electric field, the wave heating term is constrained to prevent excessive energization of the ions near boundaries. Perpendicular to the field lines, the standard deviation of this envelope is 1/6th of the domain size in that direction. Parallel to the field line, at 1/20th of the distance (measured in terms of the field aligned variable  $x_1$ , which is  $q$  in the notation of Huba *et al.* (2000)) from the top of the simulation, a hyperbolic tangent is used to quickly, over 1/100th of the range, taper off the heating term to prevent spurious boundary interactions. This transition region is well outside the area of interest to this study so the results are not impacted by the selection of altitude at which the wave heating is removed.

For simulations that include geographic northward (or southward) neutral winds, these are specified using components parallel and perpendicular to the magnetic field. The following parallel component is given by:

$$v_{n,x_1} = v_{n,0} \cos(I) \left( 0.5 + 0.5 \tanh \left( \frac{z - z'_1}{\Delta z_1} \right) \right), \quad (4.2)$$

where here  $v_{n,0}$  is the northward geographic neutral wind and  $I$  is the inclination of the magnetic field lines from the horizontal. Thus  $v_{n,0} \cos(I)$  determines the component of the geographic neutral wind along the magnetic field lines, in the  $z$  direction (altitude). The hyperbolic tangent is used to, over an altitude span of  $\Delta z_1 = 10$  km, centered at  $z'_1 = 90$  km, taper the winds to full strength preventing lower boundary artifacts. The perpendicular neutral wind component uses a similar relationship:

$$v_{n,x_2} = v_{n,0} \sin(I) \left( 0.5 + 0.5 \tanh \left( \frac{z - z'_1}{\Delta z_1} \right) \right), \quad (4.3)$$

where  $v_{n,0} \sin(I)$  determines the component perpendicular to the magnetic field lines,

the  $x_2$  direction. Geographically eastward (and westward) winds, which here are parallel (and antiparallel) to the  $\mathbf{E} \times \mathbf{B}$  drift direction, do not need to be broken into components and are described by

$$v_{n,x_3} = v_{n,0} \left( 0.5 + 0.5 \tanh \left( \frac{z - z'_1}{\Delta z_1} \right) \right) e^{\left( \frac{-(x_2 - b)^2}{2c^2} \right)} \quad (4.4)$$

In this equation,  $v_{n,0}$  is the geographic eastward neutral wind,  $c$  is the standard deviation, set here to 1/7th of the domain, and  $b$  is the location of the center field line.

## 4.1 Low-altitude wave heating effects on ion upflow

GEMINI-TIA is used here to study the impacts of DC electric fields, wave heating, and the synergistic effects of both processes. First presented in this section are a set of three simulations: (1) a run with just a DC electric field, (2) a run with just wave heating, and (3) a run with both a DC electric field and wave heating. Figure 4.1 shows ionospheric state parameters for each of these cases, extracted along the center geomagnetic field line from the simulation, as a function of time and altitude. The first column of plots contain parameters, from a simulation that used  $E_{0\perp} = 80$  mV/m (constant for the full ten minute duration of the simulation). In descending order these parameters are  $O^+$  density, field aligned velocity, and temperature anisotropy factor (defined as  $T_{\perp}/T_{\parallel}$ ). Column 2 contains the same parameters for a simulation that used  $|E_0|^2 = 0.3$  (mV/m)<sup>2</sup>/Hz (constant for the entire simulation). Column 3 also contains the same parameters taken from a simulation that used both  $E_{0\perp} = 80$  mV/m and  $|E_0|^2 = 0.3$  (mV/m)<sup>2</sup>/Hz (again, constant for the duration of the simulation).

There is a distinct density decrease in the F region in the simulations that include a DC electric field, c.f. Figure 4.1 panel 1a, panel 3a. This density decrease is due to conversion of F-region  $O^+$  into molecular ions (a very temperature-sensitive process (*St.-Maurice and Laneville, 1998*)) which recombine quickly (*Schunk, 1975; Zettergren and Semeter, 2012*). The average temperature of the model is used within the



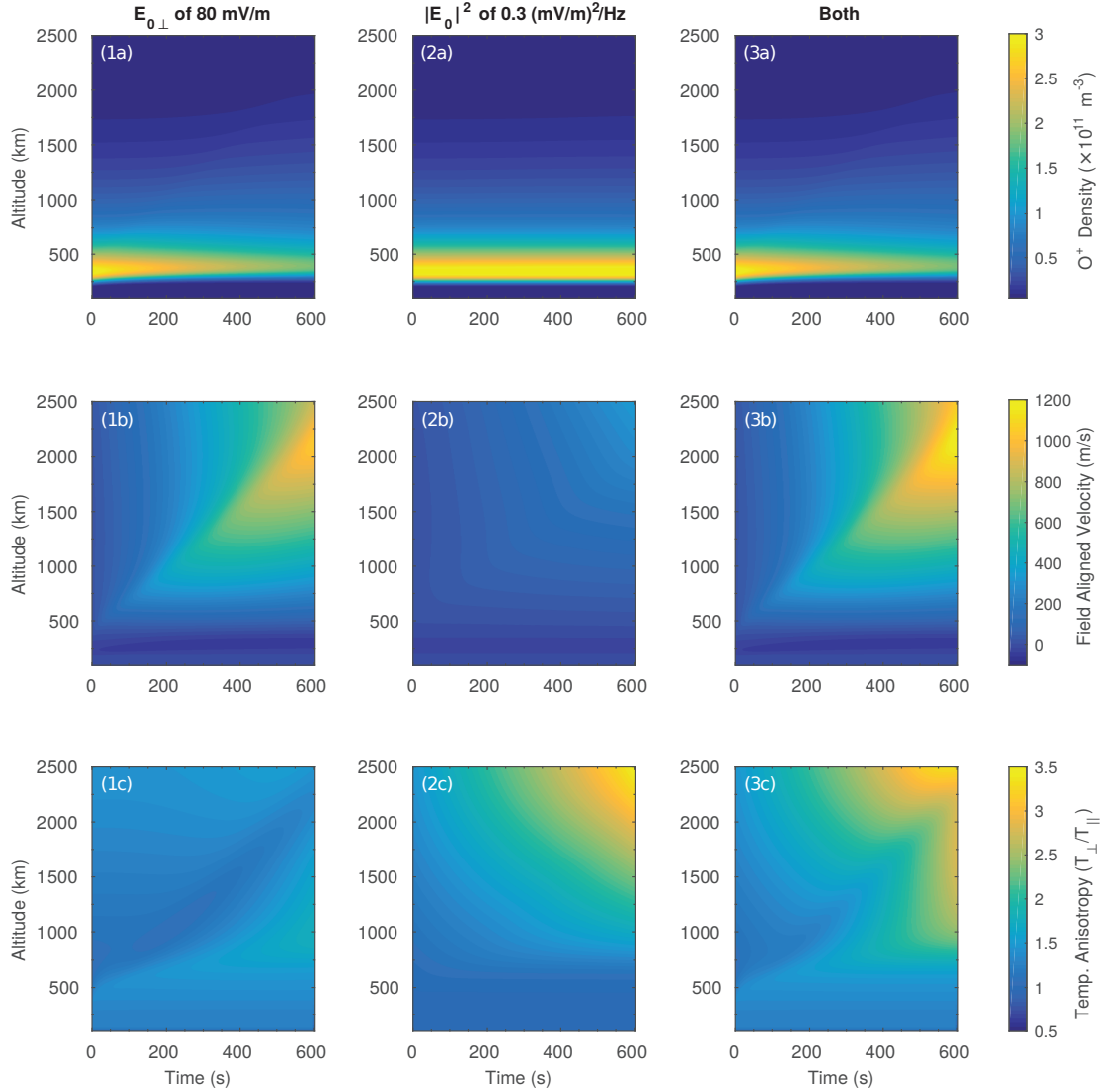


Figure 4.1:  $O^+$  responses to a DC electric field of  $E_{0\perp} = 80$  mV/m, wave heating of  $|E_0|^2 = 0.3$  (mV/m) $^2$ /Hz, and both energy sources applied simultaneously. Simulation results are plotted as a function of time and altitude for the center geomagnetic field line of the grid. Panels 1a-c show the electron density, parallel velocity, and temperature anisotropy, respectively, for the simulation with just the DC electric field. Panels 2a-c likewise show electron density, parallel velocity, and temperature anisotropy, respectively, for the simulation with just wave heating. Panels 3a-c show electron density, parallel velocity, and temperature anisotropy, respectively, for the simulation with a DC electric field and wave heating.

reaction coefficients to account for the fact that particles of all pitch angles undergo these reactions. By comparison, the simulation with only wave heating shows an F-region density, in panel 2a, that is relatively unchanged with time. The wave heating primarily impacts ion populations above the F-region peak, and does not greatly affect  $N_m F_2$ . The limited altitude region of ionospheric response to wave heating is also seen in the field aligned velocity in Figure 4.1, panel 2b, which only shows significant responses at the highest altitudes ( $> 1000$  km). In this example (with only wave heating) there is a maximum field aligned velocity of approximately 400 m/s at 2,500 km by the end of the simulation. Both panel 1b and 3b have larger field aligned velocity response (driven by the DC electric field) with the case shown in Figure 4.1, panel 3b, having the largest velocities which result from the combined effects of frictional heating and wave heating. In this case, the field aligned velocity at 2500km at the end of the simulation is 1200 m/s, panel 3b, a 200 m/s increase from the 1000 m/s seen in panel 1b, the case with just the DC electric field driven frictional heating. The DC electric field driven anisotropies are primarily at lower altitudes, Figure 4.1 panel 1c, and the wave heating-driven anisotropies are at higher altitudes, Figure 4.1 panel 2c. In general, the model shows that the effectiveness of cyclotron wave heating is mitigated, to a degree, by the presence of collisions at the lower altitudes, both ion-ion and ion-neutral. As a result the wave heating-driven temperature anisotropies are only present down to 500 km for this level of wave heating. The simulation that uses both a DC electric field and wave heating has significant temperature anisotropies throughout the entire altitude range of  $\sim 150$ -2500 km.

To further examine the synergistic effects of frictional heating and wave heating at low altitudes a set of twelve simulations with different combinations of these parameters has been run; Table 4.1 summarizes these configurations. For purposes of comparison, a control simulation where no drivers are applied (case I listed in Figures 4.2 and 4.3, and Table 4.1) is also included. Figure 4.2, panel a, shows the temperature anisotropy response and, panel b, field aligned velocity response of  $O^+$  extracted along the center geomagnetic field line at 30 s for each of the twelve simulations. Note that the parallel and perpendicular energy transport equations naturally create

a modest temperature anisotropy at altitudes greater than 600 km even under equilibrium conditions (see the control simulation, case I in Figure 4.2, panel a). The reference value for the wave power spectral density,  $|E_0|^2 = 0.3 \text{ (mV/m)}^2/\text{Hz}$  (case II), creates an increase in the temperature anisotropy seen down to 500 km. This is the nominal minimum altitude that it is normal to see wave heating effects at since the lower altitudes are highly collisional (*Archer et al.*, 2015). Increasing the wave power spectral density increases the anisotropy factor at high altitudes but also serves to increase the penetration depth of the wave heating effects into the ionosphere. Using  $|E_0|^2 = 3.0 \text{ (mV/m)}^2/\text{Hz}$ , a strong value within the bounds of the observations, creates significant anisotropies down to 300km and an extreme value of  $|E_0|^2 = 10.0 \text{ (mV/m)}^2/\text{Hz}$ , selected for illustrative purposes, can create an observable temperature anisotropy down to 250km after 30 s of wave heating. At that point in time, the main field aligned upflow perturbation has reached, on average, 520 km altitude as seen by the location of the peak velocities of Figure 4.2, panel b. Wave heating also increases upflow velocities to a smaller degree at altitudes above the peak of the upflow (e.g. compare the different colors of each line type used in Figure 4.2, panel b). When the wave heating is concurrent with a DC electric field, the electric field effects can completely mask any low-altitude wave heating effects on temperature anisotropy.

At altitudes above the main ion perturbation, a smaller level of upflow is generated by electrons that gain energy through heat exchange with frictionally heated ions deep in the ionosphere (i.e. near the F-region peak). Electrons have a high thermal conductivity so any energy input at low altitudes is quickly conducted along the field line. Hence an ion heat source can serve to generate, indirectly, electron pressure enhancements and ambipolar upflow in the topside ionosphere, here at 600-1000 km, before the main ion perturbation (seen in Figure 4.2, panel b, at about 520 km altitude) can reach these altitudes. As an example of this effect, the simulation using only a DC electric field of 150 mV/m (case 9) has a field aligned velocity  $\sim 60 \text{ m/s}$  larger at 800 km, well above the main ion perturbation, than the simulation that does not use any upflow drivers (case I).

Figure 4.3 shows the time evolution of the  $\text{O}^+$  flux at 1000 km (panel a) and 2500 km (panel b) on the center geomagnetic field line of the twelve simulations

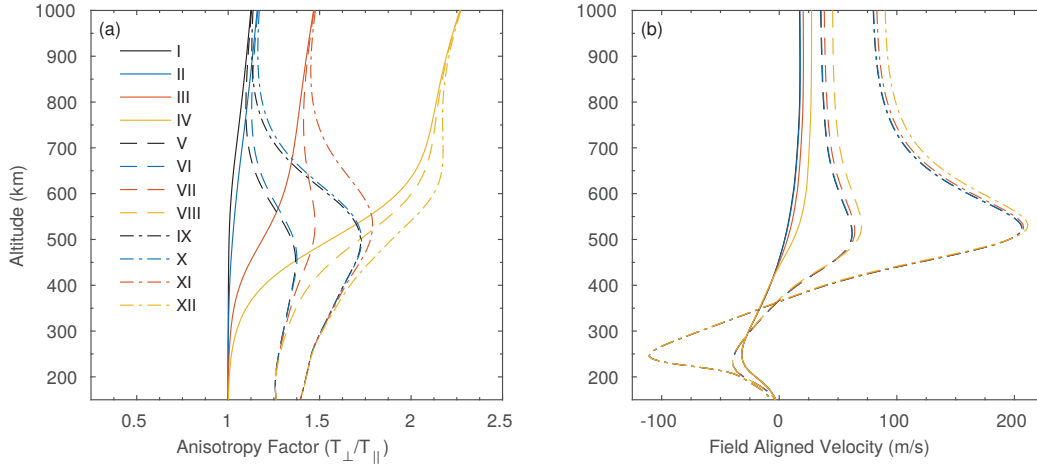


Figure 4.2: The O<sup>+</sup> temperature anisotropy factor (panel a) and field aligned velocity (panel b) from different combinations of DC electric fields and wave heating, at  $t_0+30$  seconds, extracted from the center geomagnetic field line of the simulations. See Table 4.1 for a complete listing of the drivers used in each simulation. Increasing the wave power spectral density not only increases the anisotropy factor at high altitudes but also serves to increase the penetration depth of the wave heating effects into the ionosphere. If the wave heating co-occurs with a DC electric field, the DC electric field generates larger anisotropies at lower altitudes and can completely mask any low-altitude wave heating effects on temperature anisotropy.

summarized in Table 4.1. The rapid increase in ion flux, e.g. between 110 s and 180 s for case IX at 1000 km, in this figure indicates the arrival of the main ion perturbation primarily driven by frictional heating from DC electric fields. The wave heating only simulations, cases II, III, and IV, take a longer period of time for the ion flux response to build to full strength; a maximum response rate is not reached by the end of the simulation (ten minutes) at 2500 km. This may limit the impact on plasma supply to higher altitudes in absence of another upflow mechanisms, except in some extreme cases. When a DC electric field is included with wave heating effects there is a definite increase in the flux response at 1000 km and the flux maximum occurs more quickly. However these strong fluxes decrease more rapidly than those generated by smaller DC electric fields or wave heating only situations.

Overall, the effects of wave heating plays a larger role at 2500 km than at 1000

Table 4.1: The wave power spectral density,  $|E_0|^2$ , and DC electric field,  $E_{0\perp}$ , used in simulations I - XII plotted in Figure 4.2 and 4.3.

Simulation	I	II	III	IV	V	VI	VII	VIII	IX	X	XI	XII
$ E_0 ^2$ (mV/m) <sup>2</sup> /Hz	0.0	0.3	3.0	10.0	0.0	0.3	3.0	10.0	0.0	0.3	3.0	10.0
$E_{0\perp}$ (mV/m)	0.0	0.0	0.0	0.0	80	80	80	80	150	150	150	150

km. At 2500 km, cases IV, VIII, and XII, which all used an extreme wave power spectral density of  $|E_0|^2 = 10$  (mV/m)<sup>2</sup>/Hz, consistently result in a larger flux than other ion driver combinations. An exception to this is the main ion perturbation arrival at 510 s of case XI, which is slightly larger than the ion flux response of the wave heating only simulation, case IV, at that point in time. At 1000 km the DC electric field plays a stronger role. Cases IX, X, XI, and XII all use an intense DC electric field of  $E_{0\perp} = 150$  mV/m in addition to various levels of wave heating (c.f. Table 4.1) and the resulting upward ion fluxes are the largest, and quickest, ranging in ion flux from  $6.9 \times 10^{13}$  to  $8.9 \times 10^{13}$  m<sup>-2</sup> s<sup>-1</sup>. The indirect heat transfer from the ions to electrons has the effect of increasing ion flux at times before the arrival of the main ion perturbation. This indirect heat transfer mechanism can create a significant amount of ion flux, for example  $2 \times 10^{13}$  m<sup>-2</sup> s<sup>-1</sup> after 150 s at 1000 km for case V which doesn't contain any wave heating, only a DC electric field of 80 mV/m.

## 4.2 Thermospheric wind effects on ion upflow

Strong thermospheric (neutral) winds are fairly commonplace at high-latitudes (e.g. *Anderson et al.*, 2011), are known to play a role in regulating F-region ion dynamics, and have the potential to significantly impact the ionospheric upflow process. These winds would rarely be large enough to, alone, generate a large upflow. However, when coupled with other upflow mechanisms (e.g. DC electric fields and wave heating) winds may regulate upward ion fluxes and velocities. A sequence of simulations has been conducted using geographically horizontal neutral winds in different directions, in addition to DC electric fields and wave heating, to evaluate the degree to which winds may affect ionospheric upflow.

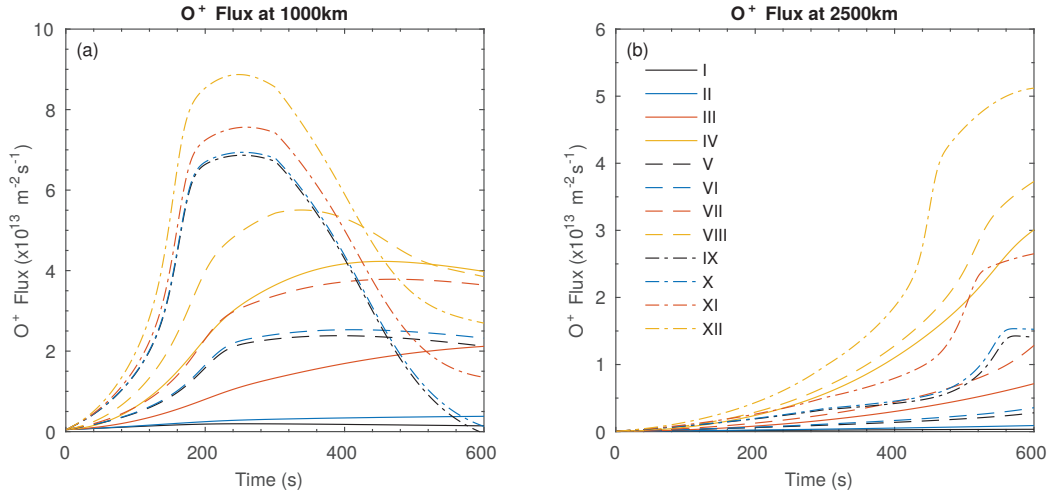


Figure 4.3:  $O^+$  flux vs. time for different combinations of DC electric field and wave heating. Panel a contains the  $O^+$  flux from the center geomagnetic field line of the model at 1000km while panel b shows the flux at 2500km (along the center geomagnetic field line of the model) for the twelve simulations listed in Table 4.1.

The first group of simulations, comprising of eight model runs, illustrates the effects of wind in the geographic north-south direction. This set includes two reference simulations that lack any neutral winds, one that uses a moderate DC electric field only of  $E_{0\perp} = 50$  mV/m (case II) and one that uses both a moderate DC electric field of  $E_{0\perp} = 50$  mV/m and a typical wave heating with a power spectral density of  $|E_0|^2 = 0.3$  (mV/m)<sup>2</sup>/Hz (case VI). These two reference cases are compared to cases where horizontal neutral winds of  $v_{n,0} = 100$  m/s southward, 200 m/s southward, and 100 m/s northward are individually added to these “base” upflow drivers. Table 4.2 lists the specific parameters used in each simulation. The neutral winds are specified as geographically horizontal and must be rotated into dipole coordinates (using Equations 4.2 and 4.3) prior to inclusion into the ion momentum and energy equations. In the northern hemisphere, southward winds have a component upward along the field line that induces upward plasma transport through drag and will tend to act synergistically with other ion upflow drivers included in the simulations. The northward winds have component downward along the field line and will tend to suppress ionospheric upflow.

Table 4.2: The power spectral densities,  $|E_0|^2$ , DC electric fields,  $E_{0\perp}$ , and geographic neutral winds,  $\mathbf{v}_{n,0}$ , used in simulations I - VIII plotted in Figure 4.4.

Simulation	I	II	III	IV	V	VI	VII	VIII
$\mathbf{v}_{n,0}$ (m/s)	100 N	0.0	100 S	200 S	100 N	0.0	100 S	200 S
$ E_0 ^2$ (mV/m) <sup>2</sup> /Hz	0.0	0.0	0.0	0.0	0.3	0.3	0.3	0.3
$E_{0\perp}$ (mV/m)	50	50	50	50	50	50	50	50

Figure 4.4 plots the O<sup>+</sup> flux (panel a) and field aligned velocity (panel b) along the center field line of the simulation domain after 10 minutes for the eight different combinations of applied drivers documented in Table 4.2. As shown in this figure, increasing the strength of southward neutral winds induces progressively larger O<sup>+</sup> field-aligned velocities and flux. A 200 m/s southward neutral wind exerts an upward force (through drag) that is enough to almost cancel the tendency for the F-region peak to drift downward due to pressure gradient and gravitational forces. Northward neutral winds exert a downward force enhancing the downflow under the F-region peak and suppressing upflow at higher altitudes below the main ion perturbation, which has reached approximately 2000 km by the end of the simulation. In case V, downward flux created by the northward neutral wind and upward flux driven by the wave heating balance resulting in the same amount of flux as the no wind, no wave heating simulation (case II) after 10 minutes at roughly 800 km. It is notable that through lifting of the F-region plasma and through imparting parallel momentum to the ionosphere at lower altitudes dominated by ion-neutral collisions, neutral winds can significantly enhance upward flux and drift speeds at very high altitude regions.

A secondary effect of the neutral wind is through the frictional heating terms in Equations 2.67 and 2.68. A second set of simulations was constructed to elucidate the impact of winds in the  $\mathbf{E} \times \mathbf{B}$  drift direction on ion upflow through the regulation of differential ion-neutral velocities, hence frictional heating. This set of simulations was conducted alongside a reference simulation that used both a DC electric field,  $E_{0\perp} = 50$  mV/m, and wave heating,  $|E_0|^2 = 0.3$  (mV/m)<sup>2</sup>/Hz but lacked any neutral wind influence (case II, Figure 4.6 and Table 4.3). This reference case is compared against two cases, where horizontal neutral winds are used in conjunction with the reference

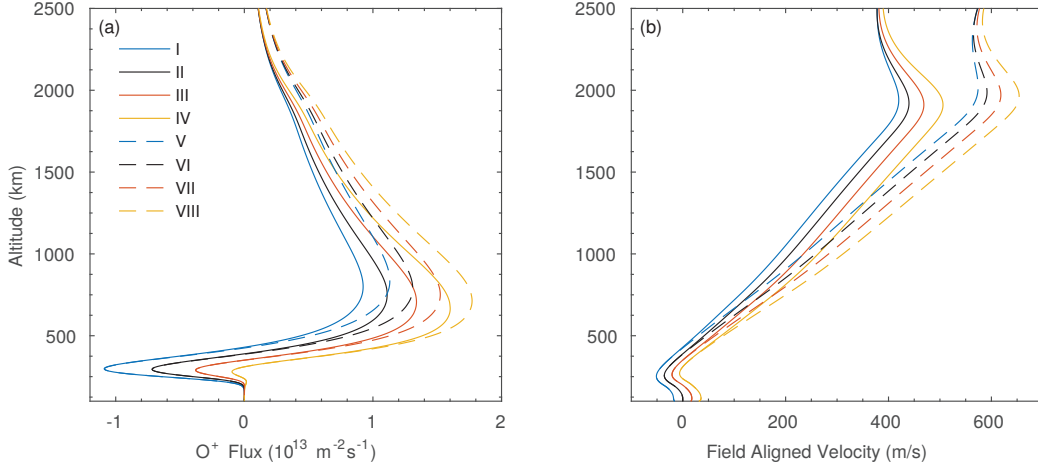


Figure 4.4: Results from eight simulations illustrating the impact thermospheric winds have on ion upflow at  $t_0+10$  minutes. Each profile shown in this plot has been extracted from the center geomagnetic field line of the simulation. By this point in time, the main perturbation has reached approximately 2000 km as seen in the velocity peak in panel b. The specific simulation drivers used are tabulated in Table 4.2. Southward neutral winds increase ion velocities and flux rates (cases III, IV, VII, and VIII) while northward neutral winds decrease ion velocities and flux rates (cases I and V) with respect to the control simulations (cases II and VI) due to the direction of the resulting ion-neutral drag forces.

simulation upflow drivers,  $E_{0\perp} = 50$  mV/m and  $|E_0|^2 = 0.3$  (mV/m)<sup>2</sup>/Hz, 150 m/s along  $\mathbf{E} \times \mathbf{B}$  (case I, Figure 4.6 and Table 4.3) or 150 m/s against  $\mathbf{E} \times \mathbf{B}$  (case III, Figure 4.6 and Table 4.3). These winds are implemented using Equation 4.4. Since there is not a component of these winds along the field line to cause ion-neutral drag, this wind orientation affects upflow through the frictional heating terms, in Equations 2.66 - 2.68. As it can be seen in Figure 4.5, when the neutral winds are antiparallel to the  $\mathbf{E} \times \mathbf{B}$  drift (panel c) then there is an increase in frictional heating which increases upflow but when the neutral winds are parallel to the  $\mathbf{E} \times \mathbf{B}$  drift then there is a decrease in frictional heating which suppresses upflow (panel a).

Figure 4.5 plots a snapshot of the  $O^+$  perpendicular temperature of these three simulations after ten minutes of the applied drivers, the end of the simulation. The simulation using winds along  $\mathbf{E} \times \mathbf{B}$  is in panel a, the reference simulation with no winds is in panel b, and the simulation using winds against  $\mathbf{E} \times \mathbf{B}$  is in panel



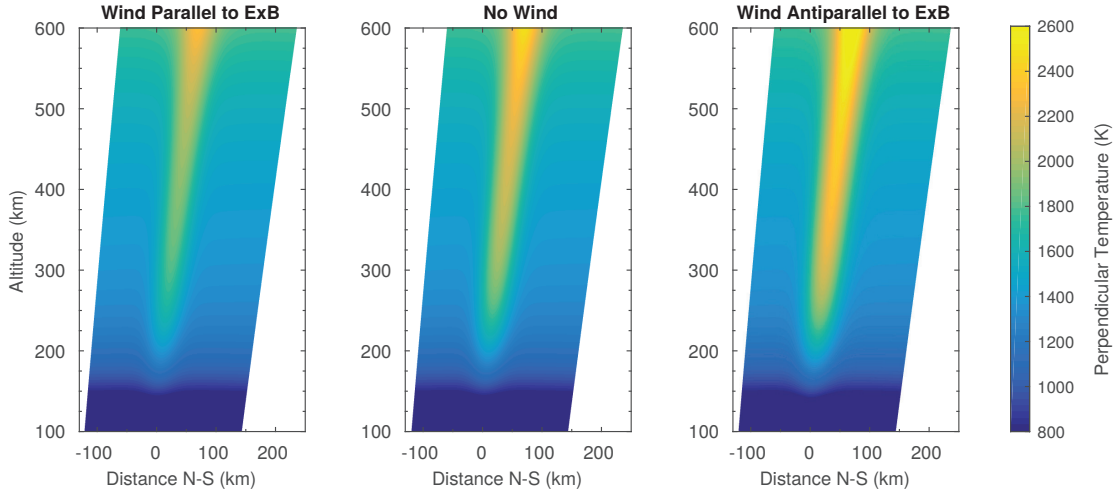


Figure 4.5: Perpendicular temperature vs. altitude and meridional distance after ten minutes of  $E_{0\perp} = 50$  mV/m and  $|E_0|^2 = 0.3$  (mV/m)<sup>2</sup>/Hz with 150 m/s winds along  $\mathbf{E} \times \mathbf{B}$  in panel a, with no winds in the panel b, and with 150 m/s winds antiparallel to  $\mathbf{E} \times \mathbf{B}$  in panel c. Temperature increases are localized in the center of the grid by constraining the electric potential boundary conditions using Equations 4.1-4.4. At 400 km, the winds antiparallel to  $\mathbf{E} \times \mathbf{B}$  have increased perpendicular temperatures by 11.5% while the winds along  $\mathbf{E} \times \mathbf{B}$  decrease them by 9.7% with respect to the control case.

c. Note that both the electric field boundary conditions and wind inputs have a Gaussian envelope in the direction perpendicular to the field lines which generates the central temperature structure seen in these panels of Figure 4.5. By the end of the simulations, on the center geomagnetic field line, at 400 km, the against  $\mathbf{E} \times \mathbf{B}$  winds (panel c) increase the  $O^+$  perpendicular temperature by 11.5% while the along  $\mathbf{E} \times \mathbf{B}$  winds (panel a) decrease it by 9.7% from the no wind simulation due to the differences in frictional heating rates.

The resulting  $O^+$  flux from these three simulations is plotted in Figure 4.6. The along  $\mathbf{E} \times \mathbf{B}$  wind simulation is case I, the no wind simulation is case II, and the against  $\mathbf{E} \times \mathbf{B}$  wind simulation is case III. The against  $\mathbf{E} \times \mathbf{B}$  neutral wind simulation not only increases the perpendicular temperature but also increases the  $O^+$  flux generated through the frictional heating mechanism. The leading edge of the primary upflow reaches 1000 km by 240 s (panel a, Figure 4.6) and is still propagating towards 2500 km by the end of the simulation (panel b, Figure 4.6). The flux at 2500 km is an

Table 4.3: The power spectral densities,  $|E_0|^2$ , DC electric fields,  $E_{0\perp}$ , and geographic neutral winds,  $v_{n,0}$ , used in simulations I - III plotted in Figure 4.5. Eastward winds here are parallel to the  $\mathbf{E} \times \mathbf{B}$  drift direction and westward winds are antiparallel.

Simulation	I	II	III
$v_{n,0}$ (m/s)	150 E	0.0	150 W
$ E_0 ^2$ (mV/m) <sup>2</sup> /Hz	0.3	0.3	0.3
$E_{0\perp}$ (mV/m)	50	50	50

order of magnitude smaller than the flux at 1000 km, and is primarily driven by wave heating and the indirect heating mechanism whereby frictionally heated ions undergo heat exchange with electrons, which then transport the energy quickly along the field line.

A third and final group of simulations examine the dependence of the ion upflow response to neutral wind disturbance onset timing. It is highly unlikely that multiple ion drivers will occur at the exact same moment in time, so it is helpful to investigate

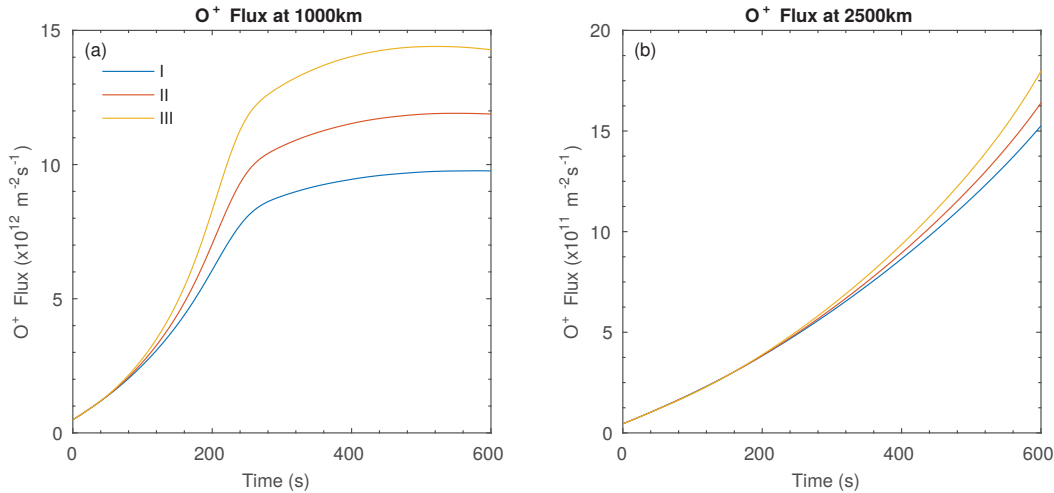


Figure 4.6: The O<sup>+</sup> flux from three simulations at 1000 km (panel a) and 2500 km (panel b) along the center field line for the full ten minute duration of the simulation. For case descriptions see Table 4.3. Winds antiparallel to  $\mathbf{E} \times \mathbf{B}$  (case III) increase the O<sup>+</sup> flux response while winds parallel to the  $\mathbf{E} \times \mathbf{B}$  drift (case I) decrease the O<sup>+</sup> flux response with respect to the reference simulation lacking winds (case II).

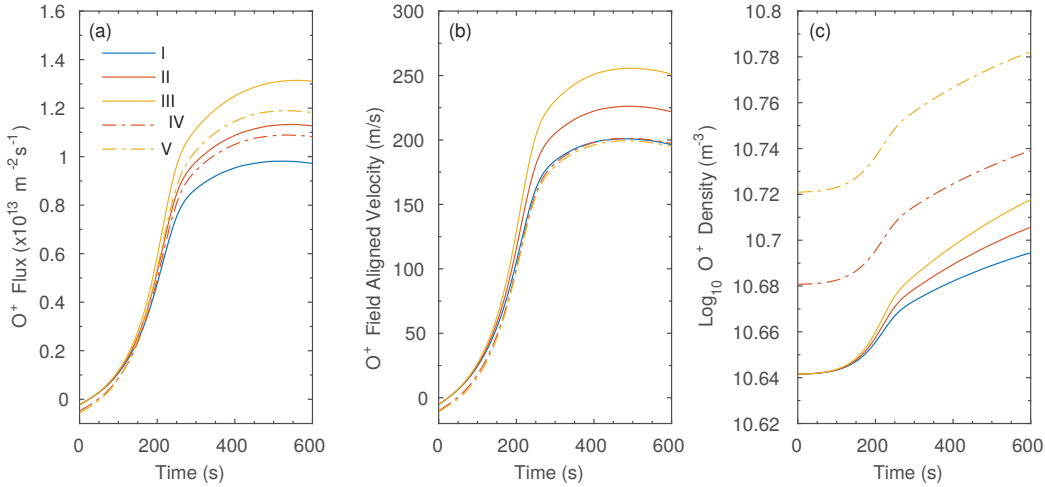


Figure 4.7: The O<sup>+</sup> flux (panel a), field aligned velocity (panel b), and the density (panel c) on the center geomagnetic field line, at 1000 km, for five simulations illustrating the effects of neutral wind onset time on the upflow responses. See Table 4.4 for a description of the different cases. Running neutral winds for a period of time prior to applying a DC electric field serves to increase densities and fluxes at higher altitudes but not significantly increase the field aligned velocity.

how the relative timing of different energy source may affect ion upflow. Figure 4.7 shows the O<sup>+</sup> flux (panel a), field aligned velocity (panel b), and the density (panel c) for the last ten minutes of five simulations used for this part of the study. For three of these simulations, first the model was run for an hour without any drivers being applied, then for case I  $E_{0\perp} = 50$  mV/m was active for ten minutes (reference case), for case II  $E_{0\perp} = 50$  mV/m and a southward  $v_{n,0} = 100$  m/s was active for ten minutes, and for case III  $E_{0\perp} = 50$  mV/m and a southward  $v_{n,0} = 200$  m/s was active for ten minutes. For the next simulation the model was run for an hour with a constant southward  $v_{n,0} = 100$  m/s and then  $E_{0\perp} = 50$  mV/m was also activated for ten minutes in case IV. For the last simulation, the model was run for an hour with a constant southward  $v_{n,0} = 200$  m/s and then  $E_{0\perp} = 50$  mV/m was also active for ten minutes for case V. Hence, these five simulations vary in whether the neutral wind begins an hour before the main DC electric field or at the same time. For reference, the case parameters are also summarized in Table 4.4.

Table 4.4: The DC electric fields,  $E_{0\perp}$  and geographic neutral winds,  $v_{n,0}$ , used in simulations I - V plotted in Figure 4.7, where  $t_0$  corresponds to 0. In simulations IV and V, the neutral wind was started an hour prior to the onset of the DC electric field.

Simulation	I	II	III	IV	V
$v_{n,0}$ (m/s)	0	100 S	200 S	100 S	200 S
$v_{n,0}$ Onset Time (s)	$t_0$	$t_0$	$t_0$	$t_0-3600$	$t_0-3600$
$E_{0\perp}$ (mV/m)	50	50	50	50	50
$E_{0\perp}$ Onset Time (s)	$t_0$	$t_0$	$t_0$	$t_0$	$t_0$

Running neutral winds for an hour prior to the DC electric field onset serves to increase ion densities at higher altitudes through ion-neutral drag. The 100 m/s southward neutral wind increases the  $O^+$  density by 9% after one hour and the 200 m/s southward neutral wind increases it by 20% at an altitude of 1000 km. These mark the initial state,  $t = 0$ , for Figure 4.7, panel c. The resulting flux, by the end of the simulation, in case V is 22% larger, case IV is 11% larger, case III is 35% larger, and case II is 16% larger than the case without winds (case I). In either onset time scenario, given the parameters used here, larger neutral winds generate larger the  $O^+$  flux responses as shown in Figure 4.7, panel a. However, by starting the neutral winds an hour prior to the onset of a DC electric field the resulting  $O^+$  flux is lower than from the mutual onset case. Additionally, there is not an increase in the field aligned velocity above that which is caused by the DC electric field alone. The sudden onset of a neutral wind disturbance has a larger impact on ion upflow but in reality the neutral winds will act somewhere in between the two extremes simulated here, potentially taking tens of minutes to ramp up to speed if driven by magnetospheric energy inputs.

### 4.3 Chapter conclusions

GEMINI-TIA has been used to examine the synergistic effects of frictional heating and wave heating at low altitudes. At lower altitudes ( $<300$  km) temperature anisotropies are largely driven by DC electric fields while wave heating effects dominate above  $\sim 500$  km. The strength of the power spectral density of broadband ELF waves determines

how deep into the ionosphere these waves are able to generate anisotropy. Extreme levels of wave heating (e.g. power spectral density of  $10.0 \text{ (mV/m)}^2/\text{Hz}$ ) are required overcome the collisional relaxation and generate significant impacts at altitudes  $<300$  km. This extreme power spectral density is much larger than the reference rate of  $0.3 \text{ (mV/m)}^2/\text{Hz}$  taken from *Bouhram et al.* (2003) and would not be representative of a typical upflow/outflow event.

Neutral winds also play an important role in influencing ion dynamics. They can aid or hinder ion flow, and given enough time impart momentum to the ions at low altitudes, can impact the high altitude ion populations available for secondary acceleration processes that lead to outflow to the magnetosphere. A geographically southward neutral wind of  $100 \text{ m/s}$  aids ion upflow, through ion-neutral drag, and can increase the  $O^+$  flux response by  $15\%$  at  $1000 \text{ km}$  after  $10$  minutes in a simulation that uses both that southward neutral wind and a DC electric field of  $50 \text{ mV/m}$  when compared to the DC electric field only simulation. On the other hand, geographically northward winds hinder ion upflow. A  $100 \text{ m/s}$  northward neutral wind coupled with a DC electric field of  $50 \text{ mV/m}$  results in an ion flux that is  $13\%$  smaller, at  $1000 \text{ km}$  after  $10$  minutes, than a similar simulation without winds. Neutral winds antiparallel to the  $\mathbf{E} \times \mathbf{B}$  drift (westward here) exacerbate frictional heating, resulting in more ion upflow. A neutral wind against  $\mathbf{E} \times \mathbf{B}$  of  $150 \text{ m/s}$ , coupled with a DC electric field of  $50 \text{ mV/m}$  and wave heating with a power spectral density of  $0.3 \text{ (mV/m)}^2/\text{Hz}$ , increased the  $O^+$  flux response by  $11.5\%$  at  $400 \text{ km}$  but a neutral wind along  $\mathbf{E} \times \mathbf{B}$  of the same strength decreased the  $O^+$  flux response by  $9.7\%$  at  $400 \text{ km}$  after ten minutes. The time history of neutral winds has also been shown to be important. By starting the neutral winds an hour prior to the onset of a DC electric field driven upflow the resulting  $O^+$  flux is reduced by up to  $11\%$  in the case of  $200 \text{ m/s}$  southward winds by the end of the simulation when compared to cases when the neutral winds and DC electric fields are started at the same time. These results suggest that thermospheric dynamics can be an important factor affecting ion upflow and outflow.

## Chapter 5

# Modulation of low-altitude upflow by nonlinear gravity waves

It is well-established that the ionosphere can be modulated by thermospheric winds, which may arise from solar forcing, plasma convection, and/or acoustic-gravity waves (to name a few sources). Neutral winds affect ionospheric motions through collisions (viz. ion-neutral drag), and alter upflow or perpendicular motions, potentially modifying source populations available for secondary acceleration mechanisms. Acoustic-gravity waves (GWs) (*Hines, 1960*), which are of primary interest to this study, are often driven at high latitudes by heating produced by auroral electric fields, energetic particle precipitation, and shear forces in the ionosphere (*Hocke and Schlegel, 1996*). Studies have also shown that the solar terminator or the Moon's umbra projected onto the Earth during a solar eclipse can produce GWs (*Fritts and Luo, 1993; Altadill and Sole, 2001; Sauli et al., 2006; MacDougall and Jayachandran, 2011*).

GWs are often classified on the basis of their scales. Large-scale GWs propagate in the thermosphere and have horizontal velocities between 400 and 1000 m/s, horizontal wavelengths greater than 1000 km and periods in the range of 30 minutes to 3 hours. Medium-scale GWs, which typically propagate in the lower atmosphere have horizontal velocities between 100 and 250 m/s, wavelengths of several hundred kilometers and periods between 15 and 60 minutes (*Hunsucker, 1982; Ogawa et al., 1987; Hocke and Schlegel, 1996*). GW amplitudes grow rapidly with increasing altitude because

of the decreasing background density (*Hines*, 1960). In the thermosphere, GWs are further affected by dissipative processes including kinematic viscosity, thermal diffusivity, ion drag, wave-induced diffusion, and nonlinear wave interactions (*Francis*, 1973; *Richmond*, 1978; *Maeda*, 1985; *Fritts and Alexander*, 2003; *Vadas and Fritts*, 2005). Additionally, GWs moving against a background wind tend to propagate to higher altitudes because they are refracted by the background wind to a more vertical trajectory than those moving in the same direction (*Fritts and Vadas*, 2008).

GWs propagating in ionospheric regions interact with the ions through collisions and result in the neutrals driving ion transport along the magnetic field lines creating advection and compression of the plasma, traditionally called traveling ionospheric disturbances (TIDs) (*Kirchengast et al.*, 1995; *Hocke and Schlegel*, 1996). TIDs are broken into three different classes: large-, medium-, and small-scale. Large-scale TIDs arise typically during geomagnetic storms accompanying large energy and momentum inputs in the auroral zones. These inputs result in strong heating, acceleration, and potentially very large amplitudes in the neutral and plasma density, temperature, and wind fields extending to high altitudes and readily propagate to equatorial latitudes (*Hocke and Schlegel*, 1996). Medium- and small-scale TIDs appear more frequently during geomagnetically quiet or moderately disturbed times and do not have a corresponding increase in occurrence frequency with increasing geomagnetic activity (*Ogawa et al.*, 1987). At the medium and small scales TIDs have many sources. Some of these sources include the manifestations of GWs entering the thermosphere-ionosphere system from sources in the lower atmosphere (*Hunsucker*, 1982), the effects of Joule heating and Lorentz forces in the auroral electrojet, the presence of particle precipitation (*Richmond*, 1978; *Bertin*, 1983), and instabilities associated with E and F region coupling processes (*Yokoyama et al.*, 2009).

## 5.1 Data Motivating and Guiding Modeling Efforts

When TIDs are observed with incoherent scatter radar (ISR), such as Arecibo, PFISR, RISR, EISCAT, and Sondrestrom, there can be oscillations in all of the primary parameters, i.e. electron density, electron temperature, ion temperature, and line-of-sight ion velocity (*Thome, 1964; Bertin, 1983; Kirchengast et al., 1995; Hocke et al., 1995; Nicolls et al., 2004; Vlasov et al., 2011; David et al., 2018*). Recent work has also shown that GW parameters may be derived from ISR measurements, provided sufficient spatial coverage is achieved (*Nicolls and Heinselman, 2007; Vadas and Nicolls, 2007; Nicolls et al., 2013*). From a study of 45 high-latitude TIDs, observed by the EISCAT radar at Tromsø (*Hocke et al., 1995*), it has been suggested that the line-of-sight velocities are the best tracer for gravity waves since other ionospheric parameters can be easily disturbed by electron precipitation and frictional heating (*Bertin, 1983*).

On May 31st, 2003 Sondrestrom’s incoherent scatter radar (ISR) observed line-of-sight velocity perturbations of  $\sim 50\text{-}150$  m/s alternating upward and downward ion flow, extending in some cases below  $hmF_2$ , with a downward phase progression that suggests the presence of a gravity wave (shown in Figure 5.1). Under normal ionospheric conditions it is fairly unusual to see upflow below  $hmF_2$  – to do so ostensibly requires neutral winds to overcome the effects of gravitational and pressure gradient forces (both downward). The radar, throughout this experiment, utilized a single look direction with an elevation of 80.5 degrees which is well aligned with the local magnetic field lines. A time integration of 3 minutes and a height resolution of  $\sim 40$  km were used. Regions in this data of large uncertainty,  $>90\%$ , have been left white in lieu of error-bars to indicate our confidence in the measurements.

Within the field of view for Sondrestrom, the GW perturbation appears, enhances, then diminishes in amplitude over  $\sim 7$  hours (panel d) and generates significant ionospheric flux (panel e). The ISR data also shows signatures of electron precipitation at 0:10-1:10 UT and 4:36-5:36 UT in the form of low altitude ( $<200$  km) electron density (panel a) increases and high altitude ( $>400$  km) upflow in the line of sight velocity (panel d). There are also instances of frictional heating, evident in the ion temperature (panel b) from 3:24-3:30 UT and 4:36-4:42 UT. Neither of these energy



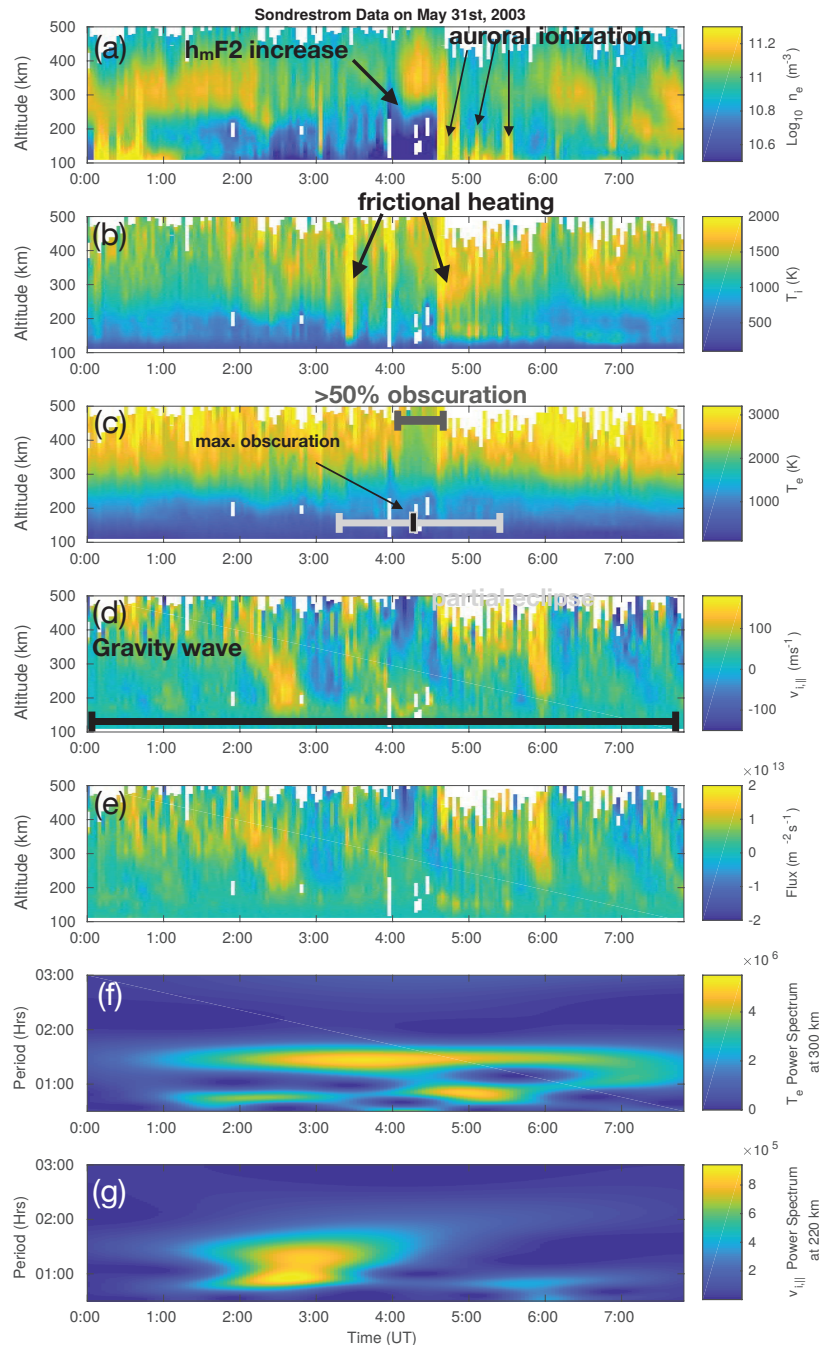


Figure 5.1: Sondrestrom incoherent scatter radar (ISR) data on May 31st 2003, and the corresponding Morelet wavelet analysis of electron temperature at 300 km (panel e) and line-of-sight velocity at 220 km (panel f), from 0:10-8:00 UT. The  $\sim 50$ -150 m/s alternating upward and downward ion flow (panel d) with a downward phase progression extends in some cases below  $h_m F_2$  over the course of this data set and suggests a GW influence.

inputs are spatially or temporally aligned with the line of sight velocity oscillations, indicating a GW/TID observation and not frictional heating-driven upflow (Type 1 of *Wahlund et al. (1992)*) or electron heating-driven upflow (Type 2 of *Wahlund et al. (1992)*).

There is also an annular eclipse that occurs within the observation window. At Sondrestrom, partial obscuration begins at 3:29 UT but local sunrise is at 4:00 UT. The full eclipse, where the disk of the moon is, visually, completely within the disk of the sun begins at 4:23 UT and continues until 4:26 UT; a peak obscuration of 87.9% is achieved. The remaining partial eclipse ends at 5:20 UT. This eclipse event accounts for the decrease in E region density (panel a) from 4:00-4:36 UT. There is also a  $\sim 500$  K decrease in electron temperature (panel c) at this time due to the reduction of EUV heating. The temperature decrease results in the lowering of the equilibrium scale height which drives the downward transport of ion, seen above the F region in the data at this time (panel d), and potentially accounts for the rise in  $hmF_2$  from 388 km to 429 km and increase in F region density (panel a) from 4:00 UT to 4:36 UT (*Evans, 1965*). F region dynamics are also subject to field aligned and  $E \times B$  transport. The elevated ion temperatures from 3:24-3:30 UT and 4:36-4:42 UT suggests the presence of significant  $E \times B$  drift and as a consequence the higher F region densities may have been convected into view from other latitudes and local times. At 4:36 electron precipitation, mentioned previously, occurs and obscures any remaining eclipse effects. The GW exists for several hours before, and after, the eclipse event and thus seems unlikely to originate from the eclipse.

A Morlet wavelet analysis is applied to the line-of-sight velocity oscillations, which has the clearest GW/TID signal in the data (see Figure 5.1, panel f for the power spectrum at 220 km). The output is averaged at each altitude to get a single dominant period and then averaged again over all altitudes to provide the average period of the observed GW. One of the drawbacks of the averaging is that it results in the removal of any smaller scale, or higher frequency, variability in the data. Averaging across time and all available altitudes yields an estimated frequency of 78 minutes and vertical wavelength of 350 km for this GW event. The horizontal wavelength, according to the anelastic gravity wave dispersion relation (c.f. *Fritts and Alexander, 2003*), is 1800

km. These estimated wave parameters have been used for our data-inspired modeling study of GW impacts on upflow in subsequent sections.

The wavelet analysis, when applied to the electron temperature at 300 km, also yields a GW/TID signal (Figure 5.1 (panel e) which is more difficult to see when looking at the electron temperature directly (panel c). At this altitude there is a consistent dominant period of 88 minutes and sub-harmonics at a smaller average period of 44 minutes. The clear GW/TID signal in both the line-of-sight velocity, from ~0:30-4:00 UT and electron temperature, from ~0:30-8:00 UT, illustrates an interconnected response in the ion parameters to the wave to be examined via numerical simulations in later sections. The eclipse impacts the GW/TID signature in the wavelet analysis of the line-of-sight velocity from ~4:00 UT onwards and the electron temperature when the eclipse obscuration exceeds ~50%. The frictional heating and particle precipitation within the electron density and the ion temperature obscure the GW/TID signature in wavelet analysis of these parameters (which are not shown).

## 5.2 Modeling Approach

It is common to consider the ionosphere a passive tracer of the neutral gas with no feedback to the thermosphere (e.g. *Clark et al. (1971); Testud and Francois (1971); Davis (1973); Kirchengast et al. (1992)* and *Hocke and Schlegel (1996)*). For this study we use the ionospheric model of *Burleigh and Zettergren (2017)* and the atmospheric model of *Snively (2013)* coupled via the approach discussed in *Zettergren and Snively (2015, Appendix A)*. This allows for the GW perturbations from the neutral atmospheric model to drive the dynamical evolution (including upflow and outflow) in our ionospheric model.

The neutral dynamics model used in this study, informally referred to as MAGIC (Model for Acoustic-Gravity wave Interactions and Coupling), solves the conservative form of the Euler equations with the inclusion of the gravitational force and a Navier-Stokes description of viscosity. It is a variation of the model described by *Snively and Pasko (2008)*, *Snively (2013)* and *Zettergren and Snively (2015, Appendix A)*. It

solves the Euler equations in conservative form using a Finite Volume method based on LeVeque’s “f-wave” approach (*LeVeque, 1997, 2002*), with the inclusion of gravity via the method described in *Bale et al. (2003)*.

The ionospheric model used in this study and described in detail in *Burleigh and Zettergren (2017)* (GEMINI-TIA), is an anisotropic extension of the model originally developed in *Zettergren and Semeter (2012)* and expanded in *Zettergren and Snively (2013)*; *Zettergren et al. (2014)*; *Zettergren and Snively (2015)*. This fluid model solves the 2D nonlinear equations for the conservation of mass, momentum, parallel energy, and perpendicular energy for each species  $s$  relevant to the E and F regions, and topside ionosphere ( $s = \text{O}^+, \text{NO}^+, \text{N}_2^+, \text{O}_2^+, \text{N}^+, \text{and H}^+$ ) and is coupled to an quasi-static treatment of auroral and neutral dynamo electric currents.

Perturbations from the atmospheric background state are passed from the neutral dynamics model into the ionospheric model in a one-way coupling. Presently NRLMSISE-00 (*Picone et al., 2002*) is used to define background conditions in both models though user specified profiles may be used as well. Perturbations communicated between the models include variations in neutral species density (specifically O, N<sub>2</sub>, and O<sub>2</sub> for this study), velocity, and temperature. The passing of these coordinated disturbances incorporate influences of the simulated gravity wave from the neutral atmospheric model into the ionospheric model through ion-neutral collisions/reactions, and dynamo source terms in the electrodynamic equations solved by GEMINI-TIA. Neutral variations are communicated between the models every minute and interpolated to the current time step. In addition, there is also a spatial interpolation and rotation step to convert from the neutral dynamics model’s Cartesian grid to the ionospheric model’s tilted-dipole grid.

Figure 5.2 shows the grids used by the two models for the simulations presented in this study. The blue outline indicates the extent of the ionospheric grid and the green outline shows the atmospheric grid (the black line represents the surface of the Earth). The overlap region between the blue area and the green area is where the neutral dynamics are coupled into the ionospheric model. The atmospheric model uses a uniform mesh that has horizontal grid spacing (x-direction) of 5 km and a vertical grid spacing (z-direction) of 1 km with an upper boundary of 500 km and a

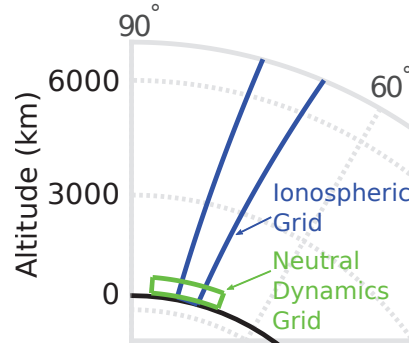


Figure 5.2: The ionospheric and atmospheric model grid alignment. The black line represents the surface of the Earth. The blue outline indicates the extent of the ionospheric model’s grid (which extends up to 14,000 km above ground level and is well outside the range of this figure) and the green outline is for the atmospheric model. The overlap region between the blue area and the green area indicates where the models are coupled.

lower boundary of 88 km. The width is large enough to contain one wavelength, 1800 km for this study. The ionospheric grid uses a tilted dipole configuration (*Huba et al.*, 2000) and has variable spacing currently set to  $\sim 6\text{-}8$  km in the E and F regions, with increasing grid size towards higher altitudes, and a top boundary altitude of  $\sim 14,000$  km. The upper reaches of the ionospheric grid ( $> 2,500$  km) act as a buffer region to avoid boundary effects from impacting the solutions (*Burleigh and Zettergren*, 2017). The model’s geographic location for the simulations presented in this paper has been centered on Sondrestrom,  $66.99^\circ$  N and  $309.05^\circ$  E, where the ISR data motivating this study was recorded.

### 5.3 Ionospheric Response to Gravity Wave Forcing

Four simulations are presented here to illustrate the ion field-aligned transport response to different strengths of large-scale atmospheric gravity waves. The initial conditions of the ionospheric model for each simulation have been tuned to resemble the background level densities observed via ISR (Section 5.1). Since we do not have detailed knowledge of the source location, strength, propagation direction, and excitation mechanism, the gravity wave is excited in the neutral atmosphere model by vertical body forcing chosen to approximately describe the spectrum of the observed

ionospheric responses. The forcing function is given by

$$F_z(x, z, t < t_c) = A n_n \exp\left(-\frac{(z - z_c)^2}{2\sigma_z^2}\right) \exp\left(-\frac{(t - t_c)^2}{2\sigma_t^2}\right) \cos\left(\frac{2\pi}{\tau}(t - t_c) - \frac{2\pi}{\lambda_x}x\right) \quad (5.1)$$

where  $A$  is the peak acceleration of the vertical wind, set to 0.4, 2, 4, and 7 m/s<sup>2</sup> for the four simulations (labeled A, B, C, and D respectively), which gets multiplied by the local neutral mass density ( $\rho_n$ ) to produce the forcing amplitude. In Equation 5.1 a forcing altitude ( $z_c$ ) of 110 km and a half-width ( $\sigma_z$ ) of 10 km are chosen. The half-width is used to generate localized wave forcing and produces a quasi-monochromatic spectrum of waves rather than a single mode. The period of the GW source ( $\tau$ ) in all four simulations is 78 minutes with a horizontal wavelength  $\lambda_x$  of 1800 km and a vertical wavelength of  $\sim 350$  km. Note that the vertical wavelength of the simulated GW does not remaining constant with altitude due to temperature variations. The GW source in all of the simulations is ramped up slowly over 117 minutes ( $\sigma_t$ ) to avoid transient wave breaking and acoustic waves. When the GW reaches full strength ( $t \geq t_c$ ), the forcing takes the form of

$$F_z(x, z, t \geq t_c) = A n_n \exp\left(-\frac{(z - z_c)^2}{2\sigma_z^2}\right) \cos\left(\frac{2\pi}{\tau}(t - t_c) - \frac{2\pi}{\lambda_x}x\right) \quad (5.2)$$

until the end of the simulation (Heale *et al.*, 2014). All of the Simulations run from 0:00 - 8:00 UT.

The field-aligned velocity component of the GWs generated by the neutral dynamics model and interpolated onto the ionospheric grid is presented in Figure 5.3. The four simulations presented here differ as they depend critically on the GW strength. For Simulation A (panel A - corresponding to the smallest amplitude wave) the GW is very regular in motion and once the GW has been ramped up to full strength there is a maximum neutral upflow (downflow) of 38 m/s (-28 m/s). This GW does not break and there are minimal nonlinear wave effects (e.g. energy deposition into other wave modes). For Simulation B (panel B), there is significant momentum deposition into the mean flow but minimal wave breaking. This combination of effects is responsible for the increase in the mean flow, from 4:30 UT onwards to the end of

the simulation, converting the wave upflow/downflow pattern to a weaker, yet net, upflow. If the GW were to be traveling in the opposite direction, this momentum deposition would result in a decrease in the mean flow and larger downflows. The

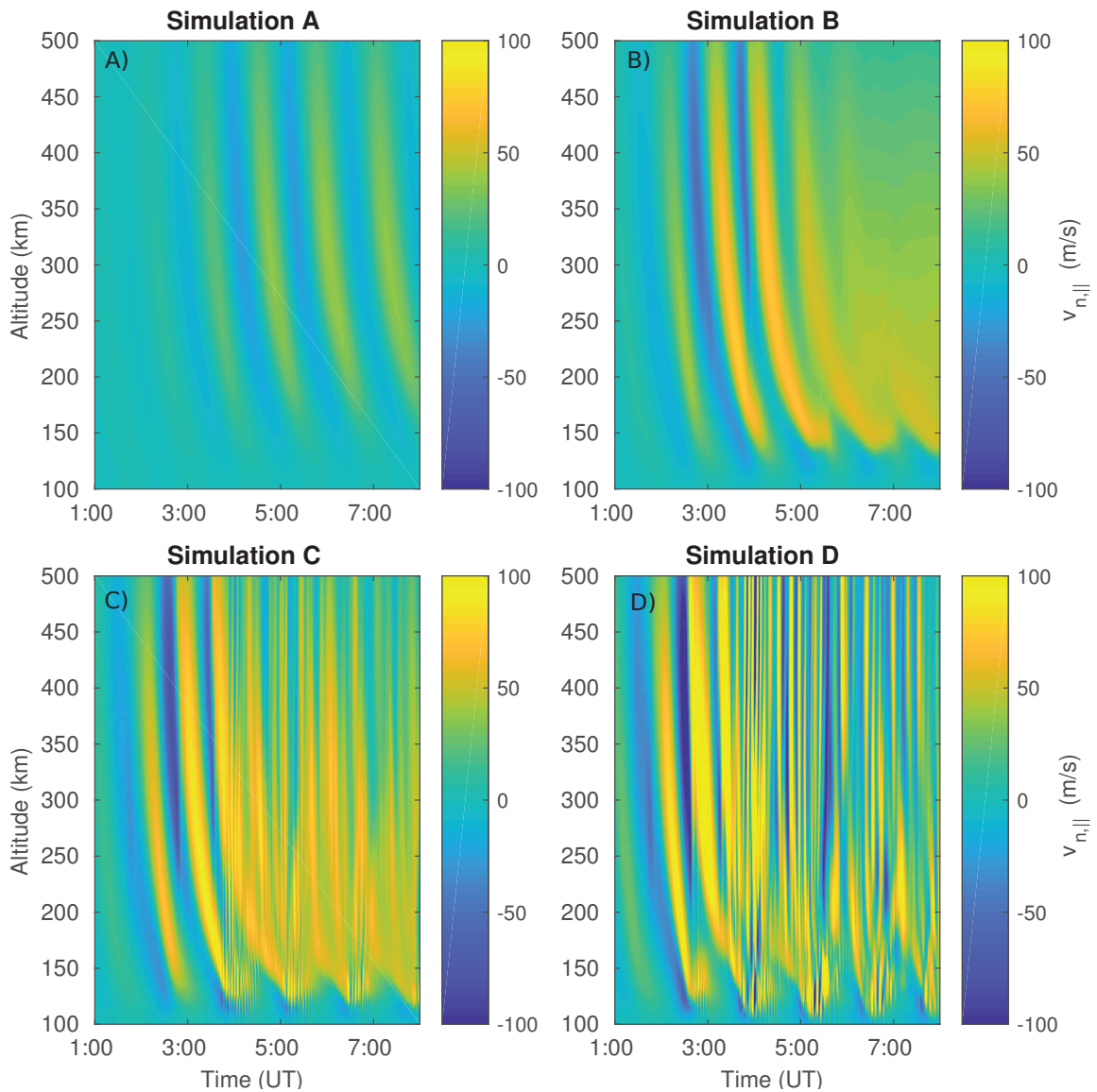


Figure 5.3: The field-aligned velocity component of the GWs generated by the neutral dynamics model after rotating into the ionospheric model's tilted-dipole grid structure. In all four simulations, A, B, C, and D, the gravity wave is excited by vertical body forcing with a period of 78 minutes. The strength of the wave is ramped up slowly over 117 minutes to avoid start-up wave breaking and acoustic waves, and then held steady until the end of the simulation.

GW still generates a maximum upflow (downflow) of 76 m/s (-52 m/s) before the nonlinear wave effects dominate the dynamics. For Simulation C there is not only an increase in the mean flow, from 4:00 UT onwards to the end of the simulation, but there is also small scale, intense, upflow/downflow generated from wave breaking effects below  $\sim 200$  km. This GW generates an upflow (downflow) of 100 m/s (-77 m/s) before the breaking occurs and a maximum of 195 m/s (-87 m/s) is reached within a region of wave breaking. For Simulation D (panel D), there is only modest momentum deposition into the mean flow but significant wave breaking. More energy is deposited into small scale wave modes generated by wave breaking and less into the mean flow than that seen in Simulations B and C. An upflow (downflow) of 108 m/s (-122 m/s) before the breaking occurs, and a maximum of 339 m/s (-291 m/s) is reached within a region of wave breaking, is generated by this GW in Simulation D.

As the gravity wave dynamics evolve over time, the neutral atmosphere perturbations act upon the ionosphere and drive ion upflow/downflow (see Figure 5.4). Nonlinear wave effects and wave breaking play an important role in modifying the ion response in each simulation. The  $O^+$  density (panels 1A-1D) is modulated by the GW motions, through ion-neutral drag. It should be noted that the general increase in ion density over the latter half of each simulation is due, in part, to photoionization from a changing solar zenith angle. It is summer so the regions  $>110$  km are still illuminated by the sun. This has a tendency to reinforce the ion response to neutral forcing as the day progresses.

The smallest amplitude GW, Simulation A (panel 1A), drives density perturbations that are very regular with a clear wavelike structure. The increase in mean flow, within the driving GW for Simulations B and C, results in more transport and a larger density (panels 1B and 1C). These densities reach  $1.0 \times 10^{11} \text{ m}^{-3}$  and  $1.1 \times 10^{11} \text{ m}^{-3}$  at an altitude of 500 km respectively by the end of the simulation. This is much larger than the corresponding values of  $7.5 \times 10^{10} \text{ m}^{-3}$  or  $8.8 \times 10^{10} \text{ m}^{-3}$  in Simulations A and D respectively. Simulation D contains a large amount of wave breaking, which passes energy into smaller scale wave modes resulting in very irregular, but strong, density perturbations (panel 1D). The ion-neutral drag in this case is strong enough to lift the F region peak to higher altitudes, see  $\sim 4:15$  UT in panel 1D where this



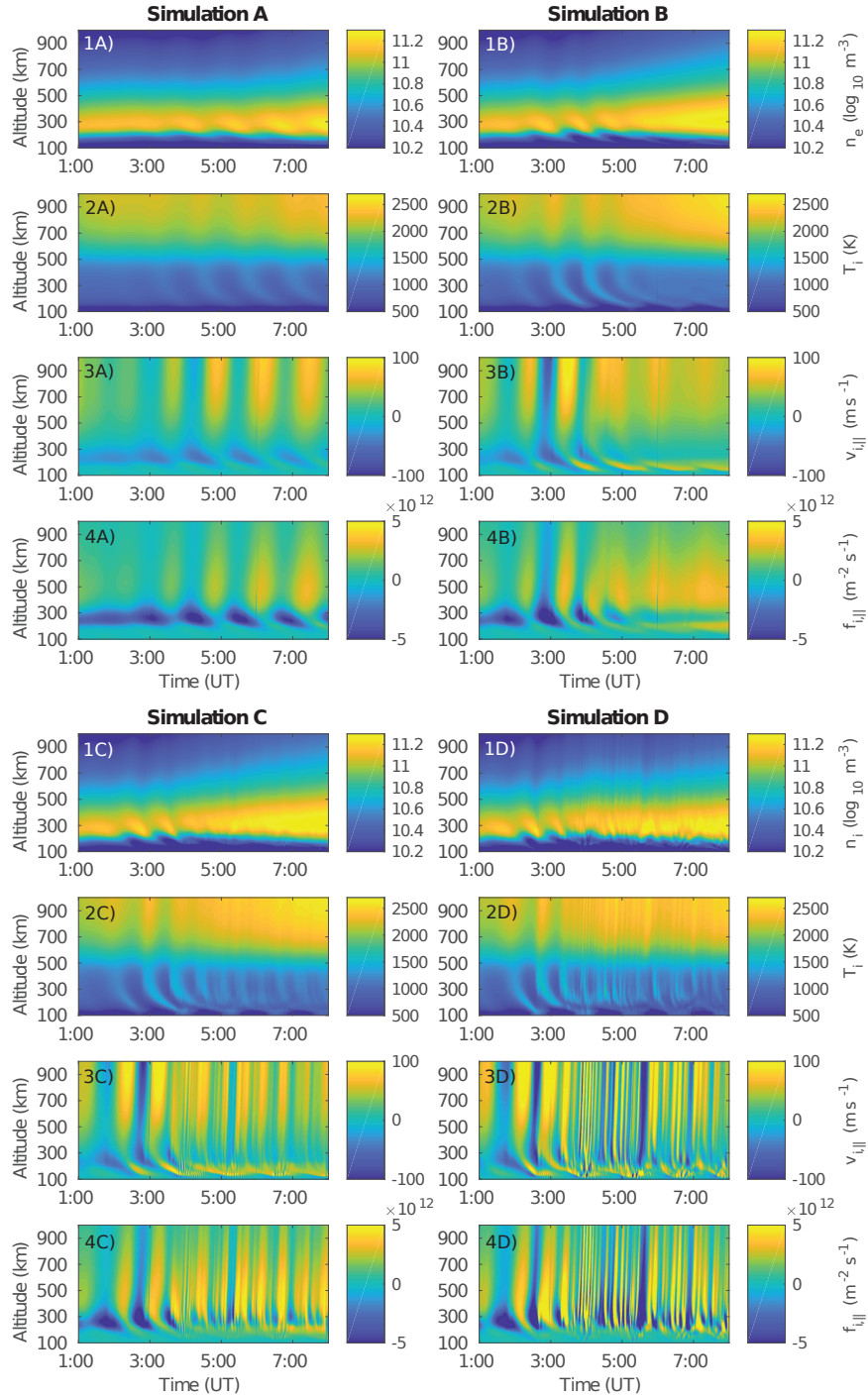


Figure 5.4: The ion dynamics from the center field line of the model grid from 1:00-8:00 UT, for Simulations A, B, C, and D for the  $O^+$  density (1A-1D), absolute temperature (2A-2D) where the parallel and perpendicular temperatures have been averaged as  $1/3T_{\parallel} + 2/3T_{\perp}$ , the field-aligned velocity (3A-3D), and flux (4A-4D).

effect is the greatest.

In addition to the ion density perturbations there is also strong coupling between the atmospheric temperature and the ion temperature from the bottom of the simulation up through the F region peak. The average ion temperature (defined as  $1/3T_{\parallel} + 2/3T_{\perp}$ ) of  $O^+$  from each of the simulations is presented in panels 2A-2D. The GW dynamics passed between models included temperature perturbations which drive the ion-neutral thermal coupling (via heat exchange) within the model coupled region.

The ion upflow driven in Simulation A, like the modulating GW, is very regular. At 1000 km, it reaches a maximum upflow of 80 m/s at 6:12 UT. Driving with a larger amplitude GW which contains significant momentum transfer into the mean flow, such as that in Simulation B, generates persistent upflow, on average 54 m/s, from 4:00 UT onwards for altitudes above the F region peak (panel 3B). Prior to that, a maximum upflow of 108 m/s at 1000 km at 3:30 UT was reached. The mean flow increase effect is also present in Simulation C. Coupled with wave breaking, it transports more ions to higher altitudes, results in a smaller average field aligned velocity, 48 m/s from 4:00 UT onwards at 1000 km, than the maximum upflow of 127 m/s reached at 3:18 UT, and produces a larger ion particle flux (see panel 4C here and Figure 5.9 for more detail). The wave breaking effects are also present in Simulation D and dominate the GW driven dynamics resulting in fine scale, intense upflow/downflow. At 1000 km the  $O^+$  field aligned velocities maximize at 134 m/s at 3:00 UT before the GW breaks and reaches in excess of 240 m/s after breaking.

The ion flux, generated by the modulating GW, maximizes in the F region where densities are still large. Comparing the four simulations at 500 km, Simulation A generates a maximum flux of  $2.9 \times 10^{12} \text{ m}^{-2} \text{ s}^{-1}$  at 7:27 UT (panel 4A), Simulation B generates a maximum flux of  $3.2 \times 10^{12} \text{ m}^{-2} \text{ s}^{-1}$  at 7:20 UT (panel 4B), Simulation C generates a maximum flux of  $5.3 \times 10^{12} \text{ m}^{-2} \text{ s}^{-1}$  at 5:31 UT (panel 4C), and Simulation D generates a maximum flux of  $1.7 \times 10^{13} \text{ m}^{-2} \text{ s}^{-1}$  at 4:06 UT (panel 4D). Within Simulation D, the effects of wave breaking also generates a strong downwards flux of  $-1.1 \times 10^{13} \text{ m}^{-2} \text{ s}^{-1}$  at 5:36 UT at this altitude. The Simulations that contain significant wave breaking, Simulations C and D, generate large fluxes several hours sooner than Simulations A and B. *Wahlund and Opgenoorth* (1989) suggests a minimum threshold

of  $\times 10^{13} \text{ m}^{-2} \text{ s}^{-1}$  is needed for an ion flux to have the potential to become outflow. Only Simulation D exceeds this threshold but with just the GW driving ion motions escape speed is not reached. All of the simulations contain transport that is enough to alter the ion populations available for other energization processes at this altitude, such as frictional heating, auroral precipitation, or transverse wave heating.

Because the ISR velocity data were analyzed for wave parameters and used to inspire the coupled model study, this is the primary parameter used to compare the model outputs back to the ISR data. Velocity was chosen for the comparison as it is most closely mirrors the effects of the GWs whereas electron temperature is directly altered by auroral precipitation and ion temperature is controlled to a large degree at high latitudes by frictional heating from strong  $E \times B$  drifts. Lastly density is extremely complicated as because it is affected by precipitation, heating (which alters chemistry), and convection of density gradients. Of the four simulations presented here, the ionospheric response to the GW in Simulation C most closely resembles the data from the May 2003 GW presented in Figure 5.1. The field aligned velocity has a similar dynamic range when compared to the data, viz.  $\sim 50\text{-}150 \text{ m/s}$ . Although Simulation C contains moderate wave breaking, evidence of wave breaking, if present in the data, is difficult to ascertain due to the long integration time of the ISR data.

The  $O^+$  velocity period that contains the most power at every altitude and time step is plotted in Figure 5.5 using a Morelet wavelet analysis (*Torrence and Compo, 1998*) of the field-aligned  $O^+$  velocity. This highlights the ion response to the four wave situations used in this study and where the nonlinear GW effects have the greatest impact. All of the Simulations contain, at the lowest altitudes, a primary ion velocity period that matches the GW forcing period of 1.3 hours. In Simulation A, there is a coherent ion response to the GW (evidenced by the relatively stable, in altitude and time, periodicities) that contains minimal nonlinear effects, including wave breaking (panel A). Self acceleration (*Fritts et al., 2015*) leading to shear that destabilizes the GW in Simulations B and C, from 200-500 km, drives the ion velocity period to shorter periods from 2-6UT (panels B and C respectively). In Simulation C (panel C) the locations of dark blue in this panel, where the dominant velocity period is 5 minutes or less, indicate the presence of moderate wave breaking and occurs most

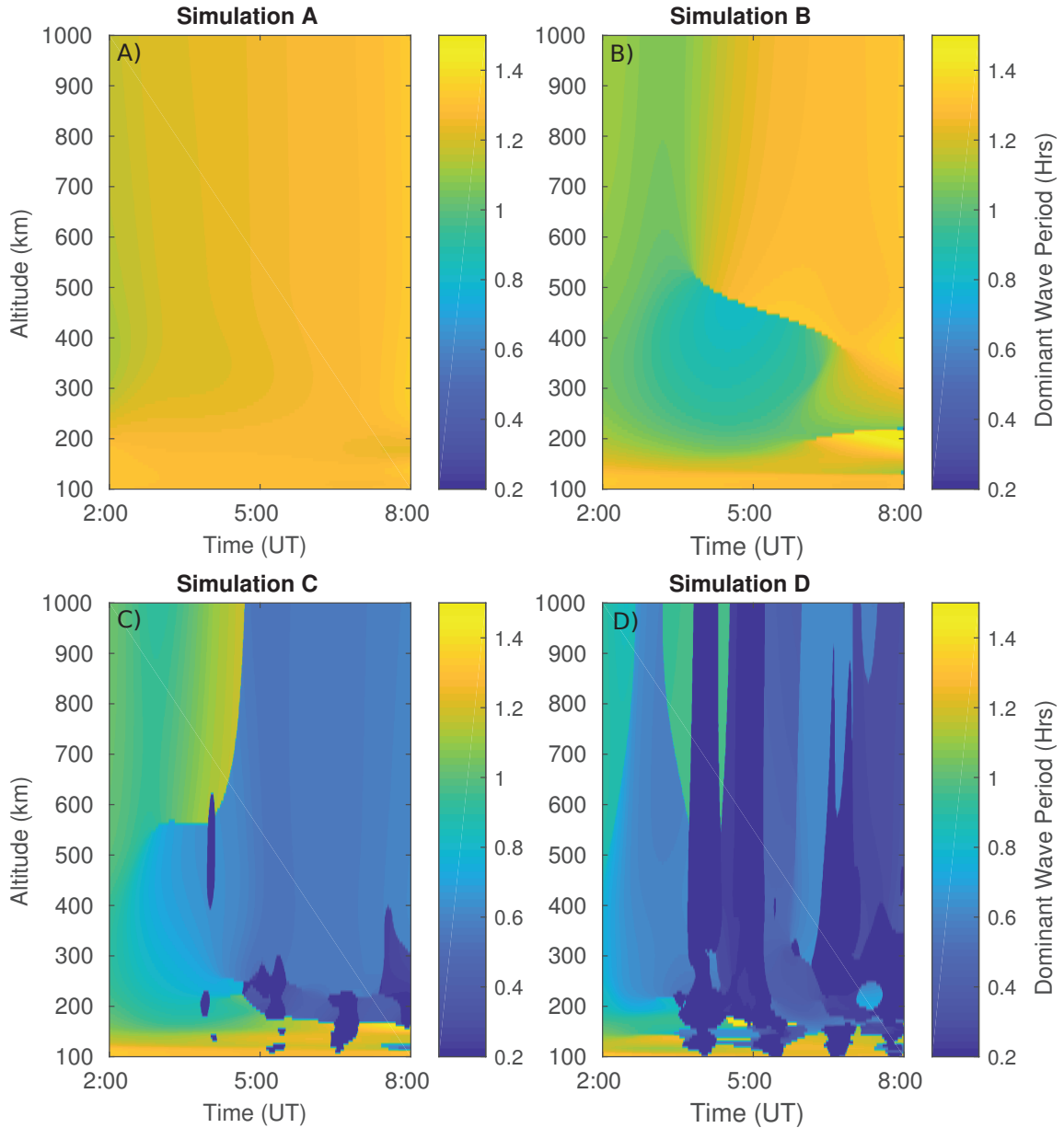


Figure 5.5: The results of a Morelet wavelet analysis on the field-aligned  $O^+$  velocity and selecting the period that contains the most power at every altitude and time step illustrates the transition between a simple GW/TID with minimal nonlinear effects and no wave breaking (panel A), to situations where there is predominantly momentum transference (panel B), to a combination of momentum deposition and wave breaking (panel C), to the other extreme where there is primarily wave breaking (panel D).

readily at altitudes below 250 km, where viscous effects are not too strong. Times of strong wave breaking dominate the wave power and resulting ion response (panel D) in Simulation D throughout all altitudes as indicated by many abrupt transitions to very short periods in panel D.

Ion motions are driven by GWs through a series of interconnected processes and may result in upflow above the F region peak. This is illustrated in Figure 5.6, which has background conditions from a control simulation subtracted from the simulation results to isolate the GW driven responses. This background subtraction also has the added benefit of removing the effects of changing solar zenith angle on photoionization rates. From GW driven ion-neutral drag, electron density modulations (panels 1A-1D) alter the electron temperature (panels 2A-2D) largely by controlling the relative amounts of photoionization heating and collisional cooling. In general, at low altitudes (<250 km) the electron temperature modulation is due to density perturbations. At higher altitudes (>250 km) electron temperature variations are due to the quick transport of heat (i.e. thermal conduction) along the field lines. These higher altitude electron temperature variations then modulate the ambipolar electric field driving ionospheric upflow and downflow (panels 3A-3D) above the regions directly modified by the gravity wave.

Ion densities are controlled by the interplay between the production, loss, and inflow transport processes that are described by the continuity equation

$$\frac{\partial \rho_s}{\partial t} = \underbrace{-\nabla \cdot (\rho_s \mathbf{v}_s)}_{\text{Inflow}} + \underbrace{m_s P_s}_{\text{Production}} \underbrace{-L_s \rho_s}_{\text{Loss}} \quad (5.3)$$

where  $\rho_s$  is the ion mass density,  $\mathbf{v}_s$  is the velocity,  $m_s$  is the ion mass for species  $s$ .  $P_s$  is the species volumetric production rate ( $\text{m}^{-3}\text{s}^{-1}$ ) and includes ion creation from chemical production, photoionization, and impact ionization while  $L_s$  is a loss frequency term ( $\text{s}^{-1}$ ) encompassing chemical loss processes. Inflow transport is directly influenced by the ion-neutral drag motions.

The inflow transport, production, and loss terms from Equation 5.3 for  $\text{O}^+$  are each integrated over 200-225 km altitudes (Figure 5.7, panel b) and 300-325 km (panel a), and across the horizontal span of the ionospheric grid. Hence we are

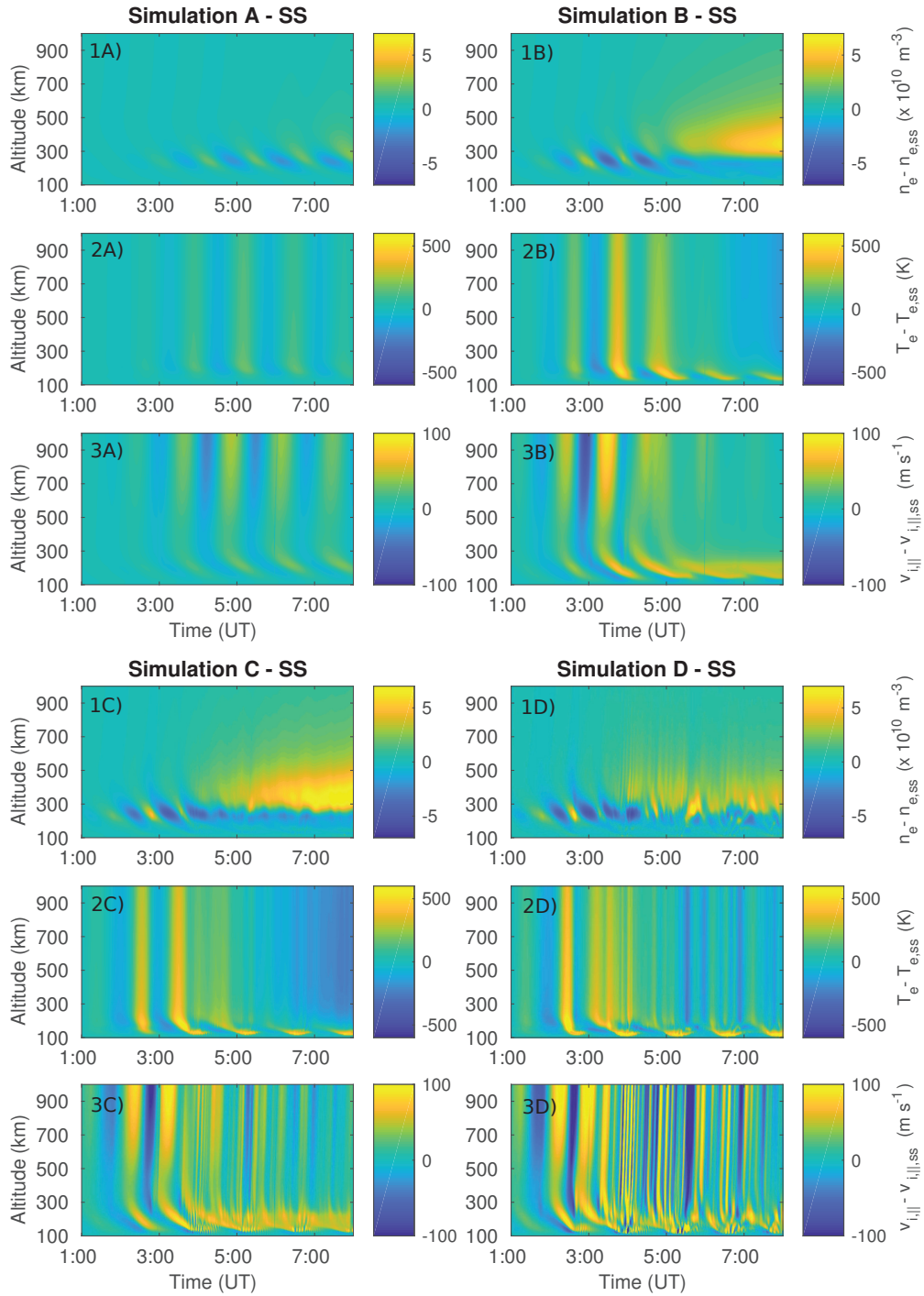


Figure 5.6: A no-GW, control simulation has been subtracted from the four Simulations: A, B, C, and D, to isolate the GW driven effects. The electron density difference, electron temperature difference, and the field-aligned ion velocity difference for each simulation are presented in descending order.

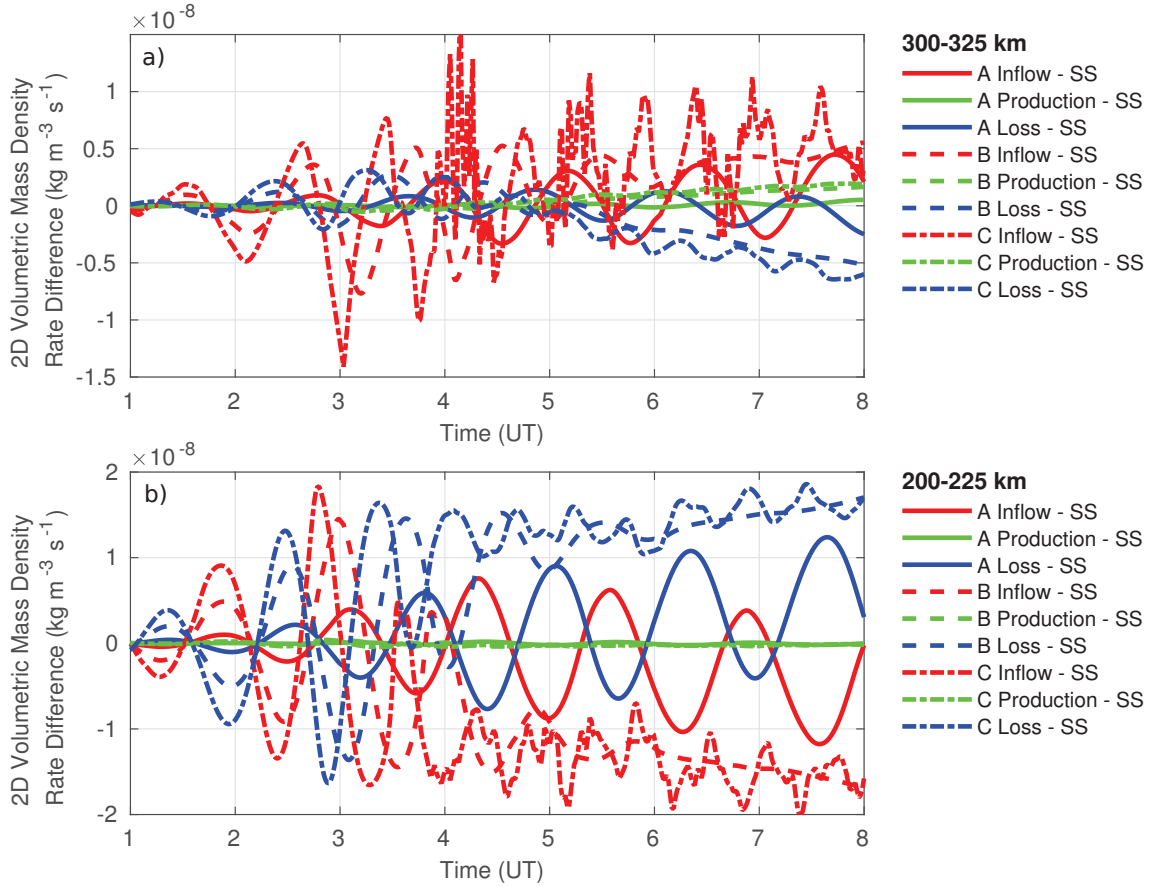


Figure 5.7: A comparison of the production, loss, and inflow transport terms, for  $O^+$ , integrated over 25 km altitude ranges from 300-325 km (panel a) and 200-225 km (panel b) across the span of the model grid to encompass latitudinal differences. The results from the no-GW control simulation (SS) has been subtracted to isolate the GW driven changes. Simulation D has been left out of this Figure due to the excessive breaking rendering it illegible.

able to decompose the relative effects of transport vs. chemical loss vs. production variation in producing the GW-driven plasma density fluctuations that dominate the ionospheric response in these two distinct altitude regions. In this analysis the results from the control simulation have been subtracted to isolate wave-driven parts of the responses.

In the lower altitudinal region (panel b), for Simulations B (red dash line) and C (red dot-dash line), the GW motions have generated significant upflow, which results in outflow from this region (characterized by negative inflow). This depletes the local

density and reduces chemistry loss processes for Simulations B (blue dash line) and C (blue dot-dash line). Simulation A, corresponding to a linear GW, contains quite idealistic perturbations in both inflow transport (panel b, red solid line) and loss (panel b, blue solid line).

At higher altitudes, 300-325 km (panel a), GW motions drive an increase in inflow transport from 4:00 UT onwards through the end of the simulation, for Simulations B (red dash line) and C (red dot-dash line). This increases the local density, and the rate of chemistry loss processes in response to the increase in density, for both Simulations B (blue dash line) and C (blue dot-dash line). This behavior is opposite from what was observed in the 200-225 km altitude range (panel b). The GW increase in mean flow from ~4:00 UT onwards is directly responsible for the  $O^+$  density increases seen within Simulations B and C, and the lack of a similar density increase in Simulation D which contains more wave breaking and Simulation A which isn't strong enough to generate this effect (see Figure 5.6, panels 1A-1D).

As the gravity wave modulates the neutral and ion densities, the electron collisional cooling (Figure 5.8 panels 1A-1D, for Simulations A-D respectively) and the photoionization heating rates (panels 2A-2D) are also directly altered. Background conditions from a control simulation have been subtracted from the simulations in Figure 5.8 to isolate the GW impacts. These effects are strongest at altitudes between 150 and 200 km where the neutral atmosphere density perturbations have the greatest impact. Density increases at F-region altitudes give the plasma a larger effective heat capacity yielding a smaller temperature response to the fixed photoionization input (manifesting as cooler electron temperatures in the latter portion of Simulations B and C). These periods of reduced/increased heating quickly conduct up the magnetic field lines and contribute significantly to the electron temperature variations in the topside ionosphere.

The total effect of the combined photoionization heating rate and electron collisions cooling rate (panels 3A-3D) drives the electron temperature response. The total effect ranges from -5 to 9 K/s in Simulation A with the minimum and maximum occurring at 6:50 and 7:10 UT respectively at 230 km. The GW modulating this simulation continues undisturbed over time due to the lack of wave breaking and



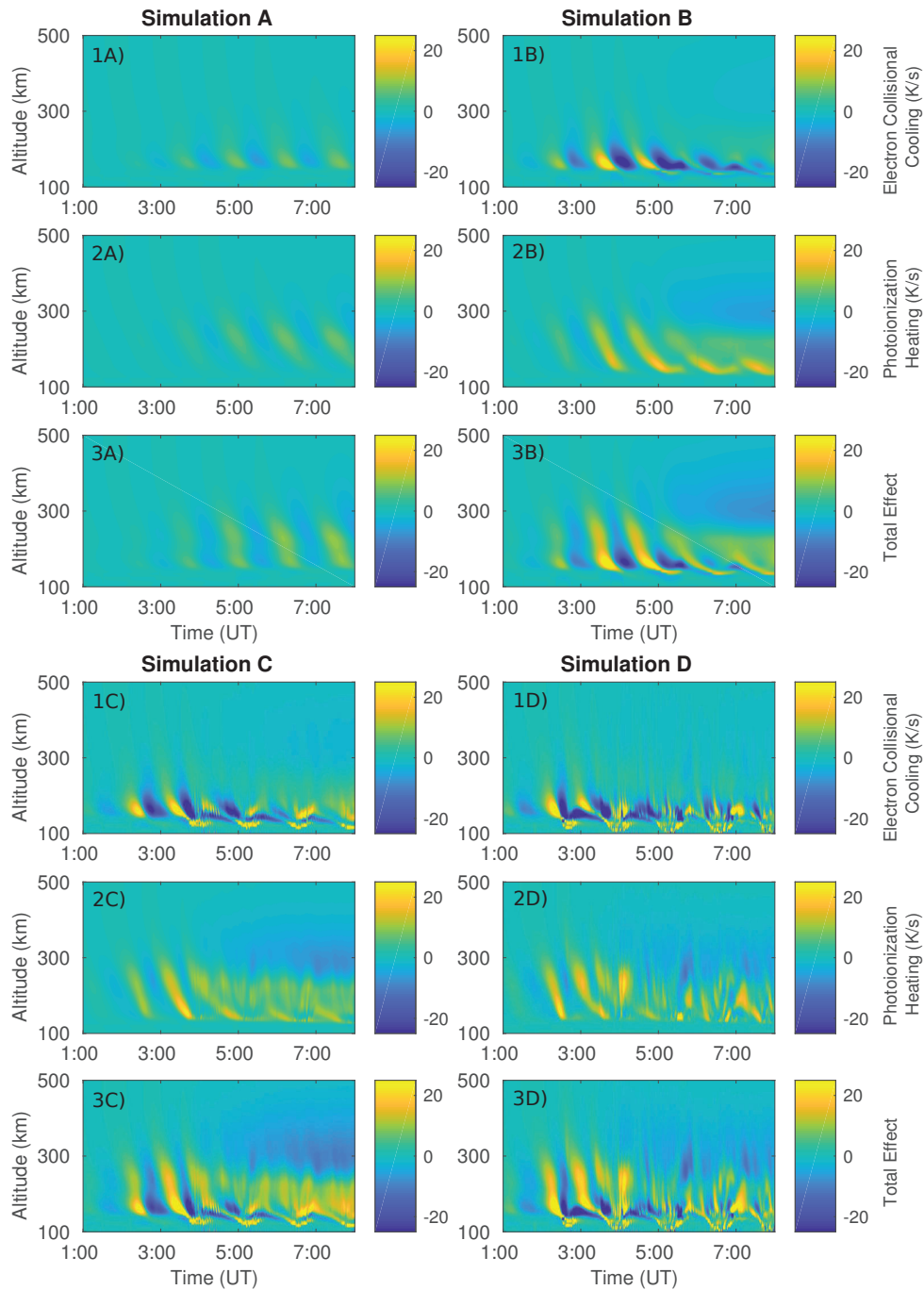


Figure 5.8: The GW modulated electron cooling rate due to ionospheric and atmospheric collisions/interactions (panels 1A-1D), the GW modulated photoionization heating rate (panels 2A-2D), and the total effect of these two processes (panels 3A-3D) have the background conditions from a control simulation subtracted off to isolate the GW effects.

nonlinear effects. From Simulations B the heating difference ranges from -26 to 34 K/s with the minimum and maximum occurring at 4:12 and 3:45 UT respectively at 156 km. The minimum occurs half a wave period after the maximum and before the momentum transfer alters the wave dynamics (see Figure 5.5 for discussion). In Simulations C the heating difference ranges from -56 to 45 K/s with the minimum and maximum occurring at 3:46 and 3:33 UT respectively at 156 km. The time shift between Simulation B and Simulation C in reaching the minimum and maximum heating rate differences is due to the self acceleration generated by the wave dynamics which alter the period of the wave. Wave breaking effects do create brief periods of comparable heating, especially near the GW forcing region in Simulation C. In panel 3C, the total heating effect of Simulation C, centered around 300 km from 5:00 UT onwards, has net cooling which is responsible for the cooling of electron temperature (Figure 5.6, panel 3C) in response to the increase in density (Figure 5.6, panel 2C) driven by the mean flow increase within the GW (Figure 5.6, panel 1C). The strongest upflow of this simulation occurs just before wave breaking which is when the maximum heating occurs as well. The heating difference ranges from -44 to 51 K/s in Simulation D with the minimum and maximum, not considering lower altitude wave breaking effects, occurring at 2:36 and 2:26 UT respectively at 156 km. The time separation between the minimum and maximum total heating effects is less than half of a wave period because of the onset of wave breaking. The wave breaking in this simulation also drives periods of short,  $\sim 5$  minute or less, intense heating near or within the forcing region (e.g. 200 K/s at 3:54 UT at 110 km).

With the electron temperature increases rapidly conducting up the field lines, heating and expanding the local population at higher altitudes, the ambipolar electric field drives an ion response well outside the region where direct, collisions ion-neutral coupling is significant. The  $O^+$  flux at 1000 km, shown in Figure 5.9, panel a, reaches a maximum of  $1.3 \times 10^{12} \text{ m}^{-2}\text{s}^{-1}$  at 7:32 UT in Simulation A,  $1.5 \times 10^{12} \text{ m}^{-2}\text{s}^{-1}$  at 3:33 UT in Simulation B,  $1.9 \times 10^{12} \text{ m}^{-2}\text{s}^{-1}$  at 6:43 UT in Simulation C, and  $5.2 \times 10^{12} \text{ m}^{-2}\text{s}^{-1}$  at 4:10 UT in Simulation D. The wave breaking in Simulation D around 4:00 UT drives the largest  $O^+$  flux (panel a) and also limits the total  $O^+$  transported upwards through this location (panel b).

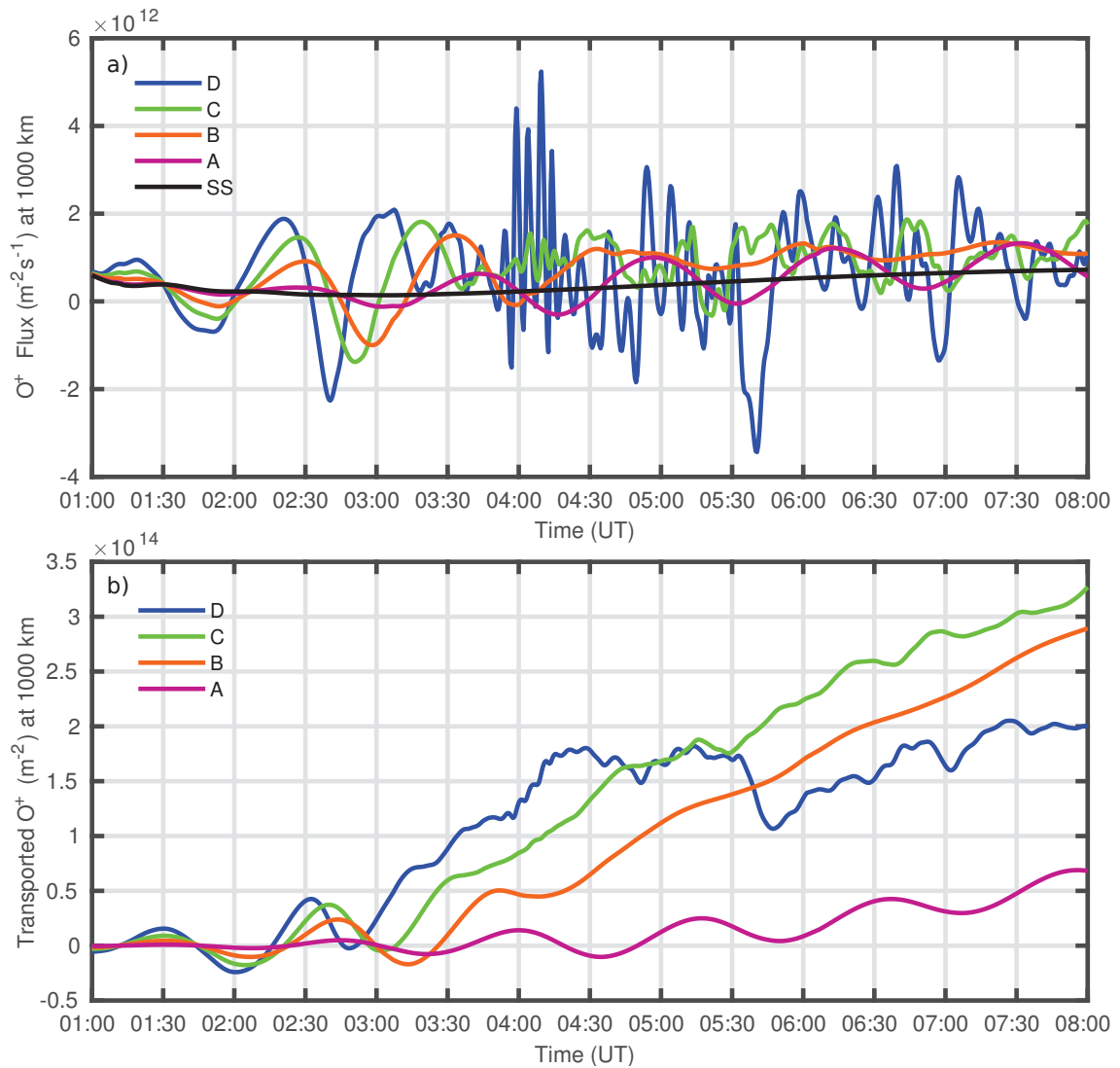


Figure 5.9: The  $O^+$  flux from Simulations A-D at 1000 km (panel a) and total number of  $O^+$  particles transported (panel b) through this location on the center field line of the ionospheric model grid from 1:00 to 8:00 UT. The control simulation, labeled with SS, has been included (black line) for comparison in panel a and subtracted from the Simulations in panel b.

Integrating the  $O^+$  flux in panel a calculates the total number of particles passing, per square meter, through the center field line of the ionospheric model grid at 1000 km and is one way of quantifying of the effectiveness of the GW to generate ion upflow. The control simulation transported  $O^+$  has been subtracted from the transported  $O^+$

in Simulations A-D (panel b) to highlight GW driven effects. By the end of Simulation A the total number of particles transported was  $5.0 \times 10^{14}$  particles/m<sup>2</sup>, Simulation B had  $7.2 \times 10^{14}$  particles/m<sup>2</sup>, Simulation C had  $7.6 \times 10^{14}$  particles/m<sup>2</sup>, Simulation D had  $6.3 \times 10^{14}$  particles/m<sup>2</sup>, and the control simulation had  $4.3 \times 10^{14}$  particles/m<sup>2</sup>. The relative coherence of the GW also affects the transport efficiency. When the GW contains excessive breaking the pulses of upflow and downflow are large but combined have a smaller net response than a smaller but more consistent upflow, i.e. excessive breaking in Simulation D vs. weaker but more consistent upflow in Simulation C (or B).

This topside transport is enough to alter the ion populations available for secondary acceleration processes, such as transverse wave heating, that can lead to outflow into the magnetosphere. Wave heating has been added at 7:30 UT for 5 minutes to the GWs driving Simulations C and D, in two additional simulations denoted Simulation C<sub>W</sub> and Simulation D<sub>W</sub> (see Figure 5.10, dashed lines evident from 7:30 onwards). In a third new simulation, denoted by SS<sub>W</sub>, the control simulation also has wave heating applied at the same UT for additional comparison. The wave heating is accomplished through the use of the resonant heating term,  $\dot{W}_{s,\perp}$ , included in the perpendicular energy equation within the model that encompasses the acceleration of ions by transverse plasma waves (*Burleigh and Zettergren, 2017*). This gyroresonant (cyclotron) energy transfer is the most efficient in regions of low ion-neutral collision rates and is therefore not very effective below 500 km except in extreme cases (e.g. *Whalen et al., 1978*). The present form of the model (*Burleigh and Zettergren (2017)*) uses an empirical specification of this heating term:

$$\dot{W}_{s,\perp}(\omega) = 2m_s n_s \left( \frac{\eta q_s^2}{4m_s^2} \right) |E_o|^2 \left( \frac{\omega}{\omega_o} \right)^{-\alpha} \quad (5.4)$$

where  $\omega$  is the local gyrofrequency for each ion,  $\eta$  is the fraction of the wave field which is left-hand polarized, assumed to be 0.125 (*Chang et al., 1986*),  $\alpha$  is the spectral power index, assumed to be 1.7 (*Crew et al., 1990*), and  $|E_o|^2$  is the wave power spectral density set here to be 0.3 (mV/m)<sup>2</sup>/Hz with the reference frequency  $\omega_o$  assumed to be 6.5 Hz (*Zeng and Horwitz, 2008; Zeng et al., 2006; Retterer et al.,*

1983). This type of heating occurs primarily in collisionless regions, the resulting ion distributions remain highly anisotropic and are accelerated by the mirror force, attaining large field aligned velocities high above the heating region.

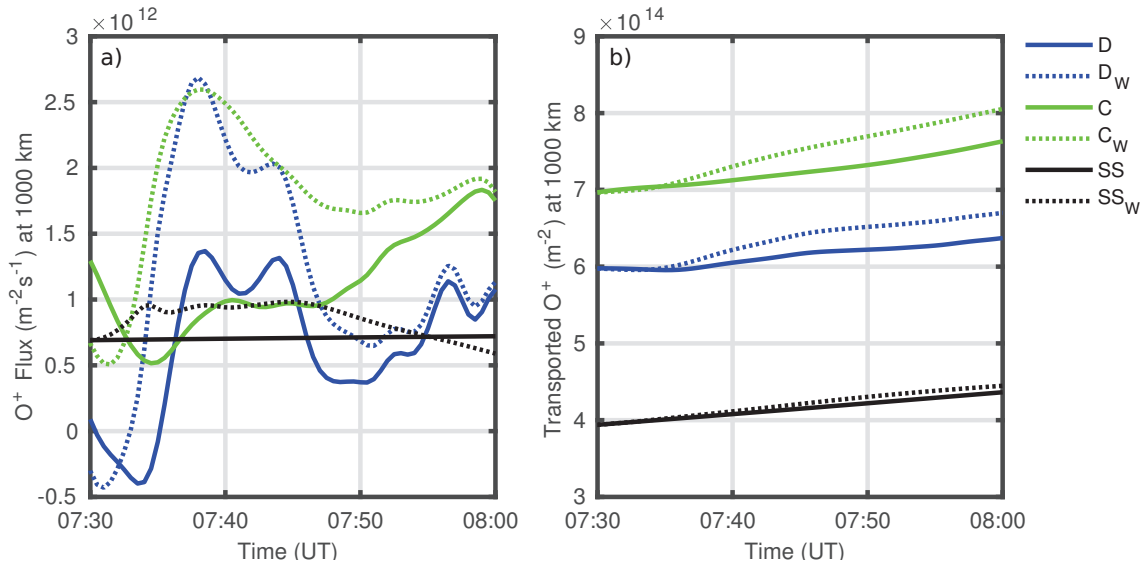


Figure 5.10: Transverse wave heating has been added at 7:30 UT, for a duration of 5 minutes, to the GWs driving Simulations C and D and the no-wave control simulation. The O<sup>+</sup> flux (panel a) and total number of O<sup>+</sup> particles transported (panel b) along the center field line of the model grid at 1000 km. In these panels the dashed lines are the new simulations that contain 5 minutes of transverse wave heating.

The applied transverse wave heating (Figure 5.10) results in the O<sup>+</sup> flux to a peak effect 8 minutes after onset (panel a), note that the wave heating was only applied from 7:30-7:35 UT. The total number of particles transported through 1000km on the center field line of the model grid is shown in panel b. The addition of transverse wave heating raises the flux at 7:38 UT from  $8.5 \times 10^{11}$  in Simulation C (green solid line) to  $2.6 \times 10^{12} \text{ m}^{-2}\text{s}^{-1}$  in Simulation C<sub>W</sub> (green dashed line) and from  $1.3 \times 10^{12}$  in Simulation D (blue solid line) to  $2.7 \times 10^{12} \text{ m}^{-2}\text{s}^{-1}$  in Simulation D<sub>W</sub> (blue dashed line). This is a percent increase of 206% and 107% respectively. For further comparison the wave heating has also been applied to the no-wave control simulation (black solid line) and only raises the O<sup>+</sup> flux from  $7.0 \times 10^{11}$  in Simulation SS to  $9.5 \times 10^{11} \text{ m}^{-2}\text{s}^{-1}$  in Simulation SS<sub>W</sub> (black dotted line) at 7:38 UT. This is a much smaller percent increase of only 35%. Ionospheric modulation by thermospheric

GWs can significantly drive ion upflow and impact the ion populations available for outflow to the magnetosphere.

## 5.4 Chapter conclusions

Four simulations have been presented here to show how the high-latitude ionosphere can be modified by the presence of large scale GWs, with particular focus on ionospheric plasma transport throughout the F-region and topside. Neutral velocity perturbations modulate the ion density as the gravity wave forcing progresses over time. These ion density modulations alter the electron collisional cooling rate as well as the photoionization heating rate. Combined, the net effect of these density dependent processes result in periods of elevated or decreased electron temperatures. These temperature variations conduct up geomagnetic field lines altering plasma populations at altitudes well above the GW coupling region and through the ambipolar electric field drive an ion response as well. The result of this chain of processes is an ion upflow/downflow response at higher altitudes, altering the populations available for secondary acceleration processes that lead to outflow into the magnetosphere.

Along the center field line of the simulation at 1000km, the  $O^+$  flux reaches a maximum of  $1.3 \times 10^{12} \text{ m}^{-2}\text{s}^{-1}$  at 7:32 UT in Simulation A,  $1.5 \times 10^{12} \text{ m}^{-2}\text{s}^{-1}$  at 3:33 UT in Simulation B,  $1.9 \times 10^{12} \text{ m}^{-2}\text{s}^{-1}$  at 6:43 UT in Simulation C, and  $5.2 \times 10^{12} \text{ m}^{-2}\text{s}^{-1}$  at 4:10 UT in Simulation D at 1000 km. The maximum upflow often occurs just before wave breaking which causes wave power to be transferred to smaller scale wave modes and out of the primary wave, except in the case of Simulation D where the wave breaking is strong enough to drive an even larger  $O^+$  flux.

The spatial and temporal structure of the GW plays a critical role in the ion upflow response. Fine scale ion motions that result from wave breaking and the mean flow increases from momentum transfer effects in the atmospheric model modulate ion upflow in the topside when compared to a simple GW (such as Simulation A). These GW effects are a natural result of increasing the forcing strength of the GW. The presence of viscous damping, which is the dissipation of gravity waves by molecular viscosity and thermal conductivity in the thermosphere, and nonlinearity (highly

evident in Simulations B and C) acts to deposit momentum into the mean flow and with the directional orientation of the waves used in this study this results in an increase in the neutral field aligned velocity. This neutral effect is transferred to the ions as well through ion-neutral drag and increases ion densities above 300 km after ~4:00 UT for Simulations B and C. This density change impacts the total effect of the heating/cooling rates. Wave breaking is another nonlinear gravity wave process that affects the ion response (highly evident in Simulation D and clearly present in Simulation C). More energy is deposited into small scale wave modes generated by GW breaking; the larger the amplitude of the GW, the quicker and stronger wave breaking occurs. It can generate periods of large field aligned  $O^+$  velocities, such as 240 m/s at 1000km in Simulation D. While this is not at escape speeds, this generates an environment ready for secondary acceleration mechanisms than could produce outflow to the magnetosphere.

This topside transport alters the ion populations available for secondary acceleration processes, such as transverse wave heating, that can lead to outflow into the magnetosphere. Wave heating has been added at 7:30 UT, for a duration of 5 minutes, to the GWs driving Simulations C and D and increases the  $O^+$  flux during this time by 206% and 107% respectively. For a baseline comparison the wave heating has also been applied to the control simulation and only raises the  $O^+$  flux from  $7.0 \times 10^{11}$  to  $9.5 \times 10^{11} \text{ m}^{-2}\text{s}^{-1}$ . A percent increase of only 35%. The modulation of the ionosphere by the GW significantly affects the response to secondary acceleration mechanisms such as this transverse wave heating by BBELF waves.

While the ISR data from Sondrestrom provided inspiration for the wave parameters used in this study, the data are 1D in space (along the geomagnetic field line), evolving in time. A phased array, or a scanning mode of the Sondrestrom ISR, has the potential to capture the multidimensional relationships of a GW event and would assist in source determination. Future work may include looking through additional ISR databases for to find more GW events; 4 very strong neutral wind events were found in the solar cycle 23 search of Sondrestrom's data that yielded the event motivating this study. The commonality of this type of high-latitude, atmosphere-ionosphere interaction can be commented on in future studies.

## Chapter 6

# Transient forcing of ion outflow

The most commonly observed processes contributing to ionospheric upflow and outflow are DC electric fields, soft electron precipitation, and gyro-resonant wave heating. Strong DC electric fields frictionally heat the ion population resulting in anisotropic increases in ion temperature (*St-Maurice and Schunk, 1979*) that cause large pressure gradients which push the ions outward and upward (*Keating et al., 1990; Wahlund et al., 1992; Foster et al., 1998; Zettergren and Semeter, 2012*). Soft electron precipitation heats F-region electrons creating electron pressure gradients which increase the ambipolar electric field, driving ion upflows (*Wahlund et al., 1992; Liu et al., 1995; Foster and Lester, 1996; Ogawa et al., 2000*). Velocity shears can also drive ion heating and upflow through lowering the threshold for field-aligned current-driven instabilities to excite ion cyclotron waves at lower altitudes (*Nishikawa et al., 1990; Ganguli et al., 1994; Liu and Lu, 2004; Semeter et al., 2003*). Upflowing ions may then undergo further acceleration from transverse wave heating by broadband ELF waves (*Whalen et al., 1991; Kintner et al., 1996; Andre et al., 1998; Moore et al., 1999*). At high altitudes, the mirror force can propel ions to escape velocities, resulting in outflow to the magnetosphere (*Moore, 1991*). Despite these processes being generally well-known (*Yoshida et al., 1999; Strangeway et al., 2005; Lynch et al., 2007; Ogawa et al., 2008*), ion outflow remains difficult to predict due to myriad processes acting over a large range of altitudes, physical regimes, and time scales.



The duration of energization regions play an intrinsic role in the generation ionospheric upflow and outflow. Brief periods of energization may lead to upflow and then downflow but not outflow. Lengthy periods of energization may support extensive upflow and outflow until the local region becomes depleted. The variable dwell time of ionospheric plasma within the energization region (*viz.* moving aurora) is an important consideration when examining the amount of ion outflow to the magnetosphere that can be produced. The time history of these energy inputs are also an important consideration (*i.e.* heating that has occurred prior to an event alters the “background state” that is acted upon). Variations in timing and spatial configuration of energy sources are capable of greatly impacting ion upflow and outflow. Realistic case studies are needed to further assess the impacts this variability has on the ionosphere. The data from the ISINGLASS sounding rocket campaign is used here to provide realistic constraints and inputs for modeling efforts. This campaign utilizes a combination of ground based data (*e.g.* ISR, all-sky imagers, *etc.*) and in-situ measurements from the sounding rocket. GEMINI-TIA is well suited to ingest these measurement and is used here to examine how the inclusion of realistic temporal and spatial variability regulate the resulting ion upflow and outflow.

## 6.1 Overview of ISINGLASS B

The ISINGLASS auroral sounding rocket mission was launched from Poker Flat Rocket Range (PFRR) in Alaska during the winter of 2017. This mission consisted of two multi-payload sounding rockets launched on separate days over an array of ground-based instruments including radars and all-sky cameras. The second rocket, ISINGLASS B, is used for this study. Launched on March, 2 from PFRR at 7:50 UT, the flight lasted ~10 minutes and the rocket reached an apogee of ~360 km.

The conditions that prompted the call to launch ISINGLASS B developed over the course of an hour. The Deep Space Climate Observatory (DSCOVR), located at the L1 Lagrange point, 1.5 million km upwind of the Earth towards the sun, provides measurements of the solar wind and allows for up to an hour advance warning of the arrival of space weather events. From 6:10 UT onwards, DSCOVR observed a

primarily southward IMF. At 6:55 UT the IMF turned northward.

The solar wind IMF change propagated to the dayside magnetopause and resulted in changes in reconnection which, through magnetospheric convection, impacts the nightside region reconnection resulting in depolarization. The Geostationary Operational Environmental Satellite system (GOES) magnetometer, in geostationary orbit 6,000 km above the Earth on the nightside, measured dipolarization 54 minutes after DSCOVR observed the IMF change. The ground based Poker Flat magnetometer measured the -400nT substorm at this time as well.

Substorms are initiated by changes in the solar wind IMF which creates favorable configurations for reconnection. This enhances the energy transfer from the solar wind to the magnetosphere (growth phase) where it is temporarily stored in the magnetotail. This energy is released suddenly in the form of massive electrical currents composed of energetic precipitating electrons (expansion phase). The beginning of the expansion phase is marked by an intensification of the aurora, a distortion of auroral forms, and the magnetotail becomes more dipolar (GOES panel in Figure 6.1 shows the dipolarization). The sudden brightening and equatorward surge of the aurora has been observed by the Venetie all-sky camera. The rocket was launched during the substorm expansion, just after the intensification and distortion of the auroral forms.

The main payload of ISINGLASS B included the energetic electron instrument Acute Precipitating Electron Spectrometer (APES) (*Michell et al.*, 2016), a scientific magnetometer, a retarding potential analyzer sensor Petite Ion Probe (PIP) (*Fisher et al.*, 2016) and a thermal electron plasma sensor Electron Retarding Potential Analyzer (ERPA) (*Cohen et al.*, 2016). Multi-point measurements were also made using PIPs carried by 4 sub-payloads known as Bobs (*Roberts et al.*, 2017a,b) which get ejected from the main payload. Each Bob contained 2 PIP sensors, an LED beacon package, and a crossed-dipole antenna for transmission of data back to the main payload.

Throughout the rocket campaign there were complementary ground based observations. The Poker Flat Incoherent Scatter Radar (PFISR) was running in a 15 beam pattern, with elevations ranging from 38-70°, that used a long pulse beam code.

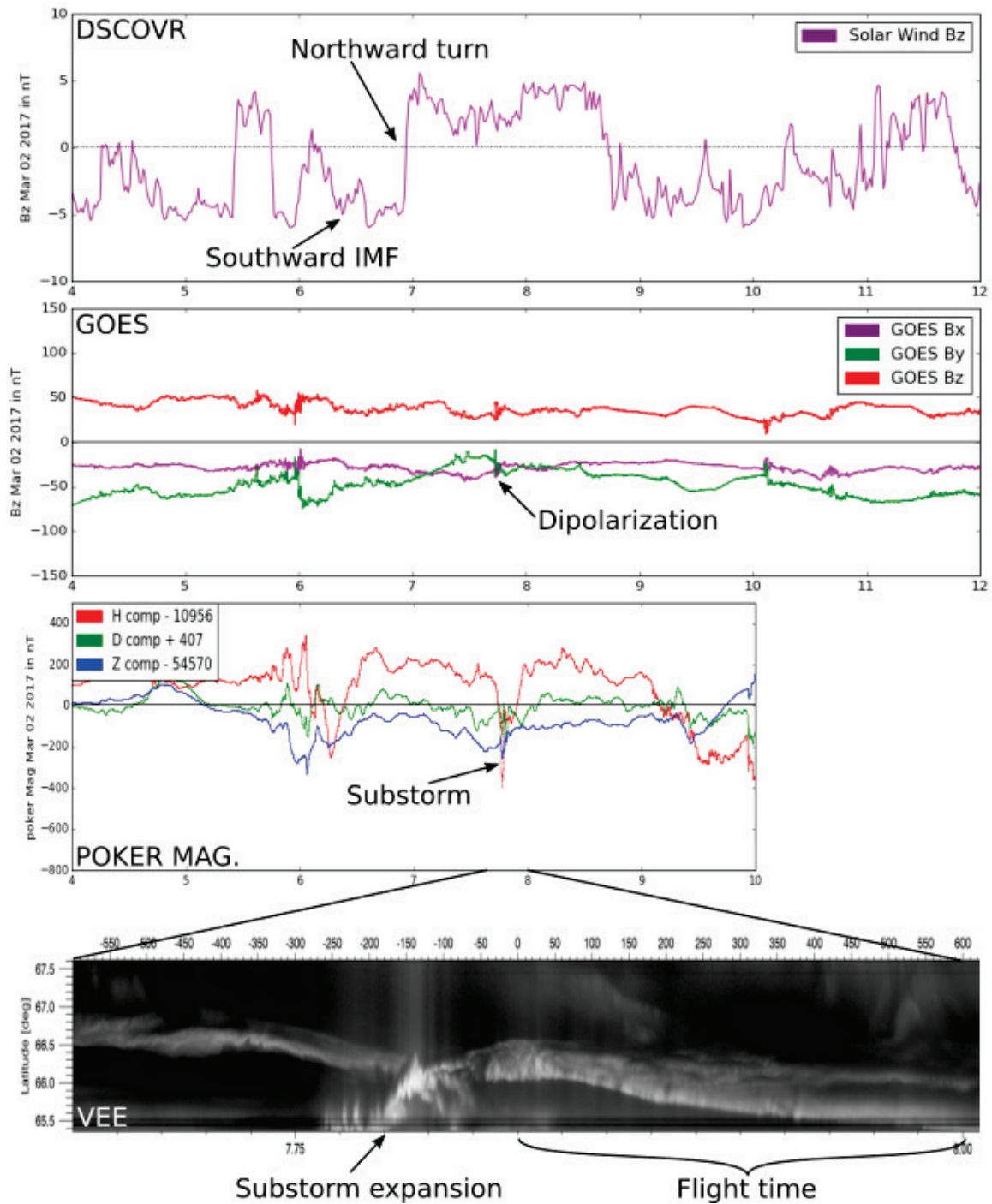


Figure 6.1: The space weather conditions observed by DCSOVR, GOES, and Poker Flat that prompted the call for launch. ISINGLASS B launched during the substorm expansion, just after the intensification and distortion of the auroral forms.

PFISR technology allows the ISR beam to be steered on a pulse-to-pulse basis with a phased array technique (*Heinselman and Nicolls, 2008*). This provides high-resolution measurements in multiple directions quickly without the need to physically steer a large dish. The measurements from this campaign have been processed at two minute integration times.

Several All-Sky Cameras (ASC) were also working throughout the campaign. Three sites, Poker Flat Optics (PKR), Venetie (VEE), and Coldfoot (COLD), captured beautiful imagery. Unfortunately the Toolik Research Station (TOO) was cloudy during the ISINGLASS B flight. PKR used an ICCD-based video system recording at 59.94 frames per seconds. VEE used a Sony A7S II camera with a frame rate of 29.97 frames per second. This camera provides high resolution (temporal and spatial) imagery of the aurora near the magnetic zenith region of the rocket trajectory and the beacons on board the BOBs. COLD also used a Sony A7SII camera with the same frame rate. Similar to VEE, this camera was also used to observe the aurora sampled by the rocket and track the BOBs on descent.

All-sky camera snapshots from 154 to 264 seconds after launch, at 10 s intervals, from VEE are shown in Figure 6.2. The rocket trajectory (blue line) is mapped to the image to show where it crosses the auroral arc. Red arrows are PFISR flow measurements while the yellow arrows are sequential in situ rocket measurements. Dark gray protrusions extending from the bottom left are trees within the camera field of view. As the rocket traverses the arc, note how the directionality of the plasma flow evolves. As suggested by *Marklund (1984)*, the  $E \times B$  drift direction is approximately tangential to the arc boundary when the rocket is within the arc. Outside of the arc the flow direction is parallel to the arc boundary. When comparing these rocket and PFISR measurements, there is general agreement but the resolution of PFISR hinders determining the arc boundary that the rocket detects clearly.

## 6.2 Ionospheric response to transient forcing

GEMINI-TIA, discussed in detail in Chapter 2, is used here to explore how the timing and spatial configuration of both in situ and ground based measurements of

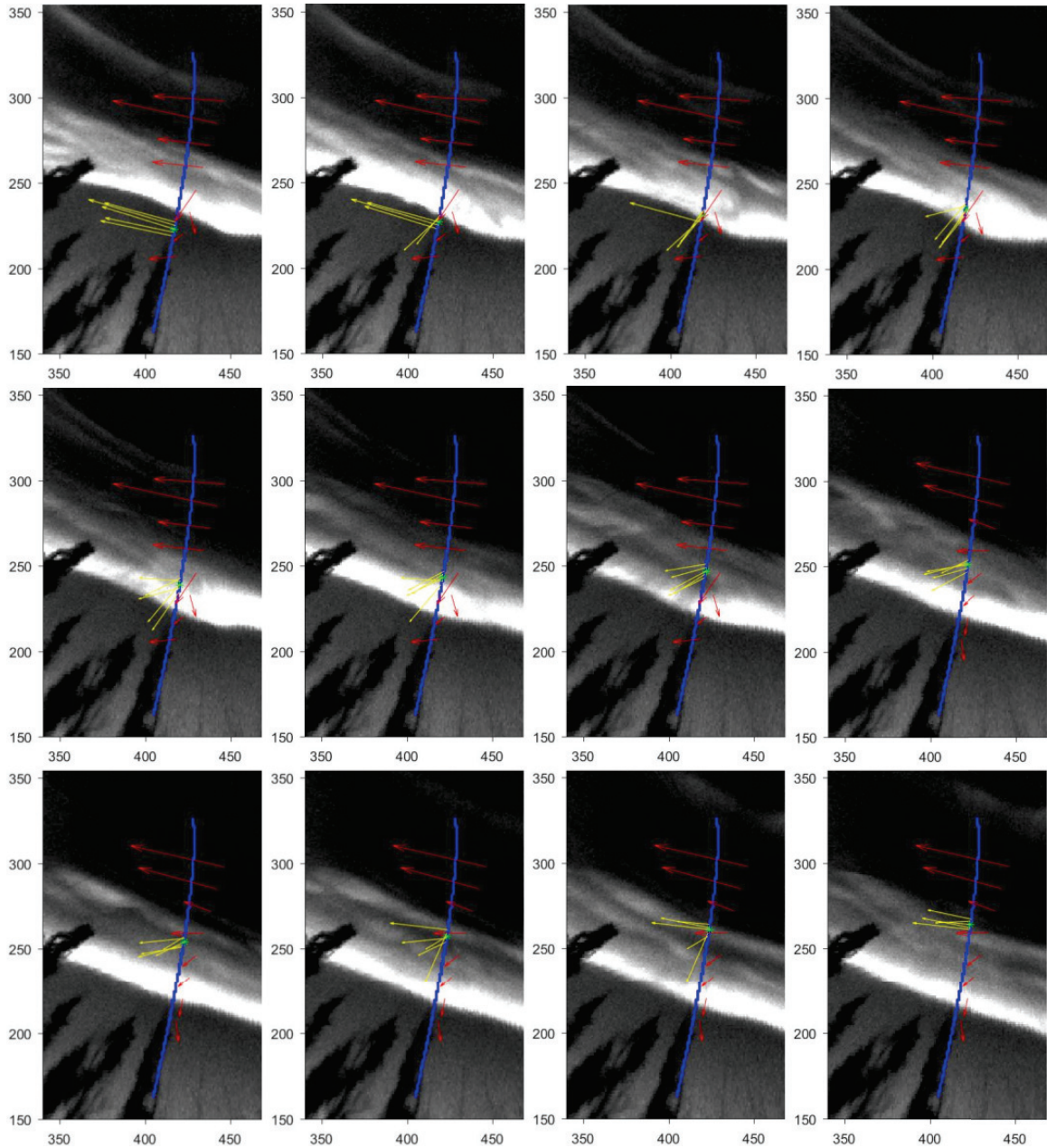


Figure 6.2: The rocket trajectory (blue line) overlaying the bright white auroral arc from 154 to 264 seconds after launch, at 10 s intervals, as observed from VEE. Red arrows are PFISR flow measurements while the yellow arrows are 5 second sequential in situ rocket measurements. Dark gray protrusions extending from the bottom left are trees within the camera field of view. Panels courtesy of Rob Clayton.

DC electric fields, soft electron precipitation, and gyro-resonant wave heating impact ionospheric upflow and outflow. A similar model configuration is used for each simulation conducted as part of this study. The grid spans L shells from 6.2-7.3 and covers altitudes from  $\sim 80$  to  $\sim 12,500$  km. The upper reaches of the ionospheric grid ( $> 2,500$  km) act as a buffer region to avoid boundary effects from impacting the solutions (c.f. *Burleigh and Zettergren, 2017*). The grid cells have a resolution in the E region of roughly  $5 \text{ km} \times 1 \text{ km}$  ( $x_1 \times x_2$ ) and in the topside is roughly  $7 \text{ km} \times 2 \text{ km}$ . Each simulation is run for 10 minutes. Initial conditions are generated by running the model for 24 hrs in a steady state mode to initialize the plasma parameters. Simulations 1-3 utilize the steady state conditions from 7:50 UT as the starting ionospheric state. Simulation 4 uses dynamic initial conditions from 7:50 UT that are generated by starting with the steady state conditions at 7:40 UT and including energy inputs from 7:40 to 7:50 UT. This will illustrate how pre-heating can affect modeled upflow/outflow while preserving the minimal diurnal variation that would naturally exist between these two start times.

Figure 6.3 shows the spatial relationship between the different instruments of the campaign. PFISR ( $\circ$ ) used a set of 15 beams ( $- - - -$ ). The ground DC electric field measurements are calculated from these measurements and are a standard data product. The PKR, VEE, and COLD all-sky camera field of views are not shown. The model grid is outlined in  $\triangle$ . ISINGLASS B's trajectory ( $-$ ) travels through the spatial locations of all of these.

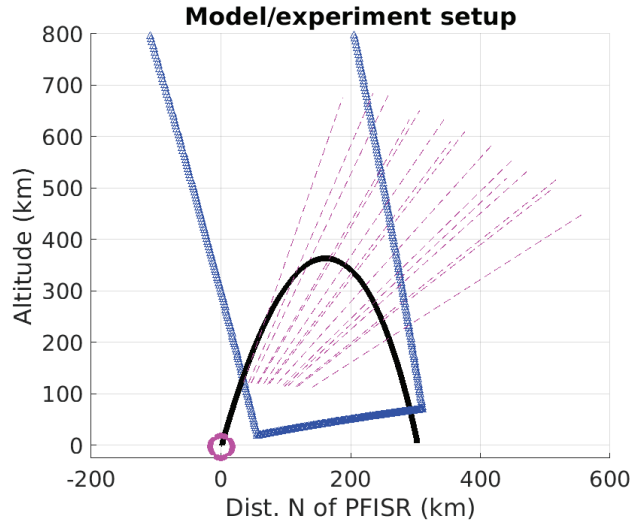


Figure 6.3: The model (outlined in  $\triangle$ ), PFISR (location  $\circ$  and beams  $- - - -$ ), and sounding rocket trajectory ( $-$ ) locations.

Table 6.1: ISINGLASS sounding rocket campaign data used to drive the model for each simulation. Parameters include DC Electric field,  $E_{0,\perp}$  (mV/m), characteristic energy,  $E_c$  (eV), total energy flux  $\Phi_E$  (mW/m<sup>2</sup>), and wave power spectral density,  $|E_0|^2$  ((mV/m)<sup>2</sup>/Hz).

Simulation Drivers - Energy Data Source		Energy Sources
1a	In situ - Temporally variable	$E_{0,\perp}, E_c, \Phi_E,  E_0 ^2$
1b	In situ - Temporally variable	$E_{0,\perp}, E_c, \Phi_E$
2a	In situ - Spatially variable	$E_{0,\perp}, E_c, \Phi_E,  E_0 ^2$
2b	In situ - Spatially variable	$E_{0,\perp}, E_c, \Phi_E$
3	Ground - Spatiotemporally variable	$E_{0,\perp}, E_c, \Phi_E$
4	Ground - Spatiotemporally variable with pre-heating	$E_{0,\perp}, E_c, \Phi_E$

### 6.2.1 In situ driven simulations

Over the course of the flight, rocket measurements relevant to this study include transverse wave heating power spectral density at a reference frequency of 313 Hz, DC electric field (northward), total energy flux, and characteristic energy, shown in Figure 6.4. These measurements (blue line) are at a higher cadence than the model can easily accommodate. The data are interpolated onto the model mesh (green line) and used to drive ionospheric dynamics. This results in the smoothing of large, or rapid, variations in the in situ measurements. The resolution of the model grid used creates a limit on the level of small scale features that can be included in the model.

The power spectral density (PSD) (panel a) determines the amount of wave heating applied in the model. The values measured here are smaller, when compared in the form of the  $\dot{W}_{s,\perp}(\omega)$  term implemented within the perpendicular energy equation, than literature values discussed in Chapter 4 and minimally impact upflow in the F region due to the high collision frequency there (see further discussion in the following paragraphs). The northward DC electric field (DCE) has a sharp gradient at the boundary of the auroral arc, around 66.3° magnetic latitude (panel b). Further north, the DCE increases again until it reaches a peak of ~83 mV/m at 67.4°. Auroral precipitation just northward of the auroral arc boundary is responsible for the peak in total energy flux (panel c) and characteristic energy (panel d).

The primary benefit of in situ measurements is excellent resolution of small scale features and direct measurement of BBLEF waves responsible for gyro-resonant wave

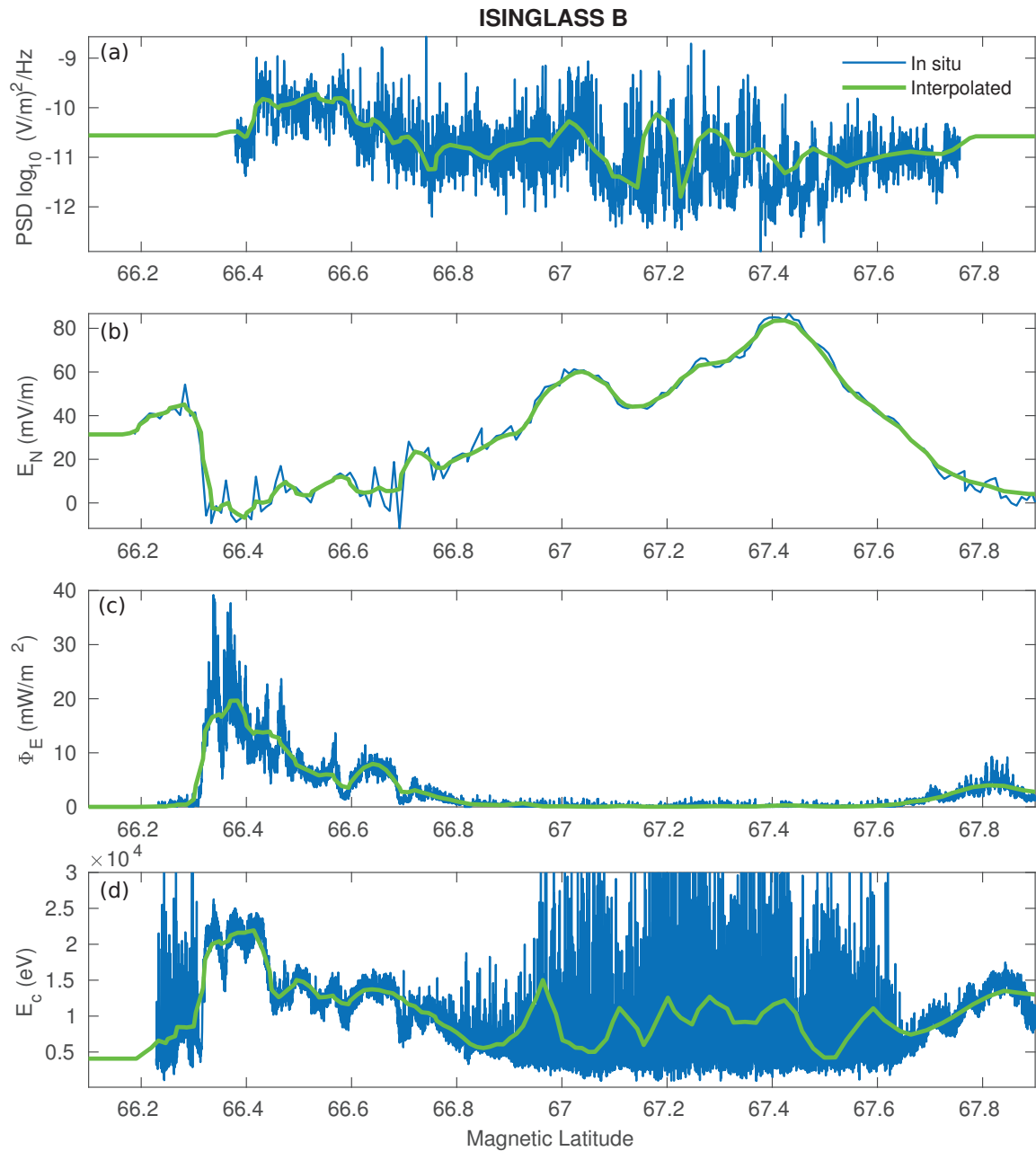


Figure 6.4: ISINGLASS B in situ measurements of the transverse wave heating power spectral density at a reference frequency of 313 Hz, DC electric field (northward), total energy flux, and characteristic energy.



heating; ground measurements of this parameter are not available. The disadvantage is that the rocket only provides a moving point source that traverses space and time (viz. a single, moving "snapshot" value of ionospheric dynamics instead of an active monitoring system).

### **Time variability**

In situ measurements are used here in two separate ways by unwrapping the space and time variability and treating them separately. First, the in situ data is considered to be representative of the temporal evolution of energy sources only; no spatial variability. Limiting the model to a single field line, variations over time of the measured energy sources in Figure 6.4 are used to drive Simulation 1a. This applies the unrealistic but illustrative assumption that the energy sources measured by the rocket last only as long as it took the rocket to fly through them and that they are all acting upon the same parcel of ionospheric plasma. Table 6.1 lists the specific parameters used in Simulation 1a (and 1b).

Note that the rocket measurements do not start at launch, 7:50 UT. By 150 s into the flight there are good measurements as seen in the ionospheric response in Figure 6.5. The auroral precipitation observed by the rocket as it crosses the arc boundary drives a sharp increase in electron temperature (panel d). This corresponds to the increase in E region densities as the impact ionization generates additional ions. The DCE drives significant anisotropies when it reached values greater than  $\sim 75$  mV/m. This is seen best when comparing the parallel (panel b) and perpendicular (panel c) temperatures at 7:57 UT in Figure 6.5. The largest, density averaged, ionospheric upflow (panel 3) of  $\sim 150$  m/s by 500 km is generated from the strong DCE at 7:57 UT. The in situ measured PSD is not large enough to have a significant impact on the ionospheric upflow response at altitudes  $< 500$  km. To illustrate this further an additional simulation (Simulation 1b) has been run with an identical setup to Simulation 1a but without including the PSD. There is a difference of less than 4% in the ionospheric flux generated at 1000km between these two Simulations (not shown).

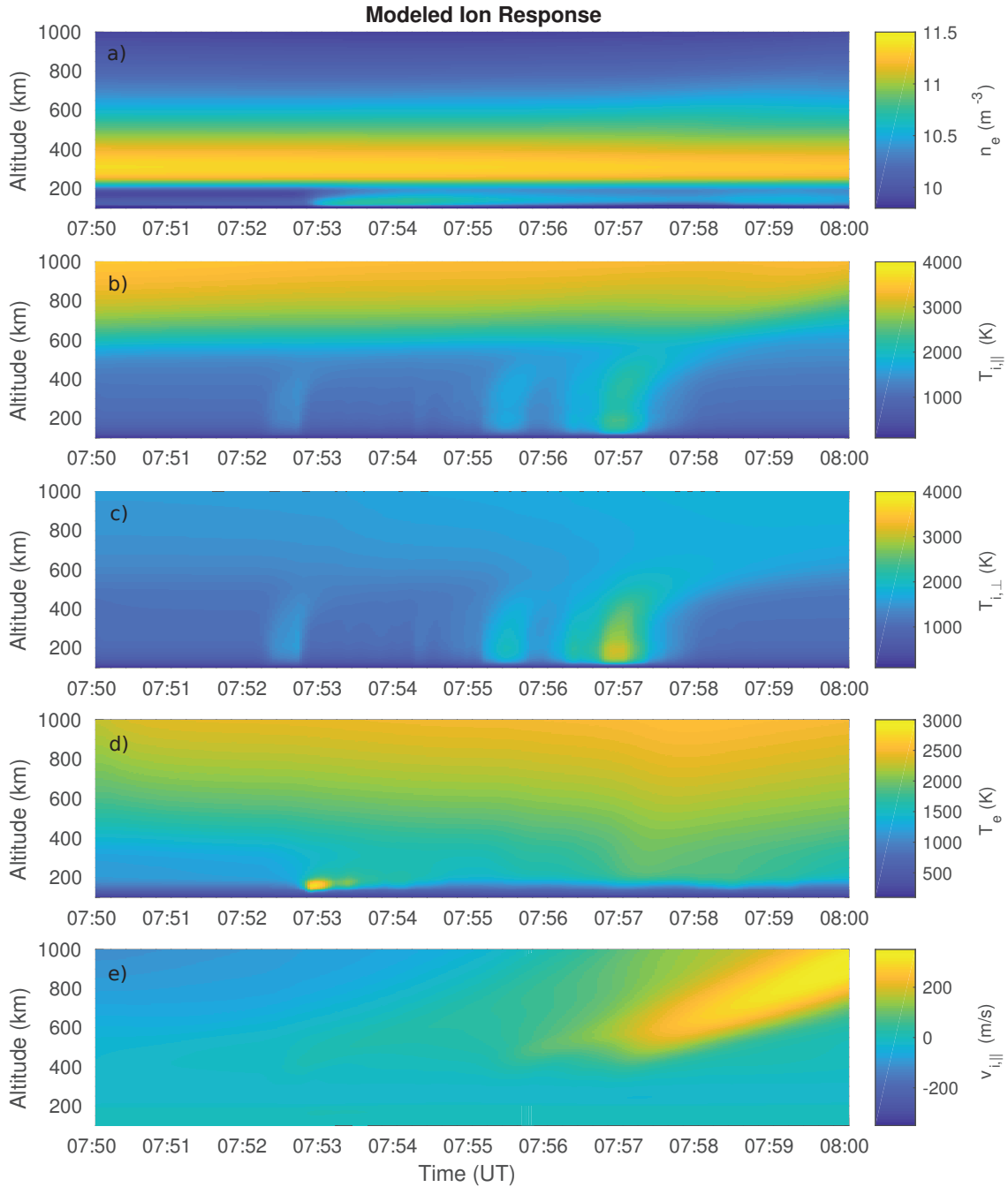


Figure 6.5: Ionospheric response to the in situ energy sources using only the time variability. Rocket measurements don't start until several minutes into the flight.

### Space variability

Unwrapping the space and time variability of in situ measurements in the other dimension, the data is considered in Simulation 2a to be representative of the spatial variability of energy sources only; no temporal variability. This applies the unrealistic but also illustrative assumption that the features measured by the rocket last the full 10 minute duration of the rocket flight and do not change spatial position or intensity.

The extended duration of the energy sources generates a larger ionospheric upflow response in Simulation 2a than the time variable, 1D Simulation 1a. The density-averaged ion responses, in addition to the electron density, after 10 minutes of applied heating from the DCE, precipitation, and wave heating are shown in Figure 6.6. E region densities (panel a) generated by the particle precipitation are three times larger, at  $1.6 \times 10^{11} \text{ m}^{-3}$ , than those generated in the time variable only simulation. The DCE drives larger temperature increases in this Simulation (panels c and d) reaching  $\sim 3300$  K in the F region. Larger anisotropies are also resultant of the extended duration of the DCE in this simulation. The F region density depletions are deeper than those generated in the time variable Simulation 1a by 500% but are only a reduction of 3% from background densities. The extended duration of the DCE drives a larger temperature increases which results in a corresponding increase in the  $\text{O}^+$  to  $\text{NO}^+$  conversion rate.

The resulting upflow (panel b) from these energy inputs reached a maximum of 410 m/s at 170 km south of the center of the model grid where the northward DCE changes from a positive to negative value near the arc boundary. The large gradient in the DCE data at the sign transition location is held steady for the duration of the simulation. The large DCE, at 25 km south of the center of the model grid, also generates a significant amount of upflow reaching 125 m/s at 500 km after 10 minutes of heating (frictional heating-driven upflow, type 1 upflow of *Wahlund et al. (1992)*).

At 1000 km, it takes the upflow  $\sim 4$  minutes to reach this altitude (see Figure 6.7). The density increases steadily over the duration of the simulation in upflow locations (panel a). Once the upflow reaches this altitude, the velocity generated by the large DCE at  $67.9^\circ$ , reaches a maximum of 880 m/s at 7:55 UT (panel b). The heating from the DC electric field at lower altitudes supports that rate of upflow for several more

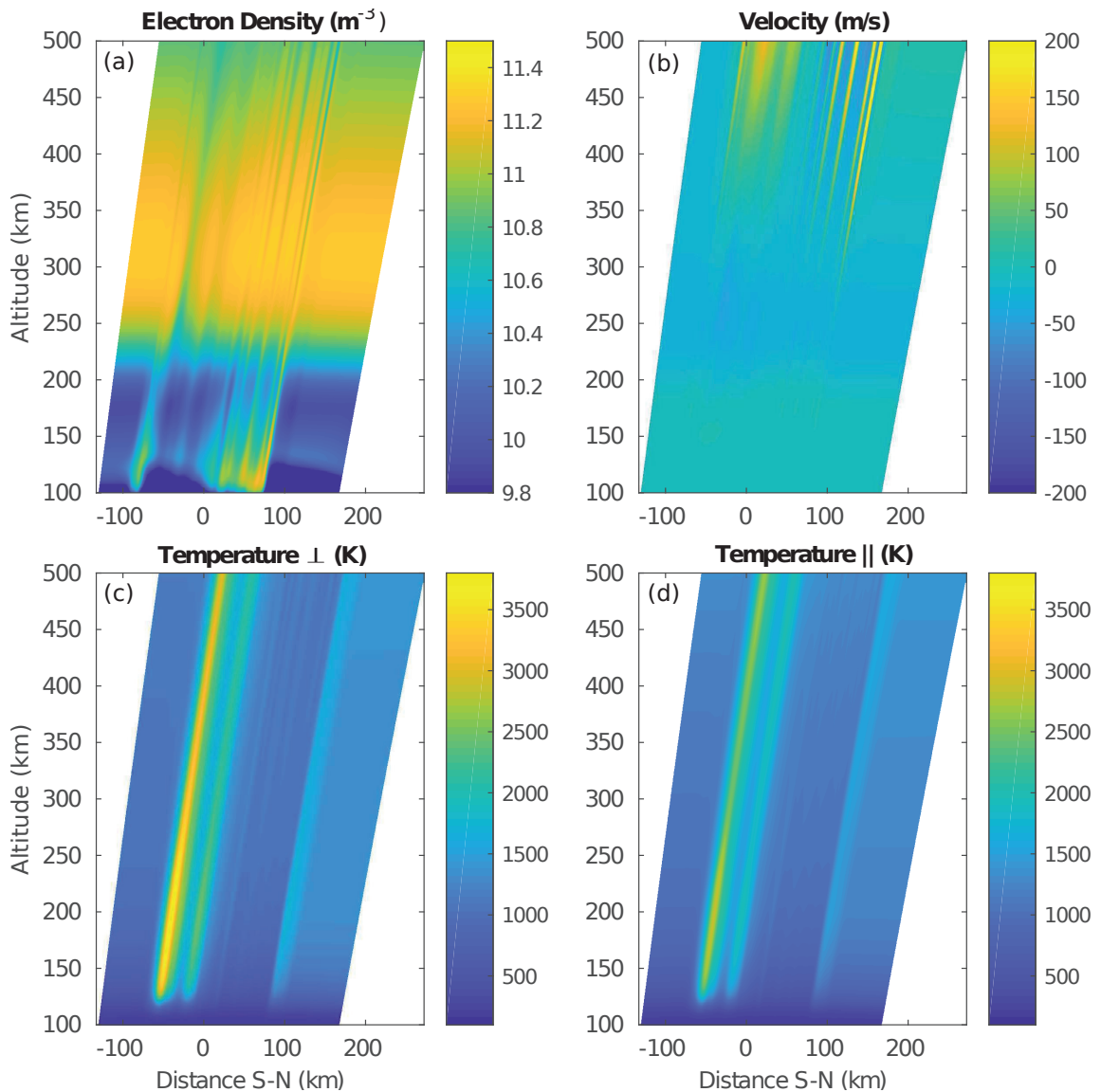


Figure 6.6: Ionospheric response, at 8:00 UT, after 10 minutes of applied heating as defined by the in situ measurements. The tilted dipole grid used by the model follows the magnetic field lines specific to this location and is responsible for the "tilt" in these panels.

minutes before the ionospheric plasma pressure begins to re-establish a force balance and the fluxes begin to decrease (panel c). This is consistent with the parametric study discussed in Chapter 4.

The structured upflow and downflow from  $66.7$  to  $67.3^\circ$  results from structure in

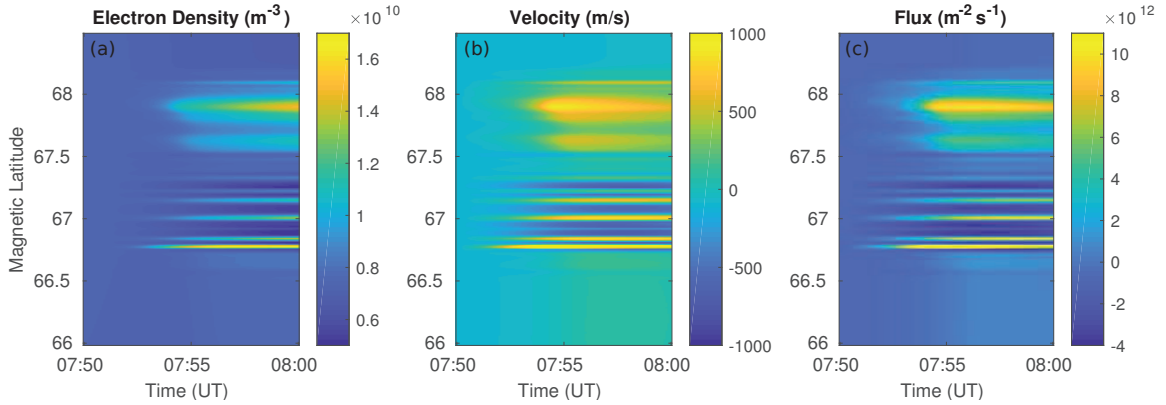


Figure 6.7: Evolution of the electron density (panel a), density averaged, ion velocity response (panel b), and the ionospheric flux (panel c) at 1000 km over the duration of Simulation 2a.

the DCE within and around the auroral arc. Throughout the arc, the small scale structures measured within the precipitation data and sign variations in the DCE measurements generate synergistic upflows. These energy sources are held artificially stable resulting in an overestimation of the upflow/downflow response.

Once again, an additional Simulation (2b) has been run using this setup but without the wave heating effects. The 10 minute duration of the transverse wave heating increases the impact on ionospheric dynamics over the temporal variation Simulation 1a. At the end of these Simulations, 2a and 2b, the ionospheric response difference between these model situations that include and exclude respectively the wave heating are shown in Figure 6.8. There is a difference of 230 K in the  $O^+$  perpendicular ion temperature (which is directly affected by the transverse wave heating) at 500 km and increases to a difference of 700 K at 1000 km (panel c). This is connected to the large anisotropy differences seen in the topside (panel d). Effective transport differences are the largest between 400 and 1000 km as seen in the flux (panel a) where there is mass being transported. The ion velocity differences are largest at high altitudes reaching 40 m/s and 1000 km.

If the transverse wave heating power spectral density were to exceed  $4 \times 10^{-3}$  using a reference frequency of 313 Hz there should be a low altitude ( $< 400$  km) impact and

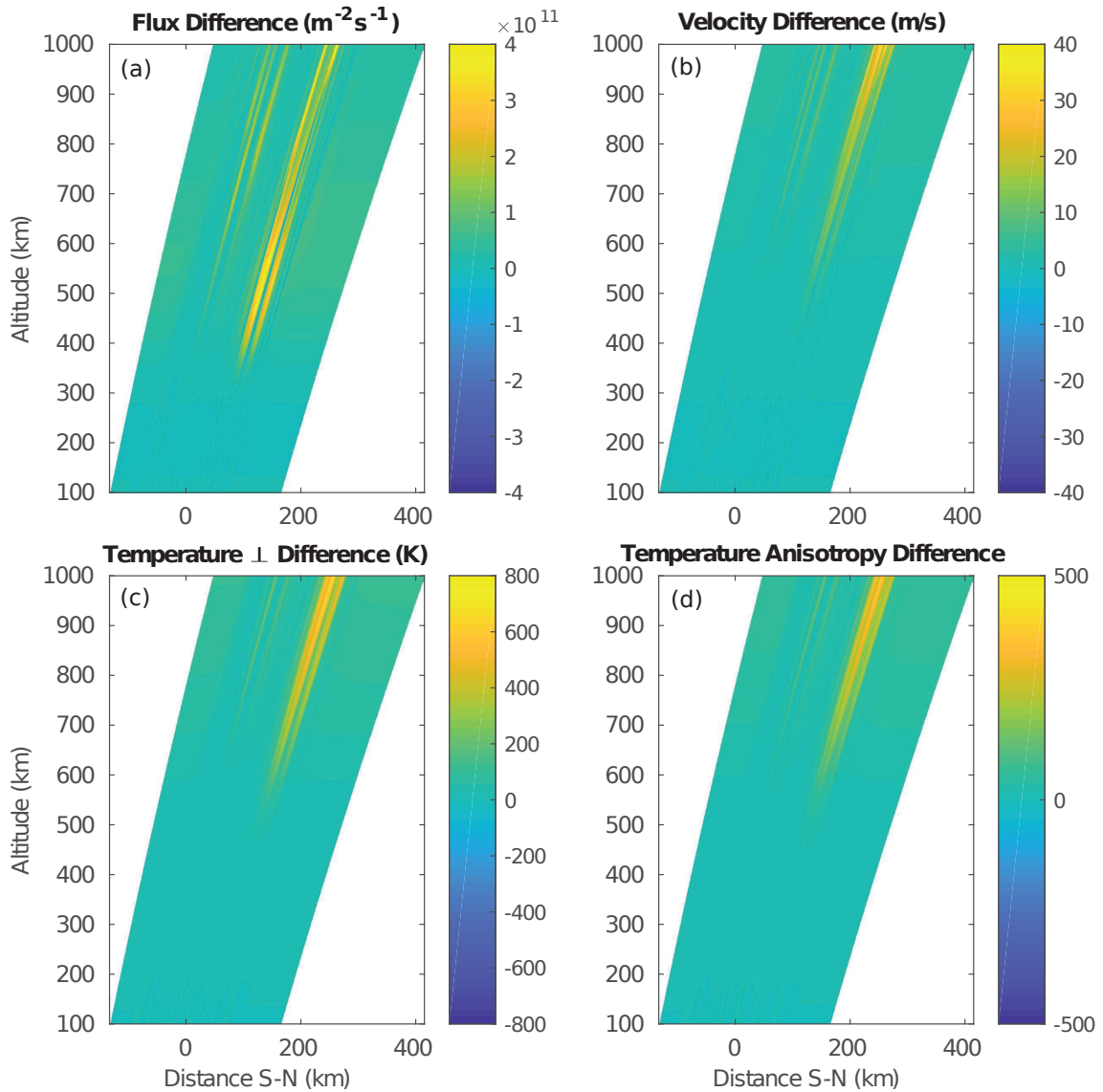


Figure 6.8: The difference including the transverse wave heating has on the spatially variable modeled in situ ionospheric response.

the wave heating will play a larger role driving low altitude upflows. This is equivalent to the strong case in *Burleigh and Zettergren (2017)* but scaled to the reference frequency used here via the wave heating power law in Equation 2.75. Typical values measured by ISINGLASS B are smaller than  $10^{-9}$ . Gyroresonant (cyclotron) energy transfer requires low ion-neutral collision rates and is therefore rarely observed below

400 km except in extreme cases (e.g. *Whalen et al.*, 1978).

Using the in situ measurements from ISINGLASS B in a spatially variable but static in time form over estimates the ion upflow response because features are artificially durable and not moving in space so the same parcel of plasma is constantly being affected. Using the in situ measurements in a temporally variable form underestimates the ion upflow response because energy sources are artificially short in durations. The rocket is transversing features rapidly and the latitudinal extent is not always equivalent to the duration of the feature. Realistic ionospheric responses will mostly likely fall between the two methods of handling the in situ data considered here and probably include additional energy sources not observed by the rocket. Having realistic spatial *and* temporal variability in the model input drivers is necessary for an accurate ionospheric response description.

## 6.2.2 Comparing in situ to ground data

The ground measurements from PFISR and VEE can be used as an alternative for energy input sources for GEMINI-TIA. There is a distinct trade off in resolution to have the spatially and temporally varying inputs. PFISR DCE data, found in the PFISR data product commonly called `vvels1`, is coarse in space and time relative

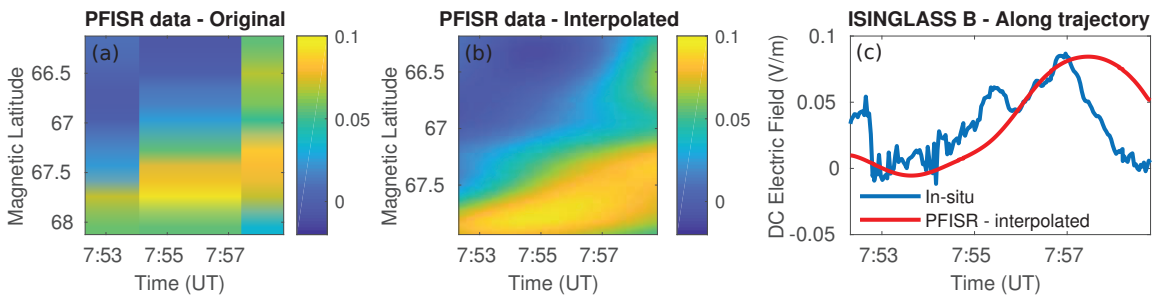


Figure 6.9: PFISR provides low, relative to the in situ measurement spatiotemporal cadence, resolution measurements that are binned to distinct time-space regions (panel a). This data is interpolated to provide smooth DCE values for the model to drive ionospheric upflow responses (panel b). Comparing the in situ measurements to the along-trajectory PFISR DCE data yields an acceptable level of agreement and suggests that the ground DCE measurements can be an acceptable substitute driver for the model that has both time and space variability (panel c).

to rocket sample capabilities (See Figure 6.9). There are  $\sim 8$  reliable DCE spatial bins along the trajectory that have a temporal resolution of  $\sim 2$  minutes (panel a). Rocket measurements have been processed to a temporal resolution of 2 seconds. Interpolating PFISR data using a standard MATLAB spline technique and extracting the along-trajectory values yields similar measurements to the in situ DCEs though without the small-scale features. This data is interpolated to provide smooth DCE inputs for the model to drive ionospheric upflow responses (panel b). The along-trajectory PFISR DCE measurements compare favorably to the sounding rocket in situ measurements and suggests that the ground DCE data is an acceptable substitute driver for the model that has both time and space variability (panel c).

Comparing the all-sky camera precipitation information from VEE to the in situ data requires the rocket trajectory to be traced through the field of view of the camera such as that done in Figure 6.2. The total energy flux and characteristic energy along that path is extracted and plotted in Figure 6.10, panels a and b respectively. There is an agreement in the general shape of the auroral features within the total energy flux but the ground measurements are larger by  $\sim 50\%$ . The larger differences between the ground and in situ characteristic energy from  $66.9^\circ$  to  $67.4^\circ$  is due to the current calibration of the all-sky camera. Further calibration of the all-sky camera data by the

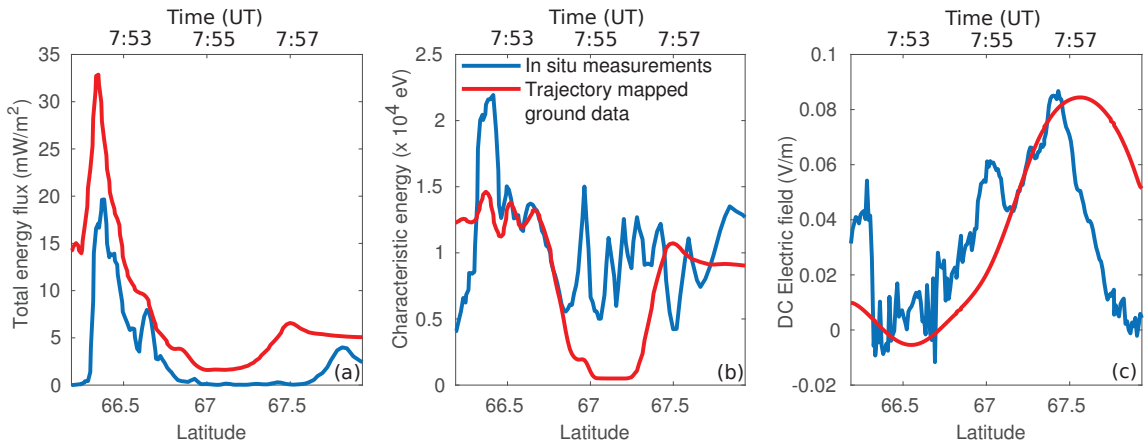


Figure 6.10: Trajectory trace of the ground measurements (red lines) and the in situ data (blue lines) after both have been interpolated onto the model mesh. There is an acceptable level of agreement between these two data sets to support the use of the ground data as model drivers.



rocket campaign team is underway. Overall, there is an acceptable level of agreement between the trajectory trace through the all-sky camera precipitation measurements and the in situ precipitation data supporting the use of these ground measurements as model drivers.

The benefit of these energy inputs, DCE from PFISR and total energy flux and characteristic energy from VEE, is that they encompass both time and spatial variations. The lower resolution of the data is a trade-off but the realistic variability captures important ionospheric dynamics including features that occur before and after the rocket flies through.

### 6.2.3 Ground data driven simulations

Two simulations are discussed in this section, Simulations 3 and 4. Simulation 3 uses the ground based measurements as inputs from 7:50 to 8:00 UT (the time of the rocket flight) to drive the model (see Figure 6.11). Initial conditions for the first simulation are generated by running the model for 24 hours in a quasi-steady state mode to initialize plasma parameters. The second simulation also uses the ground measurements as inputs from 7:50 to 8:00 UT. Initial conditions for the second simulation are created by first running the model for 23 hours and 50 minutes in a quasi-steady state and then “pre-heated” with the ground measurements from 7:40 to 7:50 UT creating dynamic initial conditions. The differences between these two simulations, the impacts of spatiotemporal variability in energy input sources to the ionosphere, and the role pre-heating plays in model Simulations are discussed below.

From PFISR, the DC electric field from 7:40 to 8:00 UT is shown in Figure 6.11, panel a. The trajectory trace through the auroral precipitation information measured at VEE during that same time are shown as well with the total energy flux in panel b and the characteristic energy in panel c. The measurements from 7:40 to 7:50 UT are used as model inputs to generate pre-heating for the dynamic initial conditions for Simulation 4. Notable features within the pre-heating include a large DCE feature from 7:40 to 7:45 UT spanning  $65.9$  to  $\sim 67^\circ$  and  $67.5$  to  $68.2^\circ$  and a strong gradient in the DCE centered around  $67.5^\circ$  from 7:44 to 7:48 UT. Both of these processes are

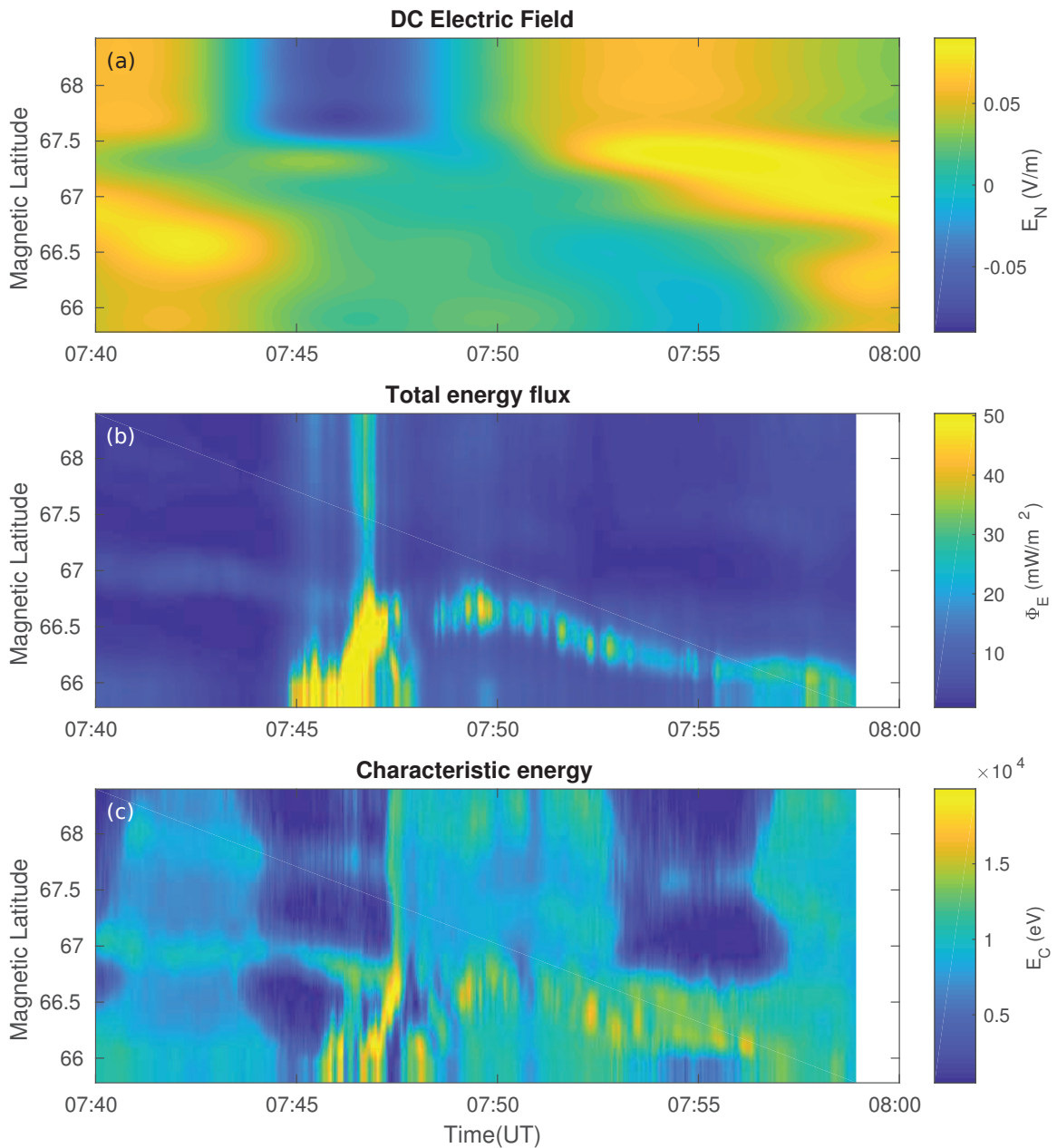


Figure 6.11: The northward DCE from PFISR and the trajectory trace through the VEE all-sky camera energy flux and characteristic energy from the VEE all-sky camera after being interpolated onto the model grid. These ground based measurements have both time and space variability.

known to drive upflow. It should be noted that the consistent in latitude features from 67.7 to 68.2° for all time in panel a are due to fitting the DCE measurement to the

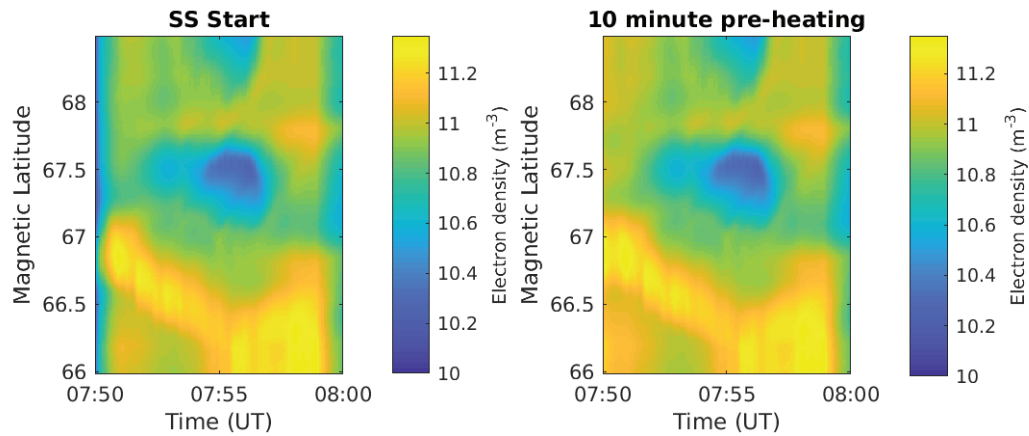


Figure 6.12: E region differences in electron density between Simulation 3 and 4. The dynamic initial conditions used in Simulation 4 generate elevated E region densities 2 minutes sooner than the steady state start in Simulation 3. After 7:52 UT there is less than a 4% difference between the electron densities at this altitude.

model grid; `repmat` was needed to fill the entire span. From VEE, the trajectory trace through the field of view of the all-sky camera provides the relevant total energy flux and characteristic energy produced by the aurora. The pre-heating measurements from 7:40 to 7:50 UT include the substorm expansion phase where the aurora has a marked intensification, at  $\sim 7:45$  UT, and equatorward surge. During the rocket flight time, 7:50 to 8:00 UT, the auroral arc propagates southward from  $\sim 66.7$  to  $\sim 66^\circ$  (panels b and c). At the southern boundary of the arc the DCE changes from positive to negative. Northward of the auroral location there is also a large DCE feature that propagates southwards as well from  $67.5$  to  $66.8^\circ$  that reaches a maximum value of  $93$  mV/m around 7:55 UT. This is larger than the maximum that occurred along the trajectory. The rocket flew through all of these features, as shown in Figure 6.10.

Simulation 3, which used steady state initial conditions, is compared to Simulation 4, which used dynamic initial conditions, first by taking a slice in the E region electron densities, Figure 6.12, at 125 km. In both simulations, the track of the auroral arc as it propagates southward leaves a clear increase in the electron density. From a steady state start it takes  $\sim 2$  minutes in Simulation 3 for the auroral precipitation to raise the local density from background conditions through electron impact ionization. The dynamic initial conditions used to start Simulation 4 have already elevated electron

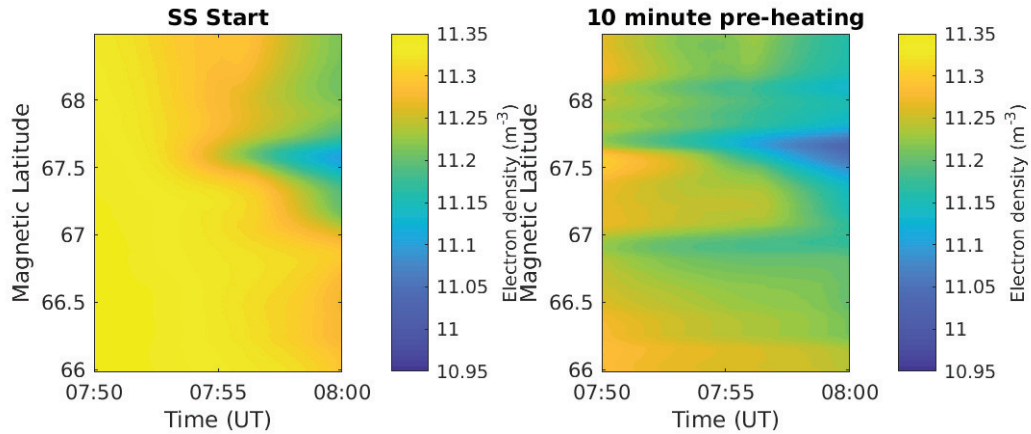


Figure 6.13: F region differences in electron density between Simulations 3 and 4. The dynamic initial conditions used in simulation generate electron density depletion differences that, by the end of the simulation, are still 35% deeper than those in Simulation 3.

densities at this altitude. After 7:52 UT there is less than a 4% difference between the electron densities at this altitude in Simulations 3 and 4. Pre-heating does not have a lasting influence at this altitude.

Taking another altitude slice, F region electron densities are compared in Figure 6.13 at 310 km. There is a significant difference between Simulations 3 and 4 at this altitude. Starting from a steady state, the effects of the strong DCE feature, mentioned prior, slowly generate a density cavity. The DC electric field drives frictional heating which elevates ion temperatures, increasing the reaction rate of  $O^+$  into  $NO^+$  which recombine quickly, and result in the density cavity. The dynamic initial conditions used in Simulation 4, have residual density cavities from previous DCEs during the pre-heating time. This pre-heating alters the source populations available for subsequent processes to act upon. Without a direct photoionization source at this UT, the re-filling process is much longer than the duration of the Simulation. By the end of the 10 minute Simulation, Simulation 3 has up to a 36% larger electron density than Simulation 4. Pre-heating has a lasting influence at this altitude.

Comparing yet another altitude, the  $O^+$  flux evolution over time at 1000 km during the rocket flight is shown in Figure 6.14 for Simulations 3 (panel a) and 4 (panel b). The dynamic initial conditions used in Simulation 4 generate upflows at this altitude early in the simulation that are not present in Simulation 3 which utilized

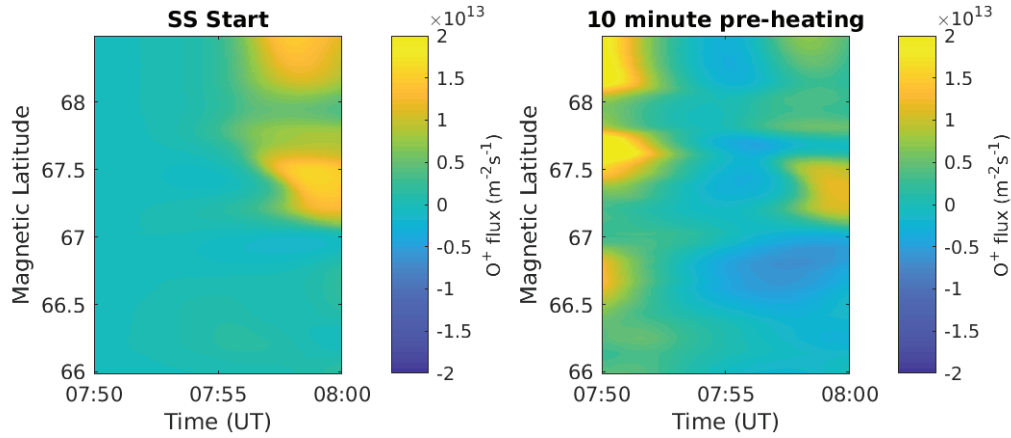


Figure 6.14: The  $O^+$  flux evolution over time at 1000 km during the rocket flight. The dynamic initial conditions used in Simulation 4 (panel b) generate upflow at this altitude early in the simulation that is not present in Simulation 3 (panel a) which utilized steady state initial conditions.

steady state initial conditions. Simulation 3 has a clear upflow response to the strong ( $>75$  mV/m) DCE that appears in the PFISR data and slowly moves southward over the course of the rocket flight. The  $O^+$  flux generated by this energy source reaches a maximum flux of  $1.6 \times 10^{13} \text{ m}^{-2} \text{ s}^{-1}$  at 7:59 UT. In comparison, this same feature in Simulation 4 has a much weaker response and reaches a maximum flux of only  $1.2 \times 10^{13} \text{ m}^{-2} \text{ s}^{-1}$ .

Within the pre-heating dynamics there is a sharp gradient in the DCE from 7:44 to 7:49 UT which increases the ambipolar electric field and drives the upflow seen in panel b around  $67.7^\circ$  at the start of Simulation 4. This level of  $O^+$  flux is only supported for  $\sim 2$  minutes into the Simulation. Then the plasma in this location begins to downflow. The downflow is large enough to overcome the upflow that results from the strong DCE during the Simulation. The overall ionospheric response, including the locations and strengths of upflows and downflow, is highly dependent on pre-heating.

Integrating the  $O^+$  flux from Figure 6.14, over time, calculates the total  $O^+$  transported through 1000 km. The spatial variability of the total  $O^+$  transported is shown in Figure 6.15. Comparing the in situ data driven simulations to the ground data driven simulations there is a marked difference in the location of maximum transport.

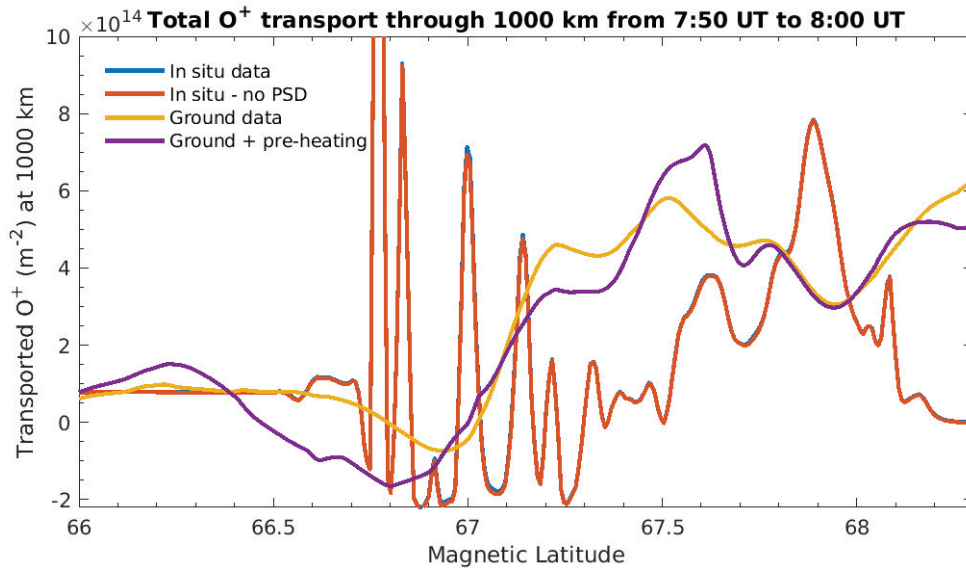


Figure 6.15: The total  $O^+$  transport, integrated over time, at 1000 km for Simulations 2a, 2b, 3, and 4.

Simulation 3 and 4 under estimate the response to the auroral arc as PFISR cannot clearly detect the arc boundary and it is smeared out spatially. Both versions of Simulations 1 and 2 over estimate the response to the auroral arc as these simulations do not capture the southward drift of the arc and instead apply a constant energy input for the duration of the simulation. The arc boundary is located near the sharp sign change in the DCE data. The large DCE gradient at this location is artificially stable which result in large transport peaks around  $66.8^\circ$  and overestimate the total number of  $O^+$  ions transported through 1000km. The feature is highly unlikely to remain stationary for the 10 minute duration of the Simulation.

For the large DCE feature north of the auroral arc boundary, the location of maximum transport also varies between in situ and data driven simulations as well as between steady state and dynamic initial conditions. The location and size of maximum  $O^+$  transport is dependent on the energy source input spatiotemporal variability. The spatial variability, naturally present in the ground based data, on Simulations 3 and 4 result in the location of maximum transport being southward of the respective response from Simulations 1 and 2. The pre-heating in Simulation 4 generates a larger total transport than Simulation 3 at some latitudes (e.g.  $67.6^\circ$ ) but other latitudes

have a smaller total transport (e.g.  $67.2^\circ$ ). The dynamic initial conditions used in Simulation 4 account for the time history of ionospheric dynamics and when used with the spatiotemporal variable, ground based, energy inputs generates the most accurate description of upflow of the four Simulations presented as part of this study.

### 6.3 Chapter conclusions

The realistic spatial and temporal variability of energy inputs (i.e., source combinations and timing consistent with observations during geophysically significant events) into the ionosphere, from both the thermosphere and magnetosphere, is important when accurately determining the ion upflow/outflow response.

ISINGLASS B was launched on March, 2 into a substorm expansion from PFRR at 7:50 UT. The flight lasted  $\sim 10$  minutes and the rocket reached an apogee of  $\sim 360$  km. This rocket flew over an array of ground-based instruments including radars and all-sky cameras. As such, there are two sets of measurements of ionospheric upflow drivers: in situ measurements and ground based data.

Using the in situ measurements in a time variable but spatially constant configuration, such as Simulations 1a and 1b, generates an ionospheric upflow response that underestimates flow due to the unrealistically short duration of the heating. When in situ data is instead handled with a spatially variable but time steady assumption, such as Simulations 2a and 2b, the general spatial shape of upflow more accurately captured but the energy inputs have an unrealistically long duration. As a consequence, strong gradients and small scale features are held artificially stable overestimating the ionospheric response. Realistic ionospheric responses will fall between these two extremes and possibly even include additional energy sources not observed by the rocket.

At altitudes outside the functional domain of the model it is likely that the WPI plays a larger role energizing the ionospheric plasma and may drive outflow to the magnetosphere. The minimal impact in situ measurements of WPI have on the generation of upflow suggests that Simulations driven by ground based data (where there are no equivalent measurements of WPI) will not be missing an important driver (at

these altitudes).

Ground data driven simulations captures the general shape of upflow more accurately by contain both time and space variability but at the loss of fine scale details. By including spatiotemporal variability in energy input sources realistic dynamics are reproduced. Within this study the auroral arc had a pronounced southward drift over the course of the rocket flight. This motion serves to slowly move energization sources across the ionosphere producing a finite amount of heating in any given location.

The time history of the ionosphere also plays a significant role when accurately describing the upflow response to auroral heating. Dynamic initial conditions allow for pre-heating to be applied to a simulation which can alter the ion sources available for transport, the total number of ions transported, and generate upflows that will not be present in simulations started from a steady state.

Realistic spatiotemporal variability is important when accurately determining the location and amount of upflow and potential outflow to the magnetosphere. Utilizing the dynamic initial conditions in Simulation 4, accounting for the time history of ionospheric dynamics, may provide the most accurate description of the response to energy sources of the four Simulations presented as part of this study.



# Chapter 7

## Conclusions and future work

In this dissertation, a new anisotropic ionospheric fluid model, GEMINI-TIA, has been developed to explore the connection between energy inputs and the upflow/outflow response in the high-latitude ionosphere. GEMINI-TIA solves the time-dependent, nonlinear equations of conservation of mass, momentum, parallel energy, and perpendicular energy for six ion species relevant to the E, F, and topside ionospheric regions. This model incorporates all of the ionospheric chemistry and collisional terms needed to properly simulate low-altitude dynamics and includes possible effects of low-altitude wave particle interactions. In order to facilitate comparisons with data, the model was designed to accept as inputs the main drivers of ion upflow and outflow: particle precipitation, DC electric fields, ELF wave power, and neutral winds and densities. Development of this model was the primary goal for the first part of this dissertation work and discussed in extensive detail in Chapter 2.

### 7.1 Science sub-queries

GEMINI-TIA has very flexible functionality and in this dissertation has been compared to GEMINI (its parent model), coupled to a neutral dynamics model, and used alongside rocket and ISR experiments to simulate ionospheric responses to different types of energy sources and neutral wind patterns. Specifically, for the second part of this work, GEMINI-TIA has been used to examine responses deep in the ionosphere to

transverse heating from wave-particle interactions in the collisional regime, determine the implications of temperature anisotropy that develops during times of strong heating, explore the effects of thermospheric winds on upflow and outflow mechanisms, and identify how the inclusion of realistic temporal and spatial variability in model drivers regulates the resulting ion upflow and outflow. The conclusions generated to the sub-queries posed in Chapter 1 are discussed in the following sections.

### **Impacts of temperature anisotropy on low altitude ionospheric dynamics**

Ion temperature anisotropies are commonly observed by incoherent scatter radar, satellites, and sounding rockets. Models of the regions measured by these instruments need to be able to resolve anisotropy that develops as a consequence of energy inputs associated with ion upflow. Only transport systems based off of a Bi-Maxwellian distribution, such as GEMINI-TIA, are appropriate for large temperature anisotropy situations (*Barakat and Schunk, 1982a*). When comparing GEMINI-TIA with its parent model, that was based off of a Maxwellian distribution, there was a significant difference in ion response between the two models. This difference is due to the fact that the frictional heating, in reality and in the Bi-Maxwellian-based model, leads to a larger perpendicular temperature than parallel temperature (as discussed in Chapter 3). Specifically, the parent model assumes equal partitioning in both directions, while GEMINI-TIA correctly accounts for a larger fraction of the energy being distributed into the field-perpendicular direction. As a consequence, isotropic fluid models overestimate many ionospheric responses and supports the need for an anisotropic fluid model.

### **Anisotropy and ion upflow from low altitude transverse plasma waves**

GEMINI-TIA has been used to examine the synergistic effects of wave heating and frictional heating at low altitudes (as discussed in Section 4.1). When comparing temperature anisotropies generated by these two processes, the DCE effects are primarily at lower altitudes and the wave heating-driven anisotropies are at higher altitudes. The power spectral density of broadband ELF waves determines how deep into the

ionosphere wave heating is able to generate anisotropy. In general, the model shows that the effectiveness of cyclotron wave heating is mitigated, to a degree, by the presence of collisions at the lower altitudes, both ion-ion and ion-neutral.

Wave heating also increased upflow velocities by a small degree at altitudes above the main ion perturbation. This is generated by electrons that gain energy through heat exchange with frictionally heated ions deep in the ionosphere (i.e. near the F-region peak). Electrons have a high thermal conductivity which allow energy input at low altitudes to quickly conducted upwards along the field line. Hence an ion heat source can serve to generate, indirectly, electron pressure enhancements and ambipolar upflow in the topside ionosphere before the main ion perturbation can reach these altitudes.

### **Role of neutral winds in regulating ion outflow**

Strong neutral wind are commonplace at high latitudes. These neutral winds impart momentum to ions at low altitudes, aiding or hindering ion flow which can impact the high altitude ion populations available for secondary acceleration processes that lead to outflow to the magnetosphere. It was shown that the direction of the wind directly impacted the amount of influence the winds had on aiding or hindering ion upflow (see Chapter 4). A southward neutral wind aided ion upflow, through ion-neutral drag. On the other hand, geographically northward winds hindered ion upflow. This is due to the field aligned component of the geographic northward wind pointing downwards. Neutral winds antiparallel to the  $\mathbf{E} \times \mathbf{B}$  drift (westward here) exacerbate frictional heating, resulting in more ion upflow. Changing the orientation of the neutral wind to be along  $\mathbf{E} \times \mathbf{B}$  decreased the  $\text{O}^+$  flux response. These results strongly suggest that thermospheric dynamics are an important factor affecting ion upflow and outflow.

Extending the study of neutral wind effects beyond static sources, GEMINI-TIA was coupled to an atmospheric model, MAGIC. This one-way coupling allowed for GW perturbations in MAGIC to be passed to GEMINI-TIA and drive the dynamical evolution of upflow and downflow within the ionospheric model (see Chapter 5). Neutral velocity perturbations modulated ion densities. These ion density modulations

altered the electron collisional cooling rate as well as the photoionization heating rate. Combined, the net effect of these density dependent processes resulted in periods of elevated or decreased electron temperatures. These temperature variations quickly conducted up geomagnetic field lines altering plasma populations at altitudes well above the GW-ionosphere coupling region and through the ambipolar electric field drive an ion response as well. The result of this chain of processes was an ion up-flow/downflow response at higher altitudes that altered the populations available for secondary acceleration processes that lead to outflow into the magnetosphere.

The spatial and temporal structure of the GW played a critical role in modulating the ion response. The presence of viscous damping and nonlinearity acted to deposit momentum into the mean flow and, with the directional orientation of the waves used in this study, resulted in an increase in the neutral field aligned velocity. Wave breaking is another nonlinear gravity wave process that affects the ion response with more energy being deposited into small scale wave modes generated by GW breaking. The larger the amplitude of the GW, the quicker, and stronger, wave breaking occurred which creates periods of large field aligned  $O^+$  velocities. While not achieving escape speed, this generated an environment ready for secondary acceleration mechanisms than could produce outflow to the magnetosphere. The modulation of the ionosphere by the GW significantly affects the response to secondary acceleration mechanisms such as this transverse wave heating by BBELF waves.

### **Impacts of realistic spatiotemporal variability on ion outflow**

The spatiotemporal limitations of data driven modeling was investigated using the ISINGLASS sounding rocket campaign (see Chapter 6). Sounding rockets provide point-source in situ measurements moving steadily through space and time. These measurements, when used to drive the model, can be considered in two ways. First is to assume that the in situ data is representative of the temporal evolution of the energy sources and run the model in a 1D configuration. This time variable but spatially constant configuration generates an ionospheric upflow response that underestimates flow due to the unrealistically short duration of heating. Second, is to assume that the in situ data represents the spatial variability of energy sources which

remain constant over time. This allows for the general spatial shape of ion upflow to be more accurate but the energy inputs have an unrealistically long duration. As a consequence, sheers and small scale features are held artificially stable overestimating the ionospheric response. Realistic ionospheric responses will fall between these two extremes and possibly even include additional energy sources not observed by the rocket.

Ground data driven simulations capture the general shape and duration of upflow more accurately by containing both time and space variability but at the loss of fine scale details. By including spatiotemporal variability in energy input sources more realistic responses are generated. Specifically within this study, the auroral arc had a pronounced southward drift over the course of the rocket flight that was not captured by the point-source rocket measurements. This motion serves to slowly move energization regions across the ionosphere and generate a finite amount of heating in any given location. In addition to the importance of spatiotemporal evolution of energy sources, the time history of the ionosphere also plays a significant role when accurately describing the upflow response to auroral heating. Dynamic initial conditions allow for pre-heating to be applied to a simulation which alters the ion sources available for transport, the total number of ions transported, and generate upflows that will not be present in simulations started from a steady state. Realistic spatiotemporal variability and time history of ionosphere drivers are important to utilize when accurately determining the location and amount of upflow, and potential outflow to the magnetosphere.

## 7.2 Future work

GEMINI-TIA is ideal for sounding rocket case studies as it has been designed to ingest the primary drivers of ion upflow, i.e. DC electric fields, particle precipitation, transverse wave heating, and neutral winds and densities, that are often measured during rocket campaigns. Future case studies may include RENU2 and VISIONS.

### 7.2.1 RENU2

The RENU2 (Rocket Experiment for Neutral Upwelling 2) sounding rocket (M. Lessard, PI) was launched on Dec 13, 2015 at 7:34 UT. This rocket was launched into the fourth poleward moving auroral form (PMAF) of the observed sequence that night to allow for heating of the ambient atmosphere and ionosphere from previous PMAFs, see Figure 7.1. The rocket trajectory, apogee of 447 km, resulted in the payload passing through the auroral arc obliquely on the down-leg while oriented closely parallel to the local magnetic field.

The time history of ion flow is important when concerned with the total dynamics of a local ion event, as discussed in detail in Chapter 6. Each pass of a PMAF provides a unique amount of energy input into the local ionosphere, primarily through soft electron precipitation, that varies over time and spatial location. By parametrically varying the duration, strength, repetition rate, and PMAF intensity the combined spatiotemporal variability and integrated upflow response can be examined. This will serve to increase our understanding of the effects a series of PMAFs has on ion downflow, upflow, and outflow.

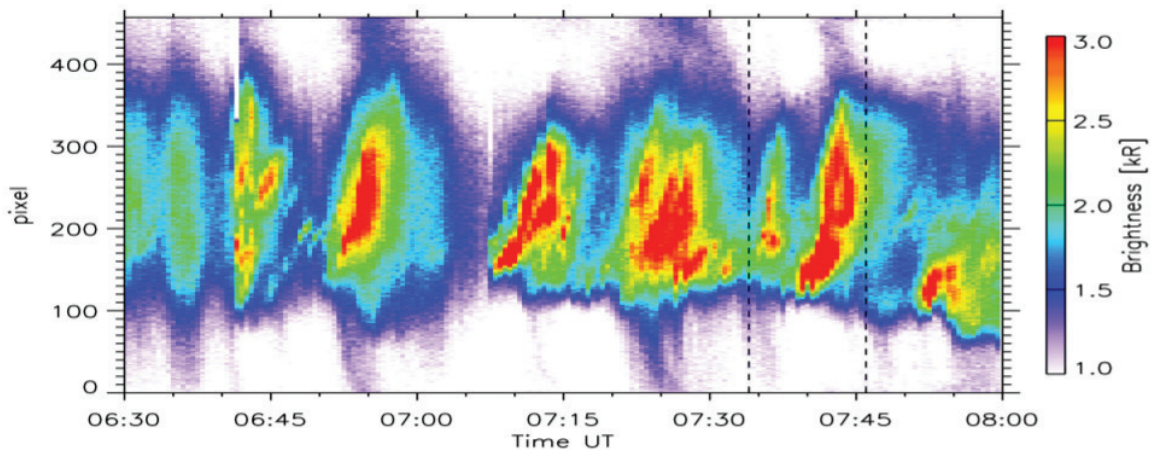


Figure 7.1: This keogram, extracted from Svalbard all-sky camera data, shows the series of PMAFs observed the night of the RENU2 launch. The dashed lines indicate the fourth PMAF which RENU2 was launched through. The upswept shape emphasizes the poleward motion of these arcs. Keogram courtesy of M. Lessard.

### 7.2.2 VISIONS

The VISIONS (VISualizing Ion Outflow via Neutral atom imaging during a Substorm) sounding rocket (D. Rowland, PI) was launched on February 7th, 2013 at 8:21 UT from Poker Flat and flew through the expansion phase of an auroral substorm. This rocket was designed to take advantage of the long range and slow motion through auroral features. VISIONS carried five instruments: (1) Miniaturized Low Energy Neutral Atom imager (MILENA), which consisted of two low-energy energetic neutral atom (ENA) imagers, covering 50 eV to 3 keV, (2) Rocket-borne Auroral Imager (RAI), a camera for measuring electron precipitation over a wide area, (3) Energetic Electron Analyzer (EEA), an energetic electron spectrometer, (4) Energetic Ion Analyzer (EIA), an energetic ion spectrometer, and (5) Fields and Thermal Plasma (FTP) suite, a package for measuring electric (DC to MHz, including BBELF/VLF waves) and magnetic fields as well as thermal plasma density and temperature. The temporal and spatial resolution of these instruments provide excellent observations of the structured regions of ion energization in the auroral zone.

Complimentary ground based measurements were taken by PFISR and University of Alaska Fairbanks all-sky imagers to provide context pre-launch, during the flight, and post-launch. The trajectory of the rocket extends beyond the observational area of these ground-based resources. VISIONS flew through and near several regions of enhanced auroral activity, and sensed regions of ion outflow both remotely (via ENA imaging) and directly (using in situ measurements). The MILENA instrument returned full-sky images of the ENAs produced by charge exchange from outflowing ions at energies between 50 eV and 3 keV. Because charge exchange is predominantly momentum and energy conserving, traditional mechanisms for ion energization produce strongly anisotropic pitch angle distributions.

It was originally expected that the majority of the ENAs seen by VISIONS would be traveling perpendicular to  $B$ . Instead, the majority of the ENAs seen were up-going while VISIONS was in the auroral zone, and transitioned to the expected perpendicular direction when VISIONS moved from the auroral zone into the polar cap. Up-going ENAs can be produced from perpendicular ion energization processes by subsequent ENA-neutral scattering at altitudes of 300-600 km. Because the charge exchange

probability is larger at low altitudes, the up-going ENAs produced in this region may dominate over horizontal ENAs produced at a higher altitude. This indicates that the energized ions must spend a significant amount of time in the region 300-600 km where the scattering processes primarily occur. The predominantly up-going ENAs in the auroral zone strongly indicate the presence of either low-altitude wave heating that extends into the thermosphere or a “pressure cooker” mechanism created by a downward parallel electric field that reflects ions downward resulting in multiple passes through a traditional wave heating region.

Incorporating VISIONS in-situ observations as input drivers for the model will provide a physical connection between energy inputs and upflow allowing for the mechanism responsible for the observed ENAs to be identified. Ground-based measurements will provide model inputs needed for determining the spatiotemporal evolution of the ion upflow region before, during, and after the VISIONS experiment. Ultimately, this effort will improve the ability to identify the cause and effect processes that result in low-altitude, high-latitude ionospheric upflows.

## 7.3 GEMINI-TIA 3D

Further model development plans include the creation of GEMINI-TIA 3D. By expanding the model to include longitudinal space, in addition to the latitudinal and altitudinal dimensions that currently exist, several additional studies can be supported.

### 7.3.1 Convection effects on transient upflows

From Chapter 6, the effects realistic spatial and temporal variability of energy inputs for the model were discussed. The next step to expand that study further would be to include the effects of convection on the variable dwell time of ionospheric plasma within energization regions. In order to do so accurately, a 3D version of GEMINI-TIA would be needed. As ionospheric plasma convects into and out of regions of localized heating the exposure time directly impacts composition, local densities, and



the total upflow generated.

### 7.3.2 Nonlinear gravity waves

While the ISR data from Sondrestrom provided inspiration for the wave parameters used in Chapter 5, the data were 1D in space (along the geomagnetic field line), evolving in time. A phased array such as PFISR, or a scanning mode of the Sondrestrom ISR, has the potential to capture the multidimensional relationships of a GW event, and assist in source determination.

Future work may include looking through additional ISR databases for to find more GW events; 4 very strong neutral wind events were found in the solar cycle 23 search of Sondrestrom's data that yielded the event motivating the study in Chapter 5. The commonality of this type of high-latitude, atmosphere-ionosphere interaction can be commented on in future studies. From the GWs identified from that database search, a detailed parameter space study of nonlinear GWs using a 3D two-way coupled model setup would provide detailed information of how non-linear neutral dynamics modulate ionospheric upflows and outflows.

## 7.4 Open-sourcing the code

GEMINI-TIA is a very useful tool for the aeronomy community. Additional future work will involve open-sourcing the code. This will be a massive undertaking to provide a user friendly and universally functioning program. GitHub is currently the host cite being considered. Several other models useful to the aeronomy community are currently available there, including GEMINI the parent model to GEMINI-TIA. As an added incentive, open sourcing the model will help fulfill one of the new data handling policies of the Journal of Geophysical Research designed to encourage the reproducibility of research in this field.

# Bibliography

- Altadill, D., and J. Sole (2001), Vertical structure of a gravity wave like oscillation in the ionosphere generated by the solar eclipse of august 11, 1999, *J. Geophys. Res.*, pp. 21,419–21,428.
- Anderson, C., T. Davies, M. Conde, P. Dyson, and M. J. Kosch (2011), Spatial sampling of the thermospheric vertical wind field at auroral latitudes, *Journal of Geophysical Research: Space Physics*, 116(A6), doi:10.1029/2011JA016485.
- Andre, M., P. Norqvist, L. Andersson, L. Eliasson, A. Eriksson, L. Blomberg, R. Erlandson, and J. Waldemark (1998), Ion energization mechanisms at 1700 km in the auroral region, *J. Geophys. Res.*, 103, 4199–4222.
- Archer, W. E., D. J. Knudsen, J. K. Burchill, M. R. Patrick, and J. P. St.-Maurice (2015), Anisotropic core ion temperatures associated with strong zonal flows and upflows, *Geophys. Res. Lett.*, 42(4), 981–986.
- Bale, D. S., R. J. LeVeque, S. Mitran, and J. A. Rossmannith (2003), A wave propagation method for conservation laws and balance laws with spatially varying flux functions, *SIAM Journal on Scientific Computing*, 24(3), 955–978.
- Barakat, A. R., and R. W. Schunk (1981), Momentum and energy exchange collision terms for interpenetrating bi-maxwellian gases, *J. Phys. D: Appl. Phys.*, 14, 421–438.
- Barakat, A. R., and R. W. Schunk (1982a), Transport equations for multicomponent anisotropic space plasmas: a review, *Plasma Physics*, 24(4), 389.

- Barakat, A. R., and R. W. Schunk (1982b), Comparison of transport equations based on maxwellian and bi-maxwellian distributions for anisotropic plasmas, *J. Phys. D: Appl. Phys.*, *15*, 1195–1216.
- Bates, H. (1973), Atmospheric expansion through joule heating by horizontal electric fields, *Planet. Space Sci.*, *21*(2073).
- Bertin, F. (1983), Observations of gravity waves in the auroral zone, *Radio Sci.*, *18*, 1059–1065.
- Blelly, P. L., and R. W. Schunk (1993), A comparative study of the time-dependent standard 8-, 13- and 16-moment transport formulations of the polar wind, *Annales Geophysicae*, *11*(6), 443–469.
- Block, L., and C. Falthammar (1968), Effects of field-aligned currents on the structure of the ionosphere, *J. Geophys. Res.*, *73*(4807).
- Bouhram, M., M. Malingre, J. R. Jasperse, and N. Dubouloz (2003), Modeling transverse heating and outflow of ionospheric ions from the dayside cusp/cleft. 1 A parametric study, *Annales Geophysicae*, *21*(8), 1753–1771.
- Brambles, O. J., W. Lotko, B. Zhang, M. Wiltberger, J. Lyon, and R. J. Strangeway (2011), Magnetosphere Sawtooth Oscillations Induced by Ionospheric Outflow, *Science*, *332*, doi:10.1126/science.1202869.
- Burchill, J. K., D. J. Knudsen, J. H. Clemmons, K. Oksavik, R. F. Pfaff, C. T. Steigies, A. W. Yau, and T. K. Yeoman (2010), Thermal ion upflow in the cusp ionosphere and its dependence on soft electron energy flux, *Journal of Geophysical Research: Space Physics*, *115*(A5), doi:10.1029/2009JA015006.
- Burgers, J. M. (1969), Flow equations for composite gases, *Tech. rep.*
- Burleigh, M. (2013), Auroral ion upflows: Sources, high altitude dynamics, and neutral wind effects, Master's thesis, Embry-Riddle Aeronautical University.

- Burleigh, M., and M. Zettergren (2017), Anisotropic fluid modeling of ionospheric upflow: Effects of low-altitude anisotropy and thermospheric winds, *Journal of Geophysical Research: Space Physics*, doi:10.1002/2016JA023329.
- Chang, T., G. B. Crew, N. Hershkowitz, J. R. Jasperse, J. M. Retterer, and J. D. Winningham (1986), Transverse acceleration of oxygen ions by electromagnetic ion cyclotron resonance with broad band left-hand polarized waves, *Geophysical Research Letters*, *13*(7), 636–639, doi:10.1029/GL013i007p00636.
- Chew, G. F., M. Goldburger, and F. Low (1956), The boltzmann equation and the one-fluid hydromagnetic equations in the absence of particle collisions, *Proc. R. Soc.*, *84*.
- Chodura, R., and F. Pohl (1971), Hydrodynamic equation for anisotropic plasmas in magnetic fields - ii transport equations including collisions, *Plasma Physics*, *13*(8), 645–658.
- Clark, R. M., K. C. Yeh, and C. H. Liu (1971), Interaction of internal gravity waves with the ionospheric f2-layer, *Journal of Atmospheric and Terrestrial physics*, *33*(10), 1567–1576.
- Cohen, I. J., M. Widholm, M. R. Lessard, P. Riley, J. Heavisides, J. I. Moen, L. B. N. Clausen, and T. A. Bekkeng (2016), Rocket-borne measurements of electron temperature and density with the electron retarding potential analyzer instrument, *Journal of Geophysical Research: Space Physics*, *121*(7), 6774–6782, doi:10.1002/2016JA022562.
- Crew, G. B., T. Chang, J. M. Retterer, W. K. Peterson, D. A. Gurnett, and R. L. Huff (1990), Ion cyclotron resonance heated conics: Theory and observations, *J. Geophys. Res.*, *95*(A4), 3959–3985.
- Daglis, I. A., R. M. Thorne, W. Baumjohann, and S. Orsini (1999), The terrestrial ring current: Origin, formation, and decay, *Reviews of Geophysics*, *37*, 407–438, doi:10.1029/1999RG900009.

- David, T., D. Wright, S. Milan, S. Cowley, J. Davies, and I. McCrea (2018), A study of observations of ionospheric upwelling made by the eiscat svalbard radar during the international polar year campaign of 2007, *Journal of Geophysical Research: Space Physics*, *123*(3), 2192–2203.
- Davis, M. J. (1973), The integrated ionospheric response to internal atmospheric gravity waves, *J. Atmos. Sol. Terr. Phys.*, *35*(5), 929–959.
- de la Beaujardiere, O., D. Alcayde, J. Fontanari, , and C. Leger (1991), Seasonal dependence of high-latitude electric fields, *Journal of Geophysical Research: Space Physics*, *96*(A4), 5723–5735, doi:10.1029/90JA01987.
- Demars, H. G., and R. W. Schunk (1979), Transport equations for multispecies plasmas based on individual bi-maxwellian distributions, *Journal of Physics D: Applied Physics*, *12*(7), 1051–1071.
- Diloy, P., A. Robineau, J. Linensten, P. Blley, and J. Fontanari (1996), A numerical model of the ionosphere, including the e-region above eiscat, *Ann. Geophys.*, *14*, 191–200.
- Doe, R., M. Mendillo, J. Vickrey, L. Zanetti, and R. Eastes (1993), Observations of nightside auroral cavities, *Journal of Geophysical Research: Space Physics*, *98*(A1), 293–310, doi:10.1029/92JA02004.
- Endo, M., R. Fujii, S. C. Buchert, S. Nozawa, S. Watanabe, and N. Yoshida (1999), Ion upflow and downflow at the topside ionosphere observed by the EISCAT vhf radar, *Ann. Geophys.*, *18*, 170–181.
- Evans, J. V. (1965), An f region eclipse, *Journal of Geophysical Research*, *70*(1), 131–142, doi:10.1029/JZ070i001p00131.
- Fang, X., C. E. Randall, D. Lummerzheim, S. C. Solomon, M. J. Mills, D. R. Marsh, C. H. Jackman, W. Wang, and G. Lu (2008), Electron impact ionization: A new parameterization for 100 ev to 1 mev electrons, *Journal of Geophysical Research: Space Physics*, *113*(A9), doi:10.1029/2008JA013384.

- Fernandes, P. A., K. A. Lynch, M. Zettergren, D. L. Hampton, T. A. Bekkeng, I. J. Cohen, M. Conde, L. E. Fisher, P. Horak, M. R. Lessard, R. J. Miceli, R. G. Michell, J. Moen, and S. P. Powell (2016), Measuring the seeds of ion outflow: Auroral sounding rocket observations of low-altitude ion heating and circulation, *Journal of Geophysical Research: Space Physics*, *121*(2), 1587–1607, doi:10.1002/2015JA021536.
- Fisher, L. E., K. A. Lynch, P. A. Fernandes, T. A. Bekkeng, J. Moen, M. Zettergren, R. J. Miceli, S. Powell, M. R. Lessard, and P. Horak (2016), Including sheath effects in the interpretation of planar retarding potential analyzer's low-energy ion data, *Review of Scientific Instruments*, *87*(4), 043,504, doi:10.1063/1.4944416.
- Foster, C., and M. Lester (1996), Observations of nightside auroral plasma upflows in the f-region and topside ionosphere, *Ann. Geophys.*, *14*, 1274.
- Foster, C., M. Lester, and J. A. Davies (1998), A statistical study of diurnal, seasonal and solar cycle variations of f-region and topside auroral upflows observed by eiscat between 1984 and 1996, *Ann. Geophys.*, *16*, 1144–1158.
- Francis, S. (1973), Acoustic-gravity modes and large-scale traveling ionospheric disturbances of a realistic, dissipative atmosphere, *J. Geophys. Res.*, *78*, 2278–2301.
- Fritts, D., and Z. Luo (1993), Gravity wave forcing in the middle atmosphere due to reduced ozone heating during a solar eclipse, *J. Geophys. Res.*, pp. 3011–3021.
- Fritts, D., and S. Vadas (2008), Gravity wave penetration into the thermosphere: sensitivity to solar cycle variations and mean winds, *Ann. Geophys.*, *26*, 3841–3861.
- Fritts, D., B. Laughman, T. Lund, and J. Snively (2015), Self-acceleration and instability of gravity wave packets: 1. effects of temporal localization, *Journal of Geophysical Research: Atmospheres*, *120*(17), 8783–8803, doi:10.1002/2015JD023363.
- Fritts, D. C., and M. J. Alexander (2003), Gravity wave dynamics and effects in the middle atmosphere, *Reviews of Geophysics*, *41*(1), doi:10.1029/2001RG000106.

- Gaimard, P., J.-P. S. Maurice, C. Lathuillere, and D. Hubert (1998), On the improvement of analytical calculations of collisional auroral ion velocity distributions using recent monte carlo results, *Journal of Geophysical Research*, *103*(A3), 4079–4095.
- Ganguli, G., M. Keskinen, H. Romero, R. Heelis, T. Moore, and C. Pollock (1994), Coupling of microprocesses and macroprocesses due to velocity shear: an application to the low-altitude ionosphere, *J. Geophys. Res.*, *99*, 8873–8889.
- Garcia, K. S., V. G. Merkin, and W. J. Hughes (2010), Effects of nightside O<sup>+</sup> outflow on magnetospheric dynamics: Results of multifluid MHD modeling, *J. Geophys. Res.*, *115*, A00J09, doi:10.1029/2010JA015730.
- Grad, H. (1949), On the kinetic theory of rarefied gases, *Communications on Pure and Applied Mathematics*, *2*(4), 331–407, doi:10.1002/cpa.3160020403.
- Heale, C. J., J. B. Snively, M. P. Hickey, and C. J. Ali (2014), Thermospheric dissipation of upward propagating gravity wave packets, *Journal of Geophysical Research: Space Physics*, *119*(5), 3857–3872, doi:10.1002/2013JA019387.
- Heinselman, J., and J. Nicolls (2008), A bayesian approach to electric field and e region neutral wind estimation with the poker flat advanced modular incoherent scatter radar, *Radio Science*, *43*(5), doi:10.1029/2007RS003805.
- Hines, C. (1960), Internal atmospheric gravity waves at ionospheric heights, *Can. J. Phys.*, *38*, 1441–1481, doi:10.1139/p60-150.
- Hocke, K., and K. Schlegel (1996), A review of atmospheric gravity waves and traveling ionospheric disturbances: 1982–1995, *Ann. Geophys.*, *14*.
- Hocke, K., K. Schlegel, and G. Kirchengast (1995), Phases and amplitudes of tids in the high-latitude f-region observed by eiscat, *J. Atmos. Terr. Phys.*, *57*.
- Huba, J. D., G. Joyce, and J. A. Fedder (2000), Sami2 is another model of the ionosphere (sami2): A new low-latitude ionosphere model, *Journal of Geophysical Research: Space Physics*, *105*(A10), doi:10.1029/2000JA000035.

- Hunsucker, R. (1982), Atmospheric gravity waves generated in the high-latitude ionosphere: A review, *Reviews of Geophysics*, *20*.
- Jones, G., P. Williams, K. Winser, M. Lockwood, and K. Suvanto (1988), Large plasma velocities along the magnetic field line in the auroral zone, *Nature*, *336*(231).
- Jones, G., P. Williams, and K. Winser (1990), Large ionospheric plasma flows along magnetic field lines: Eschat observations and interpretations, *Adv. Space Sci.*
- Jordanova, V. K., L. M. Kistler, J. U. Kozyra, G. V. Khazanov, and A. F. Nagy (1996), Collisional losses of ring current ions, *J. Geophys. Res.*, *101*, 111–126, doi: 10.1029/95JA02000.
- Keating, J. G., F. J. Mulligan, and D. B. Doyle (1990), A statistical study of large field-aligned flows of thermal ions at high-latitudes, *Planet. Space Sci.*, *38*(9), 1187–1201.
- Kelley, M. C. (2009), *The Earth's Ionosphere: Plasma Physics and Electrodynamics*, Academic Press.
- King, J., and H. Kohl (1965), Upper atmospheric winds and ionospheric drifts caused by neutral air pressure gradients, *Nature*, *206*, 699–701.
- Kintner, P. M., J. Bonnell, R. Arnoldy, K. Lynch, C. Pollock, and T. Moore (1996), SCIFER-Transverse ion acceleration and plasma waves, *Geophys. Res. Lett.*, *23*, 1873–1876.
- Kirchengast, G., R. Leitinger, and K. Schlegel (1992), A high-resolution model for the ionospheric f-region at mid-and high-latitude sites, *10*(8), 577–596.
- Kirchengast, G., K. Hocke, and K. Schlegel (1995), Gravity waves determined by modeling of traveling ionospheric disturbances in incoherent-scatter radar measurements, *Radio Sci.*, *30*, 1551–1567.
- Klumpar, D. (1979), Transversely accelerated ions: An ionospheric source of hot magnetospheric ions, *J. Geophys. Res.*, *84*(A8).



- Kohl, H., and J. King (1967), Atmospheric winds between 100 and 700 km and their effects on the ionosphere, *J. Atmos. Terr. Phys.*, *29*(9), 1045 – 1062, doi: 10.1016/0021-9169(67)90139-0.
- Kozyra, J. U., T. E. Cravens, A. F. Nagy, E. G. Fontheim, and R. S. B. Ong (1984), Effects of energetic heavy ions on electromagnetic ion cyclotron wave generation in the plasmopause region, *J. Geophys. Res.*, *89*, 2217–2233, doi: 10.1029/JA089iA04p02217.
- Lennartsson, W., R. D. Sharp, E. G. Shelley, R. G. Johnson, and H. Balsiger (1981), Ion composition and energy distribution during 10 magnetic storms, *Journal of Geophysical Research: Space Physics*, *86*(A6), 4628–4638, doi:10.1029/JA086iA06p04628.
- LeVeque, R. J. (1997), Wave propagation algorithms for multidimensional hyperbolic systems, *Journal of Computational Physics*, *131*(2), 327–353.
- LeVeque, R. J. (2002), *Finite volume methods for hyperbolic problems*, Cambridge university press.
- Lindzen, R. S. (1966), Crude estimate for the zonal velocity associated with the diurnal temperature oscillation in the thermosphere, *Journal of Geophysical Research*, *71*(3), 865–870, doi:10.1029/JZ071i003p00865.
- Liu, C., J. Horwitz, and P. Richards (1995), Effects of frictional heating and soft-electron precipitation on high-latitude f-region upflows, *Geophys. Res. Lett.*, *22*, 2713–2716.
- Liu, H., and G. Lu (2004), Velocity shear-related ion upflow in the low-altitude ionosphere, *Annales Geophysicae*, *22*(4), 1149–1153, doi:10.5194/angeo-22-1149-2004.
- Lotko, W. (2007), The magnetosphere–ionosphere system from the perspective of plasma circulation: A tutorial, *Journal of Atmospheric and Solar-Terrestrial Physics*, *69*(3), 191–211.

- Lynch, K. A., J. L. Semeter, M. Zettergren, and P. Kinter (2007), Auroral ion outflow: Low altitude energization, *Ann. Geophys.*, 25.
- Lynch, K. A., D. L. Hampton, M. Zettergren, T. A. Bekkeng, M. Conde, P. A. Fernandes, P. Horak, M. Lessard, R. Miceli, R. Michell, J. Moen, M. Nicolls, S. P. Powell, and M. Samara (2015), Mica sounding rocket observations of conductivity-gradient-generated auroral ionospheric responses: Small-scale structure with large-scale drivers, *Journal of Geophysical Research: Space Physics*, 120(11), 9661–9682, doi:10.1002/2014JA020860.
- Ma, Y.-Z., Q.-H. Zhang, Z.-Y. Xing, P. T. Jayachandran, J. Moen, R. A. Heelis, and Y. Wang (2018), Combined contribution of solar illumination, solar activity, and convection to ion upflow above the polar cap, *Journal of Geophysical Research: Space Physics*, 123(5), 4317–4328, doi:10.1029/2017JA024974.
- MacDougall, J., and P. Jayachandran (2011), Solar terminator and auroral sources for traveling ionospheric disturbances in the midlatitude f region, *J. Atmos. Sol. Terr. Phys.*, 73.
- Maeda, S. (1985), Numerical solutions of the coupled equations for acoustic-gravity waves in the upper thermosphere, *J. Atmos. Terr. Phys.*, 47.
- Marchaudon, A., and P.-L. Blelly (2015), A new interhemispheric 16-moment model of the plasmasphere-ionosphere system: Ipim, *Journal of Geophysical Research: Space Physics*, 120(7), 5728–5745, doi:10.1002/2015JA021193.
- Marklund, G. (1984), Auroral arc classification scheme based on the observed arc-associated electric field pattern, *Planetary and Space Science*, 32(2), 193 – 211, doi:10.1016/0032-0633(84)90154-5.
- Maurice, J.-P. S., and R. W. Schunk (1977), Auroral ion velocity distributions for a polarization collision model, *Planet. Space Sci.*, 25, 243–260.
- McFarland, M., D. L. Albritton, F. C. Fehsenfeld, E. E. Ferguson, and A. L. Schmeltekopf (1973), Flow-drift technique for ion mobility and ion-molecule reaction rate constant measurements. ii. positive ion reactions of n+, o+, and h2+

- with  $\text{o}^2$  and  $\text{o}^+$  with  $\text{n}^2$  from thermal to  $\sim 2$  eV, *The Journal of Chemical Physics*, *59*(12), 6620–6628, doi:10.1063/1.1680042.
- Michell, R. G., M. Samara, G. Grubbs, K. Ogasawara, G. Miller, J. A. Trevino, J. Webster, and J. Stange (2016), Apes: Acute precipitating electron spectrometer - a high time resolution monodirectional magnetic deflection electron spectrometer, *Journal of Geophysical Research: Space Physics*, *121*(6), 5959–5965, doi:10.1002/2016JA022637.
- Moore, T. E. (1991), Origins of magnetospheric plasma, *Rev. Geophys.*, *29*, 1039.
- Moore, T. E., R. Lundin, D. Alcaide, M. André, S. B. Ganguli, M. Temerin, and A. Yau (1999), Chapter 2-Source Processes in the High-Latitude Ionosphere, *Space Sci. Rev.*, *88*, 7–84.
- Nicolls, M. J., and C. J. Heinselman (2007), Three-dimensional measurements of traveling ionospheric disturbances with the poker flat incoherent scatter radar, *Geophysical Research Letters*, *34*(21), doi:10.1029/2007GL031506.
- Nicolls, M. J., M. C. Kelley, A. J. Coster, S. A. González, and J. J. Makela (2004), Imaging the structure of a large-scale tid using isr and tec data, *Geophysical Research Letters*, *31*(9), doi:10.1029/2004GL019797.
- Nicolls, M. J., S. L. Vadas, N. Aponte, and M. P. Sulzer (2013), Horizontal parameters of daytime thermospheric gravity waves and e region neutral winds over puerto rico, *Journal of Geophysical Research: Space Physics*, *119*(1), 575–600, doi:10.1002/2013JA018988.
- Nishikawa, K.-I., G. L. Ganguli, Y. C. Lee, and P. J. Palmadesso (1990), Simulation of electrostatic turbulence due to sheared flows parallel and transverse to the magnetic field, *J. Geophys. Res.*, *95*, 1029–1038.
- Oberheide, J., K. Shiokawa, S. Gurubaran, W. E. Ward, H. Fujiwara, M. J. Kosch, J. J. Makela, and H. Takahashi (2015), The geospace response to variable inputs

- from the lower atmosphere: a review of the progress made by task group 4 of cawses-ii, *Progress in Earth and Planetary Science*, 2(1), doi:10.1186/s40645-014-0031-4.
- Ogawa, T., K. Igarashi, K. Aikyo, and H. Maeno (1987), Nnss satellite observations of medium-scale traveling ionospheric disturbances at southern high-latitudes, *J. Geomag. Geoelectr.*, 39, 709–721.
- Ogawa, Y., R. Fujii, S. Buchert, and S. Nozawa (2000), Simultaneous eiscat svalbard and vhf radar observations of ion upflows at different aspect angles, *Geophys. Res. Lett.*, 27, 81–84.
- Ogawa, Y., R. Fujii, S. C. Buchert, S. Nozawa, and S. Ohtani (2003), Simultaneous eiscat svalbard radar and dmsp observations of ion upflow in the dayside polar ionosphere, *J. Geophys. Res.*, 108, 1101.
- Ogawa, Y., K. Seki, M. Hirahara, K. Asamura, T. Sakanoi, S. Buchert, Y. Ebihara, Y. Obuchi, A. Yamazaki, I. Sandahl, S. Nozawa, and R. Fujii (2008), Coordinated eiscat svalbard radar and reimei satellite observations of ion upflows and suprathermal ions, *J. Geophys. Res.*, 113(A5).
- Ogawa, Y., S. C. Buchert, R. Fujii, S. Nozawa, and A. P. van Eyken (2009), Characteristics of ion upflow and downflow observed with european incoherent scatter svalbard radar, *J. Geophys. Res.*, 114.
- Ogawa, Y., S. C. Buchert, A. Sakurai, S. Nozawa, and R. Fujii (2010), Solar activity dependence of ion upflow in the polar ionosphere observed with the european incoherent scatter (eiscat) tromso uhf radar, *Journal of Geophysical Research.Space Physics*, 115(7).
- Oraevskii, V., R. Chodura, and W. Feneberg (1968), Hydrodynamic equations for plasmas in strong magnetic fields - i: Collisionless approximation, *Plasma Physics*, 10(9), 819, doi:10.1088/0032-1028/10/9/302.
- Palmadesso, P. J., S. B. Ganguli, and H. G. Mitchell, Jr. (1988), Multimoment fluid simulations of transport processes in the auroral zones, *Washington DC*

- American Geophysical Union Geophysical Monograph Series*, 44, 133–143, doi:10.1029/GM044p0133.
- Perry, G. W., H. Dahlgren, M. J. Nicolls, M. Zettergren, J.-P. St.-Maurice, J. L. Semeter, T. Sundberg, K. Hosokawa, K. Shiokawa, and S. Chen (2015), Spatiotemporally resolved electrodynamic properties of a sun-aligned arc over resolute bay, *Journal of Geophysical Research: Space Physics*, 120(11), 9977–9987, doi:10.1002/2015JA021790.
- Picone, J. M., A. E. Hedin, D. P. Drob, and A. C. Aikin (2002), Nrlmsise-00 empirical model of the atmosphere: Statistical comparisons and scientific issues, *Journal of Geophysical Research: Space Physics*, 107(A12), SIA 15–1–SIA 15–16, doi:10.1029/2002JA009430.
- Raman, R. S. V., J. P. St-Maurice, and R. S. B. Ong (1981), Incoherent scattering of radar waves in the auroral ionosphere, *Journal of Geophysical Research: Space Physics*, 86(A6), 4751–4762, doi:10.1029/JA086iA06p04751.
- Redmon, R. J., W. K. Peterson, L. Andersson, and P. G. Richards (2012), Dawnward shift of the dayside o+ outflow distribution: The importance of field line history in o+ escape from the ionosphere, *Journal of Geophysical Research: Space Physics*, 117(A12).
- Retterer, J. M., T. Chang, and J. R. Jasperse (1983), Ion acceleration in the supraraural region: A monte carlo model, *Geophysical Research Letters*, 10(7), 583–586, doi:10.1029/GL010i007p00583.
- Richards, P., and D. Torr (1996), The field line interhemispheric plasma model, *STEP: Handbook of Ionospheric Models*, pp. 207–216.
- Richmond, A. (1978), Gravity wave generation, propagation, and dissipation in the thermosphere, *J. Geophys. Res.*, 83, 4131–4145.
- Rishbeth, H. (1972), Thermospheric winds and the f-region: A review, *J. Atmos. Terr. Phys.*, 34(1), 1 – 47, doi:10.1016/0021-9169(72)90003-7.

- Rishbeth, H., and O. Garriott (1969), *Introduction to ionospheric physics*, Academic Press.
- Roberts, T. M., K. Lynch, R. Clayton, M. Disbrow, and C. Hansen (2017a), Magnetometer-based attitude determination for deployed spin-stabilized spacecraft, *Journal of Guidance, Control, and Dynamics*, pp. 2941–2947.
- Roberts, T. M., K. Lynch, R. Clayton, J. Weiss, and D. Hampton (2017b), A small spacecraft for multipoint measurement of ionospheric plasma, *Review of Scientific Instruments*, 88(7), 073,507, doi:10.1063/1.4992022.
- Sadler, F. B., M. Lessard, E. Lund, A. Otto, and H. Luhr (2012), Auroral precipitation/ion upwelling as a driver of neutral density enhancement in the cusp, *Journal of Atmospheric and Solar-Terrestrial Physics*, 87-88, 82 – 90, doi:10.1016/j.jastp.2012.03.003.
- Sanchez, E. R., and A. Strømme (2014), Incoherent scatter radar-fast satellite common volume observations of upflow-to-outflow conversion, *Journal of Geophysical Research: Space Physics*, 119(4), 2649–2674, doi:10.1002/2013JA019096.
- Sauli, P., P. Abry, J. Boska, and L. Duchayne (2006), Wavelet characterisation of ionospheric acoustic and gravity waves occurring during the solar eclipse of august 11, 1999, *J. Atmos. Sol. Terr. Phys.*, 68, 586–598.
- Sauvaud, J.-A., P. Louarn, G. Fruit, H. Stenuit, C. Vallat, J. Dandouras, H. Reme, M. André, A. Balogh, M. Dunlop, et al. (2004), Case studies of the dynamics of ionospheric ions in the earth’s magnetotail, *Journal of Geophysical Research: Space Physics*, 109(A1).
- Schunk, R. W. (1975), Transport equations for aeronomy, *Planetary and Space Science*, 23(3), 437 – 485, doi:10.1016/0032-0633(75)90118-X.
- Schunk, R. W. (1977), Mathematical structure of transport equations for multispecies flows, *Reviews of Geophysics and Space Physics*, 15(4).

- Schunk, R. W., and A. Nagy (2000), *Ionospheres*, Cambridge University Press, Cambridge.
- Schunk, R. W., and A. F. Nagy (1978), Electron temperatures in the f region of the ionosphere: Theory and observations, *Reviews of Geophysics*, *16*(3), 355–399.
- Semeter, J., C. J. Heinselman, J. P. Thayer, R. A. Doe, and H. U. Frey (2003), Ion upflow enhanced by drifting F-region plasma structure along the nightside polar cap boundary, *Geophys. Res. Lett.*, *30*, 2139.
- Sharp, R. D., W. Lennartsson, and R. J. Strangeway (1985), The ionospheric contribution to the plasma environment in near-earth space, *Radio Science*, *20*(3), 456–462, doi:10.1029/RS020i003p00456.
- Shay, M. A., J. F. Drake, M. Swisdak, and B. N. Rogers (2004), The scaling of embedded collisionless reconnection, *Physics of Plasmas*, *11*, 2199–2213, doi:10.1063/1.1705650.
- Shelley, E. G., R. G. Johnson, and R. D. Sharp (1972), Satellite observations of energetic heavy ions during a geomagnetic storm, *Journal of Geophysical Research*, *77*(31), 6104–6110, doi:10.1029/JA077i031p06104.
- Singh, N. (1992), Plasma perturbations created by transverse ion heating events in the magnetosphere, *Journal of Geophysical Research: Space Physics*, *97*(A4), 4235–4249.
- Singh, N., D. T. S. Hwang, and P. Richards (1989), Temporal features of the outflow of heavy ionospheric ions in response to a high altitude plasma cavity, *Geophys. Res. Lett.*, *16*(29).
- Skjaeveland, A., J. Moen, and H. C. Carlson (2011), On the relationship between flux transfer events, temperature enhancements, and ion upflow events in the cusp ionosphere, *Journal of Geophysical Research: Space Physics*, *116*(A10).

- Snively, J. B. (2013), Mesospheric hydroxyl airglow signatures of acoustic and gravity waves generated by transient tropospheric forcing, *Geophysical Research Letters*, *40*(17), 4533–4537, doi:10.1002/grl.50886.
- Snively, J. B., and V. P. Pasko (2008), Excitation of ducted gravity waves in the lower thermosphere by tropospheric sources, *Journal of Geophysical Research: Space Physics*, *113*(A6), doi:10.1029/2007JA012693.
- Solomon, S., and L. Qian (2005), Solar extreme-ultraviolet irradiance for general circulation models, *J. Geophys. Res.*, *110*.
- St.-Maurice, J.-P., and P. J. Laneville (1998), Reaction rate of  $O^+$  with  $O_2$ ,  $N_2$ , and  $NO$  under highly disturbed auroral conditions, *Journal of Geophysical Research: Space Physics*, *103*(A8), 17,519–17,521, doi:10.1029/98JA01387.
- St.-Maurice, J.-P., and R. W. Schunk (1979), Ion velocity distributions in the high-latitude ionosphere, *Reviews of Geophysics*, *17*(1), 99–134, doi:10.1029/RG017i001p00099.
- St.-Maurice, J.-P., and D. G. Torr (1978), Nonthermal rate coefficients in the ionosphere: The reactions of  $o^+$  with  $n_2$ ,  $o_2$ , and  $no$ , *Journal of Geophysical Research: Space Physics*, *83*(A3), 969–977, doi:10.1029/JA083iA03p00969.
- Strangeway, R. J., R. E. Ergun, Y. J. Su, C. W. Carlson, and R. C. Elphic (2005), Factors controlling ionospheric outflows as observed at intermediate altitudes, *J. Geophys. Res.*, *110*.
- Su, Y., R. Caton, J. Horwitz, and P. Richards (1999), Systematic modeling of soft-electron precipitation effects on high-latitude f region and topside ionospheric upflows, *Journal of geophysical research*, *104*, 153–163.
- Swartz, W. E., and J. S. Nisbet (1972), Revised calculations of f region ambient electron heating by photoelectrons, *Journal of Geophysical Research*, *77*(31), 6259–6261, doi:10.1029/JA077i031p06259.



- Sydorenko, D., and R. Rankin (2013), Simulation of  $o^+$  upflows created by electron precipitation and alfvén waves in the ionosphere, *Journal of Geophysical Research: Space Physics*, *118*(9), 5562–5578, doi:10.1002/jgra.50531.
- Testud, J., and P. Francois (1971), Importance of diffusion processes in the interaction between neutral waves and ionization, *Journal of Atmospheric and Terrestrial Physics*, *33*(5), 765–774.
- Thome, G. D. (1964), Incoherent scatter observations of traveling ionospheric disturbances, *Journal of Geophysical Research*, *69*(19), 4047–4049, doi:10.1029/JZ069i019p04047.
- Titheridge, J. (1995), Winds in the ionosphere - a review, *J. Atmos. Terr. Phys.*, *57*(14), 1681 – 1714, doi:https://doi.org/10.1016/0021-9169(95)00091-F.
- Torr, M. R., D. G. Torr, and J.-P. St-Maurice (1977), The rate coefficient for the  $o^+ + n_2$  reaction in the ionosphere, *Journal of Geophysical Research*, *82*(22), 3287–3290, doi:10.1029/JA082i022p03287.
- Torrence, C., and G. Compo (1998), A practical guide to wavelet analysis, *Bulletin of the American Meteorological Society*, *79*(1), 61–78, doi:10.1175/1520-0477(1998)079<0061:APGTWA>2.0.CO;2.
- Vadas, S., and D. Fritts (2005), Inermospheric responses to gravity waves: influences of increasing viscosity and thermal diffusivity, *J. Geophys. Res.*, *110*, doi:10.1029/2004JD005574.
- Vadas, S. L., and M. J. Nicolls (2007), Using pfisr measurements and gravity wave dissipative theory to determine the neutral, background thermospheric winds, *Geophysical Research Letters*, *35*(2), doi:10.1029/2007GL031522.
- Vlasov, A., K. Kauristie, M. Van De Kamp, J.-P. Luntama, and A. Pogoreltsev (2011), A study of traveling ionospheric disturbances and atmospheric gravity waves using eiscat svalbard radar ipy-data, *Annales Geophysicae*, *29*(11), 2101.

- Wahlund, J.-E., and H. J. Opgenoorth (1989), EISCAT observations of strong ion outflows from the f-region ionosphere during auroral activity: Preliminary results, *Geophys. Res. Lett.*, *16*(7), 727–730, doi:10.1029/GL016i007p00727.
- Wahlund, J.-E., H. J. Opgenoorth, I. Häggström, K. J. Winser, and G. O. L. Jones (1992), EISCAT observations of topside ionospheric ion outflows during auroral activity: Revisited, *J. Geophys. Res.*, *97*(A3), 3019–3037.
- Whalen, B., S. Watanabe, and A. Yau (1991), Thermal and suprathermal ion observations in the low altitude transverse ion energization region, *Geophys. Res. Lett.*, *18*, 725–728.
- Whalen, B. A., W. Bernstein, and P. W. Daly (1978), Low altitude acceleration of ionospheric ions, *Geophys. Res. Lett.*, *5*(1), 55–58, doi:10.1029/GL005i001p00055.
- Whittaker, J. (1977), The transient response of the topside ionosphere to precipitation, *Planet. Space Sci.*, *25*(773).
- Wilson, G. R., C. W. Ho, J. L. Horwitz, N. Singh, and T. E. Moore (1990), A new kinetic model for time-dependent polar plasma outflow: Initial results, *Geophys. Res. Lett.*, *17*(3), 263–266, doi:10.1029/GL017i003p00263.
- Wu, X.-Y., J. L. Horwitz, G. M. Estep, Y.-J. Su, D. G. Brown, P. G. Richards, and G. R. Wilson (1999), Dynamic fluid-kinetic (dyfk) modeling of auroral plasma outflow driven by soft electron precipitation and transverse ion heating, *Journal of Geophysical Research: Space Physics*, *104*(A8), 17,263–17,275, doi:10.1029/1999JA900114.
- Wu, X.-Y., J. L. Horwitz, and J.-N. Tu (2002), Dynamic fluid kinetic (dyfk) simulation of auroral ion transport: Synergistic effects of parallel potentials, transverse ion heating, and soft electron precipitation, *Journal of Geophysical Research: Space Physics*, *107*(A10), doi:10.1029/2000JA000190.
- Yiğit, E., A. D. Aylward, and A. S. Medvedev (2008), Parameterization of the effects of vertically propagating gravity waves for thermosphere general circulation models:

- Sensitivity study, *Journal of Geophysical Research: Atmospheres*, 113(D19), doi:10.1029/2008JD010135.
- Yiğit, E., P. K. Knížová, K. Georgieva, and W. Ward (2016), A review of vertical coupling in the atmosphere-ionosphere system: Effects of waves, sudden stratospheric warmings, space weather, and of solar activity, *J. Atmos. Sol. Terr. Phys.*, 141, 1 – 12, doi:<https://doi.org/10.1016/j.jastp.2016.02.011>.
- Yokoyama, T., D. Hysell, Y. Otsuka, and M. Yamamoto (2009), Three-dimensional simulation of the coupled Perkins and Es-layer instabilities in the nighttime mid-latitude ionosphere, *Journal of Geophysical Research: Space Physics*, 114(A3), doi:10.1029/2008JA013789.
- Yoshida, N., S. Watanabe, H. Fukunishi, T. Sakanoi, T. Mukai, H. Hayakawa, A. Matsuoka, Y. Kasahara, R. Fujii, S. Nozawa, and Y. Ogawa (1999), Coordinated Akebono and EISCAT observations of suprathermal ion outflow in the nightside inverted-v region, *J. Atmos. Sol. Terr. Phys.*, 62, 449–465.
- Yu, Y., and A. J. Ridley (2013), Exploring the influence of ionospheric O<sup>+</sup> outflow on magnetospheric dynamics: The effect of outflow intensity, *Journal of Geophysical Research (Space Physics)*, 118, 5522–5531, doi:10.1002/jgra.50528.
- Zeng, W., and J. L. Horwitz (2007), Formula representation of auroral ionospheric O<sup>+</sup> outflows based on systematic simulations with effects of soft electron precipitation and transverse ion heating, *Geophys. Res. Lett.*, 34(6), doi:10.1029/2006GL028632.
- Zeng, W., and J. L. Horwitz (2008), Storm enhanced densities (sed) as possible sources for cleft ion fountain dayside ionospheric outflows, *Geophys. Res. Lett.*, 35(4), doi:10.1029/2007GL032511.
- Zeng, W., J. L. Horwitz, and J.-N. Tu (2006), Characteristic ion distributions in the dynamic auroral transition region, *Journal of Geophysical Research: Space Physics*, 111(A4), doi:10.1029/2005JA011417.

- Zettergren, M., and J. Semeter (2012), Ionospheric plasma transport and loss in auroral downward current regions, *Journal of Geophysical Research: Space Physics*, *117*(A6), doi:10.1029/2012JA017637.
- Zettergren, M., and J. Snively (2013), Ionospheric signatures of acoustic waves generated by transient tropospheric forcing, *Geophysical Research Letters*, *40*(20), 5345–5349, doi:10.1002/2013GL058018.
- Zettergren, M., J. Semeter, P.-L. Blelly, G. Sivjee, I. Azeem, S. Mende, H. Gleisner, M. Diaz, and O. Witasse (2008), Optical estimation of auroral ion upflow: 2. a case study, *Journal of Geophysical Research: Space Physics*, *113*(A7), doi:10.1029/2008JA013135.
- Zettergren, M., J. Semeter, B. Burnett, W. Oliver, C. Heinselman, M. Díaz Beneventi, and P.-L. Blelly (2010), Dynamic variability in f-region ionospheric composition at auroral arc boundaries.
- Zettergren, M., K. Lynch, D. Hampton, M. Nicolls, B. Wright, M. Conde, J. Moen, M. Lessard, R. Miceli, and S. Powell (2014), Auroral ionospheric f region density cavity formation and evolution: Mica campaign results, *Journal of Geophysical Research: Space Physics*, *119*(4), 3162–3178, doi:10.1002/2013JA019583.
- Zettergren, M. D., and J. B. Snively (2015), Ionospheric response to infrasonic-acoustic waves generated by natural hazard events, *Journal of Geophysical Research: Space Physics*, *120*(9), 8002–8024, doi:10.1002/2015JA021116.
- Zhao, K., K. W. Chen, Y. Jiang, W. J. Chen, L. F. Huang, and S. Fu (2018), Latitude dependence of low-altitude o+ ion upflow: Statistical results from fast observations, *Journal of Geophysical Research: Space Physics*, *122*(9), 9705–9722, doi:10.1002/2017JA024075.